POLITECNICO DI MILANO

School of Industrial and Information Engineering

Doctoral Program in Energy and Nuclear Science and Technology

Cycle XXXI

MEASUREMENTS TECHNIQUES FOR NON-IDEAL COMPRESSIBLE FLUID FLOWS: APPLICATIONS TO ORGANIC FLUIDS

Supervisor: Prof. Andrea Spinelli

Co-Supervisor: Prof. Alberto Guardone

Tutor: Prof. Vincenzo Dossena

Doctoral Dissertation of:

GIORGIA CAMMI

ABSTRACT

Non-ideal compressible flows of molecularly complex vapors occurring within the thermodynamic region in the close proximity of the liquid-vapor saturation curve are of interest for diverse industrial applications; in particular for the turbomachines employed in Organic Rankine Cycles. Several computational fluid dynamics tools embedding complex thermodynamic models suitable to simulate such flows are currently available. However, detailed experimental data characterizing non-ideal compressible flows, which are needed to validate these tools, are unavailable in the open literature up to date. These data can be obtained in dedicated wind tunnel facilities. However, running these facilities presents many technical challenges due to the high temperature, high pressure and thermodynamic conditions close to the fluid thermal stability limit.

This thesis presents three successful experimental campaigns conducted on a wind tunnel operated with organic vapors. Several experiments were conducted on the Test Rig for Organic VApors (TROVA) at the Compressible fluid dynamic for Renewable Energy Applications laboratory (CREA). The TROVA test section was equipped with different converging-diverging nozzles. Measurements of upstream total pressure and temperature, static pressures, local Mach numbers along the nozzle axis and schlieren visualizations were carried out for two different organic fluids octamethyltrisiloxane $C_8H_{24}O_2Si_3$ (MDM) and hexamethyldisiloxane $C_6H_{18}O_3Si_3$ (MM).

This thesis focuses on measurement techniques, with particular reference to the effect of the peculiar thermodynamic conditions in which measurements are carried out. A methodology to calibrate piezoresistive pressure transducers, permitting their use at different temperature and providing a reliable estimation of the uncertainty related to each measurement is presented. Moreover, an algorithm to automatically detect Mach waves in schlieren images and exploit them to directly measure the local Mach number was developed. Three different experimental campaigns were conducted, focused on the characterization of the expansion of molecularly complex vapors in nozzles. To this purpose three fluids having different molecular complexity and molecular mass, i.e. nitrogen, MM and MDM, were tested in four nozzles. Results in terms of pressure ratios and local Mach number along the nozzle axis are presented for each of the three experimental campaigns. The measurement techniques adopted proved to be suitable to detect non-ideal behaviors in compressible non-ideal flows.

Indeed, the analysis of the results obtained proved the non-ideal nature of both MDM and MM nozzle flows. Moreover it was found that in the thermodynamic region explored, the total compressibility factor Z_T performs better as univocal identifier of a nozzle expansion with respect to the total fundamental derivative of gas-dynamic Γ_T. The value of Z_T can thus be used to predict pressure ratios along the axis with an error lower than 5%. Moreover, the influence of total temperature on the flow was also analyzed and a

comparison between MM and MDM nozzle flows at the same total reduced conditions was performed.
In conclusion, this thesis reports a reliable methodology which is applicable to perform experiments on high temperature and potentially condensing vapor flows in highly non-ideal thermodynamic conditions. This methodology represent the starting point towards the implementation of other experimental techniques capable of measuring further data, such as the velocity vector, in non-ideal compressible flows. Moreover, it provided the first data, useful to assess the performances of Computational Fluid Dynamics (CFD) tools in the non-ideal compressible regime, currently available in the open literature.

CONTENTS

1

INTRODUCTION

1.1 OBJECTIVES AND MOTIVATION

Compressible fluid flows are found in many engineering applications including internal flows in rocket and gas turbine engines, external flows over airplanes and over space vehicles. Indeed, because of their paramount importance, such flows have been widely studied both experimentally, e.g. through wind tunnel tests, and numerically using Computational Fluid Dynamics (CFD) codes. However, most of the studies performed to date are related to flows of gases in dilute conditions following the well known ideal gas law $Pv = RT$, where P is the pressure, v the specific volume, T the temperature and R the specific gas constant.
Nevertheless, there are important engineering applications featuring flows of compressible vapors occurring close to the liquid-vapor saturation curve where the ideal gas law does not hold. All machines involving supercritical, condensing, cavitating and criogenic flows are among them. This thesis focuses on the expanding flows found in Organic Rankine Cycle (ORC) expanders. ORC systems represent an effective technology for generating electricity from low-to-medium temperature heat sources. They typical employ molecularly complex fluids also exhibiting high molecular mass. The ORC typical cycle configuration usually characterized by minimum or zero superheating and hence ORC expanders operate to a large extent in a thermodynamic region where non-negligible non-ideal compressible effects are present.
Two fundamental quantities can be used to define the degree of non ideality of a flow: the compressibility factor Z and the fundamental derivative of gasdynamic Γ.

$$Z = \frac{Pv}{RT} \tag{1}$$

$$\Gamma = \frac{c^4}{2v^3}\left(\frac{\partial^2 v}{\partial P^2}\right)_s = 1 + \frac{c}{v}\left(\frac{\partial c}{\partial P}\right)_s \tag{2}$$

where c is the speed of sound. The value of Z tells whether a flow can be modeled using the ideal gas model or not. For example, in a flow characterized by $Z \neq 1$ the non-dimensional behavior of isentropic expansions is dependent on the flow stagnation conditions and not only on the expander geometry, as it is the case of ideal-gases. This can be observed by analyzing the flow in terms of local Mach number M and static-to-total ratio of local thermodynamic quantities.
The value of the fundamental derivative of gasdynamics Γ, instead, provides information about the admissible behaviors of the flow. Indeed, as stated in equation (2) the fundamental derivative of gasdynamic can be interpreted as the non-dimensional measure

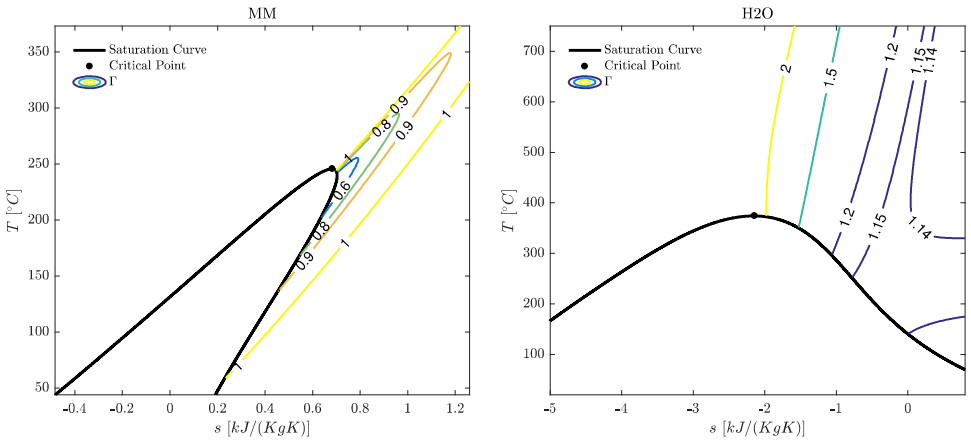

(a) *Saturation curve and* Γ *isolines drawn in the Ts diagram for the fluid MM.*

(b) *Saturation curve and* Γ *isolines drawn in the Ts diagram for water.*

Figure 1.1: Temperature vs entropy diagram for two different fluids.

of the variation of the speed of sound with the pressure along an isentropic transformation. For a Polytropic Ideal Gas (PIG), which is an ideal gas with constant specific heat capacities, it reduces to $\Gamma = (\gamma + 1)/2$ where γ is the specific heat capacity ratio and it is then always grater than 1. A thermodynamic region exhibiting $\Gamma < 1$ can be found only in fluids characterized by a high molecular complexity of the molecule. The molecular complexity of a fluid can be quantified by the value of N number of active degrees of freedom. $N = 2MCv_0(T_c)/R$ where M is the molecular weight, T_c is the critical temperature and Cv_0 is the ideal gas contribution to the specific heat capacity at constant volume evaluated at critical conditions. Following the Van der Waals equation of state one can find that only fluids characterized by $N > 7.57$ exhibit a thermodynamic region where $\Gamma < 1$. For example the complex fluid MM has $N_{MM} = 77.4$ while water has $N_{H2O} = 6.87$, both calculated at the critical point see (Harinck et al., 2009). Indeed, it can be seen, looking at Figure 1.1, that, while the former exhibits a wide thermodynamic region where $\Gamma < 1$, the latter shows no such region.

The behaviour of flows characterised by $\Gamma < 1$, depart significantly from the ideal-gas one since it makes admissible some peculiar behaviors. For example, if $\Gamma < 1$ the velocity of sound c increases along expansions and this can lead to a possible decreasing of the local Mach number (Vimercati et al., 2018). Moreover, peculiar phenomena as the discontinuous increase of Mach number across oblique shocks become possible. All these and other peculiar flow features, belong to the non-ideal classical gasdynamic regime $0 < \Gamma < 1$.
In this framework a flow is labeled as non-ideal when it is characterized by a value of the fundamental derivative of gasdynamic (Eqn.(2)) lower than 1 (Thompson, 1971). Among non-ideal flows a distinction can be made between classical ones, characterized by $0 < \Gamma < 1$, and non-classical ones having $\Gamma > 0$ (D'Angelo et al., 2018; Vimercati et al., 2018). In non-classical non-ideal compressible flows rarefaction shock waves are

admissible contrarily to the classical regimes where only compression shocks are possible. The expansion taking place in ORC turbo-expanders occur at least partly in the non-ideal classical gasdynamic regime. Furthermore, some studies show that supercritical cycle have potential for gaining in efficiency (Schuster et al., 2010). Exploit these cycles will push the expansion closer to the critical point where non-ideal effects are stronger and even non-classical flow regimes may occur. Some studies begin to illustrate the influence of non-ideal effects on the ORC turbine performance and on its design (Spinelli et al., 2011; Colonna et al., 2008b; Harinck et al., 2009; Vimercati et al., 2017).
The design and optimization of ORC expanders require software tools embedding complex thermodynamic models capable of correctly compute a flow field taking into account non-ideal compressible effects. These tools need to be validated against experimental data. Many authors, performing CFD simulations, report the lack of experimental data of organic flows in the non-ideal thermodynamic region (Colonna et al., 2008b; Vitale et al., 2015). Indeed, despite the effort that has been dedicated to advancing the numerical modeling of ORC turbine flows, nearly all the publications reporting CFD results do not report any comparison between the calculated flow-field and experimental data (Sciacovelli and Cinnella, 2014; Rinaldi et al., 2016; Sauret and Yuantong, 2014). The only exception to the author's knowledge is the study of trailing edge losses reported in (Dùra Galiana et al., 2016).
Detailed experimental data characterizing non-ideal compressible flows can be obtained only exploiting dedicated wind tunnel facilities. However, running these facilities presents many challenges since these flows take place at high temperature, relatively high pressure and at thermodynamic conditions near to saturation and to the fluid thermal stability limit. The aim of this thesis is to provide a reliable methodology applicable to perform experiments in the above mentioned conditions. The methodology proposed was applied to carry out three different experimental campaigns with the aim of providing the first ever experimental characterization of molecularly complex fluids expanding in thermodynamic regions where $\Gamma < 1$. Part of these data were already made available in the open literature (Spinelli et al., 2018) and they were used to carry out an assessment of the CFD software SU2 (SU2) (Gori et al., 2017).

1.2 THESIS OUTLINE

This thesis is organized as follows: this first chapter 1 presents in section 1.3 a review of all the experimental facilities that are worldwide dedicated to the study of ORC turboexpanders, then, section 1.4, describes the TROVA facility. Chapter 2 is devoted to the presentation of all the measurements techniques applied and developed within this thesis. In particular, section 2.2 describes the pressure measurements and the method adopted for the uncertainty quantification, section 2.3 presents the temperature measurements and finally section 2.4 reports the Mach measurement techniques developed during the thesis that employs schlieren images. Each section focuses on the technical issues encountered

due to the specific application of the measuring techniques to non-ideal compressible organic vapors.
Chapter 3 presents the three experimental campaigns conducted and their purpose. Chapters 4, 5 and 6 describe the results coming from the three experimental campaigns. Chapter 4 focuses on the characterization of nozzle expansion of four different nozzles with the PIG nitrogen. Chapter 5 is devoted to the characterization of organic vapor MDM nozzle expansion focusing on the measurements proving its non-ideal behavior. It reports also a comparison between CFD and experimental data. Chapter 6 presents the experimental results obtained using the organic vapor MM and it investigate how different parameters as for example the total compressibility factor or the total fundamental derivative of gas-dynamic influenced the non-dimensional nozzle flow-field. Moreover, it reports also a comparison between MM and MDM pressure ratio profiles obtained at the same reduced total condition.
Finally, chapter 7 illustrates conclusions and further works.

1.3 MEASUREMENTS IN NON-IDEAL COMPRESSIBLE FLUID FLOWS: A LITERATURE REVIEW

National and international policies, aiming at reducing green house gas emissions and forcing economic growth to follow a more sustainable path, are boosting scientific researches about power plants exploiting renewable sources and heat recovery systems. Organic Rankine Cycles represent a competitive and mature technology for generating electricity from low-to-medium temperature sources, compatible with liquid dominated geothermal reservoir, biomass combustion, Concentrating Solar Power (CSP) systems and Combined Heat and Power (CHP) systems and heat recovery from industrial processes. Their industrial success is documented by the increasing number of installations all over the world. The current cumulative installed capacity is well over 3 GWe and about 100 units are commissioned every year (Colonna et al., 2015a; Tartière and Astolfi, 2017).
Despite being a technology mature enough to experience such a success on the market; room for improvement is left to increase the system efficiency. Moreover, several technical challenges have yet to be faced to make feasible innovative cycle configurations as the supercritical ones, to make commercially mature small scale systems and to reduce the performance sensitivity of ORCs to variable operating conditions.
In particular, if one considers only the larger installations ranging from 100 kW to few MW, one of the key component affecting the efficiency of the system is the turboexpander (Quoilin et al., 2013). Moreover, there has recently been a large number of researches focusing on the development of turbines also for small scale ($< 100 kW$) ORCs ("Centrifugal Turbines for Mini-Organic Rankine Cycle Power Systems"; Bahamonde et al., 2017). ORC turboexpanders are currently designed as a baseline using empirical and semi-empirical loss correlations derived for ideal gases. Nevertheless, alternative methods, specifically conceived for non-ideal fluids and usually based on an extended version of the method

of characteristics suitable for the non-ideal regime, are appearing in the open literature (Bahamonde et al., 2017; Bufi and Cinnella, 2018). Although, they are applicable only to supersonic turbine designs.
The baseline can be than optimized using adjoint methods or evolutionary methods ("Design method for turbomachinery working in the NICFD regime"; Persico et al., 2018). Both the methods rely on CFD simulations performed with solvers coupled to complex thermodynamic models, as the improved Peng Robinson model proposed by (Stryjek and Vera, 1986) or the Span Wagner model (Span and Wagner, 2003b; Span and Wagner, 2003a). Nevertheless, the turboexpander efficiency prediction that is provided by these methods can be far from the reality even because the absence of detailed experimental makes impossible to assess the flow-field predicted by the CFD softwares available.
These issues have fostered the construction of facilities dedicated to the study of ORC turboexpander. An up to date list of all the facilities dedicated to this scope is reported in Table 1.1. It can be noticed that most of them are of recent construction and some are yet to become operative, which is another indicator of the growing interest towards ORC technology.
The experimental facilities can be classified as follows.

- **Turbine fitted facilities:** these facilities are devoted to the characterization of turboexpander and cycle performances. They usually include all the components that are found in an actual ORC power system; evaporator, superheater, preheater, recuperator, condenser, pump and of course the turbine. Each component, including the turbine, is seen as a black box and the measurements performed are mainly of pressures and temperatures taken at inlet and at outlet. Some of the facilities, however, permit to measure the thermodynamic conditions in term of P and T also between two stages, if a multi-stage turbine is implemented as in (Han et al., 2014; Kang, 2016), or between stator and rotor as in (Klonowicz et al., 2014). All the authors use the thermodynamic models implemented in Refprop (Lemmon et al., 2013a) to compute other useful thermodynamic quantities, as the enthalpy, starting from the (P, T) experimental data acquired. Other quantities usually measured are the mass flow rate, the rotational speed of the turbine, the torque generated at the turbine shaft and the generator electric power output. A further classification of these kind of facilities can be made on the basis of the turbine model they implement.
  - **Radial flow single stage:** these turbines are suited when small power output (from few kW to maximum few hundreds of kW), small flow rate and small specific work are required. The configuration adopted is always radial-inflow as it guarantees much compactness with respect to axial turbines. The main applications for these turbines belong to small ORC systems for waste heat recovery. Indeed, the facility presented in (Turunen-Saaresti et al., 2016) use as heat sources exhaust gas and cooling water from an actual diesel engine. Moreover, most of the work reported are devoted to the construction of

turbine performance maps. Improving the performance of the turboexpanders under off-design conditions is one of the key aspects to be researched in order to make small scale ORC systems commercially mature. Indeed, the works (Kang, 2012; Shao et al., 2017b; Pei et al., 2011a) investigate turbine and cycle efficiency under start-up transient (Pei et al., 2011a), and at varying evaporation temperatures (Kang, 2012) or heat source temperature and mass flow (Shao et al., 2017b). A facility implementing a radial inflow single stage turbine is still in the commissioning phase at the University of Queensland, up to now they reported some preliminary results (Twomey et al., 2016) and they are about to insert the expander in their loop.

- **Radial flow multi stage:** these turbines are used when higher expansion ratios are required, i.e. $\beta_t > 5$. Two experimental studies are available in the literature employing a two stage radial inflow turbine in an academic facility (Han et al., 2014; Kang, 2016); while another facility employs a two stage centripetal turbine (Klonowicz et al., 2014). These systems will be potentially used with variable heat sources. For example one of the most promising application is in micro Combined Cooling, Heat and Power (CCHP) systems where the heat power available for the ORC system depends on the contingent demand of heating or cooling power. For these reasons Kang (2016) tested the turbine at varying temperature of the heat sources. Kaczmarczyk et al. (2017) focuses on the turbine performance and tested two configurations at different rotational speed of the turbine. Finally, Han et al. (2014) reported a CFD analysis of a turbine tested and commented on the large discrepancies found between the performances of the tested and the simulated turbine.
- **Axial flow single stage**: These turbines are competitive when the target power ranges from a few hundreds of kW to a few MW, since in these cases the flow rate required increases. Usual applications are geothermal and biomass power plants but also innovative concepts exploiting the heat coming from concentrating solar power plant are being studied. Looking at the facilities reported in Table 1.1 it can be mentioned that: Klonowicz et al. (2014) tested a single stage axial turbine using as heat source an actual geothermal source and evaluating its performance at varying mass flow rates. Fu et al. (2015) tested a turbine for low-grade waste recovery applications and reported the efficiency at varying heat source inlet temperature. Even thought these turbines are more suited for larger power output, some concepts to exploit axial turbine with partial admission in the few kW target were explored (Klonowicz et al., 2014; Seume et al., 2017; Cho et al., 2015). Seume et al. (2017) tested a turbine at different degree of partialization and compared the results in term of efficiency, power and mass flow with the one simulated with a CFD solver founding discrepancies for the turbine power as large as 4.7% were found. Large discrepancies between actual and predicted performances were

found also by Cho et al. (2015) while Klonowicz et al. (2014) found a good agreement (discrepancies in the range of 1%) in term of efficiency.

  - **Axial flow multi stage**: only one experimental study conducted on a multi stage axial turbine is available in the open literature (Yang et al., 2017). A real geothermal heat source was used, the source is shared with other industrial utilities so its temperature and flow rate varies accordingly to the requested thermal loads. Thus, the performances of the cycle and of the turbine at varying temperature and mass flow rate of the geothermal water are reported.

- **Ludwieg tubes and Nozzle fitted facilities:** these facilities are devoted to the acquisition of detailed experimental data useful to the validation of loss models and CFD solvers. They do not implement a real turbine, instead, they have modular test sections where converging diverging nozzles or linear cascades can be accommodated. The test sections are conceived to be instrumented in order to acquire static/total pressure and temperature data inside the channels with a high spatial resolution. Some of the test facility are conceive with an optical access in order to perform measurements with optical techniques as schlieren visualizations, Laser Doppler Velocimetry (LDV) and Particle Image Velocimetry (PIV) (Spinelli et al., 2015). Three facilities of this kind are composed by a Ludwieg tube (Dùra Galiana et al., 2016; Colonna et al., 2008a; Fergason et al., 2003) which is intermittent and allows test times in the range of *ms*. One facility belong to TU DELFT and is devoted to speed of sound measurements in organic fluids and permits to investigate the existence of non-ideal non-classical compressible fluid effects (Colonna et al., 2015b; Colonna et al., 2008a). Another belong to the Whittle Laboratory and was used to investigate trailing edge losses in non-ideal regime using the fluid sulfur hexafluoride SF_6 (Dùra Galiana et al., 2016). The last one was constructed by the university of Colorado and was designed to verify the existence of non-classical phenomena associated with single-phase, dense gas-dynamics. However it is currently out of operation due to the technical problem encountered in testing conditions as extreme as the one needed to expect non-classical phenomena. Another batch type facility is the TROVA facility belonging to the CREA lab of Politecnico di Milano (Spinelli et al., 2015). It permits longer test times, in the range of few tens of seconds. It is the only wind tunnel for organic vapors worldwide currently in operation. The first experimental campaigns devoted to the characterization of the expansion of MDM in the non-ideal regime through converging-diverging nozzles have been published in (Spinelli et al., 2016; Spinelli et al., 2017; Spinelli et al., 2018) and they were carried on during this thesis. The last facility belonging to this category is currently under construction at the Muenster University of Applied Sciences, and it is a continuous wind tunnel based on a close gas cycle working with Novec649 (Passmann et al., 2016).

- **Hybrid Facilities:** these facilities aim at combining the purposes of the other two categories. They are composed of two parallel loops, one housing an actual expander with the aim of testing its performances and another one housing a test section where detailed measurements can be performed. One of these facilities is currently under the commissioning phase at Tu Delft, it is named Organic Rankine Cycle Hybrid Integrated Device (ORCHID) (Head et al., 2016). Another facility of this kind is under construction at the City University of London and, contrarily to all the facilities presented here, it will feature a twin screw expander instead of a turbo-expander (White and Sayma, 2018).

It can be noticed that some of the authors testing the performances of turboexpanders (Turunen-Saaresti et al., 2016; Han et al., 2014; Yang et al., 2017) had problems in reaching the design point, moreover they often register discrepancies between the simulated and the actual performances (Cho et al., 2015; Seume et al., 2017; Han et al., 2014). In order to improve the turboexpanders design process and to provide reliable performance prediction, a better insight into non-ideal compressible flow fields through the acquisition of detailed data is required. Detailed data are experimental data that can be used to assess locally the performance of a CFD solver; such data include local static pressures, temperatures, velocity vectors and Mach numbers, positions of shock waves and expansion fans. These data can be acquired in nozzle fitted and hybrid facilities. The TROVA facility is one of the few facility belonging to one of these category currently in operation and this thesis will also provide a detailed discussion on its operation.

Table 1.1: Experimental facilities devoted to the characterization of ORC turboexpanders.

	Facility	Location	Operating Conditions	Status	Ref.	Aim
Radial T. Single	LUT Micro ORC Power Plant	Lappeernanta U. of Techonology	7.9 bar, 265° C, 12 kW	Operative	(Turunen-Saaresti et al., 2016; Uusitalo et al., 2017)	Studying high temperature ORC turbine performances (Siloxane MDM)
	UQ Test Loop	U. of Queensland	200 bar, 250° C, continuous	Operative	(Twomey et al., 2016)	Cycle performance analysis and expander analysis (Refrigerants R134a, R245fa; n-Pentane, CO_2)
	KAERI ORC test bench #	Korea Atomic Energy Research I.	7.32 bar, 80° C, 30 kW	Operative	(Kang, 2012)	Low temperature cycle and turbine performance evaluation (Refrigerant R245fa)
	ZU test bench	Zhengzhou U.	3.93 bar, 72° C	Operative	(Shao et al., 2017a; Shao et al., 2017b)	ORC cycle performance evaluation (Refrigerant R123)
	USTC test bench	U. of Science and Technology of China	7.86 bar, 100° C, 3.75 kW	Operative	(Pei et al., 2011a; Pei et al., 2011b)	Dynamic testing of ORC cycle and turbine perfromances (Refrigerant R123)
Radial T. Multi S.	Busan Technopark OC System Test Loop	Seoul National U. of Sciance and Technology	20.9 bar, 124° C, 240 kW	Operative	(Han et al., 2014)	Turbine performance evaluation (Refrigerant R245fa)
	KAERI ORC test bench # 2	Korea Atomic Energy Research I.	19.3 bar, 120° C, 42 kW	Operative	(Kang, 2016)	ORC system and turbine performance evaluation (Refrigerant R245fa)
	PAS test bench	Szewalski I. of Fluid Flow	14 bar, 180° C, 3 kW	Operative	(Kaczmarczyk et al., 2017; Kaczmarczyk et al., 2018)	ORC system testing (HFE7100)

Continuing in the next page

Continuing from previous page

	Facility	Location	Operating Conditions	Status	Ref.	Aim
Axial T. Single Stage	Xi'an ORC test bench	Xi'an Jiaotong U.	6.27 bar, 120° C, 10 kW	Operative	(Li et al., 2012)	Evaluation of ORC perfromances for geothermal applications (Refrigerant R123)
	WPUT ORC test bench	West Pomeranian U. of Technology	10.92 bar, 58° C	Operative	(Klonowicz et al., 2014)	Simulation of a geothermal power plant (Refrigerant R227ea)
	UH Multi-purpose Test Bench	U. of Hannover	40 bar, 265° C, 18.4 kW	Operative	(Seume et al., 2017)	Vehicle turbochargers and ORC module examination (Ethanol)
	Experimantal ORC test bench	Gyeongsang National U.	n.a. bar, 100° C	Operative	(Cho et al., 2015; Cho et al., 2018)	Cycle performance analysis (Refrigerant R245fa)
	ITRI ORC test bench	Industrial Technology Research I. (Taiwan))	12.6 bar, 101° C, 250 kW	To be renovated	(Fu et al., 2015; Fu et al., 2016)	Mapping the performances of ORC cycles at different conditions (Refrigerant R245fa)
A.M.S.	Huabei Oil Firlds ORC Test Rig	Xi'an Jiaotong U.	7 bar, 84° C, 657 kW	Operative	(Yang et al., 2017)	ORC testing from actual geothermal source (Refrigerant R245fa)

Continuing in the next page

Continuing from previous page

	Facility	Location	Operating Conditions	Status	Ref.	Aim
Ludwieg	FAST Flexible Asymmetric Shock Tube	Delft U. of Technology	21 bar, 400° C, batch	Operative	(Colonna et al., 2015b; Colonna et al., 2008a)	Studiyng wave propagation in dense vapor of organic compounds (SIloxane D_6)
	TES Ludwieg Tube	University of Cambridge	45 bar, 150° C, batch	Operative	(Dùra Galiana et al., 2016)	Model validation for trailing edge losses and dense gas effects in transonic ORC turbine vanes (SF_4)
	Boulder Ludwieg Tube	University of Boulder	- bar, 350° C, batch	Out of operation	(Fergason et al., 2003)	verify the existence of non-classical phenomena ($PP10$)
Nozzle	TROVA Test Rig for Organic VApours	Politecnico di Milano	50 bar, 400° C, batch	Operative	(Spinelli et al., 2018; Spinelli et al., 2016; Spinelli et al., 2015)	Characterization of the expansion of dense gases in turbine blade passage (Siloxanes MDM,MM and refrigerant R245fa)
	CLOWT Closed Loop Organic Wind Tunnel	Muenster U. of Applied Sciences	6 bar, 150° C, continuous	Trial Testing (2^{nd} half of 2017)	(Passmann et al., 2016; Reinker et al., 2017)	Validation of similarity laws for dense gases and creation of loss correlations (Novec 649)
Hybrid	ORCHID ORC Hybrid Integrated Device	Delft U. of Techonology	25 bar, 320° C, 100 kW, continuous	Commissioning	(Head et al., 2016; Pini et al., 2017)	Characterisation of the expansion of dense gases and testing of ORC expanders (Siloxanes,PP2,PFC,Refrigerant R245fa)
	C.L. Test Loop	City U. of London	20 bar, 125° C, continuous	Design phase	(White and Sayma, 2018)	Characterisation of high speed flow of organic vapours and testin of twin-screw expanders (Refrigerant R1233zd)

1.4 TEST RIG FOR ORGANIC VAPORS (TROVA)

The TROVA operates as a blow-down wind tunnel for organic vapors. It was designed in partnership with a major ORC manufacturer to obtain independent measurements of pressure, temperature, and velocity in flows representative of the expansion taking place in ORC turbines (Spinelli et al., 2015). The TROVA is capable of working with a wide variety of fluids. The two fluids that were selected for plant sizing are siloxane MDM and refrigerant Pentafluoropropane $C_3H_3F_5$ (R245fa), since they are representative of siloxanes and Hydrofluorocarbons (HFS)s among the most interesting fluid families for high and low temperature ORCs respectively. Indeed, the aim was to obtain a versatile facility capable of handling a wide variety of conditions in term of pressure, temperature and a passage area in the test section big enough to let the possibility of inserting a probe with negligible blockage effects. This implies the possibility to handle relatively high mass flow rates and it drove the design choices towards a batch configuration. Indeed, the discontinuous operation mode limit the thermal power required for the operation of the facility and it contain the investment cost while keeping a broad range of thermodynamic conditions reachable. Indeed, expansion starting from pressures as high as $P_{max} = 50 bar$ and temperatures as high as $T_{max} = 400^{\circ} C$ can be performed. More information on the design of the TROVA can be found in (Spinelli et al., 2015).
The TROVA operates with a batch Rankine cycle. The plant layout is sketched in Figure 1.2 and the corresponding thermodynamic cycle, here represented for siloxane MM as an example, in Figure 1.3. The cycle is composed by the following thermodynamic transformations:

- 2⟶6: the fluid is heated up isochorically in the High Pressure Vessel (HPV) were it evaporates and it is brought to the conditions of pressure and temperature planned for the test;
- 6⟶7: the vapor expands through the test section, here the expansions is considered as isentropic;
- 7⟶8: the flow is slowed at rest conditions in the Low Pressure Vessel (LPV);
- 8_{ex}⟶9_{ex}: as the test finishes the vapor is collected in the LPV where it is isochorically cooled to saturation conditions;
- 9_{ex}⟶1_{ex}: finally the fluid condensate isochorically inside the LPV

Condition 1_{ex} represents the liquid-vapour equilibrium condition reached in the LPV. To start a new experiment, it is necessary to transfer the liquid from the LPV to the HPV this process is carried out thanks to a metering pump connecting the two vessels (1_{ex}⟶2).
The TROVA plant is composed by four main circuits:

- **The organic fluid circuit** where the thermodynamic transformations explained above take place. Its main components are:

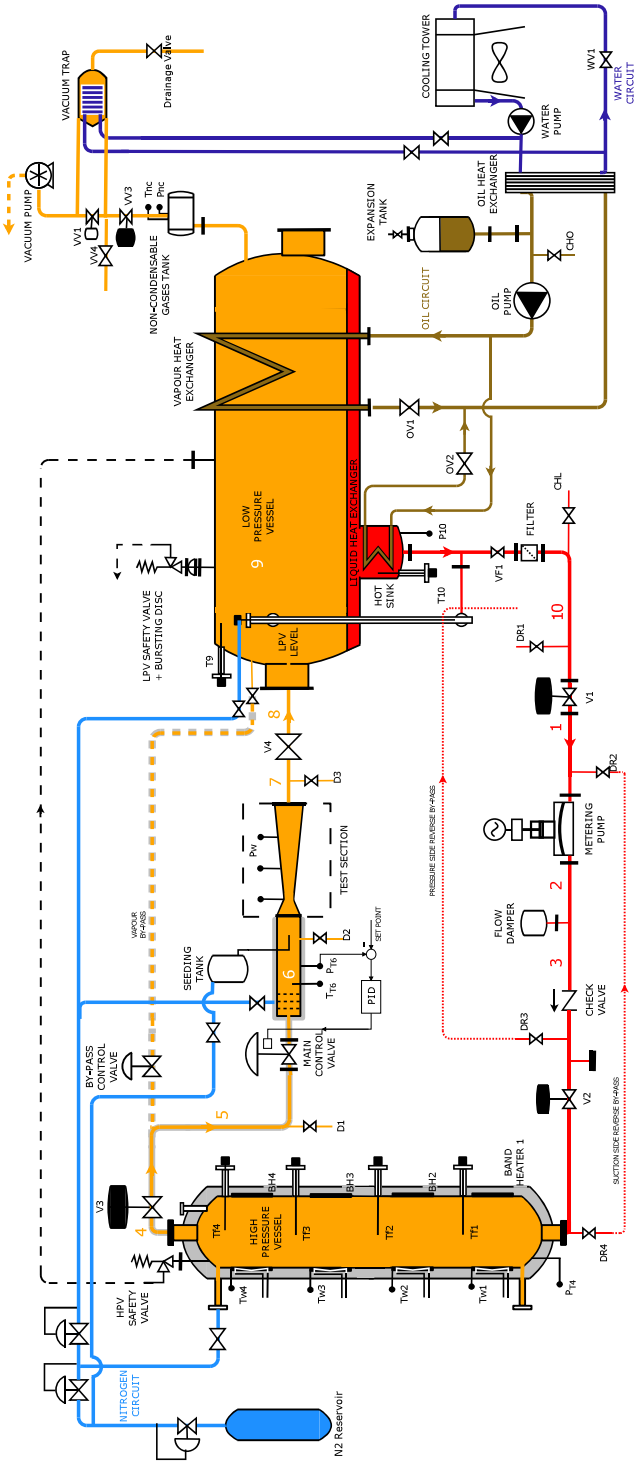

Figure 1.2: TROVA plant scheme

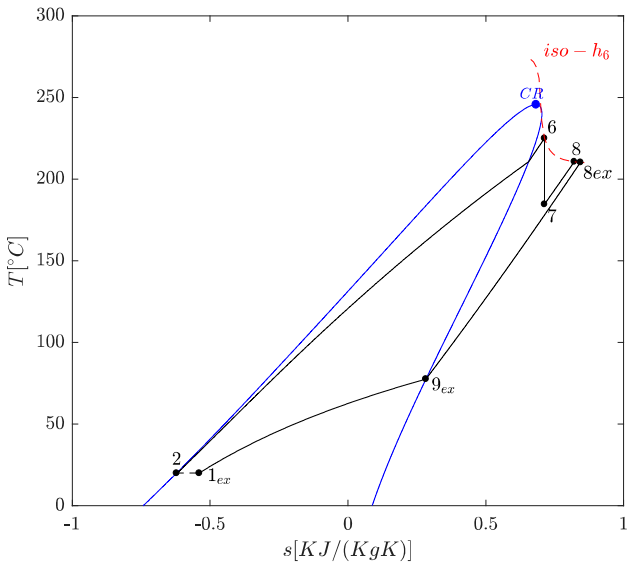

Figure 1.3: TROVA thermodynamic cycle: blu line is the saturation curve, CR is the critical point.

- *HPV*: it is a 1 m^3 vessel heated by means of electric bands and wires installed on its external walls. Four band heaters are installed along the cylindrical shell, while heating wires are on the top and on the bottom elliptical caps. The total electrical power available at the HPV is 38.5 kW. Electrical heaters are also installed on pipelines and on the test section for a total available power of 11.5 kW. The heaters are regulated by a Proportional–Integral–Derivative (PID) controller, independently operating on different power supply zones, using temperatures measured by wall thermocouples as feedback signals. The HPV is isolated from the rest of the plant by valves V2, V3 and By-Pass Control Valve. Furthermore, it is equipped with a safety valve, which discharges in the LPV, to guarantee that the maximum design pressure (50 bar) is not exceeded.
- *LPV*: it is a 5.6 m^3 vessel used to store the working fluid in between tests, and it acts as de-superheater and condenser. The LPV is equipped with a cooling system operated with refrigerant oil, which allows a fast cooling of the stored fluid at the end of a test. It is equipped with a safety valve, which discharges in ambient, to assure that its maximum design pressure (20 bar) is never overcome.
- *Valve V3*: it is a ball valve with a maximum sealing capability of 50 bar at a maximum temperature of 400 °C. It isolates the HPV from the test section and can be operated automatically via software. This valve belongs to the heated portion of pipelines.
- *Main Control Valve (MCV)*: it is a control valve regulated by a PID controller which operates on the pneumatic positioning device. Its scope is to allow the

setting of a constant stagnation pressure in the plenum (namely P_{T6}) during a test. During the experimental campaigns carried out in the present thesis work, it was decided to keep the MCV fully open during each test in order to investigate different operating conditions within a single test, (see Sec.3.1). The MCV is heated via electrical wires.

- *By-Pass Control Valve (BPCV)*: it is a control valve that can be regulated operating on the pneumatic positioning device. It permits to transfer vapor at high pressure from the HPV to the LPV, in order to have a finer control on the pressure reached in the HPV at the beginning of each test.
- *Plenum*: it is a 6 inches pipe located just upstream of the test section acting as a settling chamber. There the fluid velocity is very low, about 1 m/s, so static quantities can be assumed equal to total ones. Moreover, it is equipped with a honeycomb in order to make the flow as uniform as possible. The plenum is heated by electrical wires.
- *Test section*: it is a modular flanged body (Figure 1.4), designed to accommodate different nozzle profiles. It is designed to provide a smooth passage from the circular cross section of the plenum to a rectangular cross section. The test section features a quartz window on the front that provides an optical access. On the back side it is closed by a steel plate where a series of taps are machined for static pressure measurements. More informations on the tap design can be found in section 2.2. The plate is mirror-polished in order to provide the highly reflective surface needed for the schlieren technique, implemented with a double-pass configuration (see Sec.2.4.1.2). The geometrical shape of the planar converging-diverging nozzle is provided by a pair of steel profiles mounted on the rear plate. By changing the profiles, different geometries can be mounted. More detail on nozzle design and geometry is found in Section 3.3.
- *Metering Pump*: it is a reciprocating membrane pump able to produce a maximum pressure of 32 bar. It is used to feed the HPV with the working fluid stored in the LPV, at the beginning of each new test.
- *Vacuum Pump*: it is a volumetric pump with a maximum working temperature of 60 °C and a maximum inlet pressure of 1.25 bar, able to achieve avaccum quality of few millibars. It is used to bring the working fluid in the HPV to its saturation pressure at ambient temperature by removing the nitrogen used to fill the plant in between two tests. It is also used to set the LPV pressure at sufficient low value for guaranteeing nozzle operation in under-expanded conditions for the whole test duration. Furthermore, it is used to eliminate air in the plant portion in between valve V3 and valve V4, after operations that require the test section disassembling (i.e. nozzle and/or pressure transducers change).

  - *Valve V4*: it is a ball valve that isolates the LPV from the test section during operations that require test section disassembling.
  - *Vacuum trap*: it consists in a cross flow heat exchanger connected to the water circuit, located immediately upstream the vacuum pump. It is used to condensate the working fluid vapor diluted in nitrogen that would otherwise condensate inside the vacuum pump during its operation. Indeed, it was found that siloxane MDM tend to mix with the oil present in the vacuum pump, lowering its viscosity, causing the need of frequent oil changes and increasing the chances of pump failures.The vacuum trap is used to remove the siloxane vapor before it reaches the pump.

- **The thermal oil circuit**, it is used to cool down the organic vapor within the LPV at the end of a test. It is composed by a dedicated centrifugal pump, a serpentine placed in the hot sink of the LPV and a heat exchanger placed on the external tank shell.

- **The water circuit**, it consists in a cooling tower circuit including a circulation centrifugal pump, a plate heat exchanger used for cooling the thermal oil of the LPV oil loop and the cross flow heat exchanger of the vacuum trap.

- **The nitrogen plant** The nitrogen system was implemented after the first experimental campaigns conducted with fluid MDM to help preventing fluid decomposition. As a matter of fact, it was found that the water vapor present in the ambient air, together with the fact that the plant is made in carbon steel and it thus produce rust, can act as a trigger for the decomposition process. Indeed, silica dioxide powder coming from MDM decomposition was found even though the maximum temperature reached was $290^{\circ}C$. Accordingly to (Keulen et al., 2018) this temperature should not cause any detectable decomposition if cleaned conditions are considered. It was thus decided to prevent the reentering of the water vapor contained in the air in the plant by filling it with nitrogen. This permitted to avoid decomposition of the working fluid even at temperatures closed to the critical one. The Nitrogen plant adopts as source of nitrogen cylinders pressurized at $200bar$. The nitrogen line is connected to the TROVA plant in several points, at the LPV, at the HPV and to the test section. It is equipped with a series of adjustable pressure regulators that allow to reach a desired outlet pressure. It also permits to fill the HPV with Nitrogen at a desired pressure in order to perform tests using an ideal-gas.

The discontinuous nature of the facility makes some procedures recurrent and of paramount importance for the success of each test.

- **Working fluid transfer procedure**: this procedure is crucial to reach the desired conditions in the HPV at the end of the heating process. Indeed, since the process

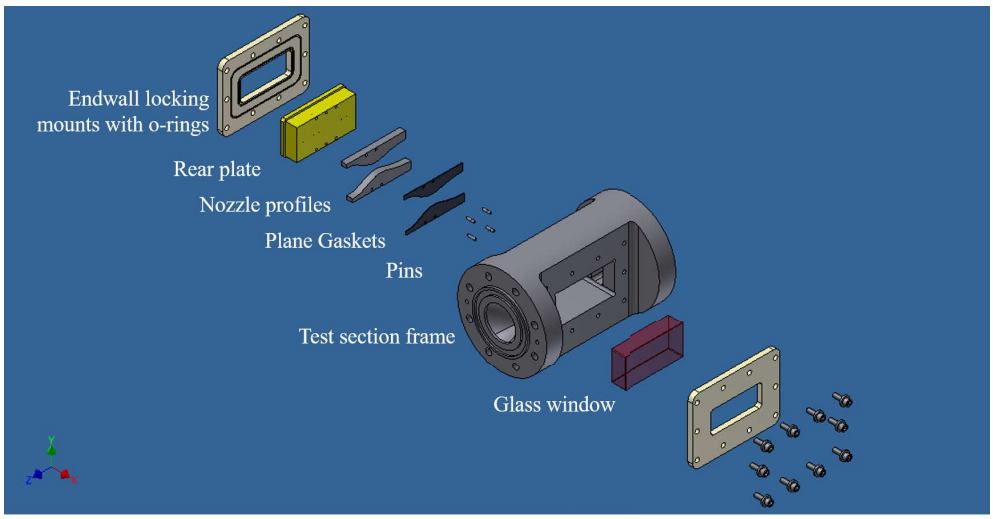

Figure 1.4: TROVA test section components.

is isochoric, the pressure reached is a function of the temperature set at the heaters and of the mass of fluid stored in the HPV at the beginning of the heating process. A visual level meter permits to monitor the level of the fluid inside the HPV, a CAD model compute the volume filled by the liquid and, by evaluating the density of the fluid at ambient condition using RefProp (Lemmon et al., 2013b), the mass inside the HPV can be controlled. However, the precision of the level meter is in the order of $0.5cm$ that means $\pm 2\ dm^3$ on the correspondent volume of fluid. Moreover, the CAD model can be slightly different from the reality adding another level of uncertainty. Thus, the condition reached at the end of the heating process may differ from the desired ones. The BPCV can be used at the end of the heating process to minimize the discrepancy between the desired and the actual HPV conditions. However, even though the total conditions inside the HPV would match perfectly the desired ones still these conditions would not be the ones at which the experiment is performed. A pressure drop is present between the HPV and the plenum because of the presence of the MCV and of the pipelines. Moreover, at the beginning of each test the opening transient of the MCV control valve lasts approximatively 2 seconds. The useful data are acquired after this transient meaning that the conditions reached in the plenum at the beginning of each test are significantly different from those reached in the HPV at the end of the heating process. A simplified dynamic model of the emptying process of the HPV during this transient has been derived, however the prediction are still different from the actual values. All these reasons, combined with the fact that the plant dispersion are influenced by the atmospheric conditions that could range from $5^{\circ}C$ to $30\ ^{\circ}C$, make it difficult to replicate exactly a test run.

- **Pre-test procedure**: this procedure consists in activating the vacuum pump, to reduce the pressure of the HPV (at ambient temperature) down to the saturation one.

In this way, all the nitrogen present is expelled and a pure vapor-liquid equilibrium of the working fluid is assured. Then, the vacuum pump is connected to the LPV to reduce its pressure slightly above the working fluid saturation pressure at ambient temperature. This is done in order to have under-expanded conditions within the nozzle during the emptying process of the HPV.

- **Post-test procedure**: this procedure is carried out to avoid contaminations of the working fluid stored in the plant. Since both LPV and HPV have a pressure below the atmospheric one at the end of each test, nitrogen is added to both of them. This is done in order to set their pressure slightly above 1 bar, to avoid air infiltrations during the time in between two experiments.

2

MEASUREMENTS IN NON-IDEAL COMPRESSIBLE FLOWS

2.1 PECULIARITIES AND CHALLENGES

Obtaining experimental data characterizing non-ideal flows presents remarkable challenges because of the particularly hostile experimental environments are involved. Indeed, these flows occur at high temperature, high pressure and at thermodynamic conditions near to saturation and to the thermal stability limit. Moreover, most of the standard measuring techniques capable of acquiring spatially resolved data of velocity and pressure in a flow field cannot be yet employed. Usually two main approaches are suitable, namely insertion of calibrated directional pressure probes and exploitation of optical techniques. Directional pressure probes (Persico et al., 2005) are capable of measuring local pressure and velocity vector. Unfortunately these probes require a fluid-specific calibration which is currently possible to perform only using air.
On the other hand, optical techniques, such as the LDV and the PIV, do not require fluid-specific calibration and they are capable of providing spatially resolved velocity measurements with negligible perturbation of the flow field, provided that the fluid is optically transparent. However, these techniques require to seed the flow and the seeding process is challenging if high temperatures, high pressures and high velocities are involved (Gallarini et al., 2016). Further researches are required in order to obtain a satisfactory seeding of a supersonic non-ideal flow.
Thus, the only experimental techniques readily employable in supersonic non-ideal flows are pressure and temperature measurements and optical techniques not requiring seeding such as schlieren imaging. This chapter is devoted to the presentation of all the measurement techniques applied and developed during this thesis work. A particular attention is given to the explanation of all the issues encountered related to the nature of non-ideal flows of organic vapors and to the solutions adopted. In particular, section 2.2 focuses on the pressure measurements, section 2.3 on the temperature measurements and section 2.4 on the schlieren imaging. Moreover, a novel technique to exploit schlieren images in a quantitative way in order to directly measure the local Mach number in the flow was developed and it is presented in section 2.4.

2.2 PRESSURE MEASUREMENT

Pressure measurements are key to characterize internal flows. Because of the unavailability of directional probes and because of the supersonic nature of the flow to

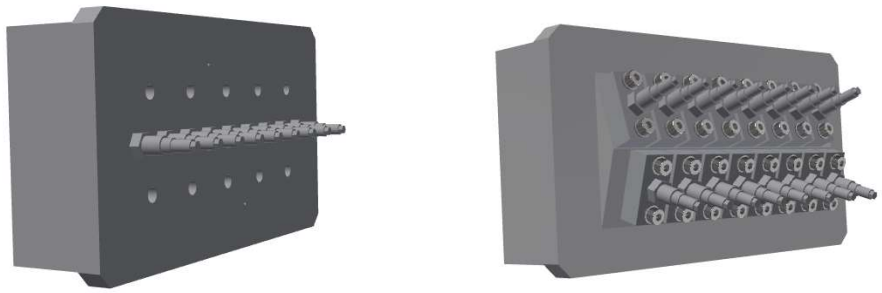

(a) *Back of the first rear plate which permits the installation of 9 pressure transducers.*

(b) *Back of the second rear plate which permits the installation of 16 pressure transducers.*

Figure 2.1

be analyzed, where the flow has non negligible velocities it is possible to perform only static pressure measurements. Static pressures can be measured, with the adoption of wall pressure taps, only in flows with negligible secondary flows. This brought to the choice of focusing on the characterization of straigh-axis planar nozzle flows. The planar configuration permits to analyze the flow on the axis, providing that the 3D effects are negligible on the transversal direction.

Small holes are drilled at the nozzle axis where the measurement is to be performed. These holes are named pressure taps and they are connected through pneumatic lines to pressure transducers. In conventional air wind tunnels, pneumatic lines are usually long thin tubes which can be designed with relative freedom. Thanks to that freedom pressure measurement can be obtained with a fine spatial discretization by keeping the pneumatic lines diameter as small as possible in the first part. Moreover, when the dynamic response of the pneumatic line is not an issue, they can be designed long enough to keep the transducer in a controlled ambient distant from the pressure tap.

Unfortunately, non-ideal compressible flows are characterized by thermodynamic conditions close to the saturation curve and this poses some problems. Condensation of the fluid inside the pneumatic lines should be avoided; liquid head and meniscus can bias the measurement. Moreover, if the condensation takes place on the sensor, its temperature can change fast and significantly possibly affecting its response.

In order to avoid condensation and temperature gradients on the sensors, the pneumatic lines and the sensor itself should be heated up to a temperature close to that of the fluid. Moreover, it can be useful to keep the lines as short as possible to minimise the heat exchanged and to enhance the frequency response of the line cavity system.

In order to keep more freedom in the design of the pneumatic lines, another solution is the adoption of a purge system. Purge systems are usually used to measure pressure in steam turbines, they exploit stream of gases as nitrogen or air to keep the pneumatic lines free from the condensate. They are suitable for steady processes and thus they are

not applicable to the TROVA facility since it is a blow-down wind tunnel. Moreover, the batch nature of the TROVA forces the transducers to measure both near their full scale and also at much lower pressure as the test proceed.
To sum up, the peculiar conditions of non-ideal flows and the discontinuous operation of the TROVA require:

- pneumatic lines to be as short as possible, to have a good time response of the sensor;
- pneumatic lines to be at a temperature close to that of the fluid, to avoid condensation;
- pressure transducers to measure from full scale to sub-atmospheric pressures maintaining a high sensitivity;
- pressure taps to be as close to each other as possible, to reach a fine spatial discretization of the pressure measurements.

Keeping the lines as short as possible means that the pressure transducer must be mounted as close as possible to the tap, in this configuration the dimension of the pressure transducer itself has to be taken in to account and the pressure taps can not be placed as close one to another as desired. In order to preserve a good spatial discretization, the solution selected was the adoption of miniaturized piezoresistive pressure transducers, capable of working at high temperatures, to be mounted directly in the back plate of the test section. At first, the system adopted was the one shown in pictures 2.1a and 2.2. It allowed the installation of 9 pressure transducers and it featured 10 housings for electrical heating cartridges. The pressure taps on the horizontal axis were separated by $17mm$. The pressure transducers were screwed directly on the back plate. Since the tests covered a wide range of thermodynamic conditions, the pressure transducers had to be unscrewed several times in order to change their position accordingly to their full scale and to the pressure to be measured. This stressed their electrical connections causing some failures.
In order to preserve the transducers longer and, more importantly, in order to halve the spatial discretization of the pressure measurements; another housing system for the transducers and new back plate were designed. The second back plate adopted, shown in Figures 2.1b, 2.3, allowed the installation of 16 pressure transducers. The pressure taps were separeted by $8.5mm$. Each pressure transducer was screwed on a small metal plate so that, to change the arrangement, it was sufficient to move the plate avoiding unscrewing the pressure transducer itself and preserving its cables from torsional stresses. Heating of the second plate was provided by the adjacent parts of the test section through conduction.
Both back plate configurations assured that the pressure taps would reach the temperature prescribed by the PID controller of the electrical heating of the plant. It was set to temperatures ranging from 220° to 290° depending on the specific test. This assured the absence of condensate. However, pressure transducers had to work at high temperatures

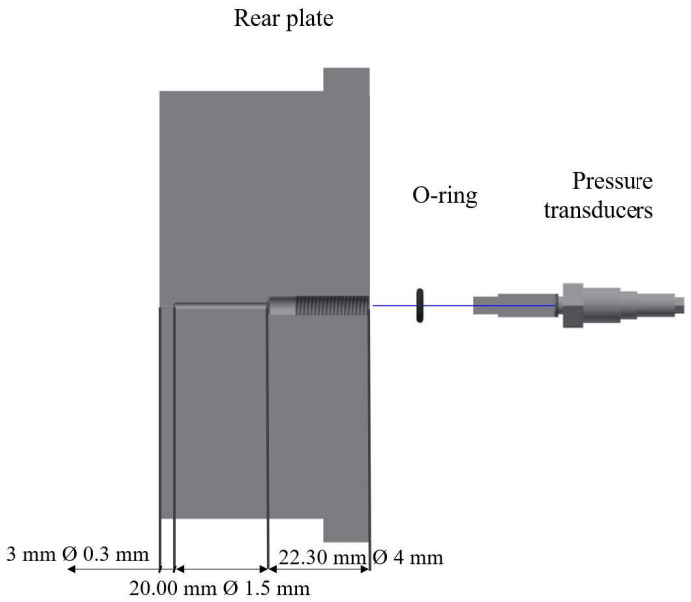

Figure 2.2: Detail of the pneumatic line of the first rear plate.

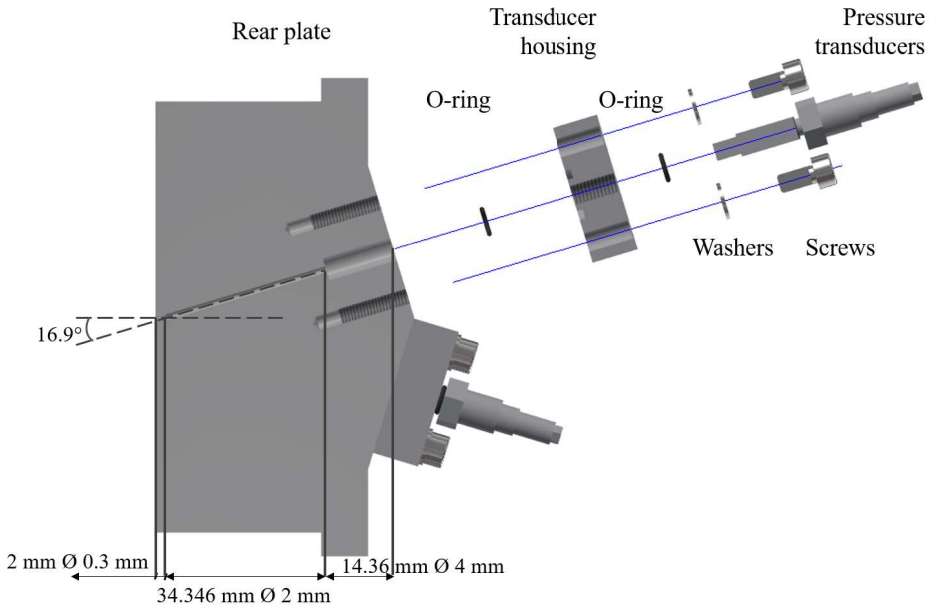

Figure 2.3: Detail of the pneumatic line and of the transducers housing of the second rear plate.

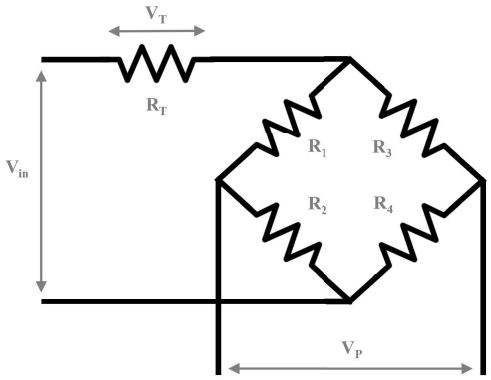

Figure 2.4: Wheatstone bridge with the added resistance R_T.

which differ from one test to the other. This was a major drawback; in fact in piezoresistive pressure transducers a temperature change determines a proportional zero shift and sensitivity change. In order to work around this problem each pressure sensor was calibrated both in pressure and in temperature, moreover, a novel procedure was devised to estimate at best its uncertainty.

2.2.1 *Pressure transducers calibration and measurement uncertainty quantification*

All pressure transducers employed at the TROVA, are of piezoresistive type and they belong to the XTEH serie manufactured by Kulite. They exploit the piezoresistive effect in semiconductors and a four active arm Wheastone bridge circuit (see Fig.2.4). Usually, if the transducer is kept at a fairly constant temperature, the output potential difference V_P is proportional only on the pressure applied ($V_P = f(P)$). Unfortunately, when the same transducer works at different temperatures the proportionality existing between P and V_P changes ($V_P = f(P, T)$) and the sensor needs to be calibrated in temperature as well. In Figure 2.5a different calibration lines are shown. They were obtained using the same pressure transducer and performing several calibrations at different temperatures. It can be seen that the slope of the P, V_P line differs visibly from one line to the other. Therefore, it was decided to add a further resistance on the supply voltage side (R_T) in-house,(Fig.2.4), whose voltage drop (V_T) is only dependent on the sensor temperature variation and can be measured independently, allowing a calibration both in pressure and in temperature.
It can be shown that a linear proportionality exists between P and V_P for a given value of V_T (Eq.(3)); while a quadratic proportionality (Eq.(4), (5)) is found between the slope and the intercept of the linear equation and V_T (Fig.2.5b), (2.5c)). As a result, the func-

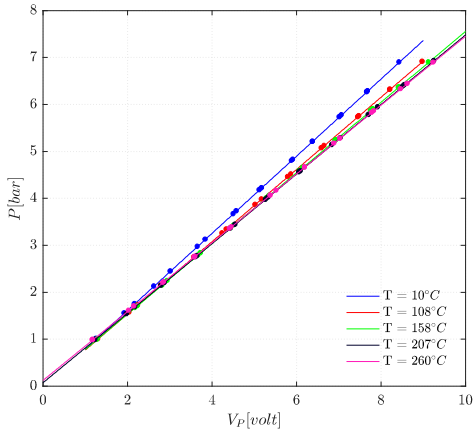

(a) *Linear calibration curves of pressure transducers G7 at different temperatures.*

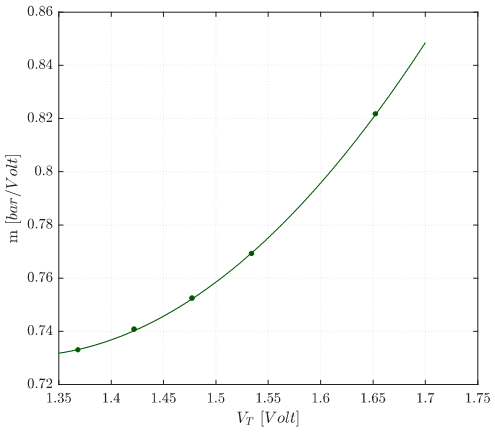

(b) *Quadratic dependence of the slope on the voltage temperature V_T.*

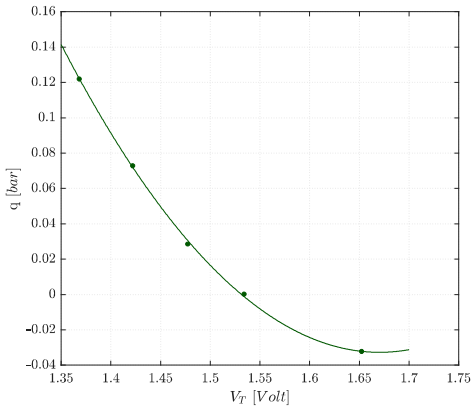

(c) *Quadratic dependence of the intercept on the voltage temperature V_T.*

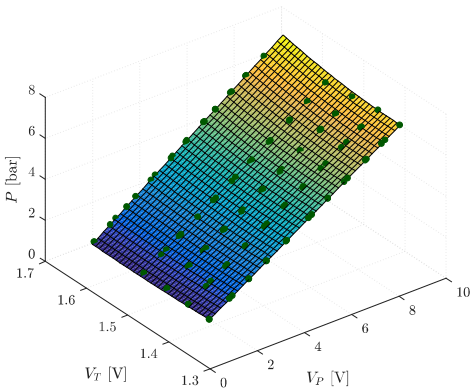

(d) *Calibration surface giving $P = f(V_P, V_T)$.*

Figure 2.5

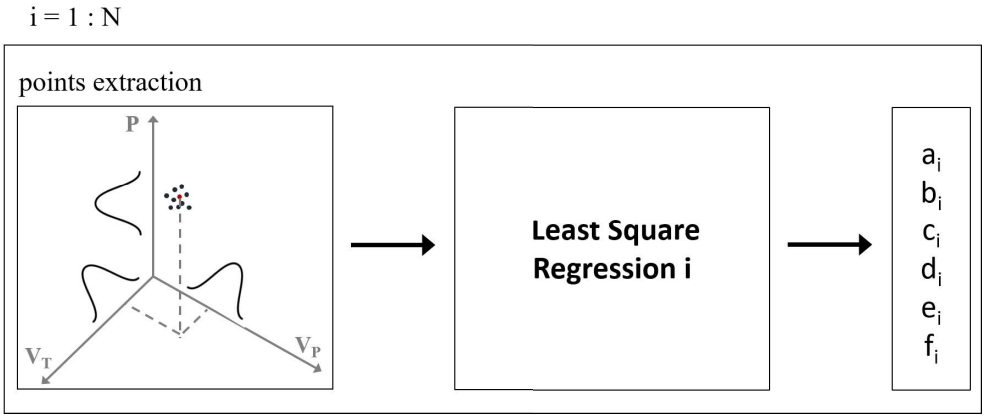

Figure 2.6

tional form imposed to model the pressure transducers behavior was eq.(6); the resulting calibration surface is shown in Figure 2.5d.

$$P = mV_P + q; \quad if \quad V_T = const; \tag{3}$$

$$m = a + bV_T + cV_T^2; \tag{4}$$

$$q = d + eV_T + f\,V_T^2; \tag{5}$$

$$P = f(V_P, V_T) = (a + bV_T + cV_T^2)V_P + (d + eV_T + f\,V_T^2); \tag{6}$$

For each pressure transducer twenty-one pressure points equally spaced in the transducer measuring span, 11 going up and 10 going down in pressure, were acquired. In such a way, the possible Wheatstone bridge hysteresis of the pressure transducers was taken into account. The procedure was repeated at five different temperatures (20 °C, 110 °C, 160 °C, 210 °C, 260 °C), covering the whole possible operating range during tests. In this way 105 triplets of values (V_P, V_T, P) were obtained for each transducer. The acquisition frequency for calibration was set equal to 250 Hz. For each calibration point, 250 values were acquired of both V_P and V_T. A digital manometer, adopted as reference instrument, was employed to measure the pressure (P) to be associated at each calibration point voltage outputs, V_P and V_T. The manometers used were calibrated and certified at ACCREDIA laboratory. They all measure relative pressures so, since pressure transducers employed are absolute, at the beginning of each calibration the ambient pressure was measured by means of a barometer. The barometer has a pressure range of 750÷1150 mbar and a maximum expanded uncertainty of 0.17 $mbar$.

The 105 points obtained must be processed by a least square regression algorithm in order to obtain the coefficients of the calibration surface. However, these data are uncertain since (V_P, V_T, P) all result from a measurement. This has to be taken in to account in order to obtain a proper measurement uncertainty estimation as an outcome of the calibration process.

Each test performed in the TROVA facility belongs to the category of single-sample

experiments (Moffat, 1988) which are not repeatable experiments. Indeed, during each test the phenomena measured are unsteady; therefore, it is impossible to acquire multiple independent observations of the same quantity. Replicate the exact same experiment is not straightforward and each test preparation requires at least couple of days (see Sec.3.1). It is, thus, not possible to repeat the experiment a number of times sufficient for obtaining a significant statistical population of measurements, from which the standard uncertainty can be calculated through statistical considerations. For this reason, the best estimation of measurement uncertainty, for single sample experiments, is evaluated during the calibration of the instruments.

Calibration must be performed using the set-up and the measurement chain that will be used during the experiment and the conditions present during the calibration process must be as much similar as possible to the conditions that will be present during the experiment itself. The result of the calibration process would be: the coefficients (a, b, c, d, e, f) defining the pressure transducer behavior, and the quantities $(u_a, u_b, u_c, u_d, u_e, u_f, cov(a,b), cov(a,c), cov(a,d), cov(a,e), cov(a,f), cov(b,d), cov(b,e), cov(b,f), cov(d,e), cov(d,f), cov(e,f), RMSE)$ needed to compute an estimation of the uncertainty of each subsequent measure acquired using the calibrated transducer. In fact the goal of the calibration process is to calculate both the function $P = f(V_P, V_T)$ and an estimation of the uncertainty for a measure obtained using the function found. This estimation is based on the sources of uncertainties affecting the measurement chain and thus the data (V_P, V_T, P) used to construct the calibration surface itself.

In order to evaluate the uncertainty in the parameters of a regression constructed using uncertain data, an adaptive Monte Carlo method for multiple outputs was implemented in a MATLAB® code. The code takes as inputs means and standard deviations (i.e. standard uncertainties) of pressures (P, u_P), pressure voltage (V_P, u_{V_P}) and temperature voltage (V_T, u_{V_T}) of each point acquired during calibration, with the hypothesis that P, V_P and V_T have a Gaussian distribution. u_P is calculated from u_{MS} which is the expanded uncertainties declared in the calibration certificate of the reference manometer and from u_{Bar} which is that of the barometer employed (see Eq.(7)). u_{V_P} and u_{V_T} were calculated as the standard deviation of the population of the $n_{pc} = 250$ values acquired for each calibration point (see Eq.(8)).

$$u_P = \sqrt{u_{Bar}^2 + u_{MS}^2} \tag{7}$$

$$\overline{V} = \frac{1}{n_{pc}} \sum_{i=1}^{n_{pc}} V_i \qquad u_V = \sqrt{\frac{\sum_{i=1}^{n_{pc}} (V_i - \overline{V})^2}{n_{pc} - 1}} \tag{8}$$

The steps of the Monte Carlo method implemented are:

1. j = 1;
    a) extract one point from each of the 105 trivariate Gaussian populations characterized by the data collected during the calibration $(P, u_P, \overline{V_P}, u_{V_P}, \overline{V_T}, u_{VT})$;

b) perform a least square regression fitting the points with the surface of Equation (3) and calculate the coefficients $(a_j, b_j, c_j, d_j, e_j, f_j)$

2. j = j+1, repeat points (a) and (b) until i = N;

3. calculate $(\overline{a}, \overline{b}, \overline{c}, \overline{d}, \overline{e}, \overline{f})$, $(u_{\overline{a}}, u_{\overline{b}}, u_{\overline{c}}, u_{\overline{d}}, u_{\overline{e}}, u_{\overline{f}})$ and $(cov(\overline{a}, \overline{b}), cov(\overline{a}, \overline{c}), cov(\overline{a}, \overline{d}), cov(\overline{a}, \overline{e}), cov(\overline{a}, \overline{f}), cov(\overline{b}, \overline{d}), cov(\overline{b}, \overline{e}), cov(\overline{b}, \overline{f}), cov(\overline{d}, \overline{e}), cov(\overline{d}, \overline{f}), cov(\overline{e}, \overline{f}))$ that are means, standard deviations and covariances of the populations composed by the N values of $(a_j, b_j, c_j, d_j, e_j, f_j)$ obtained.

The number N was found in an adaptive way as prescribed in (Metrology, 2008; *Evaluation of measurement data, Supplement 2 to the 'Guide to the expression of uncertainty in measurement' , Extension to any number of output quantities* 2008). Once that the calibration surface has been defined by the values of $(\overline{a}, \overline{b}, \overline{c}, \overline{d}, \overline{e}, \overline{f})$, two important quantities can be calculated: the Sum of Squared Errors (SSE) (Eq.(9)) and the Root Mean Square Error (RMSE) (Eq.(10)).

$$SSE = \sum_{k=1}^{n} (P_k - \hat{P}_k)^2 \tag{9}$$

$$RMSE = \sqrt{\frac{SSE}{\nu}} \tag{10}$$

Where $P_k = [P_1, P_2, ..., P_n]$ are all the calibration points, $\hat{P}_k = [\hat{P}_1, \hat{P}_2, ..., \hat{P}_n]$ are the corresponding values predicted by the model and $\nu = n - m$ is the number of degrees of freedom in the regression defined as the difference between the number of fitted data (n) and the number of fitting coefficients (m).
The uncertainty related to a new (P_{new}) measurement performed using the calibrated transducer and the corresponding calibration surface can now be computed as the composition of the uncertainties related to the calibration surface Eq. (12), the uncertainty related to the new measured value of V_T and V_P Eq. (13) and the RMSE value Eq. (10).

$$u_{Pnew} = \sqrt{u^2_{coeff} + RMSE^2} \tag{11}$$

$$u^2_{coeff} = \sum_{t=1}^{q_t} \left(\frac{\partial P}{\partial q_t} u_{q_t}\right)^2 + 2 \sum_{t=1}^{q_t - 1} \frac{\partial P}{\partial q_t} \frac{\partial P}{\partial q_{t+1}} cov(q_t, q_{t+1}) \tag{12}$$

$$u^2_{new} = \left(\frac{\partial P}{\partial V_{Tnew}} u_{V_{Tnew}}\right)^2 + \left(\frac{\partial P}{\partial V_{Pnew}} u_{V_{Pnew}}\right)^2 + 2 \left(\frac{\partial P}{\partial V_{Tnew}} \frac{\partial P}{\partial V_{Pnew}} cov(V_{Tnew}, V_{Pnew})\right) \tag{13}$$

Where $q = [\overline{a}, \overline{b}, \overline{c}, \overline{d}, \overline{e}, \overline{f}]$ are the calibration surface coefficients, V_{Tnew} and V_{Pnew} are the new values measured corresponding to the unknown pressure P_{new}. They can be single values or can be calculated averaging multiple values. In the second case $u_{V_{Tnew}}$, $u_{V_{Pnew}}$ and $cov(V_{Tnew}, V_{Pnew})$ can be calculated as the variance and covariance of the values. Otherwise these terms in Equation (13) should be omitted or better should be replaced

with an appropriate estimation.
In Equation (11), the two term u^2_{coeff} constitute fossilized contributions coming from calibration. They account for the fact that the data used to calculate the calibration surface are not exactly on the surface itself because of their measurement uncertainty. Nevertheless, even though it would be possible to obtain calibration point free of measurement uncertainties, these points may not lay on the calculated surface since the functional form (Eq.(6)) chosen is an approximation of the behaviour of the transducer. To take in to account this scatter of the calibration data with respect to the calibration surface, the RMSE (Eq.(10)) value is added in Equation (11).
Equations (6) and (11) would permit to perform static pressure measurements in the TROVA test section and to evaluate thoughtfully the uncertainties if it was not for one last problem that will be explain in the following section.

2.2.1.1 *On-line zero procedure*

Pressure transducers suffer from sensitivity to environmental conditions and as a consequence, the functional form used to model the transducers response (Eq.(6)) can change slightly from one test to another. In particular, it was evidenced that the change are due to a variation of the constant term (d) in Equation (6). Since the detection of non-ideal effects requires an accuracy in the measurements of the order of $mbar$, even a slight change would affect the results. Thus, an on-line zero procedure was adopted to correct the measurements accounting for the changes in the constant term (d).

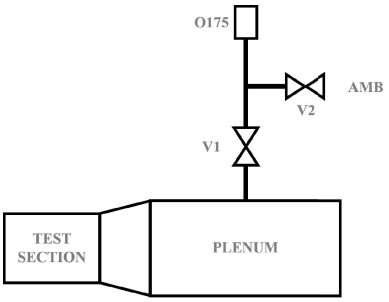

Figure 2.7: Scheme of the system employed for performing the on-line zero of acquisition pressure transducers before every test.

The on-line zero procedure is carried out thanks to a system of pipes and valves, illustrated in Figure 2.7, connected to the plenum, to the ambient and to an absolute pressure transducer called $O175$. Pressure transducer $O175$ is a piezoresistive pressure transducer of the XTE serie from Kulite. Its full scale is $1.75 bar$. It works always at ambient temperature since it is kept far from the heated portions of the plant through a long pneumatic line. For this reason its behaviour is well modeled by equation $P = m_0 V_P + q_0$. It was calibrated with a procedure similar to the one described in section 2.2.1 except that the calibration points were taken only at ambient temperature and the regression performed was a simple linear one. The on-line zero procedure consists in

- opening V2 (keeping V1 closed) to put $O175$ in communication with the ambient
  - measuring the ambient pressure P_{amb} by means of an absolute barometer calibrated by ACCREDIA laboratories

  - acquiring 100 values of V_p^{O175} and calculating their mean V_{00} and standard deviation $u_{V_{00}}$

- calculating the constant term of the functional form describing the behaviour of $O175$ as

$$q_{0corr} = P_{amb} - m_0 V_{00} \tag{14}$$

- closing V2 and opening V1 in order to put in communication $O175$ with the plenum and the test section, where, all the transducers that will be used during the upcoming test, are mounted
  - acquiring 100 values of V_p^{O175} and calculating their mean V_0 and standard deviation u_{V_0}
  - calculating the pressure present in plenum and test section as

$$P_{TS} = m_0 V_0 + q_{0corr} = m_0 V_0 + P_{amb} - m_0 V_{00} \tag{15}$$

  - acquiring 100 values of V_{Pk} and 100 values of V_{Tk} for each of the transducers mounted and calculating their mean (V_{Pk0}, V_{Tk0}) and standard deviations $(u_{V_{Pk0}}, u_{V_{Tk0}})$
  - obtaining the current corrected value for the constant term d_{corr} as:

$$P_{TS} = (a + bV_{Tk0} + cV_{Tk0}^2)V_{Pk0} + (d_{corr} + eV_{Tk0} + f\,V_{Tk0}^2) \tag{16}$$

$$d_{corr} = P_{TS} - [(a + bV_{Tk0} + cV_{Tk0}^2)V_{Pk0} + (eV_{Tk0} + f\,V_{Tk0}^2)] \tag{17}$$

This new value of the constant term is replaced to the one defined during calibration, thus correcting the pressure transducer functional form employed to convert voltage readings (V_T, V_P) in pressure measurements. The on-line zero procedure is performed right before each test, when the transducers have reached the temperature they will approximately maintain during the whole test. At this moment the test section has reached a pressure below the atmospheric one, usually $(P_{TS} = 10 \div 200 mbar)$, and it is filled with extremely rarefied vapour of organic fluid.
The on-line zero procedure introduce other uncertainties related to the evaluation of d_{corr} that are not taken in to account in Equation (11). Thus, in conclusion the behaviour of the transducer is correctly modeled by Equation (18). While the uncertainty related to a

measurement performed using the calibrated transducer after the on-line zero procedure is estimated at best by Equation (19).

$$P_{new} = (a + bV_{Tnew} + cV_{Tnew}^2)V_{Pnew} + (d_{corr} + eV_{Tnew} + f\,V_{Tnew}^2) \tag{18}$$

$$u_{Pnew} = \sqrt{\tilde{u}_{coeff}^2 + u_{new}^2 + RMSE^2 + u_{on-line}^2 + u_{bar}^2} \tag{19}$$

$$\tilde{u}_{coeff}^2 = \sum_{t=1}^{4}\left(\frac{\partial P_{new}}{\partial \tilde{q}_t} u_{\tilde{q}_t}\right)^2 + 2\sum_{t=1}^{4} \frac{\partial P_{new}}{\partial q_t}\frac{\partial P_{new}}{\partial q_{t+1}} cov(q_t, q_{t+1}) \tag{20}$$

$$u_{on-line}^2 = \left(\frac{\partial P_{new}}{\partial V_{Pk0}} u_{V_{Pk0}}\right)^2 + 2\left(\frac{\partial P_{new}}{\partial V_{Tk0}}\frac{\partial P_{new}}{\partial V_{Pk0}} cov(V_{Tk0}, V_{Pk0})\right) + \left(\frac{\partial P_{new}}{\partial V_0} u_{V_0}\right)^2 + \left(\frac{\partial P_{new}}{\partial V_{00}} u_{V_{00}}\right)^2 \tag{21}$$

$$u_{O175}^2 = \left(\frac{\partial P_{new}}{m_0} u_{m0}\right)^2 + RMSE_{O175}^2 \tag{22}$$

Where $\tilde{q}_t = [\overline{a}, \overline{b}, \overline{c}, \overline{e}, \overline{f}]$ are the calibration surface coefficients except $\overline{d}$. The term u_{new}^2 is evaluated as reported in (13). Term $u_{on-line}^2$ gathers all the random related uncertainties coming from the on-line zero procedure. Term u_{O175}^2 accounts for the uncertainties related to the calibration of transducer $O175$, and finally term (u_{bar}) account for the uncertainty of the barometer used to measured the ambient temperature. In the end, u_{Pnew} has a confidence level of 68%, to expand it to a confidence level of 95% a coverage factor of 2 was adopted. In Table 2.1 the pressure transducers available together with an indicative value for their uncertainty are reported.

2.3 TEMPERATURE MEASUREMENT

Obtaining a reliable total temperature measurement is key to perform the experimental characterization of the isoentropic expansion of a non-ideal compressible vapor since the flow properties are dependent on the stagnation condition. In particular, in the TROVA facility, the total temperature is measured using thermocouples in the settling chamber ahead of the test section since the flow within the plenum can be reasonably assumed adiabatic and with negligible friction losses.. Thermocouples have been chosen because of their reliability, low cost and possibility of miniaturization. In particular 4 different thermocouples, two type K (Nickel/Chromium-Nickel/Alumel) and two type J (Iron-Constantan), were chosen. Their characteristics are summarized in Table 2.2.

Because of the blow-down configuration of the TROVA facility, the total temperature is not constant during a test. Figure 2.8a shows the evolution of the stagnation conditions during a test performed with fluid MDM. The total temperature is measured by two different thermocouples both inserted in the plenum. It can be noticed that the total pressure monotonically decreases consistently with the emptying of the HPV. The total temperature instead first increases and then decreases. This can be explained by the fact that usually the pipes are heated up to a temperature higher than the one set in the reservoir.

Name	Full Scale $[bar]$	Type	U_P $[bar]$
$O1.75$	1.75	Absolute	0.001
$A40$	40	Absolute	0.03
$B21$	21	Absolute	0.03
$C17$	17	Absolute	0.02
$D14$	14	Absolute	0.01
$E14$	14	Absolute	0.02
$F10$	10	Absolute	0.02
$G7$	7	Absolute	0.01
$H7$	7	Absolute	0.01
$I7$	7	Absolute	0.01
$L35$	3.5	Absolute	0.01
$M35$	3.5	Absolute	0.01

Table 2.1: Pressure transducers available together with an indicative value for their uncertainty. U_P is calculated from Equation (19).

Name	Type	Junction dimension $[mm]$	Junction type	Expanded Uncertainty U $[^\circ C]$	Correlation estimated time constant τ_{HC} $[s]$	Two-thermocouples estimated time constant τ_{two} $[s]$
$TCK1$	K	0.25	sealed	1	0.162	0.327
$TCK2$	K	0.15	exposed	0.78	-	-
$TCJ1$	J	0.7	exposed	1.2	0.392	1.485
$TCJ2$	J	0.25	sealed	0.8	-	-

Table 2.2: Thermocouples available.

In terms of dynamic response the thermocouples are typically much slower than the piezoresistive pressure transducers and this can cause a delay between the pressure and the temperature measurements. In order to assess if the dynamic response of the thermocouples adopted is adequate to measure the evolution of the total temperature during a test run, the time constants τ of the thermocouples used were estimated using two different methods. First τ was estimated using heat transfer correlations and secondly the two sensor characterization method proposed by (Hung et al., 2005) was applied. Knowing the values of τ permits the reconstruction of the thermocouple input, thus of the real vapor total temperature. The results of the τ estimations are illustrated in Sec.2.3.1 and the reconstructed signal is reported in Sec.2.3.2.

2.3.1 *Time constant estimation*

The time constant for a thermocouple is the time necessary for the temperature of the junction, exposed to a step temperature signal, to reach a temperature equal to 63.2% of the step temperature signal itself. The time constant can be measured through a dynamic calibration carried out in shock-tube facilities. However, it is dependent not only on the characteristics of the thermocouple itself, but also on the thermo-physical characteristics of the working fluid. Thus, dynamic calibration is currently available only for thermocouples to be used in air. Nevertheless, a rough estimation of the time constant can be obtained by modeling the heat transfer mechanism between the fluid flow and the thermocouple junction. Moreover, several alternative, and more accurate methods, have been proposed which involve the use of two thermocouples with different time constant exposed to the same unknown temperature signal (Tagawa et al., 0998; Tagawa and Ohta, 1997; Hung et al., 2005).

2.3.1.1 *Method based on heat transfer correlations*

The evolution of the temperature of a thermocouple junction subjected to a step temperature signal can be described by the following differential equation.

$$\rho C V \frac{\partial T_j}{\partial t} = -hA_j(T_j - T_f) - A_j \sigma \varepsilon_W (T_j^4 - T_W^4) \tag{23}$$

Where T_j is the temperature of the thermocouple junction, T_f is the temperature of the fluid, T_W is the temperature of the pipe walls, C is the specific heat capacity of the junction, V is the volume of the junction, h is the convective heat transfer coefficient, A_j is the surface of the junction, $\sigma = 5.6710^{-8} W/(m^2K^4)$ is the Stefan-Boltzmann constant, ε_W is the emissivity of the pipe walls and t is the time. This model neglect conduction losses while it includes the radiative ones. Indeed, the pipe walls of the settling chamber of the TROVA are heated, thus the thermocouple is surrounded by walls at high temperature

and the radiative heat exchange cannot be a priori neglected. However, the radiative term can be linearized and Equation (23) can be non-dimensionalized obtaining Equation (24).

$$\frac{\partial T^*}{\partial t^*} + AT^* + B = 0 \tag{24}$$

$$T^* = \frac{T_j - T_f}{T_{ji} - T_f} \quad ; \qquad t^* = \frac{\alpha_j t}{L_c^2} \quad ; \tag{25}$$

$$A = \frac{h_{tot} A_j L_c^2}{k_j V} \quad ; \qquad B = \frac{4\varepsilon_W \sigma T_W^3 A_j L_c^2}{k_j V} \cdot \frac{(T_f - T_W)}{(T_{ji} - T_f)} \quad ; \tag{26}$$

$$L_c = \frac{V_j}{A_j} \quad ; \qquad h_{tot} = h + 4\varepsilon\sigma T_W^3 \tag{27}$$

Where T^* is the non-dimensional temperature, T_{ji} is the initial junction temperature and h is the convection heat transfer coefficient. The solution Equation (24) is:

$$T^* = \left[\frac{B}{A} + 1\right] e^{-At^*} - \frac{B}{A} \tag{28}$$

Eq.(28) gives the evolution of T_j with time that is exactly the information required to measure the thermocouple time constant. However, in order to evaluate it, T_f and the thermal characteristics of the fluid must be known. It is possible to give a rough estimation of all the quantities required looking at the data acquired during a test run.
Before the beginning of each test the settling chamber is in vacuum condition with no flow and its wall are heated up to a known temperature T_W; in these conditions the thermocouple junction measures the temperature T_{ji}. When the test starts the flow establishes and, the temperature registered by the thermocouple, undergo a sudden rising followed by a plateau. The temperature reached at the plateau is taken as the real fluid temperature T_f. Since also the pressure P_f is measured they can be used, together with the thermodynamic model of (Thol et al., 2017) implemented in FluidProp, to evaluate all the other quantities needed to compute A and B. The volume an the exposed area of the junction is known. To evaluate h two heat transfer correlations have been used: the correlation of Whitaker to evaluate h for the spherical exposed junction of thermocouple $TCJ1$ and the correlation of Chrchill & Bernstein to evaluate h for the cylindrical sealed junction of thermocouple $TCK1$.
Thermocouples $TCJ1$ and $TCK1$ were analyzed since they were the only thermocouples available during the first experimental campaign conducted at the TROVA; in addition, the other thermocouples are expected to have a better dynamic response thanks to their smaller junctions. Fixing $T_{ji} = 242^\circ C$, $T_f = 249^\circ C$ and $P_f = 2.996 bar$, that are the data taken from test run $MDM2L$ (see Chap.5), the time response for $TCJ1$ resulted $\tau_{TCJ1} = 0.335 s$ and the time response for $TTK1$ resulted $\tau_{TCK1} = 0.159 s$.

The same analysis was conducted neglecting the radiative losses. The adimensional equation to be solved becomes Eq.(29); whose solution is reported in Eq.(31).

$$\frac{\partial T^*}{\partial t^*} + FT^* = 0 \tag{29}$$

$$F = \frac{hA_jL_c^2}{k_jV} \tag{30}$$

$$T^* = e^{-Ft^*} \tag{31}$$

In this case, the results were $\tau'_{TCJ1} = 0.392s$ and $\tau'_{TCK1} = 0.162s$. The time constants neglecting the radiative losses are higher because, in this case, the radiation from the wall contributes to heat the junction bringing it closer to the fluid temperature faster. However, the discrepancy is negligible, thus, from now on the radiation inside the plenum will be neglected and only τ' will be considered.

2.3.1.2 *Two thermocouples method*

The plenum is usually equipped with two thermocouples, one of type K and one of type J, during each test. Their hot junctions are located at the chamber axis and, even if they have a relative distance of about 200 mm streamwise, they are supposed to measure the same quantity namely the total temperature ahead of the test section. Having two thermocouples with different junction size, thus, different time constants, measuring the same quantity makes it possible to apply the method, for the evaluation of the time constant τ, proposed in (Hung et al., 2005). This method is suitable for constant velocity flow environment as it is the case of the plenum where the velocity is so low that can be neglected.
The method model the thermocouple using Eq.(23) but neglecting the radiative term. Rearranging Equation (23) with this hypothesis the thermocouple dynamic model can be described as:

$$T_f(t) = T_j(t) + \tau\frac{dT_j(t)}{dt}, \tag{32}$$

Where T_f is the real temperature of the fluid while T_j is the temperature of the junction, thus the measured one, τ is the time constant which depend on several factors related to the sensor geometry and flow conditions. However, providing that the thermodynamic properties of the fluid are not subjected to extremely large fluctuation during one test and that the flow velocity can be assumed as almost constant in the plenum, an invariable mean time constant τ can be reasonably assumed.
In order to estimate τ it is necessary to discretized Equation (32). This can be done assuming Zero Order Hold (ZOH) on the inputs and a sampling time τ_0, resulting in Equation (33)

$$T_j(k) = aT_j(k-1) + bT_f(k-1) \tag{33}$$

$$a = e^{-\tau_0/\tau} \quad , \quad b = 1 - a \tag{34}$$

Since T_f is unknown, a and b cannot be determined directly. The fact that the same signal is measured by two different thermocouple can be used to get rid of the unknown term T_f. The output signals of the two thermocouples are expressed in equations (35) and (36).

$$T_{j1}(k) = a_1 T_{j1}(k-1) + b_1 T_f(k-1) \tag{35}$$

$$T_{j2}(k) = a_2 T_{j2}(k-1) + b_2 T_f(k-1) \tag{36}$$

As T_f is assumed to be the same for both sensors, it can be eliminated and the above relations can be rearranged as

$$T_{j2}(k) = \gamma_1 T_{j2}(k-1) + \gamma_2 T_{j1}(k) + \gamma_3 T_{j1}(k-1), \tag{37}$$

where

$$\gamma_1 = a_2, \quad \gamma_2 = \frac{1-a_2}{1-a_1}, \quad \gamma_3 = -\frac{a_1(1-a_2)}{1-a_1}. \tag{38}$$

Equation (37) is linear in the γ parameters. The γ parameters can be estimated as the one that best fitted the values $T_{j1}(k)$, $T_{j2}(k)$ measured by the thermocouples during an experiment. The Total Least Square (TLS) method (Golub and Van Loan, 1980) was used with regression vector

$$\boldsymbol{x}(k) = [T_{j2}(k-1) \quad T_{j1}(k) \quad T_{j1}(k-1)]$$

and parameter vector

$$\boldsymbol{\theta} = [\gamma_1 \quad \gamma_2 \quad \gamma_3].$$

TLS is recommended over ordinary least squares because T_{j1}, T_{j2} and T_f are all corrupted by noise, being them measured temperatures.
It can be noticed that just two of three equations in (38) are necessary to determine a_1 and a_2, so three different combinations are possible. The best method to obtain one result only is the averaging of the three results (Zimmerschied and Isermann, 2010).
Data coming from one experiment conducted using the fluid MDM were used to calculate the time constant of the two thermocouples $TCK1$ and $TCJ1$ (see Table 2.2). The evolution of the total conditions measured within the plenum during the test chosen are shown in Figure 2.8a. The first 45 seconds were considered, taking $t_0 = 0$ when the opening transient of valves MCV and V3 finished and the maximum total pressure in the plenum was reached. A zoom of the raw temperature signals registered by the two thermocouples during the firsts 45 seconds is shown in Figure 2.8c. The raw signal are acquired with a sampling interval of $0.001s$, however signal preconditioning is necessary to achieve good results since noise can significantly deteriorate the TLS model fit. A second-order Butterworth filter was used and the cut-off frequency was chosen performing a parametric study on the dependence of the time-constant estimates on the pre-filter bandwidth. The results of this analysis are shown in Figure 2.9a. Too low cut off frequency removes

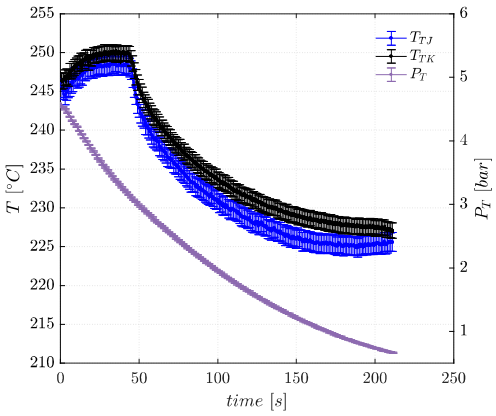

(a) *Evolution of total conditions measured in the plenum during a test performed using fluid MDM.*

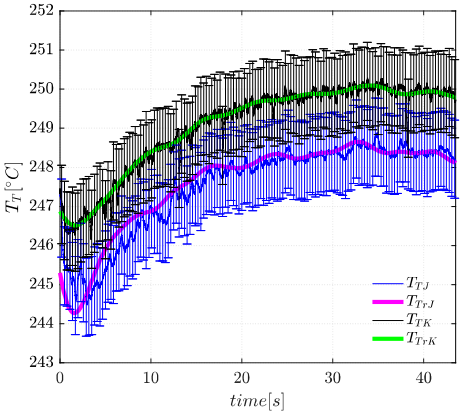

(b) *Reconstructed temperature signals of the firsts 45 seconds of a test performed with MDM. The signals were reconstructed using the time constants of the thermocouple estimated usign the two-thermocouples method presented in section 2.3.1.2.*

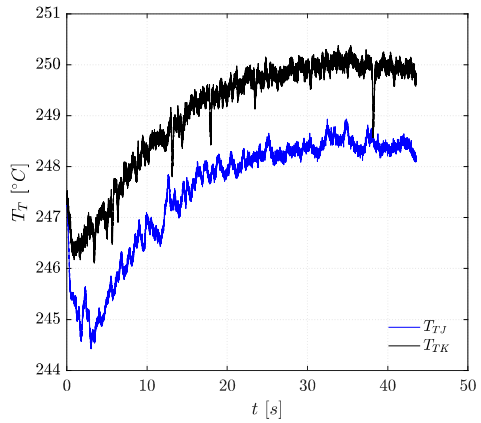

(c) *Temperature signals measured during the firsts 45 seconds of a test performed with fluid MDM.*

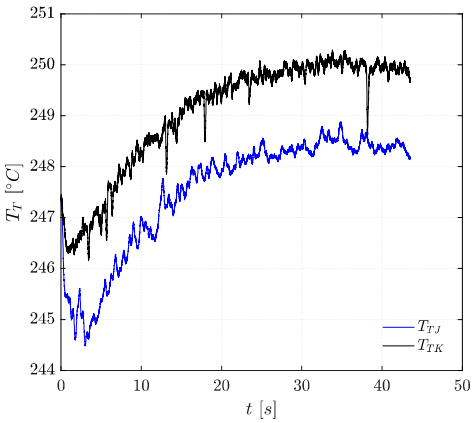

(d) *Temperature signals filtered using a second order Butterworth filter with a cut-off frequency* $f_{cut} = 100Hz$.

Figure 2.8

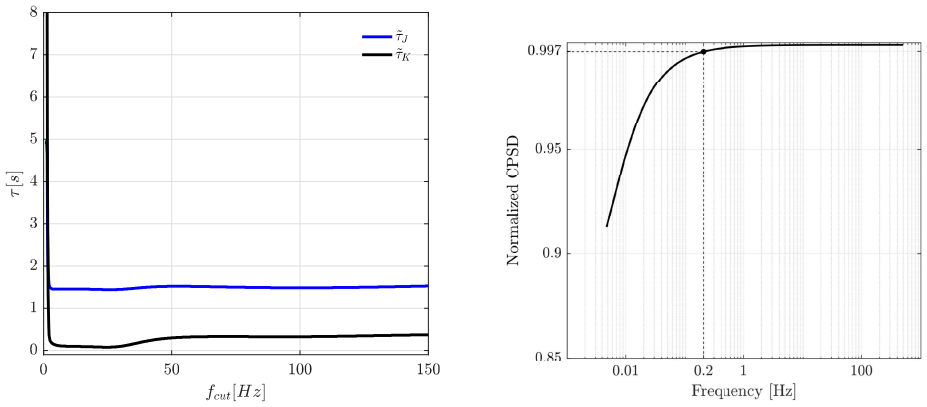

(a) *Estimated time constants from TLS fit, for different values of the pre-filtering bandwidth (second-order Butterworth filter).*

(b) *Normalized cumulative power spectrum density of the pressure signal. The dashed lines highlight the cut off frequency chosen for the post-filtering operation.*

Figure 2.9

the fundamental frequencies of the signal causing an un-physical peak in the estimated time constants. After the peaks two plateaus can be found. Finally a cut off frequency of $f_{cut} = 100Hz$ was chosen. This frequency is located in the middle of the second plateau that is the one giving the higher values of the time constants, thus the most limiting ones. The filtered temperature signals acquired during the firsts 45 seconds of the test chosen for this investigation are shown in Figure 2.8d. The two-thermocouple method used on the signals plotted in Figure 2.8d estimated time constants $\tau'_{TCJ1} = 1.485s$ and $\tau'_{TCK1} = 0.327s$. The time constants estimated using the two method; i.e. the method based on heat transfer correlations and the two-thermocouples method, are reported in Table 2.2. It can be seen that the two-thermocouples method provides higher time constant. However, the order of magnitude of the time constants estimated is fairly the same for both methods. The fact that thermocouple $TCK1$ is significantly faster is consistent with the smaller size of the sensing element with respect to thermocouple $TCJ1$.

2.3.2 *Temperature input signal reconstruction*

Once the dynamic characterization of the thermocouple has been carried out by estimating its time constant; it is possible to compensate the measured signals. This is done by computing the unknown temperature of the fluid T_f starting from the known measured temperature of the junction T_j and the estimated time constant τ and using Equation (33). The reconstruction procedure is very sensitive to the noise inevitably present using real measurements. An additional filter, here called the post-filtering operation, in contrast to the pre-filtering operation ahead of the time constant estimation, is therefore necessary to reduce unwanted noise. Post-filtering is, of course, a compromise between retaining high frequency temperature dynamics and noise removal. Post-filtering is carried out

using a two-pass Butterworth filter.
In order to decide the cut off frequency for the post-filtering operation, the total pressure measured in the plenum during the test was analyzed. The dynamic response of the piezoresistive pressure transducer used to measure the total pressure is much faster than that of the thermocouples used to measure the total temperature. Thus, the pressure signal can be used as reference for the spectral content of the blow-down process of the HPV. The spectral analysis of the pressure signal reveals that only 0.003% of the signal energy is found above 0.2 Hz (see Fig.2.9b). The latter value is therefore set as cut-off frequency of the two-pass Butterworth post-filter, thus eliminating most of the noise while keeping the essential dynamics.
Finally it is possible to compare the thermocouples output with the reconstructed signals, in order to determine whether the latter lies in the error band around the former. This comparison is shown in Figure 2.8b. For both thermocouples $TCJ1$ and $TCK1$, the reconstructed input signal is well within the uncertainty band, suggesting that dynamic compensation is not required.
This consideration is valid also for the other thermocouples $TCJ2$ and $TCK2$ available at the TROVA. Having a smaller junction their time response is expected to be lower than the one found for the analyzed thermocouples $TCJ1$ and $TCK2$. Even though the time constant estimation here presented was carried out using a portion of the signals acquired during one test; it can be stated that this estimation is roughly valid for all the test performed both using fluid MDM and fluid MM. Belonging to the same family the thermal characteristics of the two fluid are close, thus it is reasonable to expect the same order of magnitude in the thermocouple time constants when used with these two fluids.

2.4 MACH NUMBER MEASUREMENTS

As already pointed out in section 2.1, most of the measurement techniques commonly applied in ordinary air wind tunnels, are not currently employable on the TROVA facility because of the peculiarities of the investigated flows. Directional pressure probes and optical techniques requiring the seeding of the flow are among them. However, the schlieren technique is particularly suited in this framework since it is readily and easily applicable to any transparent media as complex fluid vapor flows. Indeed, the schlieren techniques does not require fluid-specific calibration nor seeding of the flow. Unfortunately, the schlieren technique does not provide any quantitative information. It is usually employed in wind tunnels to complement other quantitative measurements with a qualitative understanding of the structures present in the flow under investigation (Ghio et al., 2017; Luxa et al., 2016; Ozawa and Laurence, 2018).
Recently, research efforts are being made in order to get also quantitative information from schlieren images; in particular a growing interest is arising around the Backgroud-Oriented Schlieren (BOS) technique that aims at measuring the density field (Raffel, 2015; Cozzi et al., 2017). Moreover, the automatic detection of salient features in schlieren

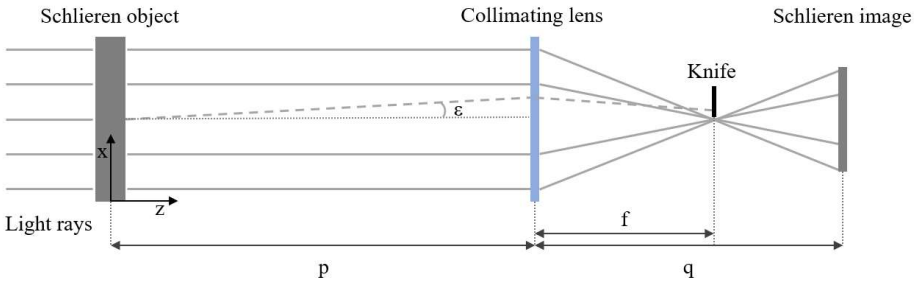

Figure 2.10: Illustrative sketch of the schlieren technique. The light rays pass through the schlieren object and one of them is deviated (ε) because of the density gradients in the x-direction. It can be seen that the deviated ray is blocked by the knife and do not contribute to the formation of the schlieren image.

images have been used to identify their position and to quantify the unsteadiness of shock waves (Smith et al., 2014; Estruch et al., 2008; Alan et al., 2005).
Modern computer vision techniques can be applied to schlieren images in order to characterize in a quantitative way the structures present within the flow. In particular during this thesis a novel technique capable of automatically detecting flow structures locally approximable with straight lines in schlieren images was conceived. The method permits the identification of the best parameters approximating slope and position of the detected lines.
Salient flow structures that can be locally approximated by straight lines are for example Mach waves, compression shocks and the edges of expansion fans. Knowing the exact slope and position of these structures provides crucial informations to characterize the flow and to be used to assess CFD simulations. Moreover, the slope of Mach waves can be directly related to the local Mach number attained in regions where the velocity direction of the flow is known. Thus, the technique here presented can be also exploited to obtain a direct measure of the local Mach number. This feature is particularly important since it permits right away to obtain detailed information of the flow field of supersonic non-ideal compressible fluids.
Section 2.4.1.1 provides a brief recalling of the principles of the schlieren technique and, more importantly, it gives insights into the issues related to the use of the schlieren technique in non-ideal compressible supersonic flows. Finally, section 2.4.2 presents the technique implemented.

2.4.1 *Use of schlieren technique in non-ideal compressible flows*

2.4.1.1 *Fundamentals of schlieren technique*

The schlieren technique is an optical method that exploits the relation existing between the density and the refractive index of a media. This relation entails deviation of light

rays crossing a transparent media, that in this case is a flow field, where density gradients are present. The refractive index n can be expressed using the Gladstone-Dale relation Eq.(39),

$$n = 1 + K\rho \tag{39}$$

where ρ is the density of the media, and K is the Gladstone-Dale constant (Gladstone and Dale, 1864). Eq.(40) describes the relation between the refractive index gradient and the density gradient that can be derived from the Gladstone-Dale equation.

$$\nabla n = K\nabla\rho \quad \longrightarrow \quad \frac{\partial n}{\partial x} = K\frac{\partial \rho}{\partial x} \tag{40}$$

$$\varepsilon \propto \frac{\partial n}{\partial x} \tag{41}$$

When light rays cross regions where refractive index gradients in direction x are present, they undergo an angular deflection ε along the same direction. Figure 2.10 shows the path of light rays crossing a flow, identified in the picture as the schlieren object. In the sketch one of the rays is deviated to show how the deflection can be exploited to selectively block it. This is possible thanks to the knife edge which is a key component of a schlieren apparatus. The blocked ray cannot contribute to the formation of the image causing the appearance of darker regions, which are placed where a refractive index gradient has deviated the rays toward the knife edge. Contrarily, opposite gradients result in brighter areas. The technique is thus sensitive only to gradients that are perpendicular to the knife edge. Further details on the schlieren technique can be found in (Settles, 2001).

2.4.1.2 *TROVA optical bench*

The optical bench for schlieren visualizations used in this work is schematized in Figure 2.11. The system employs a double-passage configuration. A single-passage configuration would have required a second optical access in place of the steel rear plate of the test section, leading to a complicated configuration to accommodate pressure taps and nozzle profiles. Moreover, the use of a double-passage configuration allows one to place all optical components on a single optical bench, making system alignment (performed with a laser point light source) much simpler.
The most important components of the optical bench are summarized in Table 2.3. There are two light sources available; a mercury vapor lamp and a LED. There are also multiple lenses with different focal lengths available as $L2$ so it is possible to choose the best focal length in order to obtained an image framed on the interesting portion of the flow.
The light rays coming from the light source are collimated by a bi-convex lens $L1$ and enter the test section perpendicularly to it. They are deflected by density gradients in the fluid flow and are reflected by the mirror-polished rear steel plate. The reflected beams cross the test section again and are focused by lens $L1$ (which therefore also constitutes

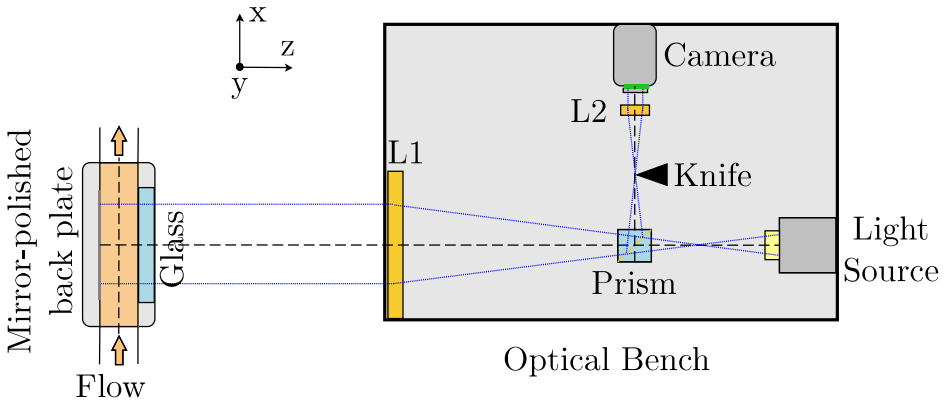

Figure 2.11: Schematic representation of the optical bench used in the TROVA for schlieren visualizations.

the schlieren head) at the knife edge, after a 90° rotation operated by a beam splitter cube. The schlieren image is then formed onto the sensor of a high-speed CMOS camera by a second lens *L2*. The distance between components is determined from the fundamental law of optical geometry for thin lenses.

In order to visualize the horizontal density gradients (along the nozzle axis), the knife is set in the vertical direction. The position of the knife is such that positive density gradients (compressions and shock waves) appear dark whilst negative density gradients (expansions and expansion fans) appear bright.

The camera acquisition frame rate is set as the maximum one allowed by computer performance and it ranged from 10 to 40 frame per second. The exposure time is a trade off between various requirements. A lower exposure time leads to higher-definition images, but also to overall darker images. The latter aspect can also be manipulated through the regulation of the light source. Therefore, exposure time and the light source were regulated so as to ensure high quality image and an appropriate brightness level. Indeed, the initial brightness level must ensure that no image saturation occurs during the test. Density gradients in the fluid flow cause an increase or a decrease in the brightness level in certain portions of the image: if the initial brightness level is too high, information loss occurs, because parts of the sensor may immediately become saturated and insensitive to stronger density gradients. Exposure time of about 1 *ms* was employed in the present experimental campaigns.

Component	Characteristics
Light Source	100 W Mercury vapors lamp
	LED $P = 630 - 1120\ mA$ $\lambda_{peak} = 460\ nm$
Camera	CMOS 1936 x 1216 pixels (IDS uEye CP)
Lens L1	$f_1 = 1000\ mm$, $d_1 = 150\ mm$
Lens L2	$f_2 = 50\ mm$, $d_2 = 52\ mm$
	$f_2 = 75\ mm$, $d_2 = 52\ mm$
	$f_2 = 100\ mm$, $d_2 = 52\ mm$

Table 2.3: Main characteristics of the optical bench components. f is the focal length and d is the diameter of each lens. Lens L2 can vary from a focal length of 50 mm up to 100 mm.

2.4.1.3 *Measuring range issues in non-ideal compressible flows*

As illustrated in the previous section the schlieren bench at the TROVA was arranged to visualize dark positive density gradients and bright negative ones. However, it was found out that expansion fans, that were supposed to appear bright, resulted instead dark at highly non-ideal conditions. This phenomenon was caused by measuring range issues affecting the schlieren images (Conti et al., 2017).

These issues are particularly visible when nozzle $M2$ is employed and when highly non-ideal conditions are reached. Nozzle $M2$ was designed with a step located at the geometrical position of the throat (see Sec.3.3 for further explanations on the nozzle design). The presence of the step originates complex flow features: an expansion fan is present at the step edge (point A in Figure 2.12), followed by compression waves at the reattachment point of the separation bubble at the step edge, which eventually coalesce into a compression shock. A second expansion fan occurs where the flat section of the recessed step ends and the nozzle curvature begins (point C in Figure 2.12).

The schlieren images taken during one of the experiments conducted using MDM as working fluid and nozzle $M2$ are shown in Figure 2.13. From top to bottom of Figure 2.13 the stagnation conditions at which the nozzle is operated change from high pressure and temperature corresponding to a higher degree of non-ideality towards more dilute and almost ideal conditions (see Sec. 3.1 for further explanations about the evolution of conditions during one test).

It can be noticed that in the top three images 2.13a, 2.13b and 2.13c the expansion fans that were supposed to appear bright appear instead dark. However, expansion fans lighten going towards more diluted conditions (bottom of Fig.2.13). This phenomenon is attributed to the strong density gradients occurring in non-ideal flows of MDM, causing refractions intense enough to deflect light onto some system aperture stop. In order to verify this

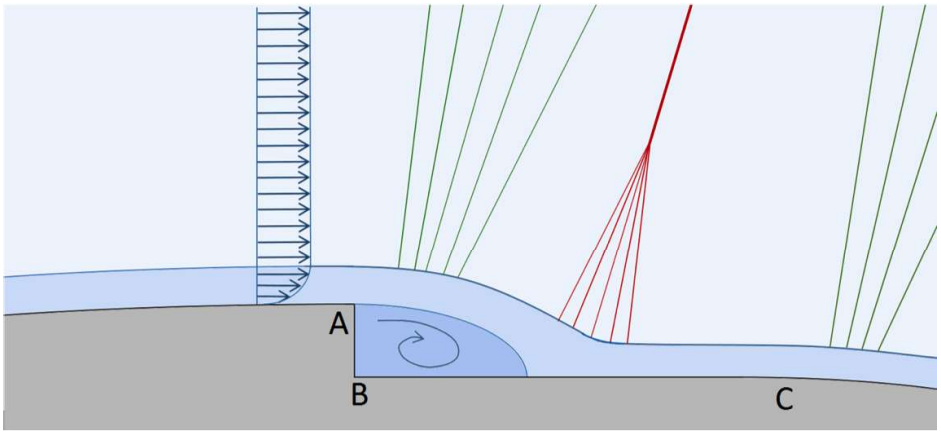

Figure 2.12: Qualitative representation of the complex flow pattern occurring at the recessed step at the $M2$ nozzle throat (Cozzi et al., 2015).

hypothesis, ray tracing calculation was performed along the nozzle axis. Moreover, the evolution of density gradients and refractive index gradients in MDM flows having different total conditions was studied and compared with the gradients that would be obtained in the same nozzle operated with air treated as a polytropic ideal gas.

Ray tracing involves discretizing the light source into a finite number of rays and tracking their path through the optical bench apparatus. A *Matlab*® code was purposely written to do so, with the aim of understanding if and where the aperture stops in the ray path occur.

In the modeling of the TROVA optical bench, the lenses, the glass and the prism are assumed to have no geometrical imperfection and to have perfectly clean surfaces, whilst the rear plate is considered to be perfectly mirror-polished. Optical axes of all components are assumed to be perfectly aligned and coincident along the z-direction, perpendicularly to the test section.

The code models the path of rays through the test section as well as through the rest of the optical bench. In order to determine the disturbance through the compressible flow, a trend of the refraction index and of the density gradient along the nozzle axis is calculated from CFD results that match quite well with the experimental data (see Section 5.2.1 for more detail on the CFD calculations). The data from the CFD simulation were used instead of the experimental ones as the spatial discretization of experimental measures (nine pressure taps along the nozzle) is inadequate for the accurate evaluation of the local density gradients along the nozzle axis. The number of light rays modeled corresponds to the domain discretization employed in CFD simulations, thus as much rays as the mesh node points on the axis were simulated. The origin of the reference x-axis is the inlet of the nozzle geometry.

Ray tracing is performed on rays at the axis of the nozzle (i.e. at a y-coordinate equal to zero) and not in the whole test section, because this is where experimental data is

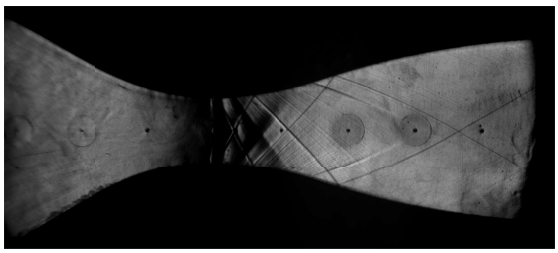

(a) *Total conditions:* $P_T = 4.58\ bar$, $T_T = 246\ ^\circ C$, *corresponding to* $Z_T = 0.82$.

(b) *Total conditions:* $P_T = 3.98\ bar$, $T_T = 249\ ^\circ C$, *corresponding to* $Z_T = 0.85$.

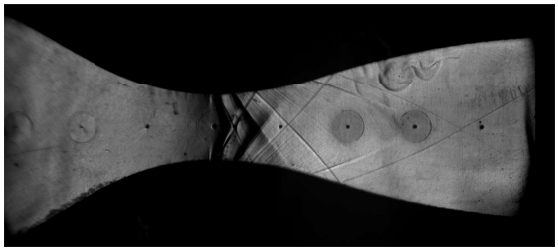

(c) *Total conditions:* $P_T = 3.38\ bar$, $T_T = 250\ ^\circ C$, *corresponding to* $Z_T = 0.88$.

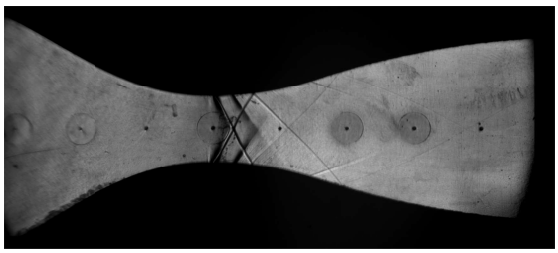

(d) *Total conditions:* $P_T = 1.80\ bar$, $T_T = 232\ ^\circ C$, *corresponding to* $Z_T = 0.93$.

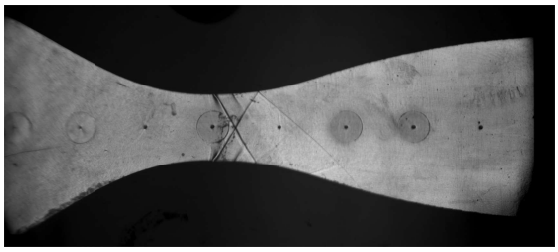

(e) *Total conditions:* $P_T = 0.62\ bar$, $T_T = 226\ ^\circ C$, *corresponding to* $Z_T = 0.97$.

Figure 2.13: Schlieren images of a test with MDM and nozzle $M2$ at different total conditions going from higher level of non ideality (top $Z_T = 0.82$) to almost ideal conditions (bottom $Z_T = 0.97$). Measuring range issues associated with expansion fans noticeably decrease as Z_T increases.

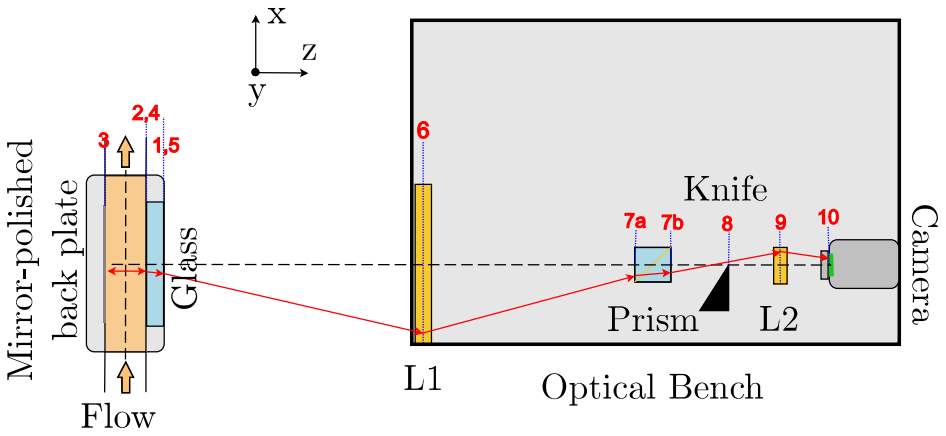

Figure 2.14: TROVA optical bench modelling, the horizontal dash-dotted line is the optical axis of the system, the red line is the path of a generic light ray. The components are modelled as if they were all on the same line perpendicular to the test section even though they are in reality placed as in Figure 2.11. The optical path shown here is equivalent to the one a ray would follow on the bench depicted in Fig.2.11.

available for validation of CFD results. Moreover, since the x-axes of the nozzle and of the optical system are assumed to be perfectly aligned (at the same y-coordinate), no ray tracing calculation in the y-direction needs to be considered.

As explained in the previous Section (2.4.1.2), light rays from the light source are collimated by lens $L1$ before entering the test section. Light rays are assumed to reach the outer surface of the glass perpendicularly to it (this is where light rays modelling starts), and are thus unaffected by refraction in the glass since incidence is null (points 1 to 2 in Figure 2.14).

Passing through the glass, the rays enter the test section perfectly parallel to the z-direction (point 2) and are deflected by the density gradients (so by refractive index gradients) in the x-direction. The change in the x position of a ray as it crosses the test section (back and forth) is assumed negligible: the position of each ray at the inlet (point 2), at the rear plate (point 3) and at the outlet of the test section (point 4) is thus the same. The direction of each ray, though, does change in its path across the compressible flow. In order to calculate this ray deflection, the density gradient in the flow, provided by the CFD calculation, is assumed to be constant along the depth of the cross section, and so along the whole ray path through the flow. The ray deflection can be calculated as:

$$\varepsilon = \frac{L}{n_\infty} K \frac{d\rho}{dx} \tag{42}$$

where n_∞ is the refractive index at the inlet of the disturbed region, K is the Gladstone-Dale constant and L is the depth of the flow in the z direction.
The Gladstone-Dale constant for the fluid MDM was calculated starting from the Lorentz-Lorenz Equation (43).

$$\frac{(n^2-1)M_m}{(n^2+2)\rho} = R_M \quad \longrightarrow \quad n = \sqrt{\frac{M_m + 2R_M\rho}{M_m - R_M\rho}} \tag{43}$$

where R_M is the molar polarization that is considered constant and was calculated for the MDM liquid $R_M^{MDM} = 0.0670\ m^3/kmol$, M_m is the molar mass and ρ is the density. Using Equation (43) a curve $n = n(\rho)$ was plotted for a significant range of densities. This curve resulted to be well interpolated by the Gladstone-Dale Equation (44).

$$n = 1 + K_{\mathrm{MDM}}\rho \tag{44}$$

The interpolation provides the value $K_{\mathrm{MDM}} = 4.3 \cdot 10^{-4}\ m^3/kg$.
The rays deflection at the exit of the test section (before crossing the glass, point 4) is actually twice the one calculated by Equation (42), since the ray is disturbed both in its forward and backward paths through the flow.
Rays are refracted by the glass at their exit from the test section because they are no longer perpendicular to it. Angles at the MDM-glass (point 4) and glass-air (point 5) interfaces are calculated by applying the Snell-Descartes Law of refraction in a homogeneous medium at each x-coordinate ($n_{air} = 1.000293$ at $T = 273.15\ K$ and $P = 101325\ Pa$ and $n_{glass} = 1.47$):

$$n_1 \sin i = n_2 \sin r \tag{45}$$

where n_1 and n_2 are the refractive indices of the first and second medium respectively and i and r are the incidence and refraction angles.
The x-position of each ray at the exit of the glass (point 5) and at lens $L1$ (point 6) easily follow from trigonometry, since the glass thickness and the distance from the glass to $L1$ are known quantities and the ray inclinations were just calculated.
Rays are then deflected by lens $L1$ at point 6. Rays deflection can be calculated following the principles of thin lenses, knowing $L1$ focal length. The ray x-coordinate at the inlet of the prism (point 7a) can be easily determined from trigonometry, since the ray angle and the distance between $L1$ and the prism are known quantities. Refraction through the prism is considered. Angles at the air-prism (point 7a, in the prism) and prism-air (point 7b, in air) boundaries are determined from the Snell-Descartes law ($n_{prism} = 1.5168$), and the x-positions at the exit of the prism are calculated by applying trigonometry (size of the prism is known).
The x-coordinate of each ray at the knife (point 8) and lens $L2$ (point 9) is easily calculated from trigonometry as well, since distances between components and angles at the exit of the prism (7b) are known. The deflection of each ray by lens $L2$ is determined just as in the case of $L1$ from the principles of thin lenses knowing $L2$ focal length. Finally, the x-coordinate at the camera sensor (point 10) is determined from trigonometry.

The path of each light ray is therefore completely determined. The key aspect is that every time the ray intercepts a component of the optical bench, a check on whether it is let through or blocked by that component is performed, thus allowing to determine if and where rays are blocked, and by which component. This is done by comparing the x-coordinates of the rays at each optical component and the x-coordinates of the component itself. If the former lie within the latter, then the rays are let through by that component; if this is not true, those rays are blocked by the component or fall out of its field of view, and thus do not contribute to image formation at the sensor. An example of the graphical output of the *Matlab*® code is presented in Figures 2.15a and 2.15b. The Figure 2.15a shows the path of all modeled rays and the position of optical bench components, numbered according to Figure 2.14. Rays blocked by some system aperture (in red) are set to $x = 0$ before reaching the blocking component, so as to highlight the latter. Rays that proceed their path all the way to the sensor with no blockage are in blue. The nozzle profile (with correct scaling) is reported at the top of the figure in orange and it is superimposed on the corresponding experimental schlieren image. The regions on the axis (at the throat) where the red rays are found should be bright since they correspond to two distinct expansion fans, but are actually dark due to ray blockage by the knife frame (as the ray path shows).

The code output indicates that the rays at the extremities of the nozzle are lost because the diameter of lens L1 is smaller than the nozzle size: this is a trivial result, as indeed the schlieren image does not include the ends of the nozzle (the first pressure tap is not visible). The right end of the image is dark too whilst the light rays are blue (they are not 'lost' out of L1 in the calculation) and clearly shows the shadow of lens L1: this inconsistency between calculation and the actual image is probably due to optical aberrations that reduce the effective diameter of lens L1. Also, the left end of the image is sharply cut, unlike the right end. This is probably due to the fact that the sensor might not be perfectly centered on the optical axis of the system: as a result, part of the image is not present, whilst the modeled light rays are blue (meaning that they are not lost anywhere in the system in the calculated ray path).

More informatively, the code shows how, in this particular test condition, a substantial number of rays in the region just after the throat is not reaching the sensor. Figure 2.15a and the analysis of successive scatter plots (as explained in Figure 2.15b) indicate that most of these rays are blocked by the knife frame. The density gradient in the expansion fans is so intense that the rays deviation leads to blockage at the frame holding the knife (see the description in Figure 2.15a). These rays would have contributed to the formation of the image on the camera sensor but were prevented from doing so by this aperture stop, causing the dark image portions at the throat in the reported schlieren image. This is the reason why the expansion fans appear as dark instead of bright in the analyzed image.

However, this measuring range issue appear only in some flow conditions. If the same $M2$ nozzle is operated with air the phenomenon is almost unnoticeable. Moreover, looking

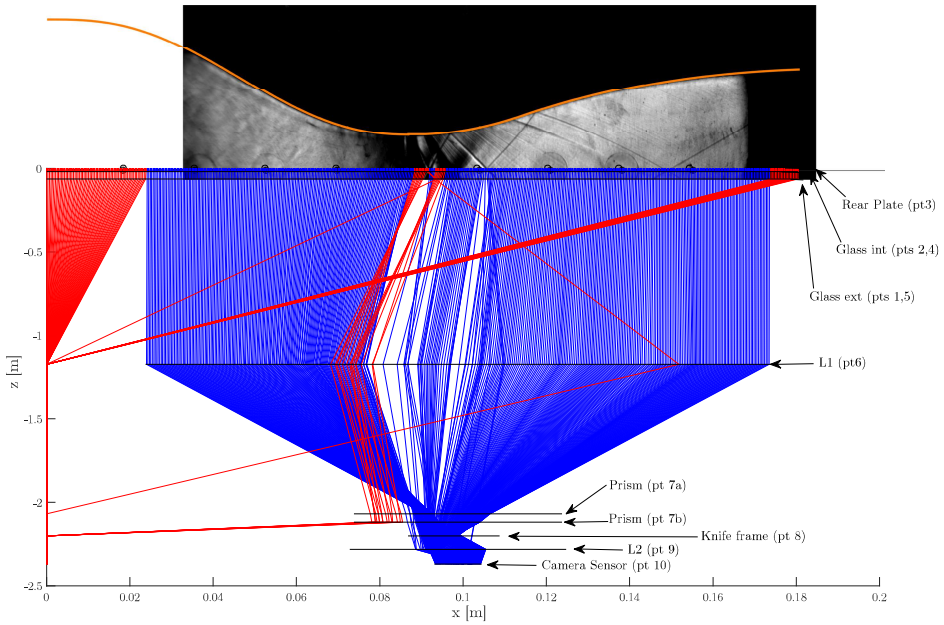

(a) *The figure shows the path of all modeled rays and the position of optical bench components, numbered according to Figure 2.14. Rays blocked by some system aperture (in red) are set to $x = 0$ before reaching the blocking component. Rays that proceed their path all the way to the sensor with no blockage are in blue.*

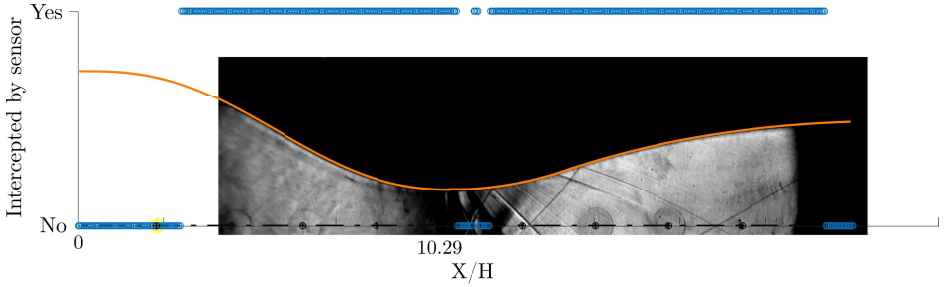

(b) *The figure is a scatter plot of the initial rays x-coordinates indicating whether they reach the camera sensor or not.*

Figure 2.15: Ray tracing output for MDM flowing in nozzle $M2$ at total conditions $P_T = 4.58\ bar$, $T_T = 246\ ^\circ C$, corresponding to $Z_T = 0.82$.

at the tests performed using fluid MDM, the measuring range issues reduced when the nozzle is operated at almost ideal total conditions, as shown in Figure 2.13. These trends can be explained by analyzing the quantities affecting the refractive index gradients. In order to get a better insight into the refractive index trend and extrapolate more general conclusions, the density gradient in an isentropic flow can be linked to the pressure gradient and the speed of sound and can be rewritten as follows:

$$\left(\frac{\partial \rho}{\partial x}\right)_s = \left(\frac{\partial \rho}{\partial P}\right)_s \frac{\partial P}{\partial x} = \frac{1}{c^2}\frac{\partial P}{\partial x} \tag{46}$$

where $1/c^2$ represents the flow *compressibility*, P is the pressure and ρ the density.
Also, the total pressure at the inlet is conveniently highlighted by rewriting the expression in terms of the pressure ratio gradient. Therefore, the following complete expression for the refractive index is obtained:

$$\frac{\partial n}{\partial x} = K\frac{1}{c^2}P_T\frac{\partial (P/P_T)}{\partial x} \tag{47}$$

This equation is valid for any fluid since no thermodynamic model was employed, provided that the Gladstone-Dale relation can be considered as applicable.
The analysis proceeds by considering first of all two different PIG: the fluid MDM treated as a PIG having $\gamma_{MDM} = 1.018$ and $M_m^{MDM} = 236.5\ g/mol$, and air treated as a PIG having $\gamma_{air} = 1.4$ and $M_m^{air} = 29\ g/mol$.
For a PIG, the speed of sound can be written as:

$$c = \sqrt{\gamma \frac{R}{M_m} T_T \left(1 + \frac{\gamma - 1}{2} M^2\right)^{-1}} \tag{48}$$

where R is the universal gas constant, M_m is the molar mass, γ is the specific heat ratio, M is the Mach number and T_T is the total temperature.
Equation (47) makes it clear that the main quantities affecting the refractive index gradients, in a nozzle operated at the same total pressure P_T with different polytropic ideal gases, are:

- **The Gladstone Dale constant** K, that is quite higher for the MDM, $K_{MDM} = 4.30 \cdot 10^{-4}\ m^3/kg$, than for the air $K_{air} = 2.27 \cdot 10^{-4} m^3/kg$. This contributes in making the refractive index gradients in a MDM flow higher than the one present in air, possible leading to the measuring range issues encountered.

- **The pressure ratio gradient** $\frac{\partial P/P_T}{\partial x}$, that is shown in Figure 2.16b. For a PIG this gradient is a function of the fluid and of the nozzle geometry only. It can be noticed that the two profiles derived for air and MDM treated as PIG are almost coincident. The contribution to the difference in refractive index gradients, especially at the throat where the measuring range issues are present, is thus negligible.

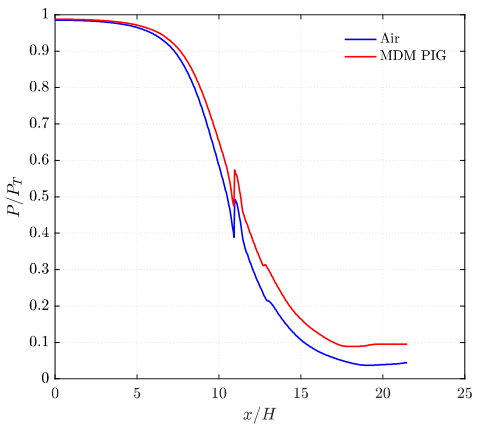

(a) *Pressure ratio profile along the nozzle axis.*

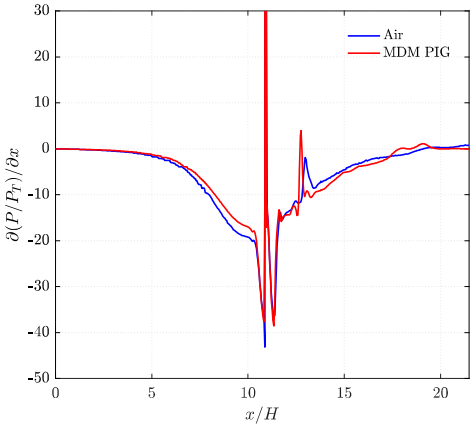

(b) *Pressure ratio gradient profile, the y-axis has been limited so the maximum value at the peak is not displayed but the trend along the axis is well visible.*

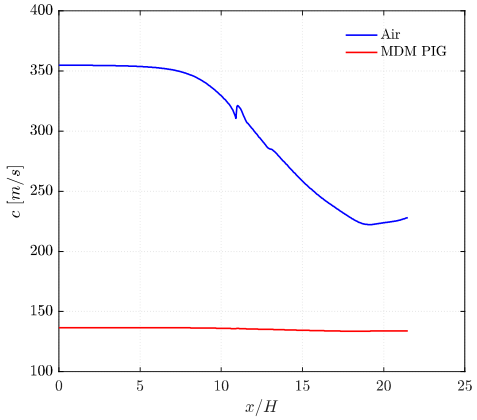

(c) *Speed of sound profile along the nozzle axis.*

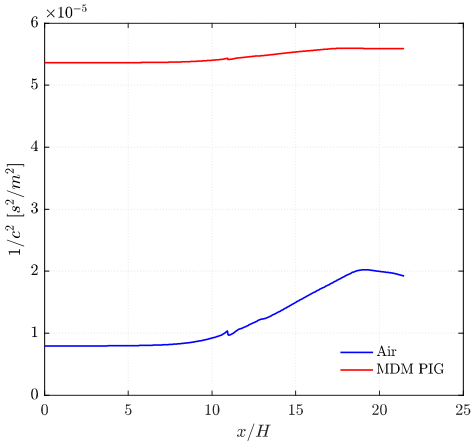

(d) *Compressibility $1/c^2$ profile along the nozzle axis.*

Figure 2.16: Profiles of relevant quantities for the determination of the refractive index gradients along the axis of nozzle $M2$ for air and MDM both treated as polytropic ideal gases having $\gamma_{air} = 1.4$, $M_m^{air} = 29\ g/mol$, $\gamma_{MDM} = 1.018$, $M_m^{MDM} = 236.5\ g/mol$.

- **The compressibility** $1/c^2$, that is dependent on the fluid molar mass and the heat capacity ratio γ, on the total temperature and on the Mach (see Eq.(48)). Nevertheless, focusing the attention at the throat where the measuring range issues are encountered, the Mach number there is close to one for every fluid thus it does not contribute to change the value of the compressibility at changing fluid. The influence of the molar mass M_m on the value of c is predominat with respect to the parameters γ and T_T. This can be seen in Figure 2.16c where it is clear that value of the speed of sound in air is much higher that the value of c in MDM, even though the two profiles were obtained for a value of $T_T^{MDM} > T_T^{air}$ ($T_T^{MDM} = 246^\circ C$, $T_T^{air} = 40^\circ C$). Thus, the value of the compressibility is higher for MDM that for air, as it can be seen in Figure 2.16d, and this too contributes in worsening the measuring range issues when performing schlieren visualization in an organic fluid.

It can be concluded that the most important parameters determining the difference in refractive index gradients for different PIGs, in the same nozzle and with the same total pressure, are the Gladstone-Dale constant and the compressibility (predominantly dependent on molecular mass). Being both these quantities higher for MDM than for air, this can explain why the measuring range issues were unnoticeable when the nozzle $M2$ was operated with air.

Finally it can be analyzed why the measuring range issues are stronger when the nozzle is tested with MDM at lower Z_T thus higher levels of non-ideality (see Fig.2.13). For this analysis MDM cannot be treated anymore as a PIG and it must be modeled using a proper complex thermodynamic model, thus, the improved Peng Robinson Stryjek–Vera (iPRSV) model (Stelt et al., 2012) was used to compute the CFD simulations.

Non-ideal gas effects on the refractive index gradient are analysed by comparing CFD simulations of MDM flow simulated using iPRSV thermodynamic model to the respective MDM flows simulated with the polytropic ideal gas assumption. This is done in Figure 6.17 for the most non ideal condition among the ones analyzed: $P_T = 4.58[bar]$, $T_T = 246^\circ C$ corresponding to $Z_T = 0.82$.

Total conditions and the Gladstone-Dale coefficient are equal for both the non-ideal and the PIG simulations. The direct and explicit impact of these variables is thus eliminated and differences in the refractive index gradients between non-ideal and ideal case (shown in Figure 2.17) can be attributed to real gas effects only. The latter implicitly depend on total inlet conditions and have an impact on the pressure ratio gradient (see Fig.2.17a) and on compressibility (see Fig.2.17b). Even though discrepancies are visible in the plots of pressure ratio gradients (see Fig.2.17a) non-ideal effects are responsible for fairly weak quantitative differences in pressure ratio gradients between real and PIG simulations, yielding limited contribution to the difference in their respective refractive index gradients. Instead, real gas effects have a significant impact on the speed of sound and, thus, on quantity $1/c^2$ that is much lower in the flow of MDM treated as a PIG. Thus in the end in a MDM flow the non-ideal effects contribute in making the density gradients and

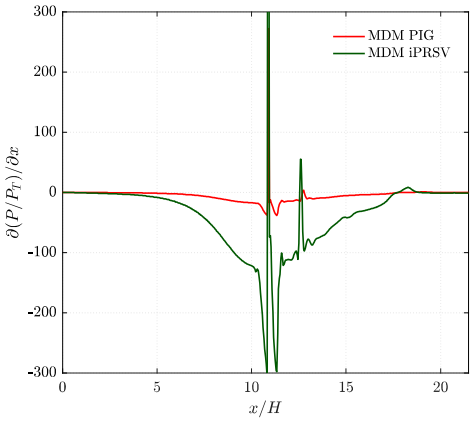

(a) *Pressure ratio gradient profile, the y-axis has been limited so the maximum value at the peak is not displayed but the trend along the axis is well visible.*

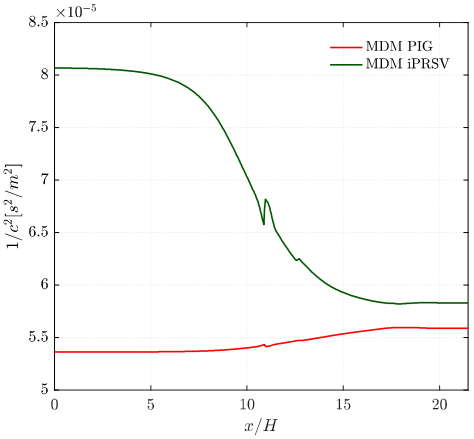

(b) *Compressibility $1/c^2$ profile along the nozzle axis.*

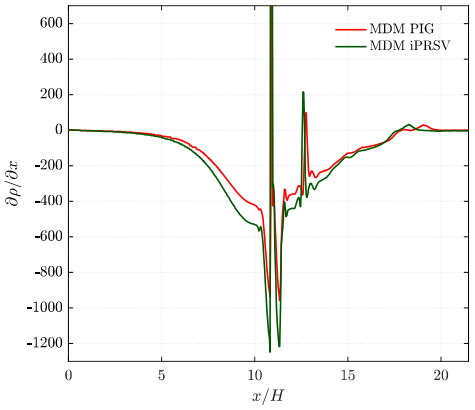

(c) *Density gradient profile, the y-axis has been limited so the maximum value at the peak is not displayed but the trend along the axis is well visible.*

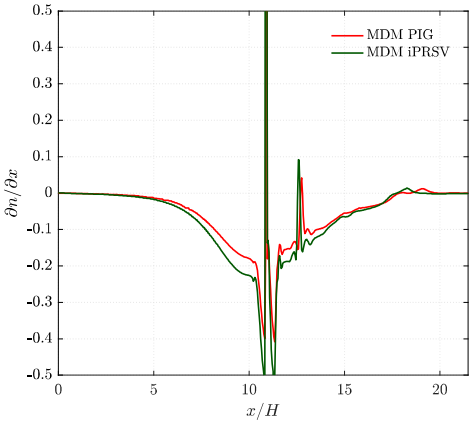

(d) *Refractive index gradient profile, the y-axis has been limited so the maximum value at the peak is not displayed but the trend along the axis is well visible.*

Figure 2.17: Profiles of relevant quantities derived from CFD simulations of MDM flow simulated using iPRSV thermodynamic model and from MDM flow simulated with the polytropic ideal gas assumption. Both simulations shared the same total initial conditions: $P_T = 4.58[bar]$, $T_T = 246^\circ C$ corresponding for the iPRSV case to $Z_T = 0.82$.

Fluid	Z_T	P_T $[bar]$	T_T $[^\circ C]$
MDM	0.82	4.58	246
MDM	0.85	3.98	249
MDM	0.88	3.38	250
MDM	0.93	1.80	232
MDM	0.97	0.62	226
Air	1.00	4.00	40

Table 2.4: Summary of the test conditions analysed in Figure 2.18.

consequently the refractive index gradients higher.
In conclusion different non-ideal MDM flows are compared to one another in Figure 2.18. First of all it must be noticed by looking at Table 2.4 that lower lower values of Z_T correspond to higher P_T. This translate straightforwardly in an increase of the refractive index gradients (see Eq.(47)). Moreover, a lower magnitude of real gas effects corresponds to a larger value of c at the throat. Thus, quantity $1/c^2$ is always larger at lower values of Z_T (Figure 2.18b), contributing to a stronger absolute value of the refractive index gradient (Figure 2.18d). Although, among the tested conditions, compressibility changes by a factor lower than 2, whilst total pressure changes by a factor larger than 7 (Table 2.4). It can therefore be concluded that, even though real gas effects do have an impact, the most important parameter in determining the different values of the refractive index gradient, and thus, the extent of the measuring range issues during the test, is total pressure.
All the aspect here analyzed bring to the conclusion that obtaining schlieren images of non-ideal compressible flows of siloxanes is more tricky that obtaining schlieren images of air flows. It requires optical components of a larger size so that the higher deflection, caused by the higher absolute value of the refractive index gradient, does not bend the light rays over some aperture stops. However, higher refractive index gradients can be exploited to obtain a clear visualization of small perturbations such as Mach waves.

2.4.2 *The line detection technique and its application to Mach measurement*

Modern computer vision techniques can be applied to schlieren images in order to characterize in a quantitative way the structures present within the flow. In particular in this thesis a novel technique to detect straight lines by identifying the best parameters approximating their slope and position is presented.
Salient flow structures that can be locally approximated by straight lines are for example

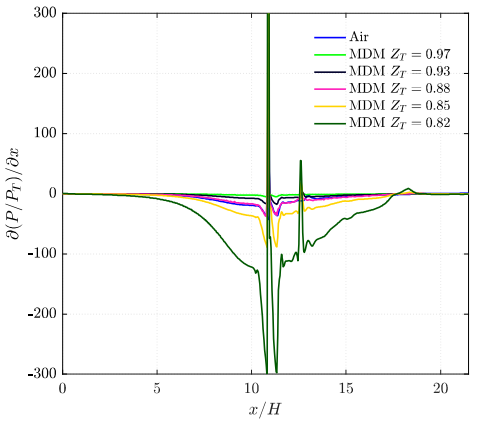

(a) *Pressure ratio gradient profile, the y-axis has been limited so the maximum value at the peak is not displayed but the trend along the axis is well visible.*

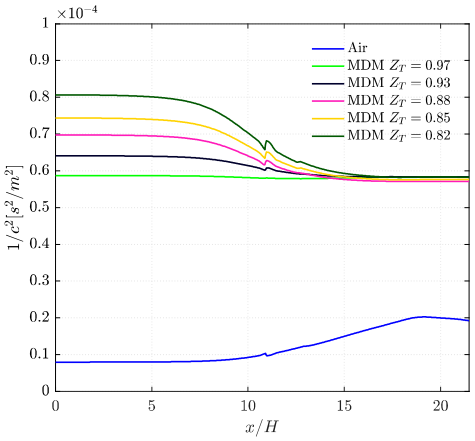

(b) *Compressibility $1/c^2$ profile along the nozzle axis.*

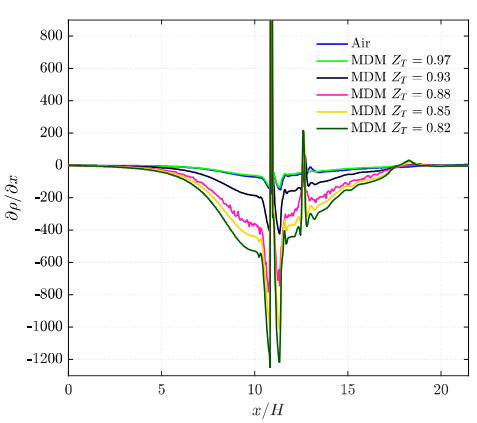

(c) *Density gradient profile, the y-axis has been limited so the maximum value at the peak is not displayed but the trend along the axis is well visible.*

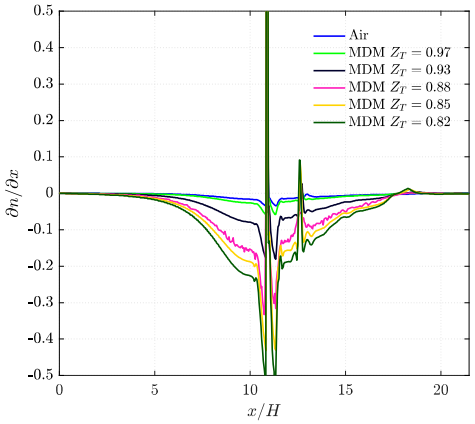

(d) *Refractive index gradient profile, the y-axis has been limited so the maximum value at the peak is not displayed but the trend along the axis is well visible.*

Figure 2.18: Profiles of relevant quantities derived from CFD simulations of MDM flow simulated using iPRSV thermodynamic model and plotted together with the data coming from a simulation conducted with air as working fluid. The simulations of the MDM flows are done changing the initial total condition thus the level of non-ideality of the flow; a summary of the conditions tested can be found in Table 2.4.

Mach waves, compression shocks and the edges of expansion fans. Knowing the exact slope and position of these structures provides crucial informations to be used to assess CFD simulations. Moreover, the slope of Mach waves can be directly related to the local Mach number attained in regions where the velocity direction of the flow is known. Thus, the technique here presented can be also exploited to obtain a direct measure of the local Mach number.
Due to the associated strong density gradients, shocks and expansion fans are always clearly visible in almost any schlieren image. This is usually not the case of Mach waves. Indeed, Mach waves are infinitely weak local perturbations produced wherever the flow undergoes a slight change in its direction. For example, the Mach waves originate in supersonic flows attached to a solid surface because of its roughness. They propagate downstream with a slope that is function of the local Mach only. This makes them exploitable to measure the local Mach number. However, being the associated density gradient extremely small, Mach waves may not be visible in a schlieren image. To overcome this issue the following actions can be undertaken:

(a) Increase the roughness of the walls

(b) Increase the sensitivity of the schlieren apparatus
    - by moving the knife to reduce the size of the light source image;
    - by increasing the focal length of the collimating lens.

(c) Increase the refractive index gradient caused by the perturbation; this is possible because the refractive index gradients are directly related to the flow total pressure (see Sec.2.4.1.3 and Eq.(47)).

However, fortunately the fact that the refractive index gradients are intrinsically higher in non-ideal flows of organic vapors, as demonstrated in section 2.4.1.3, makes the above actions usually unnecessary in these kind of flows. Once that Mach waves are visible, and when the angle α between the wave and the flow direction can be measured; it is possible to easily evaluate the local Mach number through Equation (49).

$$M = \frac{1}{\sin \alpha} \tag{49}$$

Thus, for example at the axis of a planar nozzle or at wall of an attached flow, where the flow direction is known, the local Mach can be directly measured by detecting the slope of Mach waves. An algorithm was implemented to this purpose in the present thesis.
Identification of straight lines is quite a common task in the computer vision framework. Here the algorithm based on the Hough transform presented in (Lo and Tsai, 1995) is used to identify flow structures approximable with straight lines in schlieren images. In this way it is possible to automate the task, while reducing the arbitrariness introduced by human operators. Indeed, with regards to Mach waves, being infinitely weak perturbations, they appear in schlieren images as gray lines with dull edges (see Fig.2.19) and they are not

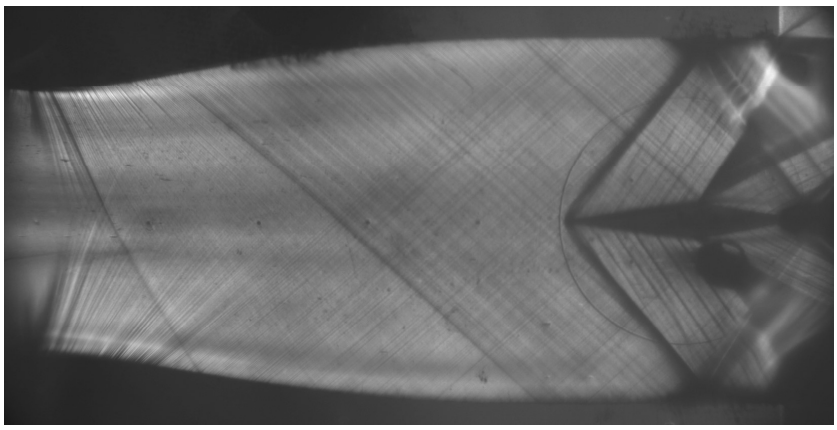

Figure 2.19: Schlieren image taken with fluid MDM. The flow expands in a nozzle and it encounters a diamond shaped airfoil at the exit (see (Zocca et al., 2019) for a complete description of the experiment). The image is here reported as an example of image in which Mach waves, shocks and expansion fans can be found.

formed by only one row of pixels (as sketched in Fig.2.22), they are instead bands of dark gray pixels (as sketched in Fig.2.24b) in which multiple lines can be inscribed. Moreover, also schock waves captured in schlieren images (see Fig.2.19) appear as rather thick dark bands in which more than one line can be inscribed. In Figure 2.19 two expansion fans are also present and it is easy to notice that locating the correct location of their edges is not straightforward. When dealing with these structures a human operator would introduce an unacceptable level of arbitrariness if not supported by suitable computer detection techniques capable of providing a rigorous repeatable procedure.
The algorithm implemented supports the operator by detecting automatically the possible straight structures present in the image and by evaluating the best approximating slope and position. The algorithm steps are the followings:

1. Image cut and contrast enhancement (Sec.2.4.2.1)
2. Binarization of the image (Sec.2.4.2.2)
3. Hough transform and peak detection (Sec.2.4.2.3)
4. Computation of lines slope and positions (Sec.2.4.2.4)
5. Computation of uncertainties (Sec.2.4.2.5)
    a) Computation of Mach numbers and related uncertainties

2.4.2.1 *Image cut and contrast enhancement*

A sub-picture containing only a manageable number of lines to be detected (< 15) has to be cut from the whole schlieren image. In each sub-picture contrast enhancement is

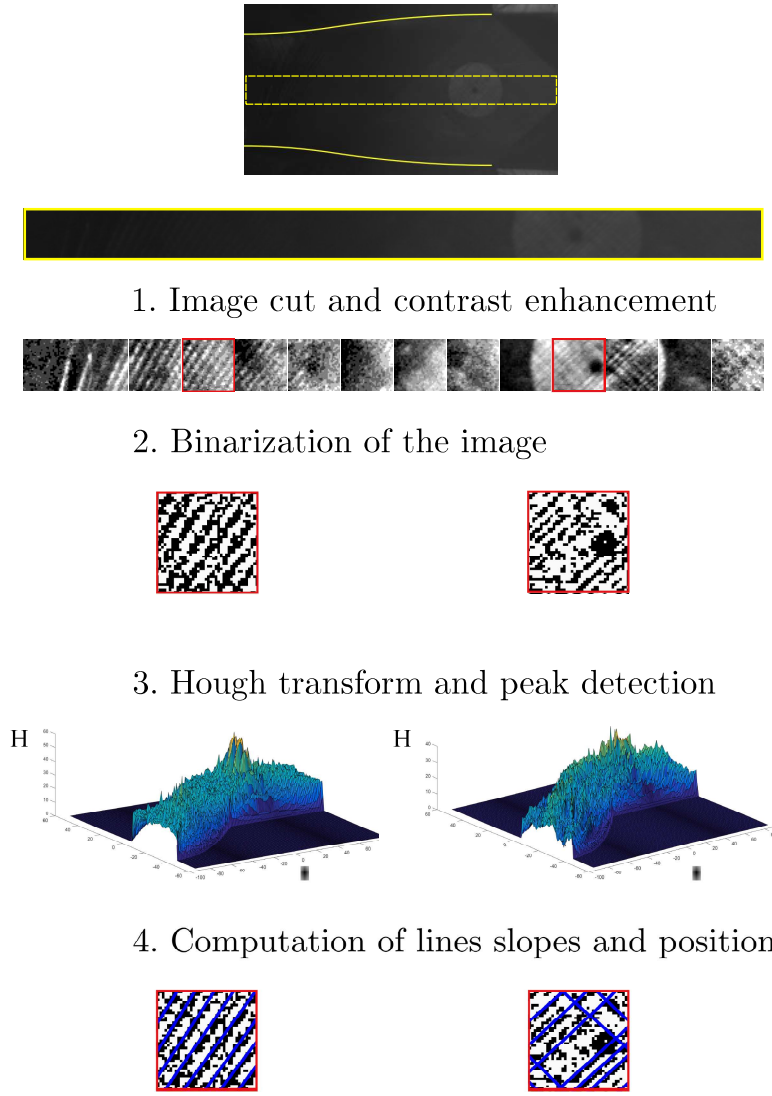

Figure 2.20: Algorithm steps illustrated using schlieren image 5.14e taken from a test performed with fluid MDM and nozzle $M15$ (see Sec.5.3).The image correspond to highly non ideal stagnation conditions (Z_T = 0.65).

performed so to obtain 1% of saturated pixels and 1% of black pixels (see top of Fig.2.20). This step is particularly important in all cases where small perturbation have to be detected in schlieren images having a poor contrast, as in it happened in some of the tests performed during the MDM vapor expansion campaign (See Chap.5). Figure 2.20 reports at the top a schlieren image of a nozzle operated with fluid MDM and characterized by highly non-ideal stagnation condition ($Z_T = 0.65$). In this case it is clear that a human operator would not be capable of detecting any structure as they are invisible to the human eye before the contrast enhancement. Moreover, the structures to be detected may be not straight but still approximable as straight lines if only a portion of the flow is considered. In this case it is essential to cut the schlieren image in a proper way. In principle the smaller the image cut is, the better approximation with a straight line can be obtained. However, it must be taken in mind that the sub-images must have sides larger than 40 $pixels$ in order to obtain a good performance of the algorithm. Indeed, sub-images made of few pixels produce Hough transforms (see Sec.2.4.2.3) with blurred spread undetectable peaks, leading to a failure in the line detection process.

2.4.2.2 *Binarization of the image*

The sub-images obtained are grayscale ones and need to be converted into black and white images. This step of the algorithm computes the black and white version of each sub-pictures based on the Bradley's method (Bradley and Roth, 2007). First, a locally adaptive threshold proportional to the local mean intensity $\bar{I}$ in the neighborhood of each pixel is computed.

$$pixel(x_i, y_i)\ \ black\ \ if\ \ I(x_i, y_i) < t\bar{I} \tag{50}$$

$$\bar{I} = \frac{\sum I(x_j, y_j)}{N} \tag{51}$$

where $I(x_j, y_j)$ is the pixel intensity. The local mean intensity $\bar{I}$ is obtained as an average of the intensities of the neighbor pixels. The neighborhood pixels are distributed around the considered pixel and their number is fixed as $N = 2 * floor(T/16) + 1$ where T is the total number of pixels in the sub-image and $floor()$ represents the function approximating its argument to the nearest lower integer. A proper value for the sensitive parameter t has to be set. Increasing this parameter increases the number of pixel detected as foreground, thus, in this case, as black. In Figure 2.21 the performances of the line detection algorithm changing the value of t are shown. It can be seen that low values of t lead to brighter images where the number of white pixels is too high, on the other hand high values of t makes the lines present in the image to merge into one another, making different lines indistinguishable. A value of $t = 0.6$ provides an optimal compromise for all images extracted in the analyzed cases.

2.4.2.3 *Hough transform and peak detection*

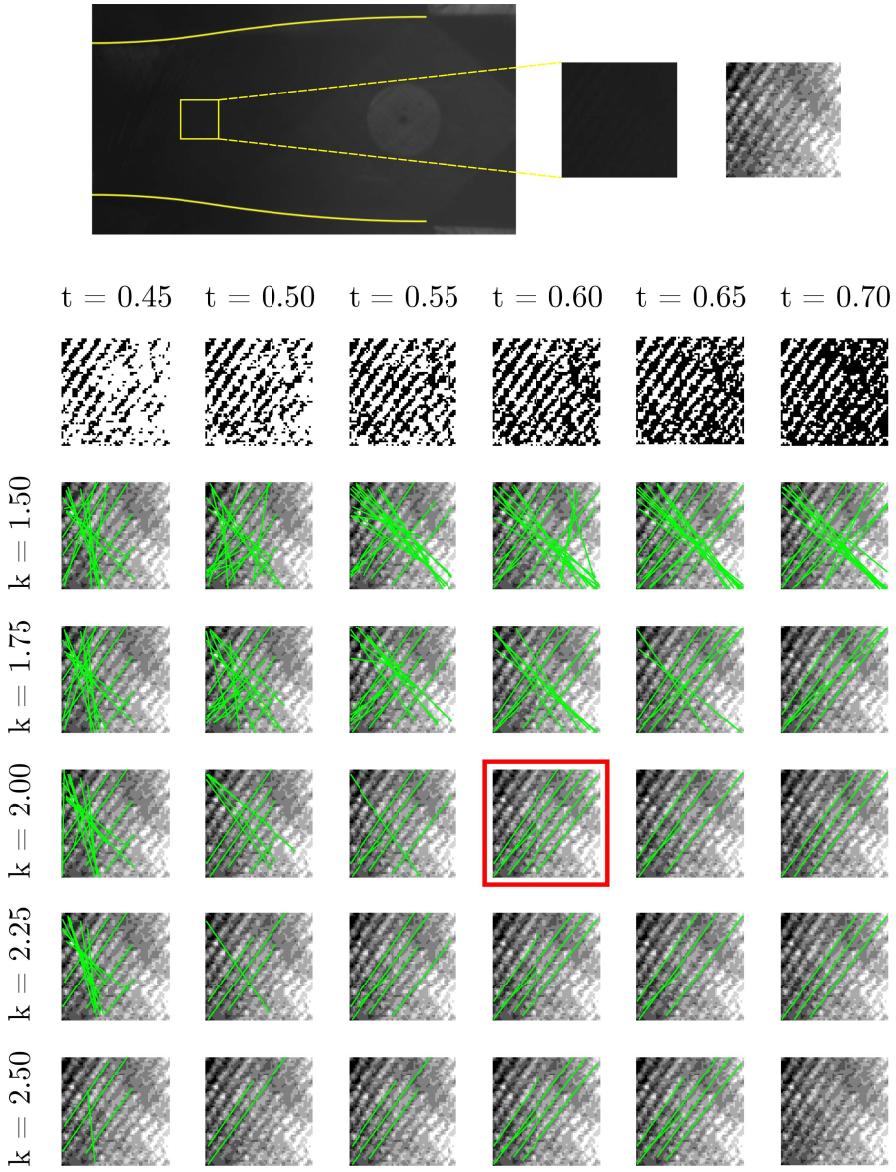

Figure 2.21: Comparison of performance of the line detection algorithm at variable t which influences the binarization process (see Sec.2.4.2.2), and k which influences the peak detection in the Hough transform (see Sec.2.4.2.3). t increases from left to right in the range $0.45 \div 0.70$ while k increases from top to bottom in the range $1.5 \div 2.5$. The best performance, highlighted by the red rectangle is found for $t = 0.60$ and $k = 2.0$, this combination permits to find the maximum number of physically meaningful lines minimizing the number of unphysical ones.

Once that a binary image is obtained the Hough transform, as proposed in (Duda and Hart, 1972), is used to find all possible straight structures present in the image. The Hough transform takes the binarized sub-image in its original spatial cartesian coordinates and maps it into a new parameter space where the new coordinates are the parameters ρ and θ, capable of describing all the possible lines lying in the original sub-image. Indeed, each line can be specified by its distance ρ from the origin and by the angle θ of its normal. Thus, considering one pixel identified by its spatial coordinates (x_i, y_i), the family of straight lines passing through that pixel is defined by the relation:

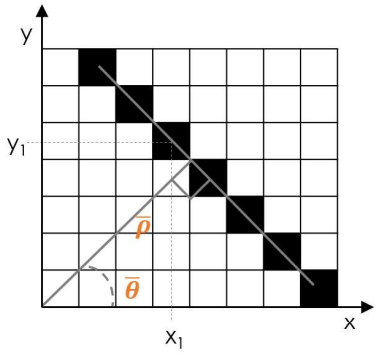

Figure 2.22: Sketch of a line formed by one raw of foreground pixels. The line is uniquely identified by the distance ρ and the angle θ.

$$\rho = x_i \cos(\theta) + y_i \sin(\theta) \tag{52}$$

We consider as foreground pixels all the black pixels present in the image. Each foreground pixel having coordinates (x_i, y_i) can be mapped in a sinusoidal curve in the parameter space (ρ, θ) using Eq.(52). Points lying on the same straight line in the original Cartesian space are associated to curves passing through a common point in the parameter space. The problem of finding collinear points can thus be solved by finding the concurrent curves in the parameter space.
In order to do that, the space (ρ, θ) is discretized and a mesh, as the one shown in Figure 2.23b, is created. For each foreground pixel Eq.(52) is written finding the corresponding sinusoidal curve. The discretized values of θ are substituted into the equation to find the corresponding values of ρ. When a pair of values $(\overline{\rho}, \overline{\theta})$ is found it means that in the original Cartesian image there is a black pixel lying on that line. In the parameter space, it means that the sinusoidal curve corresponding to that foreground pixel is passing on the cell of the mesh where $(\overline{\rho}, \overline{\theta})$ are contained. The cumulative count H of all the sinusoidal curves passing through each cell is stored creating a discretized surface $H(\rho, \theta)$, whose peaks correspond to the most probable lines present in the original image (see Fig.2.23b).
Unfortunately, the flow structures that are being detected are not formed by a single row of black pixels (as sketched in Fig.2.22), they are instead a band of multiple adjacent rows of foreground pixels (as sketched in Fig.2.24). A local peak of the surface H would identifies the red line in Figure 2.24b as it is the one crossing the maximum number of pixels. However, it would not be the correct line best approximating the band of foreground pixels. Thus, it is necessary to consider not only the local maximum identified

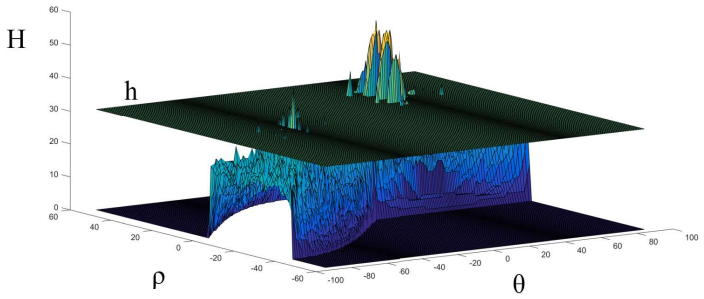

(a) *The surface here plotted is the Hough transfrom $H(\rho, \theta)$, thus the cumulative count of all the foreground pixels lying on a line identified by $(\overline{\rho}, \overline{\theta})$. The surface is cut by the plane identified by the chosen threshold h.*

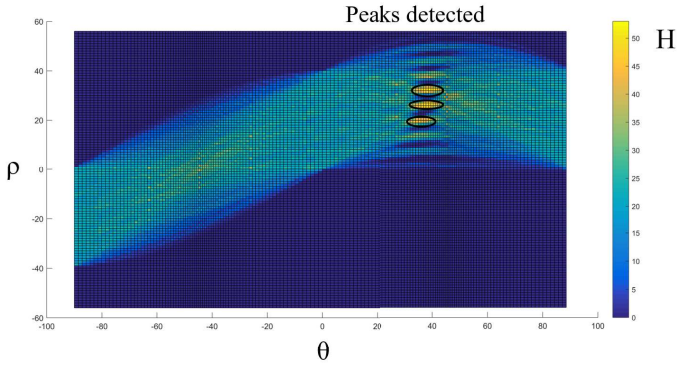

(b) *Projection of some of the main peaks detected for Fig.2.23a. Here it can be seen clearly the mesh discretizing the (ρ, θ) space.*

Figure 2.23: Hough transform of one of the sub-images reported in Fig.2.20.

by a peak in $H(\rho, \theta)$ but instead, a set of ρ values and θ values identifying all the lines lying in the black band (see Fig.2.23b). In order to do that a threshold h have been set as

$$h = k \cdot \sigma_H \tag{53}$$

$$\sigma_H = \sqrt{\frac{\sum_{\rho_i} \sum_{\theta_j} \left(H(\rho_i, \theta_j) - \overline{H}\right)^2}{N}} \quad ; \quad \overline{H} = \frac{\sum_{\rho_i} \sum_{\theta_j} H(\rho_i, \theta_j)}{N} \tag{54}$$

where N is the number of cells in the (ρ, θ) mesh. The parameter k can be seen as a coverage factor discriminating the statistical meaningful peaks. It was set to 2 after having evaluated different outcomes obtained by changing $k = 1.5 - 2.5$ (see Fig.2.23a). The parameter study performed to decide which value of k to set is shown in Figure 2.21. It can be seen that a low value of k causes the detection of several lines that do not correspond to physical flow structures. On the other hand a high value of k prevents the detection of most of the real flow structures present in the sub-image. Thus, it was found that the algorithm perform at best by keeping $k = 2$.

2.4.2.4 *Computation of lines slopes and positions*

Now that all the straight lines lying within the band of black pixels that forms the flow structure are identified, the best approximating one has to be chosen. The algorithm proposed in (Lo and Tsai, 1995) is exploited. Among all the possible θ_i lying within the peak region the more suitable one, $\overline{\theta}$, is the one showing

$$\overline{\theta} \longrightarrow \max \sum_{\rho_i=\rho_b}^{\rho_i=\rho_e} \left(H(\rho_i, \overline{\theta})\right) \tag{55}$$

where ρ_b and ρ_e are the boundary values of ρ defining the peak. Indeed, fixing $\theta_i = \overline{\theta}$ and computing $\sum_{\rho_i=\rho_b}^{\rho_i=\rho_e} \left(H(\rho_i, \overline{\theta})\right)$ brings to the computation of the number of black pixels lying under multiple parallel lines encompassing the band of black pixels see Fig. 2.24b, 2.24c, 2.24d. The maximum is found only when $\overline{\theta}$ approximate at best the slope of the band considered (see Fig. 2.24d). Finally, the position of the line is found by setting $\overline{\rho} = (\rho_b + \rho_e)/2$.

2.4.2.5 *Computation of uncertainties*

The lines present in the image are now identified both in terms of position and slope. It is now possible to scan the image in order to find the first and last pixel forming the flow structure detected. Moreover it is possible to compute the angle α between the line and the x-axis together with its uncertainty which can be related to the fact that the image is discrete as it is formed by pixels. Indeed, the beginning and the end of a line found can lie at any point within the two boundary pixels. It can be, therefore, defined a set of non-resolvable slopes ranging from α_{min} to α_{max}, as shown in Figure 2.25. The uncertainty related to α is computed by assigning a uniform probability distribution

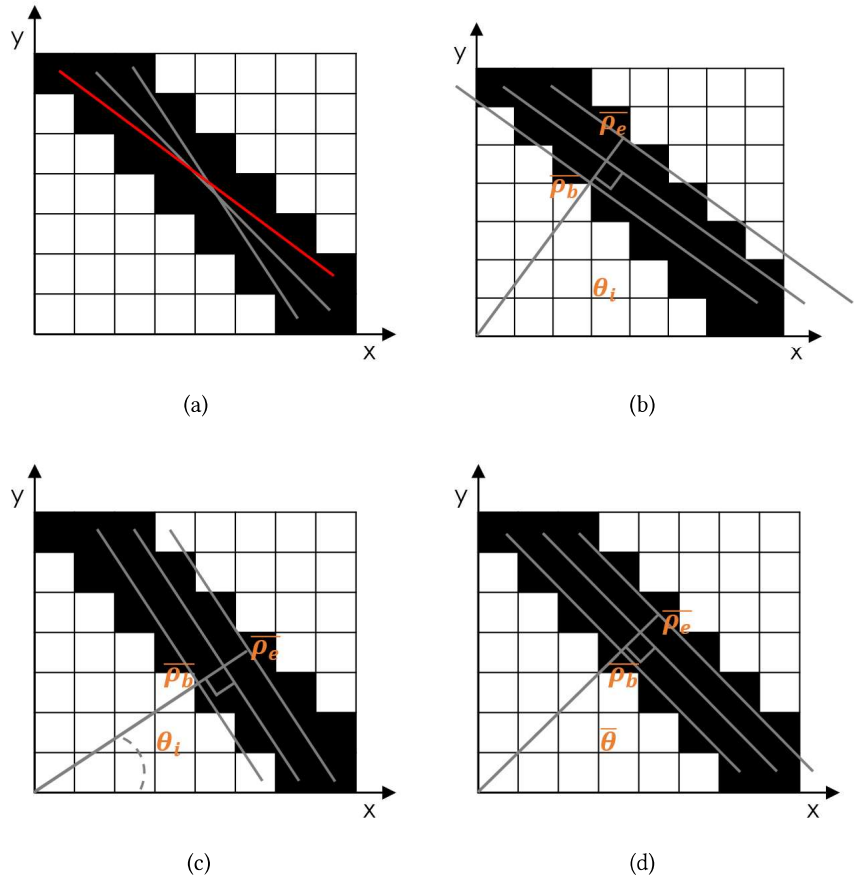

Figure 2.24: Figures explaining how to discriminate the best approximating line among the set of lines inscribable in the band of foreground pixels identifying a flow structure. Figure 2.24a shows the sketch of a band of black pixels that can represent a Mach wave on a binarized schlieren image. The red line is the one corresponding to the maximum value of the Hough transform. Figures 2.24b,2.24c, and 2.24d illustrate the meaning of keeping θ_i fixed and computing $\sum_{\rho_i=\rho_b}^{\rho_i=\rho_e}\left(H(\rho_i,\overline{\theta})\right)$. This brings to the computation of the number of black pixels lying under the lines drawn in figures 2.24b, 2.24c, 2.24d. The maximum is found in 2.24d since all the black pixel forming the band are intercepted.

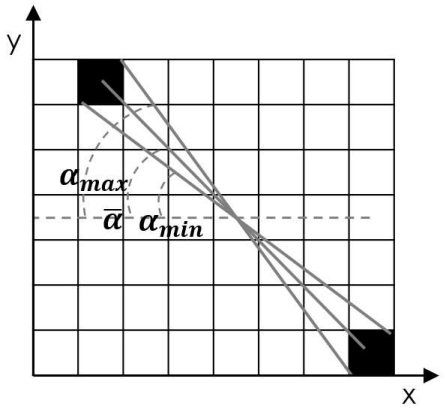

Figure 2.25: Range of slopes identified by the algorithm once the two boundary pixels of a line are detected.

between α_{min} and α_{max}. Therefore, the expanded uncertainty U_α with a confidence level of 95% is given by eq.(56).

$$U_\alpha = \frac{(\alpha_{max} - \alpha_{min})}{2\sqrt{3}} k_{p095} \quad , \quad k_{p095} = 1.65 \tag{56}$$

The angle α obtained and its uncertainty can be exploited to measure the local Mach number and to have an estimation of the uncertainty related to the measurement. Equation (49) provides the value of the local Mach number while the uncertainty is evaluated propagating the uncertainty U_α related to α using the Taylor series method (see Eq.(57)).

$$U_M = \sqrt{\left(\frac{\partial M}{\partial \alpha}\right)^2 {U_\alpha}^2} \quad \rightarrow \quad U_M = M\sqrt{(M^2 - 1)} U_\alpha \tag{57}$$

It can be noticed that, as M increases the uncertainty U_M is becomes proportional to M^2. Thus, the measurement of M obtained is affected by a higher uncertainty as M increases.

3

EXPERIMENT DESIGN

During this thesis work the TROVA facility was exploited with the aim of characterizing the expansion of molecularly complex organic fluids. Three experimental campaigns were planned using three fluids and four different nozzles. Firstly this chapter presents the evolution of a test, the raw data acquired and how they are elaborated (Sec.3.1). Secondly, it is described how the experimental campaigns conducted were planned, their aims and how the nozzle used were designed 3.3.

3.1 TEST DESCRIPTION

Each test run performed on the TROVA facility evolves alike in time, regardless of the fluid and of the nozzle specifically used. First, the HPV is pressurized up to a pressure ranging from 4 to 20 bar; while the LPV is vacuumized at pressures ranging from few millibars to 200 $mbar$. At time $t = 0$ two signals are sent by the control system. One triggers the opening of valve $V3$ and the other triggers the recording of the schlieren images. The triggering procedure is fundamental in order to synchronize the schlieren images with the other measurements performed.
Pressure and temperature signals are acquired at a sampling frequency of 1 kHz, while schlieren images are saved at a rate of 20 frames per second (fps).
Once that valve $V3$ is fully opened valve MCV starts opening. At the end of the opening transient the maximum total pressure P_T and the minimum total compressibility factor Z_{Tmin} are reached in the settling chamber upstream of the nozzle. As the test proceeds the HPV empties and the LPV fills; time dependent signals are therefore acquired.
In particular, the whole set of pressure signals acquired both in the settling chamber and along the nozzle decrease. While, the total temperature measured in the settling chamber first slightly increases and then decreases. Correspondingly, the total compressibility factor increases going from Z_{Tmin} to Z_{Tmax}. Indeed, the vapor total conditions move from a region close to the saturation curve towards more dilute conditions. This clarified by Figure 3.1 which shows the evolution of the total conditions during a test run. In particular, the plotted data refer to a test performed with fluid MDM in a converging diverging nozzle designed to reach a Mach number at the exit of about 2.
The $P - T$ plot in Figure 3.1a shows the saturation curve of fluid MDM and the $iso - Z$ curves. The total conditions of this particular test span from $Z_T < 0.85$ to $Z_T > 0.95$. Moreover, Figure 3.1b shows the total conditions measured during the test run in a $T - s$ diagram, reporting in addition the expansion processes happening inside the nozzle for three different conditions.

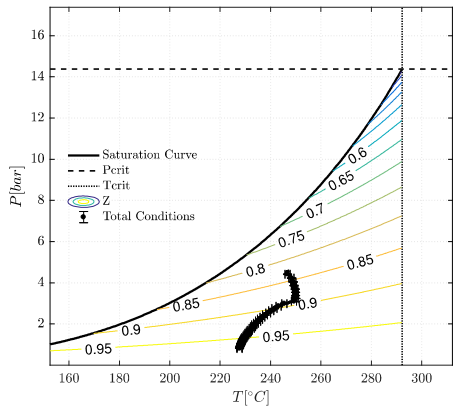

(a) *P – T diagram showing the total condition measured during a test run.*

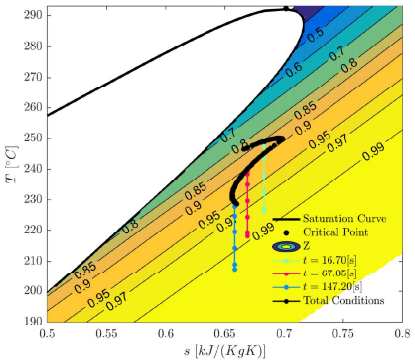

(b) *T – s diagram reporting isentropic expansion processes proceeding from three different total conditions.*

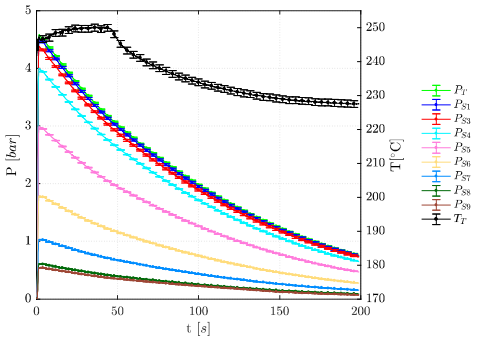

(c) *Total conditions and static pressures measured plotted against time.*

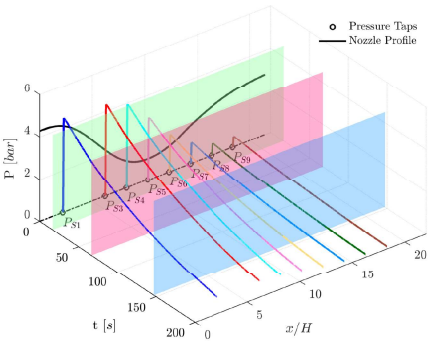

(d) *3D plot showing the evolution of the nozzle flow during a test run.*

Figure 3.1: Data measured during a test run performed with fluid MDM and nozzle *M2*.

Figure 3.1c shows the set of pressure and temperature data recorded during the test run. They are plotted against time so it is possible to see how they evolve as the test proceeds. Figure 3.1d shows the static pressures measured along the nozzle axis. The axes in this $3D$ picture correspond to time, non-dimensional nozzle axial coordinate, and pressure. The nozzle non-dimensional semi-profile (black line) is superimposed to the $P - x/H$ plane at $t = 0$.

The three-dimensional plot clarifies that samples of the entire data set (P_T, T_T, P) can be taken cutting planes at different time t. Each sample provides a steady-state nozzle flow field, characterized by different level of non-ideality, marked by the value of Z_T. Meaningful time instants for the data extraction were chosen to cover the compressibility factor range of each test run.

Each time instant can be consider as a steady state nozzle flow. This is possible since the characteristic time of the nozzle is more than two order of magnitude lower than the one related to the emptying process of the HPV (Spinelli et al., 2015). All the data presented within the following chapters are treated as steady state data characterizing a nozzle flow.

Measurements are acquired first as raw voltage values at a sampling frequency of 1 kHz. These data are average in packages of 50 or 100 points obtaining a data rate of 10 or 20 data per second. As it was shown in section 2.3, the 99.7% of pressure signal energy is found below 0.2 Hz. Thus, the averaging procedure preserve unaltered the dynamic content of the signal.

The nozzle operates initially in under-expanded conditions, due to the extremely low initial pressure in the LPV. However, as the LPV pressure increases and the HPV one decreases the nozzle flow becomes adapted and then over-expanded. The latter condition brings the formation of normal shocks entering the nozzle. Normal shock are visible in schlieren images and thay are detected by the pressure sensors placed within the nozzle. As a shock passes through a pressure tap, the signal acquired by that pressure sensor suddenly rises. All the data presented within this thesis correspond to under-expanded conditions.

Indeed, all data corresponding to over-expanded conditions are identified by looking at pressure signals and schlieren images and discarded. The measurements acquired are trimmed so to consider only the meaningful data. The beginning of the accepted data is set in correspondence of the end of the opening transient of the MCV, marked by the maximum total pressure reached.

However, condensation can occur at the beginning of a test. This happens when the conditions to explore are extremely close to the saturation curve, if some portions of pipes connecting the HPV to the test section are not heated uniformly. This led to the creation of colder spots triggering condensation. The colder spot are heated up by the fluid itself and the condensation disappears as soon as the test proceeds. Therefore, there could be some instants in which the total temperature measured coincides with the saturation temperature. All these instants are discarded and the beginning of the meaningful data is set as the temperature reaches a minimum required level of over-heating.

3.2 NON-IDEAL COMPRESSIBLE FLUID DYNAMICS

3.2.1 *1D Nozzle theory*

The three experimental campaigns conducted during this thesis were conceived in order to characterize expansions in converging-diverging nozzles. The focus was on the peculiarities which can be found in non-ideal compressible nozzle flows. Indeed, the value of the fundamental derivative of gasdynamic Γ influences some features of nozzle flows. This can be illustrated by resorting to the *quasi-one-dimensional* approach. Under the hypotheses that: at any axial location the radius of curvature of the nozzle is large compared to the nozzle cross-sectional length, the cross-sectional area distribution changes smoothly and gradually, the flow is adiabatic, and body forces are negligible; the mass, momentum and energy balance equations reduced to:

$$\frac{1}{\rho}\frac{d\rho}{dx} + \frac{1}{u}\frac{du}{dx} + \frac{1}{A}\frac{dA}{dx} = 0 \tag{58}$$

$$\rho u\frac{du}{dx} + \frac{dP}{dx} = 0 \tag{59}$$

$$\frac{dh_T}{dx} = 0 \tag{60}$$

where x is the axial coordinate, ρ is the fluid density, u is the axial component of the flow velocity, $A = A(x)$ is the cross-sectional area distribution, P is the pressure and h_T is the specific total enthalpy defined as

$$h_T = h + \frac{1}{2}u^2 \tag{61}$$

In most applications, including the experiments here presented, converging-diverging nozzle operate at sufficiently large Reynolds numbers for viscous effects to be neglected while maintaining a good approximation of the real flow, provided that shock waves are absent and the nozzle operate in under-expanded or adapted conditions. Indeed, the Reynolds number computed from the measured data, using the thermodynamic model presented in (Thol et al., 2017), in the proximity of the throat span from $2 \cdot 10^6$ to $5 \cdot 10^7$ in all the considered test runs. Viscous effects are limited to the thin boundary layer region and can be neglected following the *quasi-one-dimensional* approach. The hypothesis of isentropic flow can thus be added and, consequently, the pressure gradient can be expressed in terms of the density gradient as:

$$\frac{dP}{dx} = \left(\frac{\partial P}{\partial \rho}\right)_s \frac{d\rho}{dx} = c^2\frac{d\rho}{dx} \tag{62}$$

Manipulating equations (58), (59) and (60) under the additional hypothesis of isentropic flow the gradients of all flow variables can be expressed as a function of the gradient of the cross sectional area distribution:

$$\frac{1}{u}\frac{du}{dx} = \frac{1}{M^2-1}\frac{1}{A}\frac{dA}{dx} \tag{63}$$

$$\frac{1}{\rho}\frac{d\rho}{dx} = \frac{M^2}{1-M^2}\frac{1}{A}\frac{dA}{dx} \tag{64}$$

$$\frac{1}{P}\frac{dP}{dx} = \frac{1}{1-M^2}\frac{\rho u^2}{P}\frac{1}{A}\frac{dA}{dx} \tag{65}$$

$$\frac{1}{c}\frac{dc}{dx} = \frac{(\Gamma-1)M^2}{1-M^2}\frac{1}{A}\frac{dA}{dx} \tag{66}$$

$$\frac{1}{M}\frac{dM}{dx} = \frac{1+(\Gamma-1)M^2}{M^2-1}\frac{1}{A}\frac{dA}{dx} \tag{67}$$

The relations above, where M is the Mach number and Γ is the fundamental derivative of gasdynamic (see Eq.(2)), are valid both for ideal and non-ideal gases. They highlight the role of Γ in determining the flow behaviour. In particular, it influences the sign of sound velocity and Mach number gradients. Fluids exhibiting Γ greater than 1 feature a negative speed of sound (dc/dx) gradient and a positive Mach number (dM/dx) gradient along a nozzle. The first statement is explained by looking at equation (66), where the term dA/dx is negative along the converging portion of the nozzle and positive along the diverging one. The opposite happens to term $(1 - M^2)$ since the Mach number is lower than one in the converging portion of the nozzle where the flow is subsonic and grater than one in the diverging one where the flow is supersonic. This makes the condition $\Gamma > 1$ necessary and sufficient to keep the sound velocity gradient negative.
The second statement is explained by looking at equation (67), where, again, term dA/dx is found, this time divided by term $(M^2 - 1)$. The ratio is positive both in the diverging and in the converging portion of a nozzle. By looking at the other terms present in equation (67), it can be stated that condition $\Gamma > 1$ is sufficient to keep the Mach number gradient positive.
PIGs are characterized by a value of $\Gamma = (\gamma + 1)/2$ that is always greater than 1 by definition. Thus, accordingly to the *quasi-one-dimensional* approach they feature a monotonically decreasing speed of sound and a monotonically increasing Mach number along the nozzle axis. Moreover, PIGs have constant specific heats and this feature permits to calculate entropy and enthalpy differences between two arbitrary states 1 and 2 as:

$$h_2 - h_1 = C_p(T_2 - T_1) \tag{68}$$

$$s_2 - s_1 = C_p \ln\left(\frac{T_2}{T_1}\right) - \frac{R}{MM}\ln\left(\frac{P_2}{P_1}\right) \tag{69}$$

Combining the two new hypotheses of isentropic flow and perfect gas to equations (58), (59) and (60) one can derived the well known relations:

$$\frac{T_T}{T} = 1 + \frac{\gamma - 1}{2} M^2 \tag{70}$$

$$\frac{P}{P_T} = \left(1 + \frac{\gamma - 1}{2} M^2\right)^{\frac{\gamma}{1-\gamma}} \tag{71}$$

$$\frac{\rho}{\rho_T} = \left(1 + \frac{\gamma - 1}{2} M^2\right)^{\frac{1}{1-\gamma}} \tag{72}$$

$$\frac{A}{A_t} = \frac{\left[\sqrt{\frac{2}{\gamma+1} \cdot \left(1 + \frac{\gamma - 1}{2} M^2\right)}\right]^{\frac{\gamma+1}{\gamma-1}}}{M} \tag{73}$$

where the subscript $_T$ identifies total quantities, γ is the specific heat ratio, and A_t is the cross sectional area at the throat. Equation (71) specify that the pressure ratio P/P_T is a function of only one variable namely the Mach number. Moreover, equation (73) states that the Mach number attained at a specific location inside a nozzle is a function of the area ratio A/A_t and of γ only. Therefore, the pressure ratio attained at a fixed axial coordinate inside a nozzle operated with a perfect gas, should be independent from the total conditions of the flow.

On the other hand, non-ideal vapors with a high molecular complexity, can exhibit values of Γ lower than 1. This implies that their nozzle flows are characterized by a monotonically increasing speed of sound. The most updated equations of state of some fluids, as for example the one presented in (Thol et al., 2017) for fluids MM and MDM, predicts the existence of a thermodynamic region where the speed of sound increase can lead to the decrease of the Mach number along an isentropic expansion. Moreover non-ideal fluids are characterized by non-constant values of the specific heats. This makes equations (70), (71), (72), (73) not suitable. As a consequence, in non-ideal compressible nozzle flows, the pressure ratio attained at a fixed axial coordinate is expected to be dependent on the total conditions.

None of the above peculiar features of non-ideal nozzle flows were ever observed experimentally. The dependence of pressure ratios on total conditions can be proven with experiments involving sub-critical conditions well below the thermal stability limits of the working fluids. Therefore, this has been one of the main goals of this thesis.

The observation of a decreasing Mach number along an isentropic nozzle expansion is much more challenging. It requires to perform experiments at total pressures and temperatures very closed to the saturation curve and which may overcome the thermal stability limits of most of the suitable fluids. The experimental campaigns conducted were conceived in order to acquire the know-how needed to perform experiments in such extreme conditions.

3.3 TESTED NOZZLES

Five different planar nozzles were used; all of them were designed to achieve a uniform Mach number and a velocity parallel to the nozzle axis at the exit section for a defined fluid and operating condition. However, each nozzle was tested in a wide variety of conditions and with different operating fluids.
In the nozzle design process, viscous and thermal boundary layers are assumed to have a negligible thickness with respect to the nozzle height, so effects of viscosity and thermal conductivity are neglected. Under the above assumptions, the flow is described by the potential equation for irrotational compressible flows (Zucrow and Hoffman, 1977). A polinomial function of fifth order is used to determine the shape of the nozzle converging section, with first and second derivatives set equal to the diverging section ones at the throat.
The diverging portion shape is determined through the Method of Characteristics, implemented according to (Zucrow and Hoffman, 1977), with a suitable thermodynamic model for real gases (see (Guardone et al., 2013)). To provide the initial data curve for the Method of Characteristics, the transonic flow at the nozzle throat is computed by solving the transonic potential equation (Sauer, 1947). The expansion through the diverging section to the desired exit pressure is achieved through an initial circular profile, followed by the so-called 'turning region', in which the nozzle wall geometry is determined by imposing mass conservation at each cross section.
The main characteristics of the nozzles tested are listed below:

- **Nozzle M2**: This nozzle was designed to achieve an exhaust Mach number of 2.05 if operated with fluid MDM at total condition $P_T = 4\ bar$, $T_T = 253.2^\circ C$. The curvature at the throat, identified by the ratio between the radius of the circular arc shaping the throat region and the throat semi-height, is $r_t = 10$. Nozzle *M2* features a backward facing step machined at the geometrical location of the throat. The step height is $h = 0.1\ mm$, which corresponds approximately to 1% of the throat half-height which is $8.4\ mm$. The step was machined to fix the position of the throat. Figure 3.2a shows a sketch of the geometry of nozzle *M2* together with the flow properties measured during the experiments. The step is not distinguishable in this sketch since its height is too small to be seen without a zoom. Indeed, an enlargement of the upper profile at the throat is reported in Figure 3.2c. After the step a small plateau is present, than the profile of the nozzle continues blending to its original shape designed without any step. The nozzle was used in previous works to assess the influence of the step on the flow stability (Zocca et al., 2018). During this thesis work the presence of the step was exploited to investigate the shock structures originating downstream the separated region. These structures are well visible in schlieren images as it can be seen in Figure 3.2b.

- **Nozzle M15**: This nozzle was designed to achieve an exhaust Mach number of 1.5 if operated with fluid MDM at total condition $P_T = 10\ bar$, $T_T = 277^\circ C$. The nozzle

semi-height is $h = 8.4\ mm$ and the curvature at the throat is the same as nozzle *M2*, $r_t = 10$. No step was machined, however, an increased roughness ($Ra \approx 0.6\ \mu m$) was adopted at the contoured end-walls to contribute to the formation of well visible Mach waves. Figure 3.2d shows a sketch of the geometry of nozzle *M15* together with the flow properties measured during the experiments. It can be noticed comparing figures 3.2a and 3.2d that nozzle *M15* is shorter that nozzle *M2*, this allows to include the discharge section of the nozzle inside the schlieren image, as it can be seen in Figure 3.2e.

- **Nozzle M16**: This nozzle was designed to achieve an exhaust Mach number of 1.6 when operated with fluid MM at total conditions $P_T = 21.4\ bar$, $T_T = 254°C$. The nozzle semi-height is $h = 8\ mm$. Nozzle *M16* has no step and features the same wall roughness as nozzle *M15*. It is characterized by an decreased curvature at the throat, indeed, the ratio between the radius of the circular arc shaping the throat region and the nozzle semi-height is $r_t = 5$ for this nozzle.

- **Nozzle M22**: This nozzle was designed to achieve an exhaust Mach number of 2.2 when operated with fluid MM at total conditions $P_T = 17.63\ bar$, $T_T = 240°C$. The nozzle semi-height is $h = 6\ mm$. It is characterized by an increased curvature at the throat, indeed, the ratio between the radius of the circular arc shaping the throat region and the nozzle semi-height is $r_t = 20$. This permits to have smoother gradients. Since the gradients are axially spread it is possible to obtain more static pressure measurements in positions where the expansion is actually taking place.

3.4 EXPERIMENTAL CAMPAIGNS CONDUCTED

Three experimental campaigns were conducted using the nozzle presented and three different fluids: nitrogen as representative of ideal gases, MDM and MM as representatives of organic fluids.

3.4.1 *Dilute nitrogen expansion campaign*

The *Diluite nitrogen expansion campaign* was performed using nitrogen as working fluid. The behavior of gaseous nitrogen is well approximated by the PIG model in a wide thermodynamic region. Thus, the purpose of this campaign was to obtain a characterization of nozzles *M2*, *M15* and *M16*, using an ideal gas.
Ideal gas nozzle flows are expected to have some peculiar characteristics different from non-ideal gas nozzle flows. In particular, for a given fluid the ratios between the static pressures along the nozzle axis and the total pressure are expected to be dependent only on the cross-sectional area distribution. As a consequence, for a given nozzle, pressure ratios are expected to be independent from the specific total conditions at which the

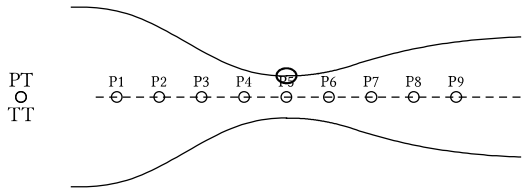

(a) *Nozzle M2: sketch of the quantities measured.*

(b) *Nozzle M2: example of a schlieren image acquired during an experiment performed with fluid MDM.*

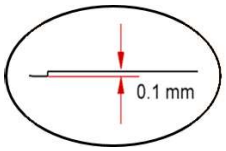

(c) *Detail of the step machined at the throat of nozzle M2.*

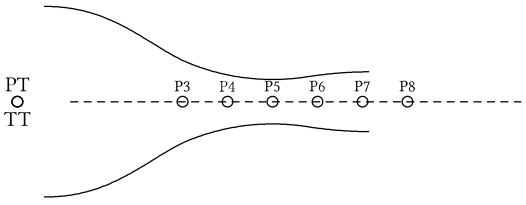

(d) *Nozzle M15: sketch of the flow properties measured.*

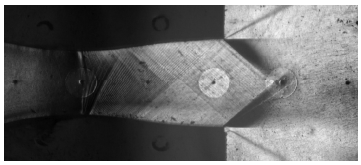

(e) *Nozzle M15: example of a schlieren image acquired during an experiment performed with fluid MDM.*

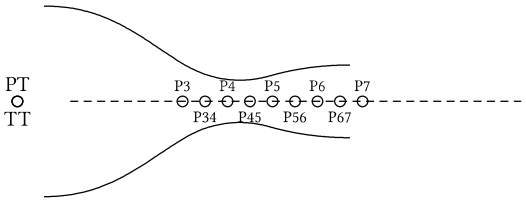

(f) *Nozzle M16: sketch of the flow properties measured.*

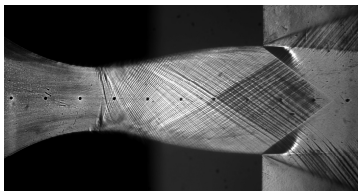

(g) *Nozzle M16: example of a schlieren image acquired during an experiment performed with fluid MM.*

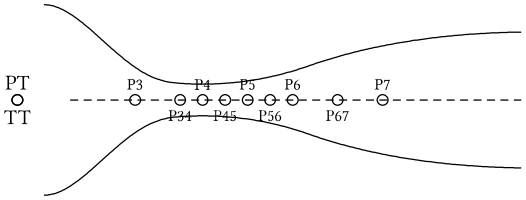

(h) *Nozzle M22: sketch of the flow properties measured.*

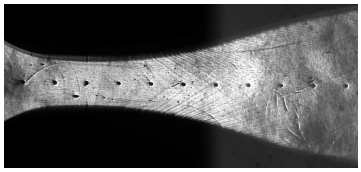

(i) *Nozzle M22: example of a schlieren image acquired during an experiment conducted with fluid MM.*

Figure 3.2: Nozzle tested and example of schlieren images obtained

nozzle is operated, thus from total pressure and total temperature. Moreover, the speed of sound along the nozzle axis it is expected to decrease monotonically; contrarily to what it is expected with a molecularly complex non-ideal vapor. The experimental campaign was conducted with the aim of confirming these foreseen characteristics.
The experiments performed during the *Diluite nitrogen expansion campaign* were designed in order to test the four nozzles *M2*, *M15*, *M16* and *M22* at different total initial conditions. Thirty-three test runs were performed, fourteen of them were selected to be analyzed within the following chapters.

3.4.2 *MDM vapor expansion campaign*

The *MDM vapor expansion campaign* was performed using MDM as working fluid. The campaign was conceived with the aim of studying the expansion of a molecularly complex vapor inside the two nozzles, *M2* and *M15*. Siloxane MDM was chosen since it is complex enough to exhibit a highly non-ideal behavior in the vapor phase and it is also widely applied in ORC power systems. The goal of this campaign was to provide evidence of some of the peculiarities of non-ideal compressible expansions. In particular, the ratio between static pressures along the nozzle axis and total pressure are expected to be dependent, not only on the nozzle geometry, but also on the total conditions identified by total pressure and total temperature. Moreover, the speed of sound along an isoentropic expansion is expected to monotonically increase.
The *MDM vapor expansion campaign* was conceived so to test the two nozzles at two different total temperatures; around $240^{\circ}C$ and around $270^{\circ}C$. Nineteen test runs were performed, nine of them were selected and are analyzed in the following chapters.

3.4.3 *MM vapor expansion campaign*

The *MM vapor expansion campaign* was performed using MM as working fluid and the two nozzles *M15* and *M16*. The campaign was conceived with two principal aims. The first one was to provide data of a second organic vapor flowing in the same nozzle used in the previous *MDM vapor expansion campaign* and starting from the same total reduced conditions. To fulfill this purpose nozzle *M15* was used and the total reduced conditions reached in two representative MDM tests were replicated with MM.
The second aim was to obtain data of nozzle expansions characterized by a wide range of total conditions so to span systematically the thermodynamic region included between the saturation curve and the critical temperature. A large number of test runs were thus performed with both nozzle *M15* and nozzle *M16*. The collected data were analyzed with the purpose of assessing the influence of P_T, T_T and Z_T on the pressure ratios measured along the nozzle axis. The results of this experimental campaign are presented in chapter 6.

3.5 CFD SIMULATIONS

Nozzle flow CFD simulations were used either to complement the experimental data acquired or to perform an assessment of the CFD software for Non-Ideal Compressible-Fluid Dynamics flows called SU2 (Vitale et al., 2015). The SU2 suite is an open-source platform designed to solve multi-physics Partial Differential Equation (PDE) problems and PDE-constrained optimization problems, which was recently extended to non-ideal compressible flows. The SU2 solver is equipped with an embedded thermodynamic library which includes the ideal equation of state, the van der Waals cubic equation of state and the improved Peng-Robinson Stryjek-Vera equation of state (Stryjek and Vera, 1986). Moreover, a C++ interface to the multi-purpose thermodynamic library FluidProp, provides access to state-of-the-art fluid models, including multi-parameter equations of state.

Nozzle flows were simulated both with the ideal gas nitrogen and with the organic fluids MDM and MM. All simulations were performed considering a $2D$ computational domain, limited to the converging and the diverging sections of the nozzle. The conditions of the fluid at the inlet boundary reproduce the total condition measured experimentally within the settling chamber. No boundary condition is required at the exit section due to the supersonic character of the flow. Numerical simulations were first carried out using different levels of grid resolution to evaluate the dependency of the solution on the spatial discretization.

Numerical results include simulations of inviscid and viscous steady flows, using diverse thermodynamic models, namely the ideal gas law, the iPRSV model and the reference fluid model based on the Helmholtz equation of state (Thol et al., 2017) implemented in the FluidProp library. Viscous flows were simulated using the $k - \omega$ SST turbulence model (Menter, 1994). The first grid point is placed in the viscous sublayer, so that no wall-functions are used.

4

DILUITE NITROGEN EXPANSION CAMPAIGN

This chapter is devoted to the experimental characterisation of nozzle expansions of a low molecular complexity fluid operating in PIG conditions. This prior characterization has been done using nitrogen as working fluid. The nozzles tested are those presented in section 3.3. Within this chapter the nitrogen expansion campaign is described thoroughly. In section 4.1 a consistency and repeatability assessment of the data collected is carried out. Then, the nozzle flows are analysed in section 4.2 through the total-to-static pressure ratios measured at the nozzle centreline. A comparison with CFD data is reported. Lastly, in section 4.3 sound speed, velocity and Mach number computed from the measurements are provided and commented. The computed Mach number is also compared with the one measured thanks to the line detection algorithm presented in section 2.4.2.

4.1 CONSISTENCY AND REPETABILITY ASSESSMENT

To assess the repeatability of the experiments the parameter of choice is the local static pressure, since it is directly measured. Therefore, it permits to evaluate the consistency of experimental measures without the introduction of inaccuracies other than the instrument uncertainty.
Several tests runs were performed with each nozzle. It was expected that, different tests performed with the same geometry and in the same conditions would result in pressure measurements lying within their uncertainty bars. In particular, due to the perfect gas behaviour of nitrogen, the static pressure along the nozzle axis should be the same for nozzle flows sharing the same total pressure.
Figures 4.1, 4.3, 4.5 and 4.7 report a plot of the static pressures measured against the corresponding total pressure for the test runs performed using nozzles *M15*, *M2*, *M16* and *M22* respectively. The test runs presented are listed in Table 4.1, together with the specific total conditions attained at test start and conclusion.
It is worth noticing that tests performed on the same nozzle are often characterised by different total temperature. For example, nozzle *M2* was tested at total temperatures ranging from $T_T = 30 \div 70\ ^\circ C$, nozzle *M15* in the range $T_T = 30 \div 120\ ^\circ C$, nozzle *M16* at $T_T = 5 \div 30\ ^\circ C$ and nozzle *M22* at $T_T = 35 \div 100\ ^\circ C$. However, the plots reported, permit to compare static pressure data taken at the same total pressure, regardless of total temperature.
Indeed, the enlargements plotted in figures 4.4, 4.2, 4.6 4.8 show that, the static pressures,

Test ID	Nozzle	Initial total condition $P_T\ [bar]\ ;\ T_T\ [^\circ C]$	Final total condition $P_T\ [bar]\ ;\ T_T\ [^\circ C]$
12N2	*M15*	P_T = 5.587 T_T = 84.4	P_T = 2.463 T_T = 57.0
13N2	*M15*	P_T = 6.091 T_T = 52.5	P_T = 2.182 T_T = 20.5
14N2	*M15*	P_T = 11.734 T_T = 122.9	P_T = 3.904 T_T = 87.7
15N2	*M15*	P_T = 6.617 T_T = 57.8	P_T = 2.306 T_T = 26.2
17N2	*M22*	P_T = 8.267 T_T = 75.1	P_T = 4.118 T_T = 36.3
19N2	*M22*	P_T = 7.559 T_T = 106.7	P_T = 3.940 T_T = 74.6
20N2	*M22*	P_T = 5.372 T_T = 68.0	P_T = 3.358 T_T = 34.3
21N2	*M22*	P_T = 5.5192 T_T = 103.3	P_T = 3.6278 T_T = 64.2
25N2	*M2*	P_T = 5.525 T_T = 55.5	P_T = 3.584 T_T = 31.6
26N2	*M2*	P_T = 5.414 T_T = 54.9	P_T = 3.204 T_T = 30.2
27N2	*M2*	P_T = 4.828 T_T = 72.6	P_T = 3.268 T_T = 54.6
31N2	*M16*	P_T = 7.645 T_T = 14.9	P_T = 3.538 T_T = 0.8
32N2	*M16*	P_T = 7.699 T_T = 16.7	P_T = 3.699 T_T = 0.8
33N2	*M16*	P_T = 5.868 T_T = 17.8	P_T = 2.607 T_T = 1.6

Table 4.1: List of the test runs belonging to the experimental campaign *Nitrogen nozzle campaign*. Each test run is composed by several different steady states characterized by different total conditions going from the initial to the final one that are here reported.

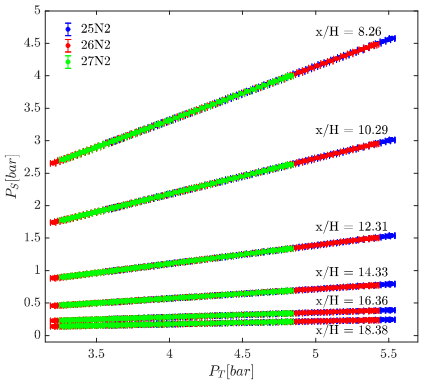

Figure 4.1: Nozzle *M2*: static pressure measured at different axial locations in tests *25N2*, *26N2* and *27N2* plotted against the corresponding measured total pressure. Curves are parametrized by the non-dimensional axial coordinate x/H. It is indicated in the labels and it specifies the pressure measurements location. For each coordinate an enlargement is plotted below for a clearer comparison of results.

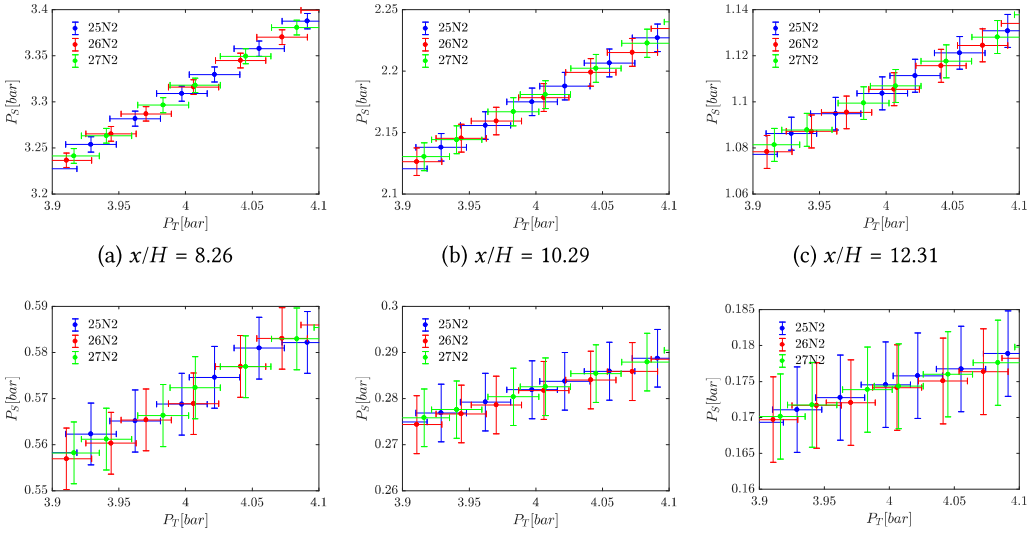

(a) x/H = 8.26 (b) x/H = 10.29 (c) x/H = 12.31

(d) x/H = 14.33 (e) x/H = 16.36 (f) x/H = 18.38

Figure 4.2: Nozzle *M2*: static pressure measured in the proximity of P_T = 4 *bar*.

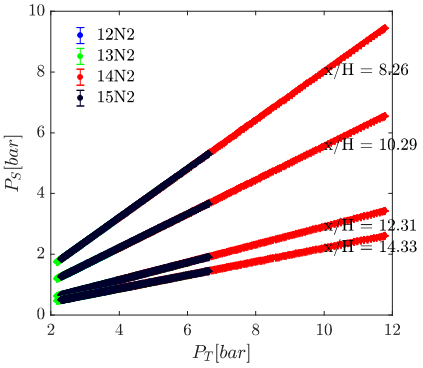

Figure 4.3: Nozzle *M15*: static pressure measured at different axial locations in tests *12N2*, *13N2*, *14N2* and *15N2* plotted against the corresponding measured total pressure. Curves are parametrized by the non-dimensional axial coordinate x/H. It is indicated in the labels and it specifies the pressure measurements location. For each coordinate an enlargement is plotted below for a clearer comparison of results.

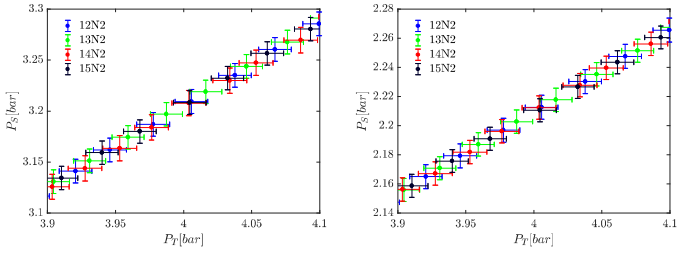

(a) x/H = 8.26 (b) x/H = 10.29

(c) x/H = 12.31 (d) x/H = 14.33

Figure 4.4: Nozzle *M15*: static pressure measured in the proximity if P_T = 4 *bar*.

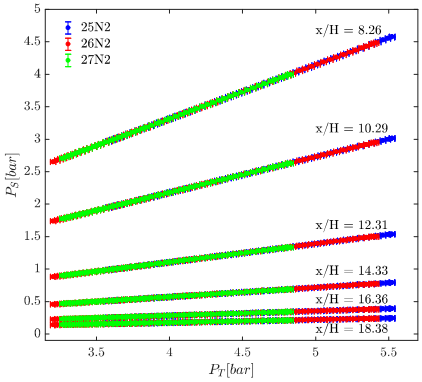

Figure 4.5: Nozzle *M16*: static pressures measured at different axial locations in tests *31N2*, *32N2* and *33N2* plotted against the corresponding measured total pressure. Curves are parametrized by the non-dimensional axial coordinate x/H. It is indicated in the labels and it specifies the pressure measurements location. For each coordinate an enlargement is plotted below for a clearer comparison of results.

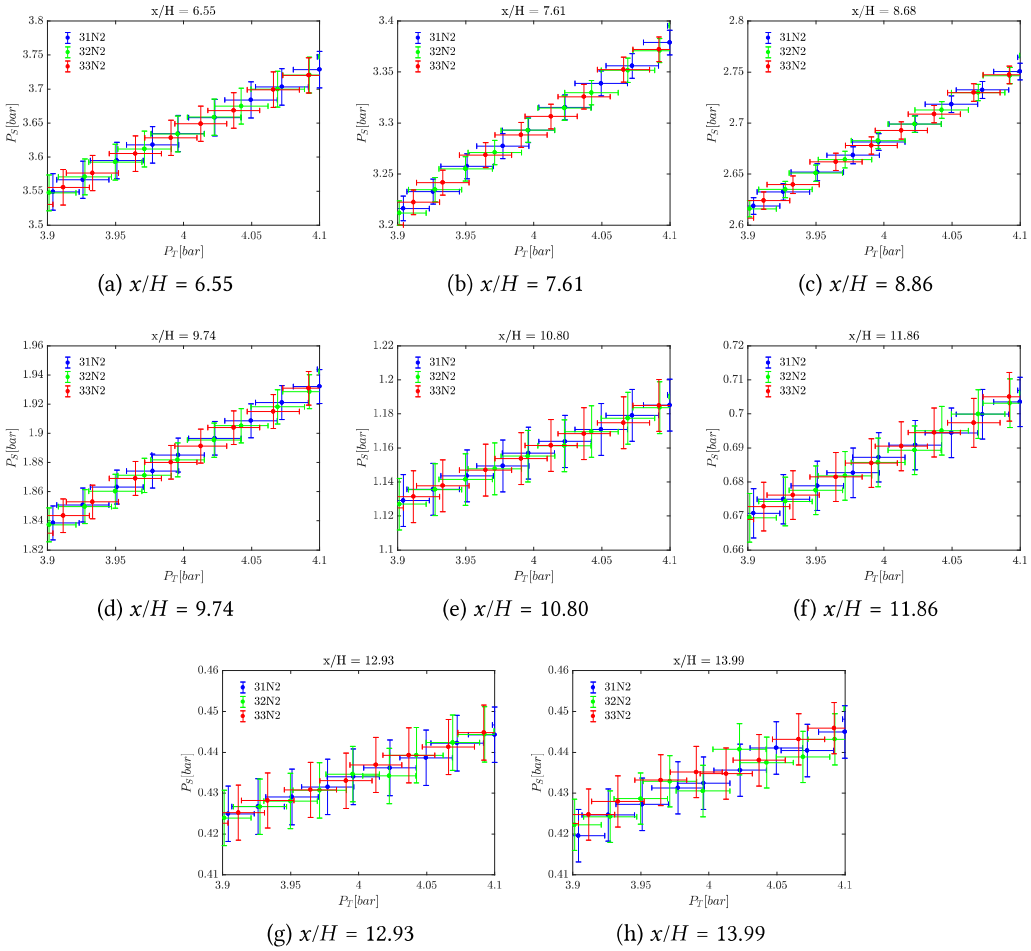

(a) x/H = 6.55 (b) x/H = 7.61 (c) x/H = 8.86

(d) x/H = 9.74 (e) x/H = 10.80 (f) x/H = 11.86

(g) x/H = 12.93 (h) x/H = 13.99

Figure 4.6: Nozzle *M16*: static pressures measured in the proximity of $P_T = 4\ [bar]$.

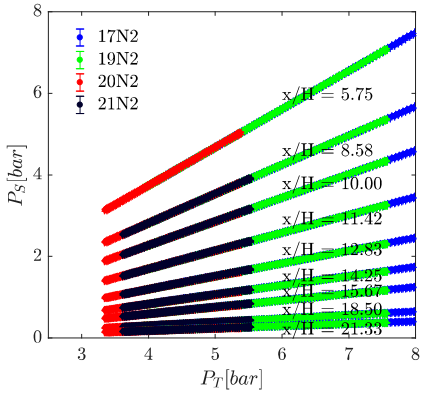

Figure 4.7: Nozzle *M22*: static pressures measured at different axial locations in tests *17N2*, *19N2*, *20N2* and *21N2* plotted against the corresponding measured total pressure. Curves are parametrized by the non-dimensional axial coordinate x/H. It is indicated in the labels and it specifies the pressure measurements location. For each coordinate an enlargement is plotted below for a clearer comparison of results.

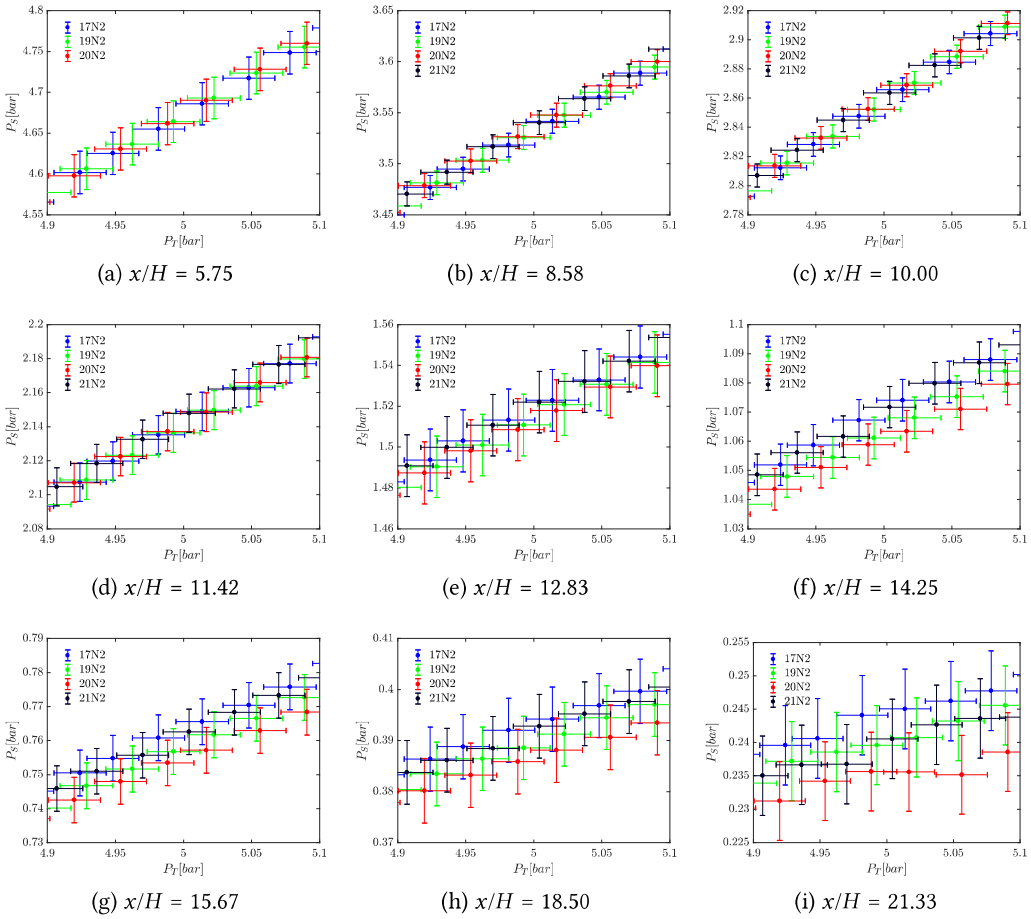

(a) x/H = 5.75 (b) x/H = 8.58 (c) x/H = 10.00

(d) x/H = 11.42 (e) x/H = 12.83 (f) x/H = 14.25

(g) x/H = 15.67 (h) x/H = 18.50 (i) x/H = 21.33

Figure 4.8: Nozzle *M22*: static pressures measured in the proximity of P_T = 5 $[bar]$.

measured at the same axial location of the nozzle, are always well inside the uncertainty bars despite the different total temperatures characterizing each test. This proves both consistency and repeatability of the experiments performed with each nozzle tested.
It is also proven that the behaviour of nitrogen is well modeled by the PIG equation of state in the range of thermodynamic conditions reached during the experiments. Indeed, total temperature has no influence on the measured static pressures and this follows directly from the PIG hypothesis. Moreover, it is confirmed that the nozzle flows is not influenced by any heat exchange and it can be, therefore, considered adiabatic. Indeed, tests 13N2 (green data) and 14N2 (red data), reported in figure 4.10b, were characterized by total temperatures around $30^{\circ}C$ and $100^{\circ}C$ respectively. Nevertheless, the pressure ratios measured overlap perfectly at every axial location. This proves that the nozzle flow can be considered adiabatic. Indeed, if the flow were not adiabatic the heat flux would be different in the two tests runs 13N2 and 14N2, leading to different pressure ratios.

4.2 PRESSURE RATIO MEASUREMENTS

The investigated nozzle flows are characterized here through the analysis of pressure ratio measured along the nozzle axis. This quantity is directly calculated using only measured data without involving any hypothesis nor using any equation of state. Figures 4.9a, 4.10a, 4.11a and 4.12a report a sketch of the four nozzles. Each sketch reports the position at which the static pressure measurements were performed. Figures 4.9, 4.10, 4.11 and 4.12 include sub-pictures showing the measured pressure ratios P/P_T plotted against the corresponding total pressure. Each of the sub-pictures refers to a specific non-dimensional axial position (x/H).
Accordingly to the *quasi-one-dimensional* theory presented in section 3.2.1 the pressure ratio P/P_T are expected to be independent from the total pressure. Indeed, even though the flow analyzed here is obviously $2D$, the qualitative flow features found in section 3.2.1 are still valid. By looking at the first series of plots presented, which are relative to nozzle *M2*, (Fig.4.9 from (c) to (h)), it can be seen that the pressure ratios measured at $x/H = 8.26$, $x/H = 14.33$, $x/H = 16.36$ and $x/H = 18.38$ (Fig.s 4.9c, 4.9f, 4.9g, 4.9h) do not show any evident trend. However, one may recognize an increasing trend of pressure ratio with the total pressure in figures 4.9d and 4.9e, corresponding to $x/H = 10.29$ and $x/H = 12.31$. Observing the figures 4.10, 4.11 and 4.12 referring to the other three nozzles, one can noticed that the same increasing trend is present in most of the axial coordinates analyzed in nozzle *M15* (Fig.4.10d, 4.10e, 4.10f) and more markedly in nozzle *M22* (Fig.4.12d, 4.12e, 4.12f, 4.12g, 4.12h, 4.12i, 4.12j, 4.12k), while it is not so well recognizable in nozzle *M16* (Fig.4.11).
In order to assess whether the qualitative spotted trend can be quantitatively demonstrated, the difference Δ (Eq.(74)) between the two pressure ratios measured in correspondence of the maximum $\Pi(P_T^{max})$ and the minimum $\Pi(P_T^{min})$ total pressure was analyzed.

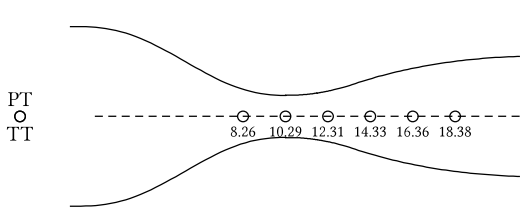

(a) *Nozzle M2*

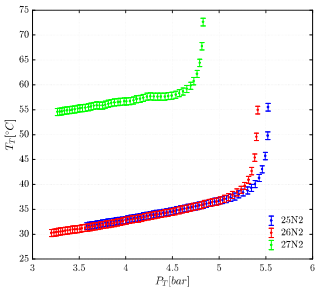

(b) *Total temperature*

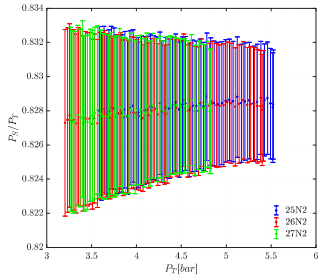

(c) *x/H = 8.26 convergent*

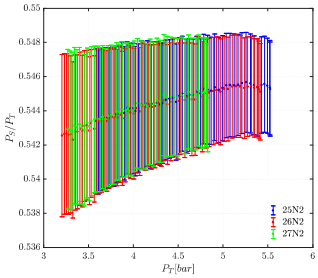

(d) *x/H = 10.29 throat*

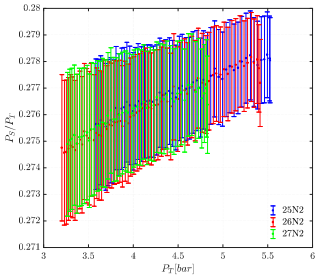

(e) *x/H = 12.31 divergent*

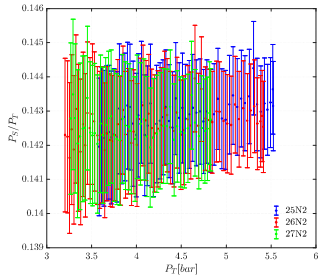

(f) *x/H = 14.33 divergent*

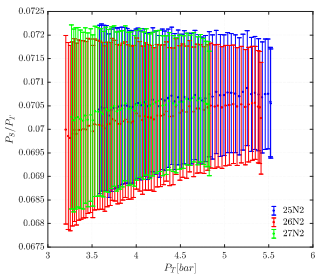

(g) *x/H = 16.36 divergent*

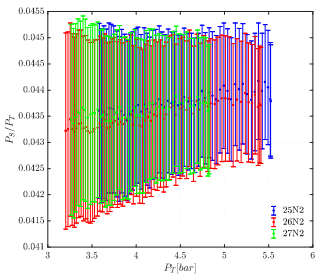

(h) *x/H = 18.38 divergent*

Figure 4.9: *(a)* Profile of nozzle *M2*, the static pressure measurement points are sketched and the value of the non-dimensional axial location is reported. *(b)* Total temperature measurements plotted against total pressure measurements for test runs 25N2, 26N2 and 27N2. *(c)* to *(h)* Pressure ratio plotted against total pressure measurements. Each picture refers to a specific axial coordinate.

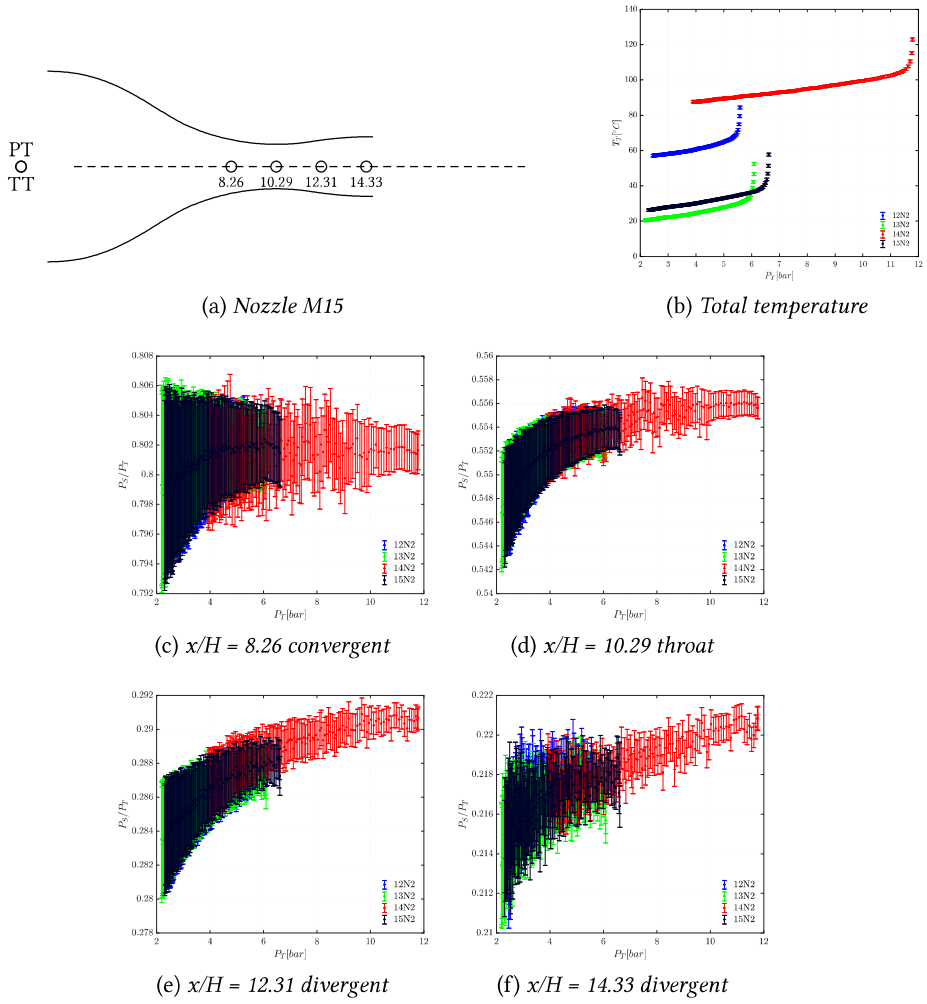

(a) *Nozzle M15*

(b) *Total temperature*

(c) *x/H = 8.26 convergent*

(d) *x/H = 10.29 throat*

(e) *x/H = 12.31 divergent*

(f) *x/H = 14.33 divergent*

Figure 4.10: *(a)* Profile of nozzle *M15*, the static pressure measurement points are sketched and the value of the non-dimensional axial location is reported. *(b)* Total temperature measurements plotted against total pressure measurements for test runs 12N2, 13N2, 14N2 and 15N2. *(c)* to *(f)* Pressure ratio plotted against total pressure measurements. Each picture refers to a specific axial coordinate.

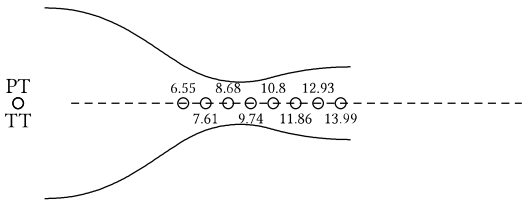

(a) *Nozzle M16*

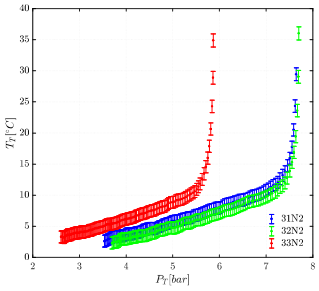

(b) *Total temperature*

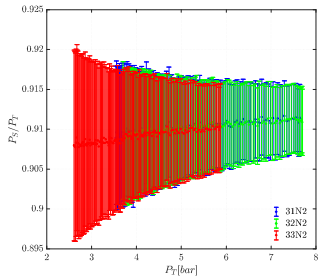

(c) *x/H = 6.55 convergent*

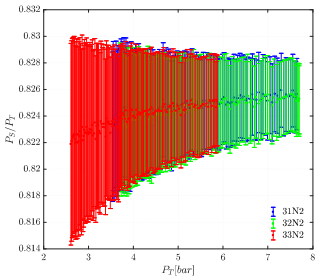

(d) *x/H = 7.61 convergent*

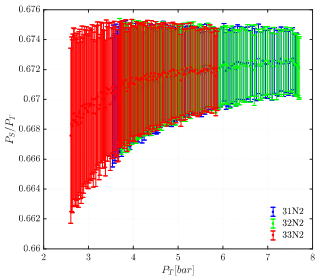

(e) *x/H = 8.68 convergent*

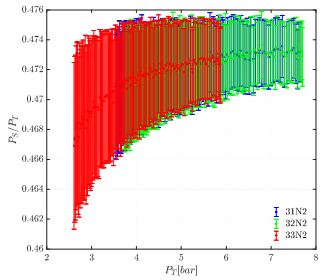

(f) *x/H = 9.74 divergent*

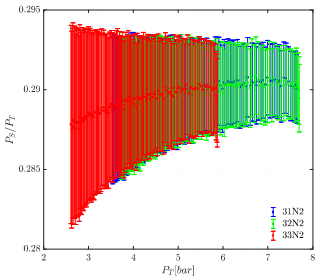

(g) *x/H = 10.80 divergent*

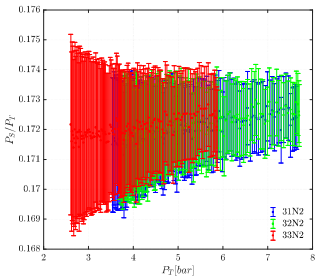

(h) *x/H = 11.86 divergent*

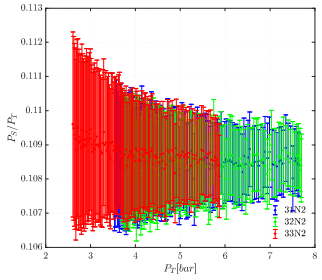

(i) *x/H = 12.93 divergent*

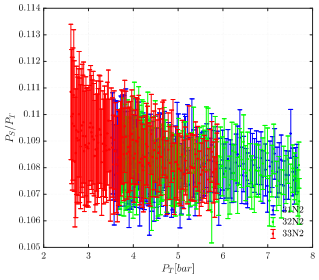

(j) *x/H = 13.99 divergent*

Figure 4.11: *(a)* Profile of nozzle *M16*, the static pressure measurement points are sketched and the value of the non-dimensional axial location is reported. *(b)* Total temperature measurements plotted against total pressure measurements for test runs 31N2, 32N2 and 33N2. *(c)* to *(f)* Pressure ratio plotted against total pressure measurements. Each picture refers to a specific axial coordinate.

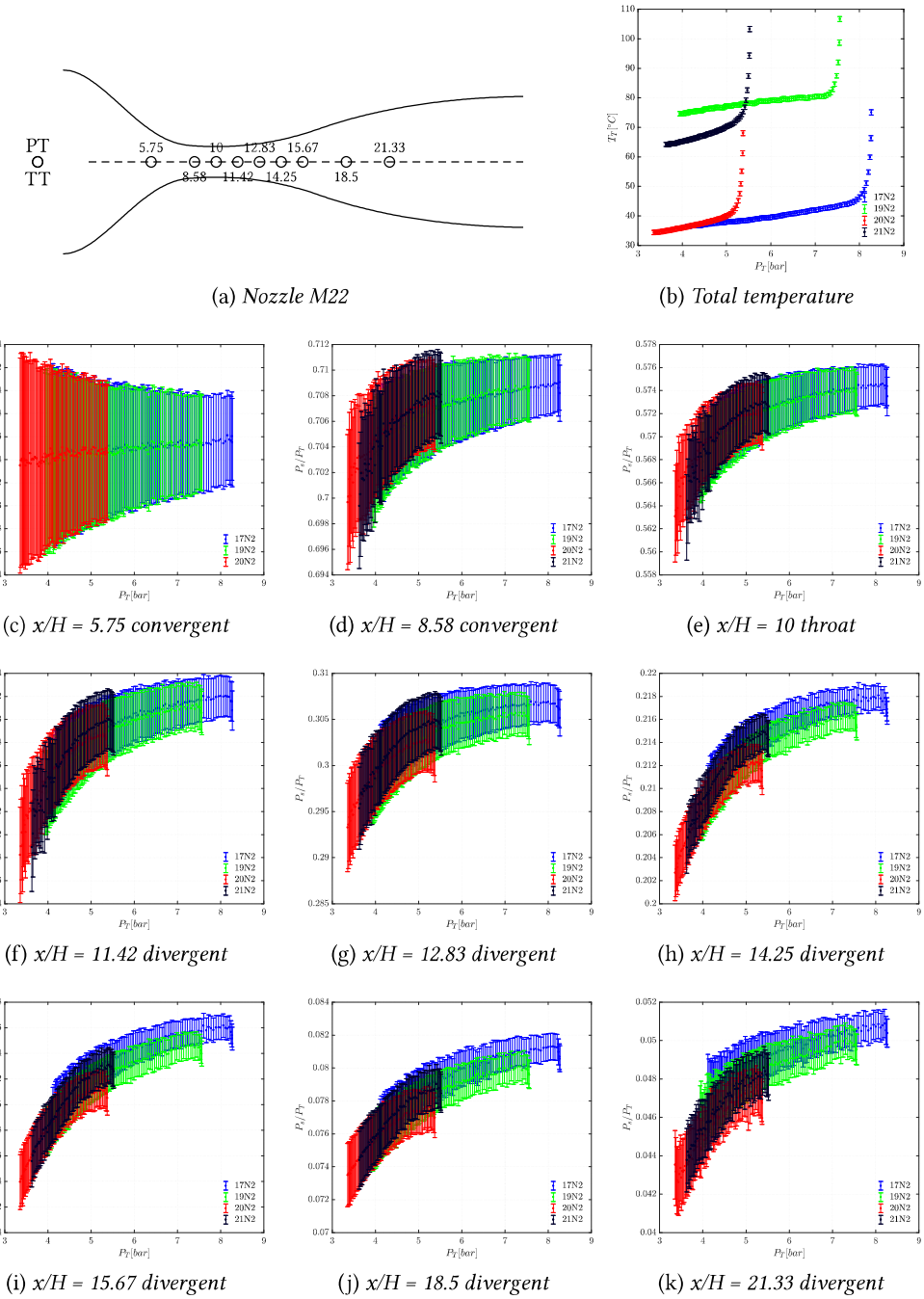

(a) *Nozzle M22*

(b) *Total temperature*

(c) *x/H = 5.75 convergent*

(d) *x/H = 8.58 convergent*

(e) *x/H = 10 throat*

(f) *x/H = 11.42 divergent*

(g) *x/H = 12.83 divergent*

(h) *x/H = 14.25 divergent*

(i) *x/H = 15.67 divergent*

(j) *x/H = 18.5 divergent*

(k) *x/H = 21.33 divergent*

Figure 4.12: *(a)* Profile of nozzle *M22*, the static pressure measurement points are sketched and the value of the non-dimensional axial location is reported. *(b)* Total temperature measurements plotted against total pressure measurements for test runs 17N2, 19N2, 20N2 and 21N2. *(c)* to *(f)* Pressure ratio plotted against total pressure measurements. Each picture refers to a specific axial coordinate..

In particular, the difference Δ was compared with its uncertainty U_Δ (Eq.(77)) obtained propagating the uncertainties U_{P_s} and U_{P_T} related respectively to the static and the total pressure measurements.

$$\Delta = \left(\frac{P}{P_T}\right)_{P_T=P_T^{max}} - \left(\frac{P}{P_T}\right)_{P_T=P_T^{min}} = \Pi(P_T^{max}) - \Pi(P_T^{min}) \tag{74}$$

$$\Delta\% = \frac{\Delta}{\Pi_{mean}} \cdot 100 \tag{75}$$

$$U_\Pi = (\Pi)\sqrt{\frac{U_P^2}{P^2} + \frac{U_{P_T}^2}{P_T^2}} \tag{76}$$

$$U_\Delta = \sqrt{U_{\Pi(P_T^{max})}^2 + U_{\Pi(P_T^{min})}^2} \tag{77}$$

$$U_\Delta\% = \frac{100}{\Pi_{mean}} \cdot \sqrt{U_{\Pi(P_T^{max})}^2 + U_{\Pi(P_T^{min})}^2 + \frac{\Delta^2}{\Pi_{mean}^2} \cdot U_{\Pi_{mean}}^2} \tag{78}$$

$$\tag{79}$$

A value of U_Δ greater than Δ confutes the existence of a quantitatively distinguishable trend in the pressure ratio measured. However, to make the comparison clearer instead of comparing Δ with U_Δ the two quantities $\Delta\%$ (Eq. (75)) and $U_\Delta\%$ (Eq. (78)) were used. $\Delta\%$ represents Δ as a percentage of the mean value Π_{mean} calculated using all the pressure ratios acquired during all the test runs; while $U_\Delta\%$ is its uncertainty. For each nozzle and pressure tap Figure 4.13 permits an immediate comparison between the two quantities $\Delta\%$ and $U_\Delta\%$. It can be noticed that the existence of an increasing trend of pressure ratios with increasing total pressures is confirmed in nozzles *M15* and *M22*. In particular, the trend is quantitatively more important for nozzle *M22*, where, at $x/H = 21.33$, $\Delta\%$ reaches a value greater than 14% while $U_\Delta\%$ is only 4%. Also in nozzle *M15*, the value of $\Delta\%$ is grater than $U_\Delta\%$, however $\Delta\%$ is always lower than 4%.

On the other hand, no trend seems to be present for the pressure ratios measured in nozzles *M2* and *M16*. Indeed, in these nozzles, the value of $U_\Delta\%$ is always higher or almost comparable to the value of $\Delta\%$ with the only exception of the value registered in $x/H = 13.99$ in nozzle *M16* where $\Delta\%$ is negative. Moreover, this value of Δ is negative, thus, indicating a trend opposite to the one identified for nozzles *M15* and *M22*.

The presence of a trend showing a dependence of the pressure ratio on the total pressure, contradicts the expected behavior of a PIG expanding in a nozzle. Nevertheless, this contradiction holds only in nozzles *M15* and *M22*. Thus, it should derive from causes excluded by the hypothesis of the *quasi-one-dimensional* theory, since this is the simplest theory stating that Π does not depend upon nozzle total conditions. This should hold also for $2D$ isentropic nozzle flows as the one studied here. Moreover, the causes must be present to a greater extent in nozzles *M15* and *M22*.

In order to understand what could be the possible cause several CFD simulations have been performed. The results are shown in Figure 4.14. The meshes used to calculate the nozzle flow were 2D meshes. A grid convergence study was performed to assure

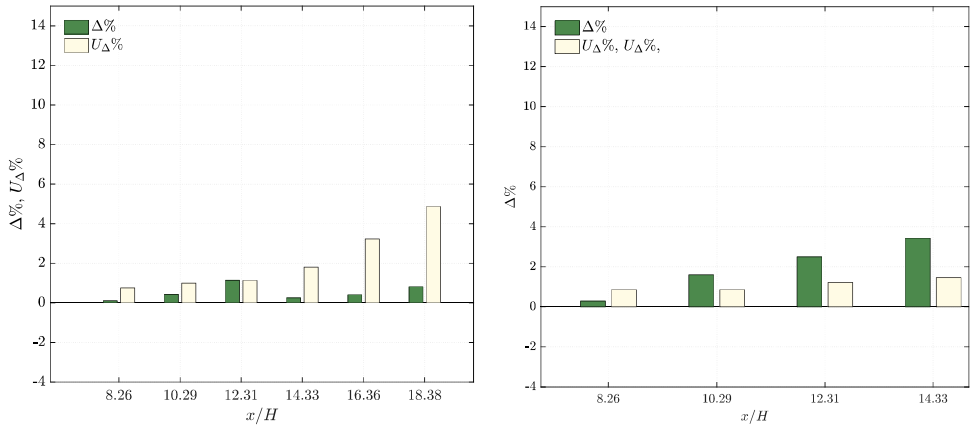

(a) *Nozzle M2* (b) *Nozzle M15*

(c) *Nozzle M16* (d) *Nozzle M22*

Figure 4.13: Bars plots of the difference Δ (Eq.(74)) between the pressure ratio measured in correspondence with the maximum and the minimum total pressure (green bar), and of its uncertainty U_Δ (Eq.(77)) (light yellow bar).

the independence of the solution from the mesh. The viscous simulations have been performed using the $k-\omega SST$ turbulence model and a value of $y^+ < 1$ at the walls was guaranteed. The simulation was carried out for nozzle *M15* only.

At first, the validity of the ideal gas equation of state was questioned by performing two simulations; one considering the fluid nitrogen as a PIG and one considering it as a non-ideal gas, thus, adopting the equation of state implemented in RefProp. The results in terms of pressure ratio are shown in Figure 4.14a and they are almost indistinguishable. Indeed, the difference between the two simulation is lower than 0.5%, thus confirming the PIG behaviour of nitrogen under the conditions encountered in this experimental campaign.

Subsequently, the impact of neglecting the viscosity has been assessed by comparing the nozzle flow simulated both using the Euler and the Navier-Stokes governing equation. In the latter the viscosity was computed using the Sutherland viscosity model. The same total conditions were imposed at the inlet, $P_T = 4.0075\ bar$, $T_T = 25\ ^\circ C$. As it can be seen in Figure 4.14b, the resulting pressure ratio distribution along the nozzle axis is very similar for the two simulations. A small discrepancy between the two simulation is present only towards the nozzle outlet. Indeed, the percentage difference between the two sets of data is almost zero up to the throat placed in $x/H = 10.29$. It rises in the diverging portion of the nozzle but keeping a value everywhere lower than 3%.

Finally, the impact of viscous effects changing with the total pressure was evaluated. The isentropic hypothesis neglects the effects of viscosity; these effects can be related to the value of the total pressure since it influences the Reynolds number. Indeed, the value of *Re* halves going from the nozzle flow characterized by the maximum total pressure to the nozzle flow characterized by the minimum one. Nevertheless, this is true for every nozzle tested and not only for nozzles *M15* and *M22*. Moreover, the range is also the same for each nozzle since the Reynolds number at the throat spans always from about 10^7 to $2.5 \cdot 10^6$.

Two nozzle flows were simulated, characterized by a Reynolds number at the throat of $Re_t = 2.85 \cdot 10^6$ and $Re_t = 10^7$ that are, respectively, the minimum and maximum Re_t registered during test runs 12N2, 13N2, 14N2 and 15N2. The results in term of pressure ratio along the nozzle axis are shown in Figure 4.14c. It can be noticed that the two profiles are almost superimposed and that their difference is below 1% everywhere. Contrarily to the trend registered by the experimental data for nozzle *M15*, the higher pressure ratios refer to the simulation characterised by the lower Re_t which correspond to the lower total pressure.

It can be concluded that the CFD simulations performed confirm the validity of the PIG equation of state for nitrogen. Moreover, they show that viscosity scarcely affects the nozzle flows under study and that the changing of viscous effects due to the changing total conditions, and thus Reynolds number, is negligible. Of course the viscous effect simulated in the CFD calculations does not model necessarily all the effects possibly present. Indeed, the simulations considers a 2D control volume placing the inlet at the

beginning of the convergent portion and imposing a uniform constant velocity at the inlet. In reality, the planar nozzle is placed after a sweep pipe accommodating the transition from the circular section of the settling chamber to the rectangular one of the test section. Three dimensional viscous effects resulting from this transition are not modeled in the CFD simulations performed.
These not modelled viscous effects could be the cause of the registered trend. Thus they should be negligible in nozzles *M2* and *M16*, limited in nozzle *M15* and relevant in nozzle *M22*. A possible cause triggering viscous effects, dependent on operating conditions (especially on P_T), have been found in the shape of the nozzle throat region. Indeed, the nozzles differ because of their non-dimensional curvature at the throat $r_t = r/H$:

- Nozzle *M2*: $r_t = 10$ with a machined step of height $h = 0.1\ mm$,
- Nozzle *M15*: $r_t = 10$,
- Nozzle *M16*: $r_t = 5$,
- Nozzle *M22*: $r_t = 20$.

It can be noticed that the two nozzles where the trend is not present are characterized by a lower radius of curvature (nozzle *M16*) or by a step located at the throat (nozzle *M2*). Both these characteristics contribute in fixing the position of the sonic line. Indeed, the position of the actual nozzle throat depends on the nozzle geometry as well as on the flow conditions, due to the presence of the viscous boundary layer that modifies the so-called equivalent internal inviscid geometry. A variable shape of the boundary layer can cause a displacement of the sonic line. This displacement can vary subjected to the modification of viscous effects not modelled in the CFD Navier-Stokes simulations.
The hypothesis that the trend observed in the pressure ratio data could be caused by a displacement of the sonic line due to the time-dependent total pressure, is supported by the fact that this trend becomes negligible when actions promoting a better fixing of the sonic line position are undertaken.
In conclusion, nozzle *M22* was discarded from the following experimental campaigns with organic vapors. It proves to be not adequate to assess the non-ideal flow effects in nozzle flows. Indeed, even its characterisation made with a PIG did not follow the expected behaviour of a PIG nozzle flow. On the other hand, the pressure ratios measured in nozzles *M2* and *M16* prove to be independent from the total conditions at which the nozzle were operated. The *M2* and *M16* nitrogen nozzle flows analyzed followed the behavior expected for isentropic expanding flows of PIG. *M15* nitrogen nozzle flow exhibited a weak dependence of the pressure ratio on the total pressure. This dependence was ascribed to viscous effects causing the displacement of the sonic line rather than to the non-validity of the PIG equation of state. The variation of the pressure ratio registered in nozzle *M15* with the total pressure was considered very limited, thus the nozzle was used in the following experimental campaigns with organic vapors.

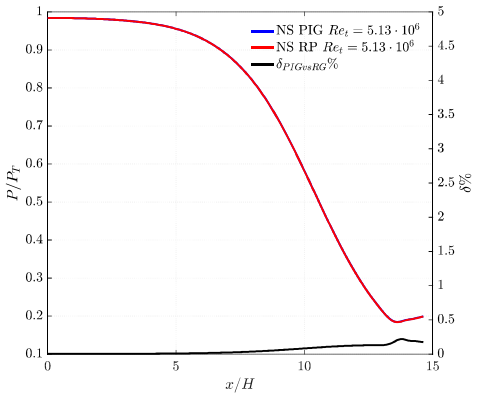

(a) *Navier-Stokes simulation with PIG law (blue line), Navier-Stokes simulation with RefProp (red line), percentage difference (black line).*

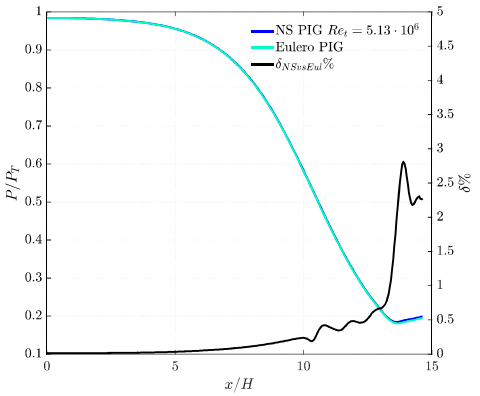

(b) *Navier-Stokes simulation with PIG law (dark blue line), Euler simulation with PIG law (light blue line), percentage difference (black line).*

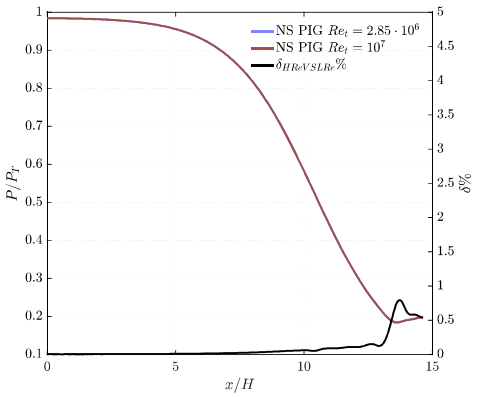

(c) *Navier-Stokes simulation with PIG law, $Re_t = 2.85 \cdot 10^6$ (purple line), Navier-Stokes with PIG law, $Re_t = 10^7$ (brown line), percentage difference (black line).*

Figure 4.14: Pressure ratio along the axis of nozzle *M15* derived from CFD calculations and plotted against the non-dimensional axial coordinate. Results from two different calculations are reported in each plot (coloured lines) together with the percentage difference between the two (black line). All the simulations were performed on 2D meshes, the $k - \omega SST$ turbulence method was used in the viscous ones and the viscosity was calculated using the Sutherland viscosity model.

4.2.1 *Comparison between experimental and CFD data*

The data acquired have been used to carry out a comparison between experimentally measured and CFD calculated pressure ratio. As it was proven in the previous section 4.2, the pressure ratio at a given axial location of the three nozzles *M2*, *M15* and *M16* does not depend on the total conditions at which each nozzle is operated. Thus, all the pressure ratio measured in the different test runs, referring to a specific location in a specific nozzle have been averaged. The averaged pressure ratio have been compared with the result of Navier-Stokes CFD calculations, treating nitrogen as a PIG, adopting the $k-\omega$ *SST* turbulence model and modeling the viscosity using the Sutherland viscosity model.
The results of this comparison are shown in Figure 4.15. Pressure ratio versus non-dimensional axial coordinate plots reported in Fig. 4.15a, Fig. 4.15c and Fig. 4.15e show a good match between the two sets of data. A better quantitative comparison is done by looking at the bar plots in figures 4.15b, 4.15d and 4.15f. They represent the difference between the two sets of data as a percentage of the experimental measured pressure ratio:

$$\delta_{CFDvsExp}\% = \frac{\left(\frac{P_{\overline{x}}}{P_T}\right)_{exp} - \left(\frac{P_{\overline{x}}}{P_T}\right)_{CFD}}{\left(\frac{P_{\overline{x}}}{P_T}\right)_{exp}} \cdot 100 \tag{80}$$

where $\overline{x}$ represents the specific axial location. Analyzing nozzle *M2* (Fig.s 4.15a, 4.15b), it can be seen that the difference between the two sets of data is always well below the 10%, actually it is lower than 2% except in two points: $x/H = 14.33$ and $x/H = 18.38$. The matching between experimental and numerical data is than considered very good.
It must be pointed out that this nozzle features a small step located at the throat. However, the CFD simulation was carried out neglecting the presence of such step. Indeed, an experimental campaign, conducted before those presented in this work, proved that the pressure profile along the nozzle axis is only mildly affected by the presence of the step. The pressure profile is locally perturbed but it superimposed to that obtained considering a clean configuration immediately downstream the nozzle throat. The experimental campaign investigating the influence of a recessed step at the throat section of a supersonic nozzle adopted air as working fluid and tested nozzle *M2* together with another one specifically designed to be operated with air. A thorough analysis quantifying the influence of the step, and documented with CFD Navier-Stokes simulations embodying the step can be found in (Zocca et al., 2018).
Figures 4.15c, 4.15d report the data referred to nozzle *M15*. It can be noticed that the matching between measured and simulated data is good ($\delta\% < 3\%$) up to the last axial position $x/H = 14.33$ where the percentage difference raises slightly higher than 10%. It must be said that the last axial position correspond to the point where the pressure ratio is the lowest measured. This means that even small absolute difference, results

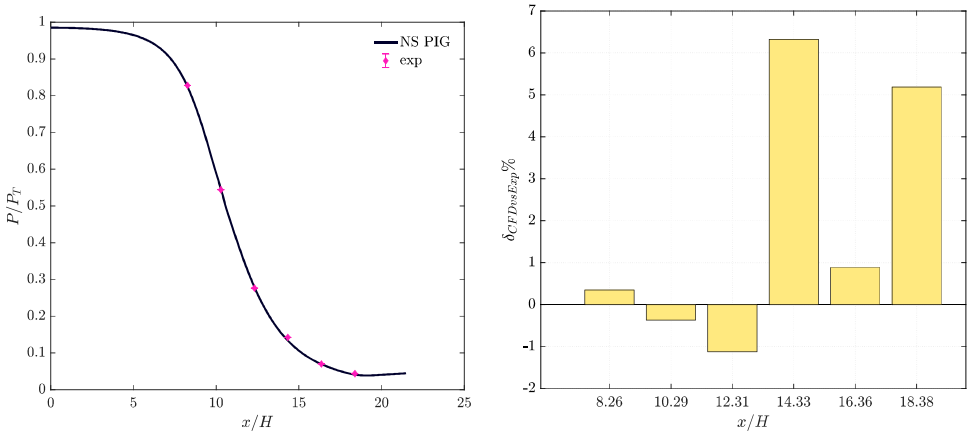

(a) *Nozzle M2 P/P_T vs x/H.*

(b) *Nozzle M2 δ% (Eq. (80)).*

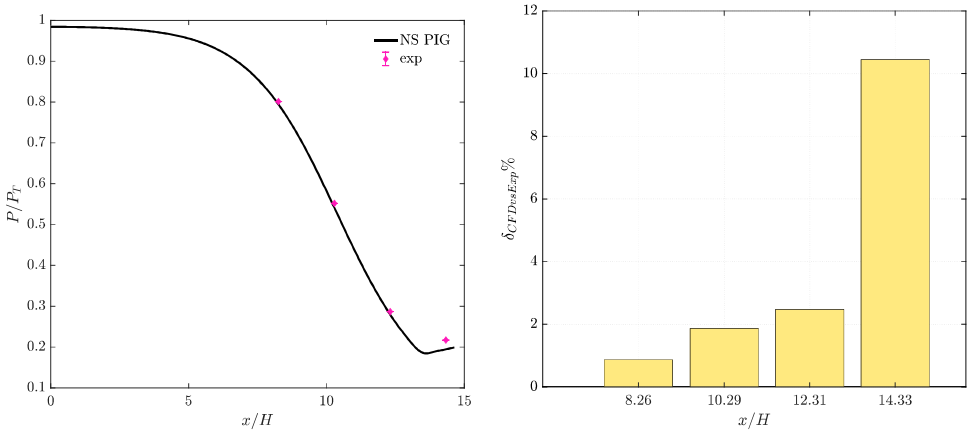

(c) *Nozzle M15 P/P_T vs x/H.*

(d) *Nozzle M15 δ% (Eq. (80)).*

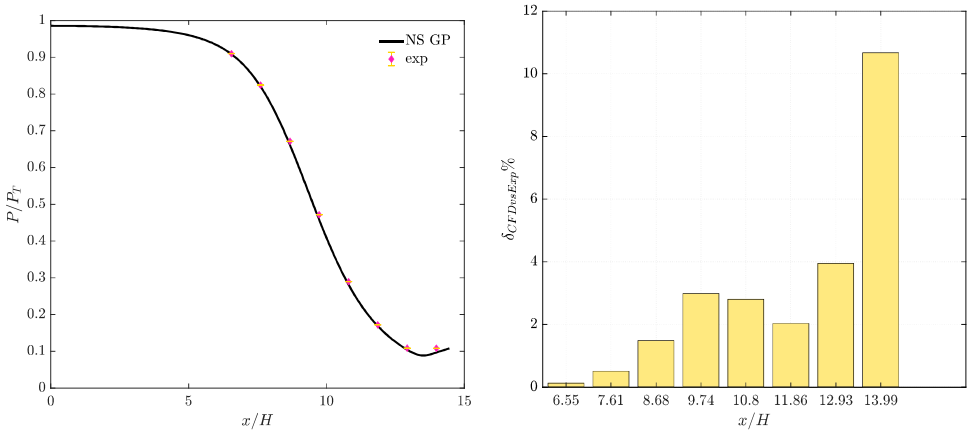

(e) *Nozzle M16 P/P_T vs x/H.*

(f) *Nozzle M16 δ% (Eq. (80)).*

Figure 4.15: Comparison between experimental and CFD data. Figures (a), (c) and (e) show pressure ratio from CFD calculations (black line) together with the one measured (pink dots with error bars). Figures (b), (d) and (f) shows the difference between the two set of data as a percentage of the measured pressure ratio.

in to a higher percentage difference if compared to the other axial positions where the pressure ratios are higher. Nevertheless, even by looking at Figure 4.15c, there is a visible discrepancy between the two set of data in $x/H = 14.33$,discrepancy which cannot be explained by the measurement uncertainty. As the boundary layer increases going from inlet to outlet, the last part of the nozzle is where it plays the major role. Thus if the CFD simulation is not modeling it well the discrepancy can be non negligible. However, given that the flow is accelerating and that the Reynolds numbers are rather high, the boundary layer is expected to play a secondary role and its possible mis-modeling can not account for such a discrepancy.

It must be noticed also that the channel in which the nitrogen flows is made by steel nozzle profiles for a depth of 17.2 mm and by cardboard gaskets for a depth of 1.5 mm (see Fig. 4.16a). The cardboard gaskets are cut out so to follow the profile of the nozzle. However, the cut out tolerance is higher than the one obtained by the machines shaping the steel nozzle profile and this can cause a small distortion of the channel. A *quasi-one dimensional* calculation of the pressure ratios along the nozzle axis was performed first assuming no distortion and then assuming a bad shaping of the cardboard gaskets. Considering a gasket blocking the channel by a height of 2 mm both from the upper and from the lower profile (see Figure 4.16b), the influence on the pressure ratio in $x/H = 14.33$ would be about 4 %. Note that Figure 4.16b reports the gaskets as they were cut loose by the same amount along all the nozzle. The calculation instead has been done by considering the cross sectional throat area not distorted. A calculation performed considering also a distorted throat section would lead to pressure ratio discrepancies around 1%. Nozzle *M15* was tested with hand made cut out cardboard gaskets, thus, an error in their shape can explain at least partially the discrepancy. All the following tests were thus made using only laser cut gaskets.

Lastly, figures 4.15e and 4.15f show the experimental versus numerical data comparison concerning nozzle *M16*. It can be noticed again that the matching between the two sets of data is good ($\Delta\% < 4\%$) up to the last axial position placed in $x/H = 13.99$ where the percentage difference reaches 10%. The same explanation given previously holds here. Moreover, since this nozzle expands up to a higher Mach with respect to nozzle *M15*, it reaches lower pressure ratios. Thus a big percentage difference in the last pressure tap corresponds to a lower absolute discrepancy. Indeed, it can be seen in Figure 4.15e that the distance between the pink dot and the black line is quite small, even though it is bigger than the error bar.

It can be concluded that the nozzle flows analysed are well reproduced by the CFD simulations performed. The discrepancy between the simulated and the measured pressure ratio profiles are always below 10% and in most cases are even lower than 5%.

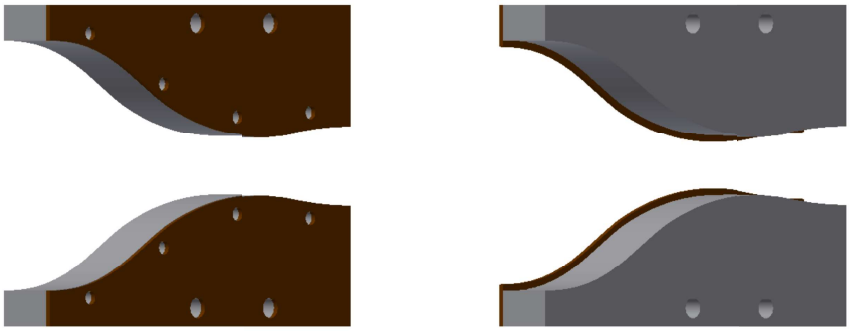

(a) *Assembly of steel nozzle profiles and cardboard gaskets perfectly cut.*

(b) *Assembly of steel nozzle profiles and cardboard gaskets distorting the channel. The gaskets are cut 2 mm loose.*

Figure 4.16

4.3 PROFILES OF FLOW DATA DERIVED FROM MEASURED PRESSURE DISTRIBUTIONS

The obtained measurements of total conditions and of static pressures along the nozzle axis can be used to compute other quantities, provided that the flow can be considered as isentropic. Using a suitable thermodynamic model, that in this case simply follows the PIG hypothesis, the total pressure and the total temperature can be used to calculate the specific entropy characterizing the whole flow (Eq. (81)). At locations where the static pressure is measured two thermodynamic properties (P, s) are available to compute any other useful thermodynamic quantity as the static enthalpy (Eq.(84)) and the speed of sound (Eq. (83)). Moreover, the total enthalpy is constant in the nozzle flow since it can be considered adiabatic, therefore, it can be computed using (P_T, T_T) (Eq. (82)) and then exploited to obtain the flow velocity on the axis (Eq.(84)). Finally the Mach number can be computes as eq. (86).

$$s(P_T, T_T) = s_T = cost \tag{81}$$

$$h(P_T, T_T) = h_T = cost \tag{82}$$

$$c_{\overline{x}} = c(P_{\overline{x}}, s_T) \tag{83}$$

$$h_{\overline{x}} = h(P_{\overline{x}}, s_T) \tag{84}$$

$$v_{\overline{x}} = \sqrt{2 \cdot (h_T - h_{\overline{x}})} \tag{85}$$

$$M_{\overline{x}} = \frac{v_{\overline{x}}}{c_{\overline{x}}} \tag{86}$$

4.3.1 *Speed of sound*

The profiles of the speed of sound along the nozzle axis, reported in Figure 4.17, have been computed following equation (83). Being a dimensional thermodynamic quantity, the speed of sound is influenced by the total pressure and temperature at which the nozzle is operated. However, it changes during a test only of about 5%. The specific total conditions referring to the profiles in Figure 4.17 are reported below each plot. It is worth noticing that all three speed of sound profiles monotonically decrease along the nozzle axis. This is exactly the expected behaviour of a PIG as it is nitrogen at the tested conditions.

4.3.2 *Mach number*

Mach number profiles are expected to be independent from the total conditions at which the nozzle is operated. Indeed, the Mach number is a non-dimensional quantity that should depend only on the non-dimensional coordinate x/H, once that the nozzle geometry and the fluid are fixed, accordingly to the PIG thermodynamic model. If calculated using the more complex equation of state reported in RefProp, the Mach number during a test run, in a given axial location, changes of about 0.5% only confirming its independence from the total conditions.
The Mach number profiles computed for each nozzle are reported in Figure 4.18 as red diamonds. In nozzles *M15* and *M16* it was possible to elaborate schlieren images with the algorithm presented in section 2.4. Thus, measurement of the local Mach number on the axis were obtained thanks to the detection of Mach waves. The identified Mach waves are superimposed to the schlieren images in figures 4.18b and 4.18c. In figures 4.18d and 4.18e three sets of data are reported: the Mach number calculated from total conditions and static pressure measurements (red diamonds), the measured Mach number from Mach waves identification (blue dots) and the Mach profile computed via CFD simulation (black line).
It can be noticed that the blue dots and the red diamonds are superimposed, showing consistency between the Mach numbers computed both from static pressures and from Mach waves slopes. The CFD profile, in Figure 4.18b, however, exhibits a positive deviation from experimental data in the last part of the nozzle (around $x/H = 14.33$). This is consistent with what was found comparing the measured and the simulated pressure ratio (see sec. 4.2). Indeed, the pressure ratio measured at the end of nozzle *M15* was the one registering the higher absolute distance from the CFD data. Since the pressure ratio simulated was lower than the measured one, it is consistent that the simulated Mach number is higher that the measured one.

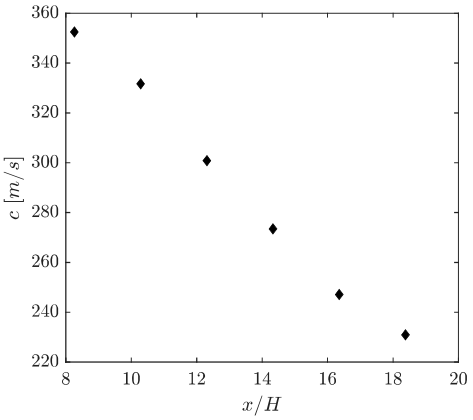

(a) *Nozzle M2, speed of sound against x/H. The plot refers to total conditions:* P_T = 5.43 *bar,* T_T = 42°*C.*

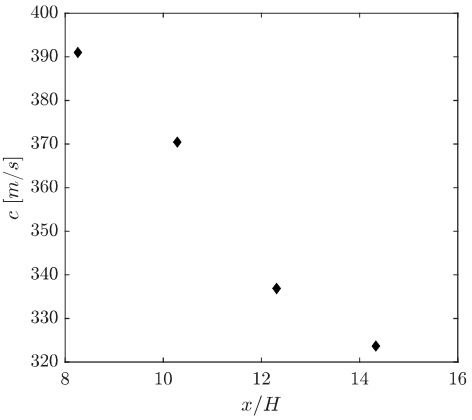

(b) *Nozzle M15, speed of sound against x/H. The plot refers to total conditions:* P_T = 11.76 *bar,* T_T = 118°*C.*

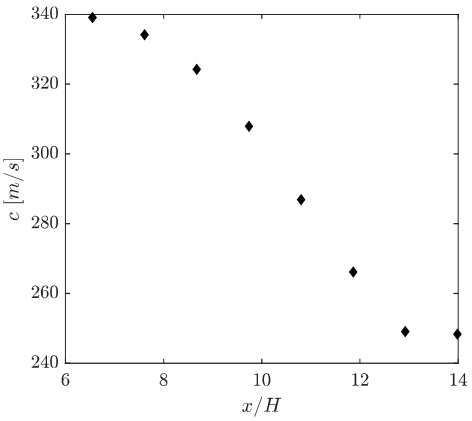

(c) *Nozzle M16, speed of sound against x/H. The plot refers to total conditions:* P_T = 7 *bar,* T_T = 9.9°*C.*

Figure 4.17: Speed of sound computed from the static pressure measurements and calculated specific entropy $s = s(P_T, T_T)$.

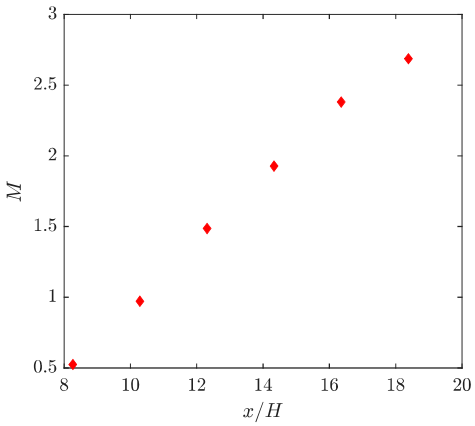

(a) *Nozzle M2. Mach number against x/H*

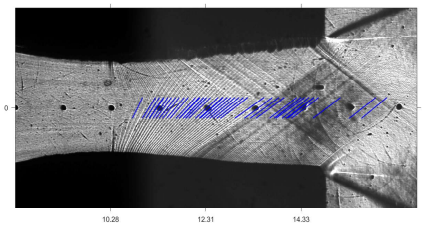

(b) *Schlieren image with visible Mach lines of nitrogen nozzle flow in nozzle M15.*

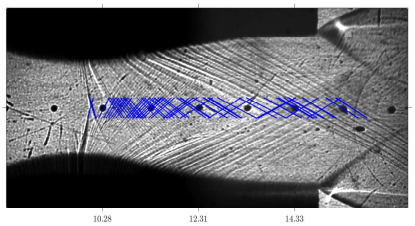

(c) *Schlieren image with visible Mach lines of nitrogen nozzle flow in nozzle M16.*

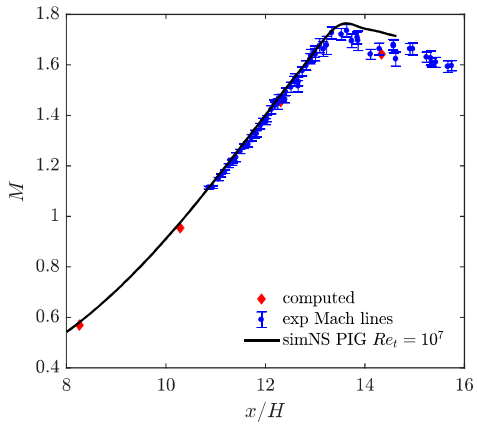

(d) *Nozzle M15. Mach number against x/H. The plot shows the Mach number computed from the total conditions and the static pressure measured (red diamond), the Mach number measured thanks to the Mach waves recognition algorithm (blue dots) (see sec. 2.4), and the Mach number coming from CFD calculation (black line).*

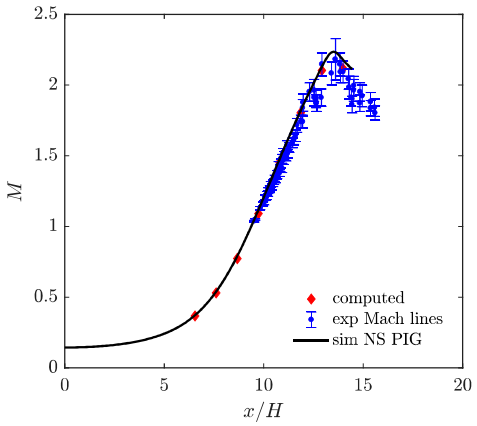

(e) *Nozzle M16, Mach number against x/H.The plot shows the Mach number computed from the total conditions and the static pressure measured (red diamond) and the Mach number measured thanks to the Mach waves recognition algorithm (blue dots) (see sec. 2.4), and the Mach number coming from CFD calculation (black line).*

Figure 4.18: Mach number.

5 MDM VAPOR EXPANSION CAMPAIGN

This chapter is devoted to the experimental characterization of nozzle expansion of organic vapor MDM. In section 5.1 the test runs performed are first analyzed to assess their consistency and repeatability. Section 5.2 presents the non-ideal compressible effects detected by analyzing the pressure ratio profiles. Section 5.2.1 reports a comparison between CFD simulated and measured pressure ratio, while section 5.3 shows the analysis of schlieren images obtained during the experimental campaign and reports the Mach number measured through image processing. The closing section 5.4 illustrates the profiles of speed of sound and of the fundamental derivative of gas-dynamic.

5.1 CONSISTENCY AND REPEATABILITY ASSESSMENT

Among all performed test, nine were chosen to carry out the analysis presented within this chapter; four of them were obtained with nozzle *M2* and five of them were obtained with nozzle *M15*. The list of the nine selected test runs together with the total conditions measured at test start and conclusion are reported in Table 5.1.
The parameter of choice to perform the repeatability and consistency assessment is the static pressures along the nozzle axis; however, assessing repeatability and consistency of experiments conducted with organic vapors is trickier than what done for nitrogen. Indeed, nozzle expansions taking place in the non-ideal regime are expected to be dependent on the specific total conditions. It is thus not possible to simply compare the static pressure measurements obtained in different tests at the same total pressure since also total temperature plays a role. Measurements repeatability can be assessed only by comparing static pressure data sharing the same total conditions.
Unfortunately, the facility operation allows to set the test conditions by adjusting the total state at the HPV and not directly at nozzle inlet. These two states are connected by a transient process which is not perfectly repeatable (see (Spinelli et al., 2015)). Thus, obtaining a high number of comparable data is not straightforward. Moreover, repeating a test run takes approximately two working days, making impossible a systematic repetition of each experiment.
Figures 5.1a and 5.2a report the evolution of the total condition during all the test runs listed in Table 5.1 for nozzle *M2* and *M15* respectively. It can be seen that the only test runs *06MDM* and *08MDM* for nozzle *M2* and test runs *11MDM*, *14MDM*, *16MDM* and *17MDM* for nozzle *M15* can be used to assess the repeatability and consistency of experimental data, since they share the same total conditions. In particular, tests *06MDM* and *08MDM* share the same total temperature in the total pressure range $P_T = 1.8 \div 4$

Test ID	Nozzle	Most non-ideal condition $P_T\ [bar]\ ;\ T_T\ [^\circ C]$	Least non-ideal condition $P_T\ [bar]\ ;\ T_T\ [^\circ C]$
04MDM	*M2*	$P_T = 4.59 \pm 0.01$ $T_T = 247 \pm 1$ $Z_T = 0.828$	$P_T = 0.796 \pm 0.009$ $T_T = 228 \pm 1$ $Z_T = 0.970$
06MDM	*M2*	$P_T = 4.636 \pm 0.009$ $T_T = 242 \pm 1.2$ $Z_T = 0.817$	$P_T = 0.090 \pm 0.009$ $T_T = 235 \pm 1.2$ $Z_T = 0.997$
08MDM	*M2*	$P_T = 4.425 \pm 0.009$ $T_T = 233 \pm 1.2$ $Z_T = 0.811$	$P_T = 0.150 \pm 0.009$ $T_T = 229 \pm 1.2$ $Z_T = 0.995$
10MDM	*M2*	$P_T = 9.02 \pm 0.009$ $T_T = 269 \pm 1.2$ $Z_T = 0.652$	$P_T = 0.7968 \pm 0.009$ $T_T = 265 \pm 1.2$ $Z_T = 0.977$
11MDM	*M15*	$P_T = 9.199 \pm 0.009$ $T_T = 268 \pm 1.2$ $Z_T = 0.634$	$P_T = 0.837 \pm 0.009$ $T_T = 264 \pm 1.2$ $Z_T = 0.976$
13MDM	*M15*	$P_T = 4.586 \pm 0.009$ $T_T = 239.4 \pm 1.2$ $Z_T = 0.814$	$P_T = 0.522 \pm 0.009$ $T_T = 229.7 \pm 1.2$ $Z_T = 0.981$
14MDM	*M15*	$P_T = 8.765 \pm 0.009$ $T_T = 272 \pm 1.2$ $Z_T = 0.682$	$P_T = 0.197 \pm 0.009$ $T_T = 264 \pm 1.2$ $Z_T = 0.994$
16MDM	*M15*	$P_T = 10.027 \pm 0.009$ $T_T = 271 \pm 1.2$ $Z_T = 0.592$	$P_T = 0.155 \pm 0.009$ $T_T = 262 \pm 1.2$ $Z_T = 0.996$
17MDM	*M15*	$P_T = 9.878 \pm 0.009$ $T_T = 272 \pm 1.2$ $Z_T = 0.611$	$P_T = 0.506 \pm 0.009$ $T_T = 264 \pm 1.2$ $Z_T = 0.986$

Table 5.1: List of test runs belonging to the *MDM vapor expansion* experimental campaign. Each test run is composed by several different steady states characterized by different total conditions evolving from the most to the least non-ideal one which are here reported.

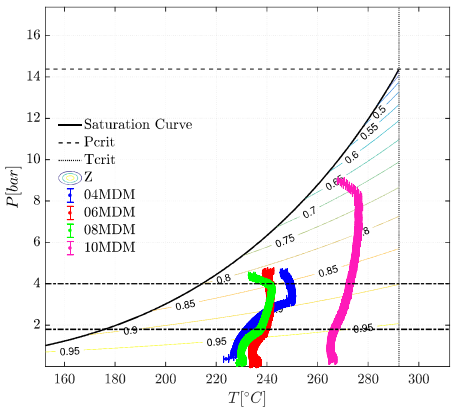

(a) *P − T diagram with the total conditions reached during test runs 04MDM, 06MDM, 08MDM and 10MDM. The solid black line is the saturation curve, the dashed black line is the MDM critical pressure and the dotted black line is the MDM critical temperature. The two dashed-dotted horizontal black lines mark the range in which tests 06MDM and 08MDM share the same total conditions .*

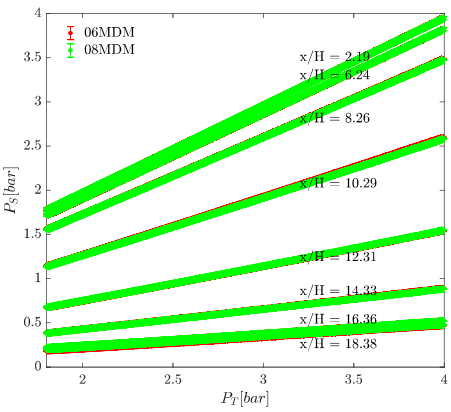

(b) *Nozzle M2: static pressure P_s measured at different axial locations in tests 06MDM and 08MDM plotted against the corresponding measured total pressure in the range P_T = [1.8 ÷ 4] bar where the total temperature for the two tests are matching. Curves are parametrized by the non-dimensional axial coordinate x/H. It is indicated in the labels and it specifies the pressure measurements location. For each coordinate an enlargement is plotted below for a clearer comparison of results.*

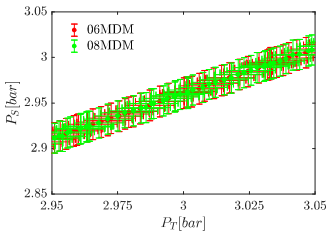

(c) x/H = 2.19

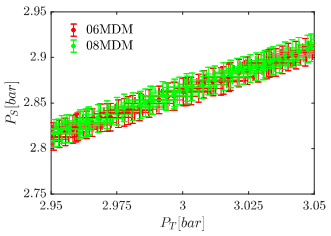

(d) x/H = 6.24

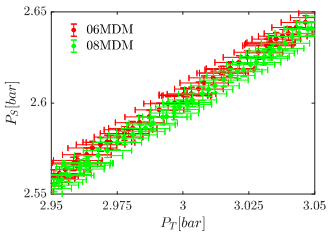

(e) x/H = 8.26

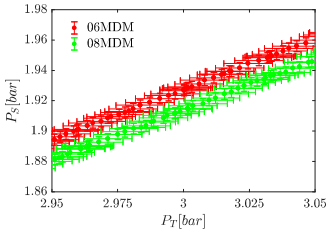

(f) x/H = 10.29

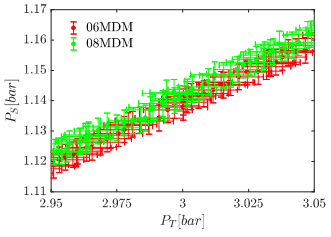

(g) x/H = 12.31

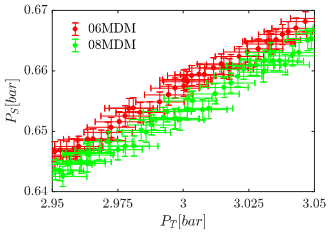

(h) x/H = 14.33

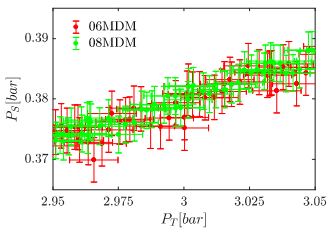

(i) x/H = 16.36

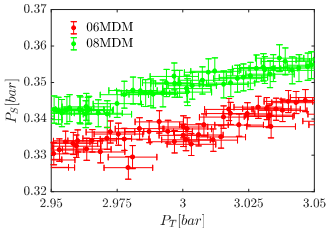

(j) x/H = 18.38

Figure 5.1: Nozzle *M2* operated with MDM, consistency and repeatability analysis.

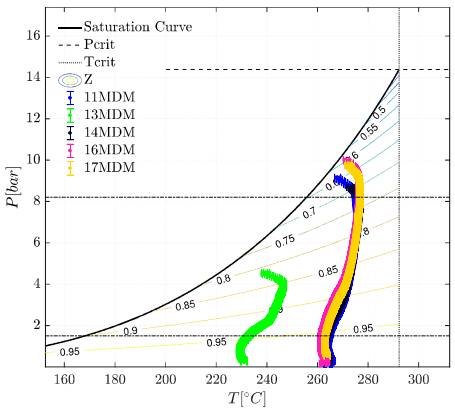

(a) *P – T diagram with the total conditions reached during test runs 11MDM, 13MDM, 14MDM, 16MDM and 17MDM. The solid black line is the saturation curve, the dashed black line is the MDM critical pressure and the dotted black line is the MDM critical temperature. The two dashed-dotted horizontal black lines mark the range in which tests in which tests 11MDM, 14MDM, 16MDM, and 17MDM share the same total conditions .*

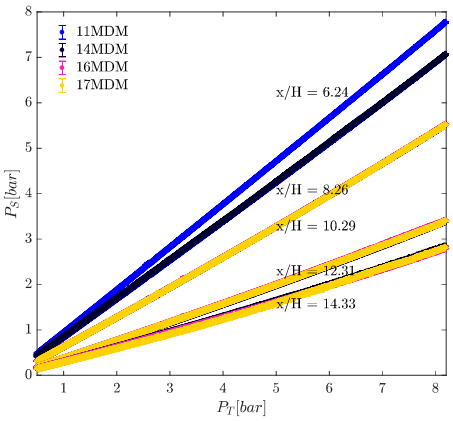

(b) *Nozzle M15: static pressure P_s measured at different axial locations in tests 11MDM, 14MDM, 16MDM, and 17MDM plotted against the corresponding measured total pressure in the range $P_T = [1.5 \div 8.2]$ bar where the total temperature for the four tests are matching. Curves are parametrized by the non-dimensional axial coordinate x/H. It is indicated in the labels and it specifies the pressure measurements location. For each coordinate an enlargement is plotted below for a clearer comparison of results.*

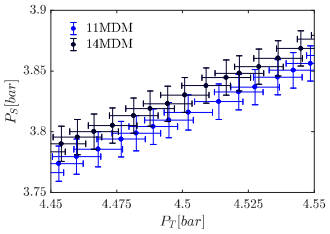

(c) $x/H = 8.26$

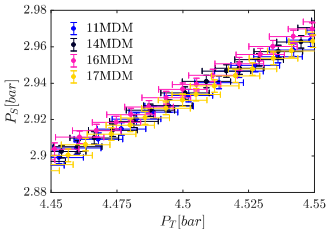

(d) $x/H = 10.29$

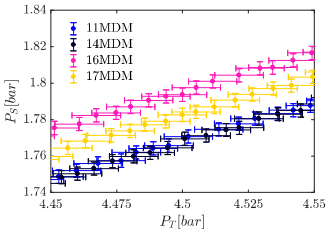

(e) $x/H = 12.31$

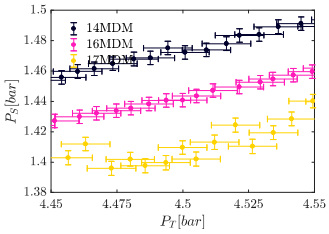

(f) $x/H = 14.33$

Figure 5.2: Nozzle *M15* operated with MDM, consistency and repeatability analysis.

bar and tests *11MDM*, *14MDM*, *16MDM*, *17MDM* share the same total temperature in the range $P_T = 0.5 \div 8.2\ bar$. The static pressures measured within these ranges are plotted in figures 5.1b and 5.2b and a detailed view of static pressures measured at each active pressure tap can be found in figures 5.1 and 5.2.
It was expected that all the data taken within the same nozzle, in the same position along the axis, and at the same total pressure and temperature, would lie inside the uncertainties bar of one another. Even though this is true for most of the data, the details reported in figures 5.1f, 5.1j, 5.2e and 5.2e show some discrepancies. Starting from the data referring to nozzle *M2*, in Figure 5.1f it can be seen that most of the data reported would have overlapping vertical uncertainty bars if shifted horizontally inside their horizontal uncertainty bar. This means that the consistency of the data is assured. The data reported in Figure 5.1j have non overlapping vertical uncertainty bars just by few millibars ($\approx 5\ mbar$). This small discrepancy can be probably ascribed to some 3D viscous effect changing from one test to the other. Beside this small discrepancy it can be concluded, by looking at the whole data set, that the experiments conducted using fluid MDM and nozzle *M2* are repeatable and consistent.
Looking at the data referred to nozzle *M15* (Fig. 5.2), it can be seen that the coordinates at which the static pressures were measured were not the same for all of the tests. In particular, only at coordinates $x/H = 10.29$ and $x/H = 12.31$ there are four measurements to compare; while at coordinates $x/H = 8.26$ and $x/H = 14.33$ only two data sets and three data sets are available respectively. It can be seen that some discrepancies are present and that they are larger than those observed for nozzle *M2*. In particular, only test runs *11MDM* and *14MDM* are consistent one to another. Tests runs *16MDM* and *17MDM* show consistency only for the static pressures measured at $x/H = 10.29$ (Fig.5.2d). For this reason they were excluded from further analysis. The well agreement found between tests *11MDM* and *14MDM* still proves the repeatability and consistency of the experimental data.
A further assessment can be done by comparing the data taken when the total compressibility factor approaches unity. In this thermodynamic region non-ideal effects weaken and measured pressure ratio values converge to the ones predicted by the dilute gas theory, which are independent from the upstream thermodynamic state. Thus, for further verification of measurements consistency, pressure ratios are compared at Z_{Tmax} , namely at the most ideal condition at which data are available for each experimental run, that corresponds to the final total condition listed in Table 5.1. The high Z values indicate the proximity to the ideal-gas conditions, while the polytropic hypothesis is supported by the limited temperature variation among the considered points (see Table 5.1), which entails negligible change in the ideal gas heat capacities. Experimental points from the whole set of 9 tests, complemented with uncertainty bars, are shown in Figure 5.3. For both nozzles, the measured pressure ratios lie within the error bars from one another, with the only exception of the already discarded test *16MDM*, thus proving the consistency of

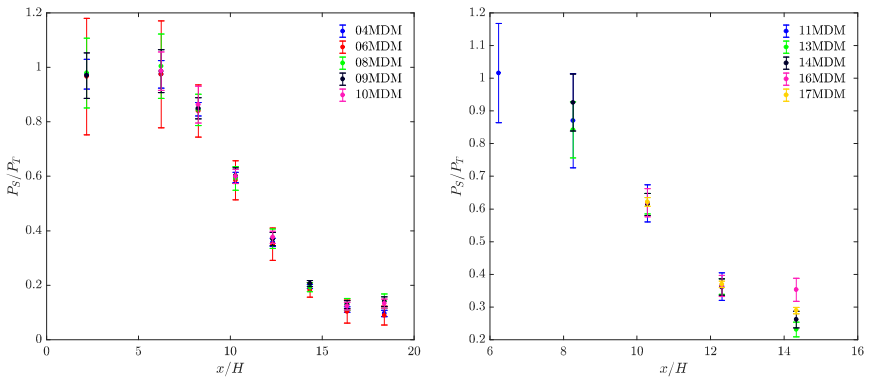

(a) *M2* (b) *M15*

Figure 5.3: Pressure ratio trends along the nozzle axis for all tests at respective Z_{Tmax} conditions.

experimental data acquired during different experimental runs.

5.2 PRESSURE RATIO PROFILES

Four tests were chosen as representative of the whole experimental campaign: tests *04MDM*, *10MDM*, *13MDM* and *11MDM*. Tests *04MDM* and *10MDM* were performed with nozzle *M2* exploring expansions in thermodynamic regions where non-ideal compressible effects are expected to be moderate and high respectively. Analogously, tests *13MDM* and *11MDM* were performed with nozzle *M15* at moderate and highly non-ideal conditions. Nozzle expansions at different non-ideal conditions are analyzed; they refer to thermodynamic states selected so to obtain operating conditions with appreciable distinction in the levels of non-ideality. For each test five to eight significant values of Z_T are therefore identified; they are the minimum value Z_{Tmin}, the maximum one Z_{Tmax} and three to six intermediate values $Z_{Tmid,i}$. All conditions are listed in Table 5.2. Figures 5.4a and 5.4c report the total conditions characterizing the nozzle expansions chosen to be analyzed. They are plotted on a $P - T$ diagram and they are superimposed to a contour of the compressibility factor Z. It is then possible to appreciate the level of non-ideality expected for each expansion. Moreover, figures 5.4b and 5.4d show the expansions measured plotted on a $T - s$ diagram where a contour of the fundamental derivative os gasdynamic Γ is reported. One can notice that most of the expansions take place in a thermodynamic region where $\Gamma < 1$, thus non-ideal compressible fluid effects are expected to be present and appreciable.

Figures 5.5a, 5.6a, 5.7a and 5.8a report the local pressure ratio P/P_T measured at the active taps at different Z_T. As a reference, a continuous expansion profile is reported as extracted at the axis line from a two-dimensional CFD viscous calculation, performed by employing the SU2 software suite (Vitale et al., 2015) and by modeling MDM as a PIG. The constant

Test ID	Nozzle	P_T $[bar]$	T_T $[^\circ C]$	Z_T	Γ_T
04MDMa	*M2*	4.578	246.9	0.828	0.805
04MDMb	*M2*	4.041	249.1	0.854	0.845
04MDMc	*M2*	3.386	249.9	0.882	0.882
04MDMd	*M2*	1.791	232.4	0.932	0.942
04MDMe	*M2*	0.796	227.5	0.970	0.981
10MDMa	*M2*	9.024	268.6	0.652	0.473
10MDMb	*M2*	8.502	274.2	0.704	0.600
10MDMc	*M2*	7.527	276.2	0.756	0.699
10MDMd	*M2*	6.277	275.9	0.806	0.780
10MDMe	*M2*	4.840	274.2	0.855	0.850
10MDMf	*M2*	3.285	271.4	0.904	0.911
10MDMg	*M2*	1.647	266.3	0.952	0.963
10MDMh	*M2*	0.797	265.1	0.977	0.988
13MDMa	*M15*	4.586	239.4	0.814	0.782
13MDMb	*M15*	3.960	246.3	0.854	0.844
13MDMc	*M15*	2.691	242.8	0.903	0.908
13MDMd	*M15*	1.289	231.2	0.952	0.963
13MDMe	*M15*	0.522	229.7	0.981	0.992
11MDMa	*M15*	9.200	267.5	0.634	0.424
11MDMb	*M15*	9.044	269.0	0.652	0.474
11MDMc	*M15*	8.508	274.4	0.705	0.601
11MDMd	*M15*	7.494	275.6	0.756	0.700
11MDMe	*M15*	6.240	275.3	0.806	0.780
11MDMf	*M15*	4.814	273.4	0.855	0.850
11MDMg	*M15*	3.272	270.6	0.904	0.911
11MDMh	*M15*	0.837	264.2	0.976	0.987

Table 5.2: Total conditions in term of measured total pressure and total temperature, computed total compressibility factor and total fundamental derivative of gas-dynamic of the expansion analyzed in sections 5.2 5.4 5.3.

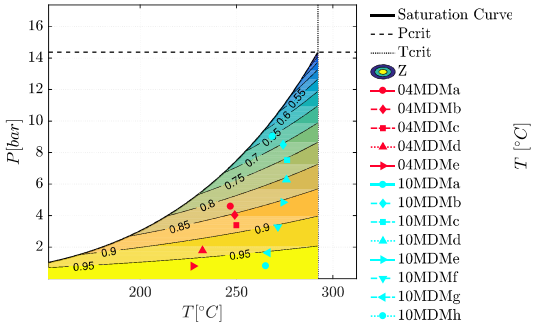

(a) *Nozzle M2, total conditions of expansions extracted from tests 04MDM 10MDM.*

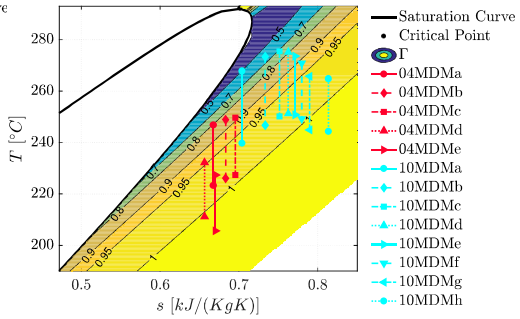

(b) *Nozzle M2, isentropic nozzle expansions measured during tests 04MDM 10MDM.*

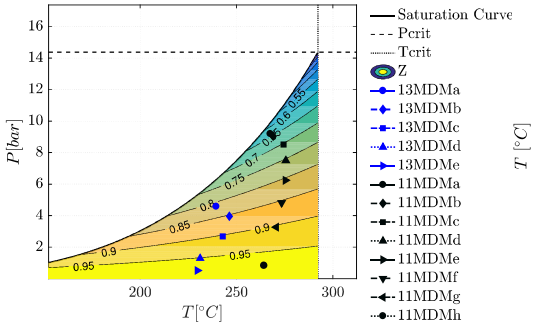

(c) *Nozzle M15, total conditions of nozzle expansions extracted from tests 13MDM 11MDM.*

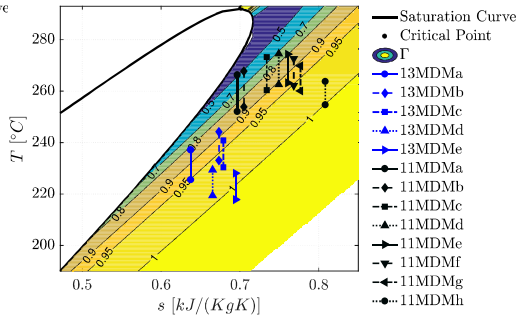

(d) *Nozzle M15, isentropic nozzle expansions measured during tests 13MDM 11MDM.*

Figure 5.4: MDM nozzle expansions analyzed for nozzles *M2* and *M15*.

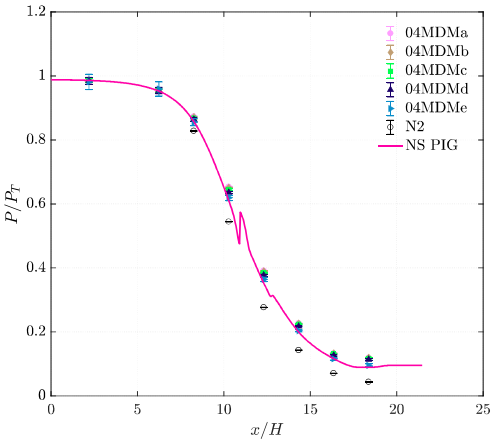

(a) *P/P_T trends along the nozzle axis extracted from test 04MDM (filled colored symbols), P/P_T trends measured in the same nozzle with nitrogen (black not filled circles), P/P_T trends from a CFD viscous calculation coupled with PIG model for MDM (purple line).*

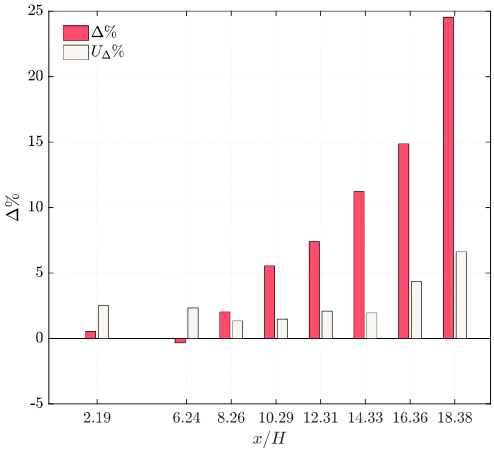

(b) *Bar plot reporting $\Delta\%$ percentage difference distribution of P/P_T between minimum and maximum Z_T conditions Eq. (87) and its uncertainty $U_\Delta\%$ Eq. (89).*

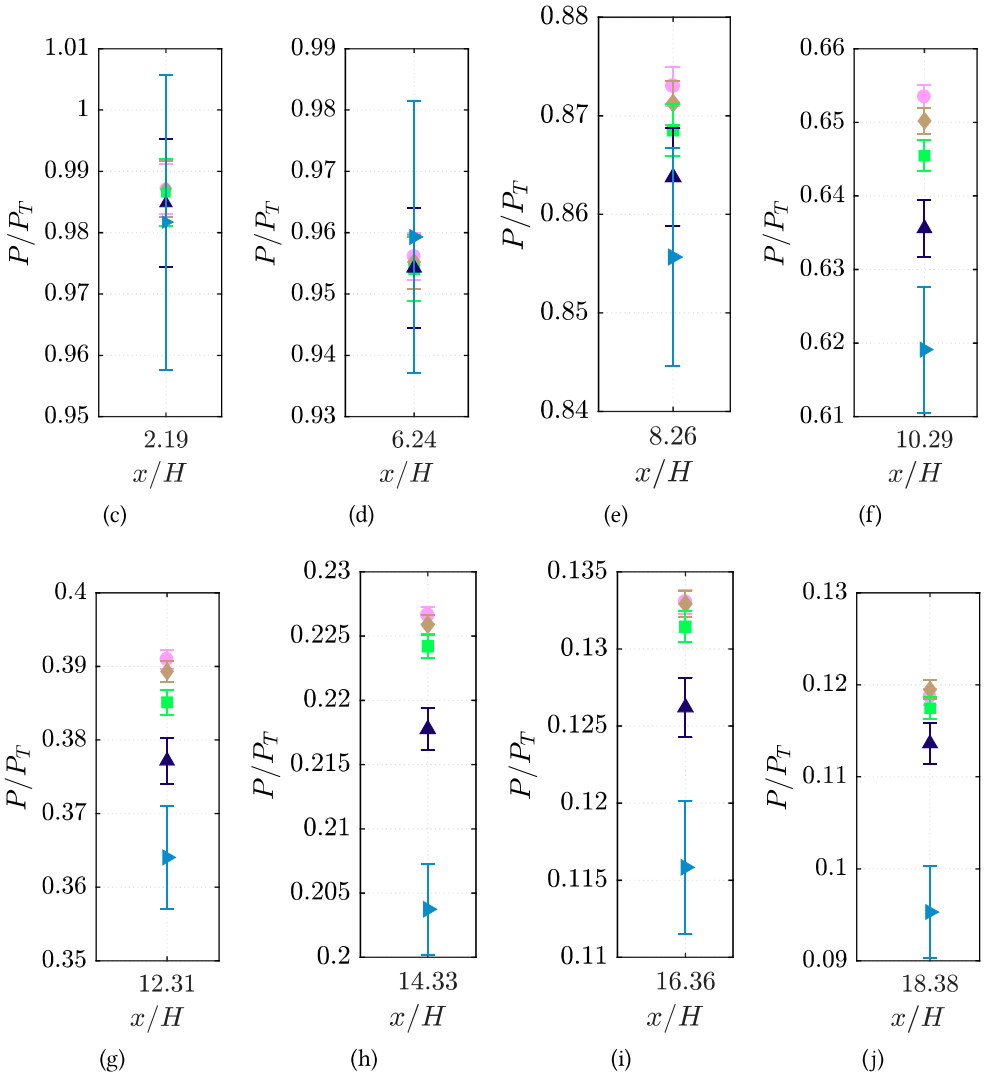

Figure 5.5: Nozzle *M2* at moderate non-ideal conditions (test run *04MDM*). (*c*) to (*j*) detail of pressure ratio measured at the different pressure taps along the nozzle axis.

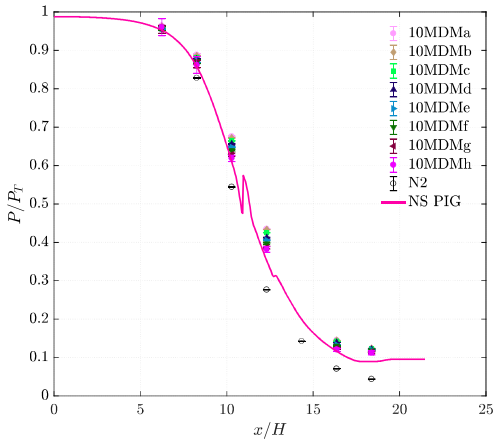

(a) *P/P_T trends along the nozzle axis extracted from test 10MDM (filled colored symbols), P/P_T trends measured in the same nozzle with nitrogen (black not filled circles), P/P_T trends from a CFD viscous calculation coupled with PIG model for MDM (purple line).*

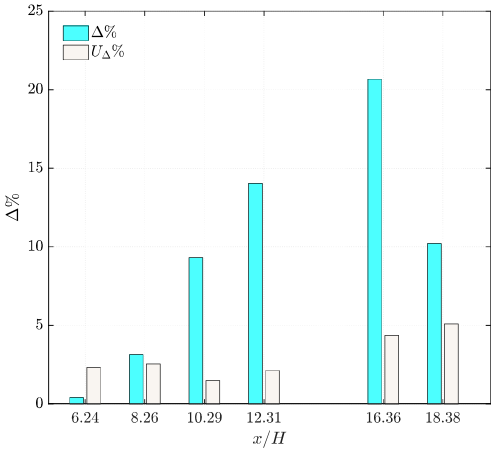

(b) *Bar plot reporting $\Delta\%$ percentage difference distribution of P/P_T between minimum and maximum Z_T conditions Eq. (87) and its uncertainty $U_\Delta\%$ Eq. (89).*

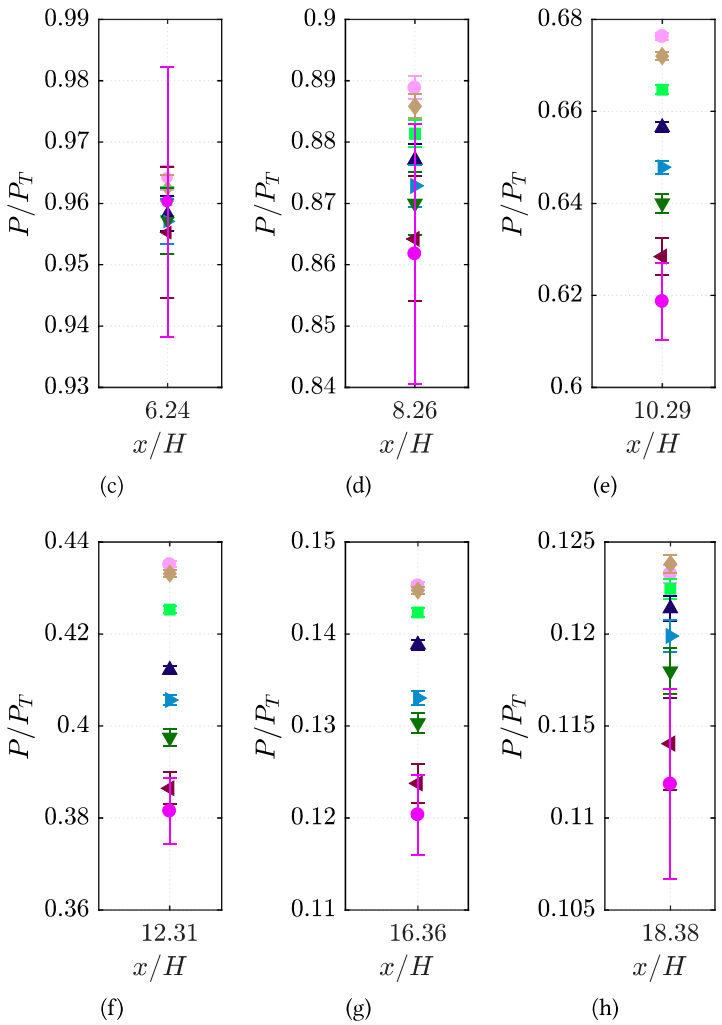

Figure 5.6: Nozzle *M2* at highly non-ideal conditions (test run *10MDM*). (*c*) to (*h*) detail of pressure ratio measured at the different pressure taps along the nozzle axis.

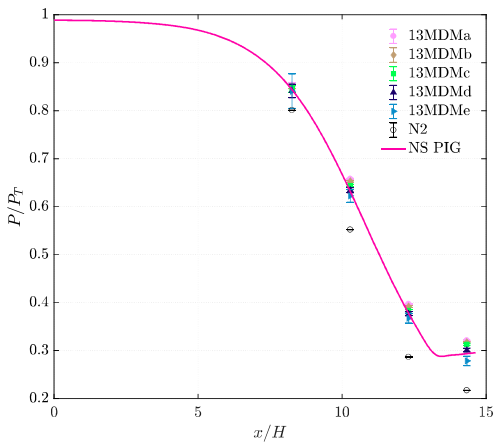

(a) *P/P_T trends along the nozzle axis extracted from test 13MDM (filled colored symbols), P/P_T trends measured in the same nozzle with nitrogen (black not filled circles), P/P_T trends from a CFD viscous calculation coupled with PIG model for MDM (purple line).*

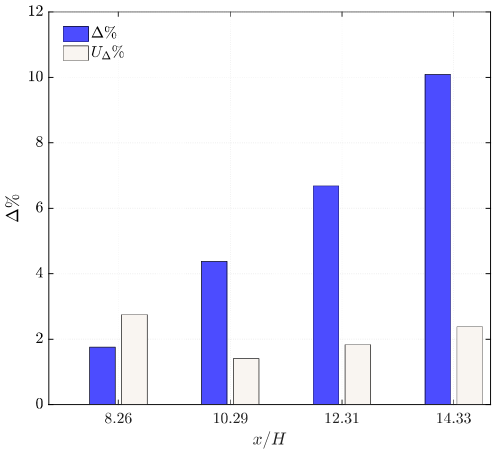

(b) *Bar plot reporting $\Delta\%$ percentage difference distribution of P/P_T between minimum and maximum Z_T conditions Eq. (87) and its uncertainty $U_\Delta\%$ Eq. (89).*

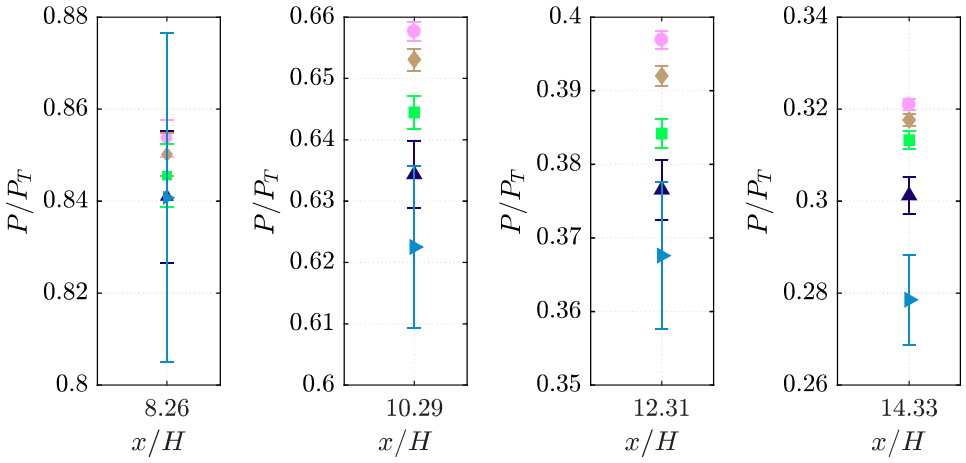

(c) (d) (e) (f)

Figure 5.7: Nozzle *M15* at moderate non-ideal conditions (test run *13MDM*). (*c*) to (*f*) detail of pressure ratio measured at the different pressure taps along the nozzle axis.

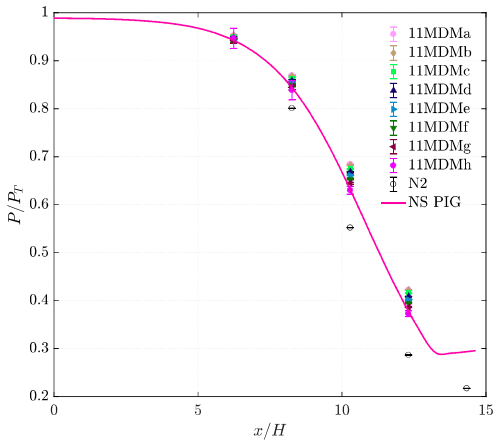

(a) *P/P_T trends along the nozzle axis extracted from test 11MDM (filled colored symbols), P/P_T trends measured in the same nozzle with nitrogen (black not filled circles), P/P_T trends from a CFD viscous calculation coupled with PIG model for MDM (purple line).*

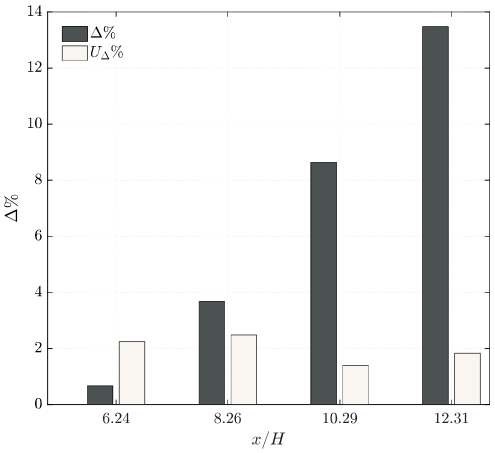

(b) *Bar plot reporting $\Delta\%$ percentage difference distribution of P/P_T between minimum and maximum Z_T conditions Eq. (87) and its uncertainty $U_\Delta\%$ Eq. (89).*

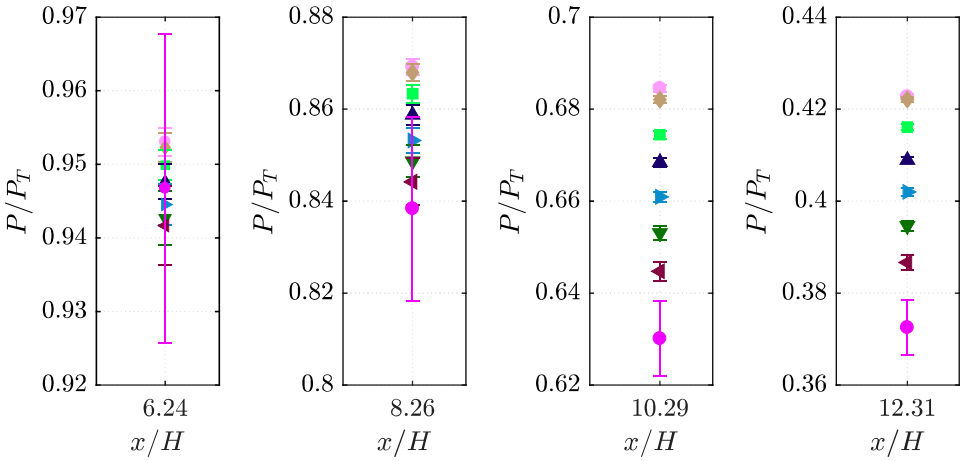

Figure 5.8: Nozzle *M15* at highly non-ideal conditions (test run *11MDM*). (*c*) to (*f*) detail of pressure ratio measured at the different pressure taps along the nozzle axis.

specific heat ratio was set equal to $\gamma = 1.018$, as obtained in the temperature range of interest for the presented experiments, accordingly to (Thol et al., 2017). Consistently, CFD results are well overlapped to data measured at maximum Z_T, namely in the almost ideal gas state.

A first comparison on the pressure ratio distribution along the axis can be made between the nozzles operated with nitrogen and with MDM at maximum Z_T, namely in almost ideal conditions. This allows to point out the effects on the expansion processes due to the different molecular complexity of the two fluids, that is, the different value of the specific heat ratio($\gamma_{MDM} = 1.018$, $\gamma_{N2} = 1.4$). At any axial coordinate the local pressure ratio is higher for MDM, due to its higher molecular complexity. This difference initially increases with the Mach number along the expansion, as compressibility effects start playing a role. The described behavior is consistent with the one predicted by the *quasi-one-dimensional* theory for isentropic expanding flows of perfect gases (Thompson, 1971) and it is not related to non-ideal effects.

To evidence non-ideal compressible flow effects, for each nozzle and operating condition with MDM, the expansion processes occurring at maximum Z_T are compared to those at lower Z_T, up to the minimum value. For all the analyzed cases, the pressure ratio P/P_T along the expansion is higher than the almost ideal-gas one at Z_{Tmax} and increases with increasing departure from ideality, as Z_T decreases. This can be clearly noticed by looking at figures 5.5 from (c) to (j), 5.6 from (c) to (h), 5.7 from (c) to (f) and 5.8 from (c) to (f). They report a detail of the pressure ratio measured at each active pressure tap.

The decreasing trend of pressure ratios with increasing Z_T is ascribed to non-ideal effects and has no relation with measuring accuracy, since the error bars are not overlapping in most cases. This evidence is confirmed by comparing the difference Δ (Eq.(87)), present between the pressure ratios Π measured in correspondence with the minimum and the maximum Z_T, with its uncertainty U_Δ (Eq.(89)).

$$\Delta = \left(\frac{P}{P_T}\right)_{Z_T=Z_T^{min}} - \left(\frac{P}{P_T}\right)_{Z_T=Z_T^{max}} = \Pi(Z_T^{max}) - \Pi(Z_T^{min}) \tag{87}$$

$$U_\Pi = \left(\frac{P}{P_T}\right)\sqrt{\frac{U_P^2}{P^2} + \frac{U_{P_T}^2}{P_T^2}} \tag{88}$$

$$U_\Delta = \sqrt{U_{\Pi(Z_T^{max})}^2 + U_{\Pi(Z_T^{min})}^2} \tag{89}$$

Both quantities are reported in figures 5.5b, 5.6b, 5.7b and 5.8b as a percentage difference with respect to $\Pi(Z_T^{min})$ representing the ideal-gas value.

$$\Delta\% = \frac{\Delta}{\Pi(Z_T^{min})} \cdot 100 \tag{90}$$

$$U_\Delta\% = \frac{100}{\Pi(Z_T^{min})} \cdot \sqrt{U_{\Pi(Z_T^{max})}^2 + \left(\frac{\Pi(Z_T^{max}}{\Pi(Z_T^{min}}\right)^2 \cdot U_{\Pi(Z_T^{min})}^2} \tag{91}$$

The opposite trend of increasing pressure ratio with decreasing Z_T is confirmed since U_Δ is well lower than Δ. However there are few exceptions in the initial converging portion

of the nozzle. Indeed, figures 5.5c, 5.5d, 5.6c, referred to nozzle *M2*, and figures 5.7c, 5.8c, 5.8d, referred to nozzle *M15*, show that at low x/H the uncertainty bars of the pressure ratio measured at different Z_T overlap. These coordinates are those showing $U_\Delta\% > \Delta\%$. In the initial converging region, higher full scale/uncertainty transducers are located; as a consequence, a higher uncertainty is obtained for pressure ratios, especially in the dilute gas state where the level of measured pressure is considerably low. Moreover, the initial part of the expansion features pressure ratios which are close to one and non-ideal compressible effects of different intensity are almost indistinguishable.
In the last part of the diverging region of nozzle *M2* (Fig.s 5.6h) the trend of increasing pressure ratio with decreasing Z_T is still well distinguishable. However the error bars related to the measurements performed are overlapping, this is mainly due to the fact that here the pressure ratio is low so the relative uncertainty is high. Moreover, the local compressibility factor is approaching unity and the flow is not expanding anymore thus, the non-ideal compressible effects are diminishing. These considerations are also pointed out by the values of $\Delta\%$ and $U_\Delta\%$ whose difference reduces at this specific tap.
Summarizing, for a given fluid and nozzle geometry, a dependence of the pressure ratio on the inlet stagnation conditions is documented here for the first time, which proves the non-ideal nature of the flow in all the analyzed cases. Indeed, this is consistent with the non-ideal behavior of quasi-one-dimensional isentropic expansions predicted by (Colonna et al., 2008b). The described trend of pressure ratio measured is qualitatively in agreement with the one predicted by the Van der Waals model applied to a quasi-one-dimensional nozzle expansion of MDM vapor.
The dependence of the flow field on the inlet conditions is found to be not negligible, for both cases of moderate and high deviations from the ideal-gas state. For example, at the geometrical throat, the deviation Δ of P/P_T with respect to the one obtained at Z_{Tmax} is of about 5.6% for $Z_T = 0.81$ (test 13MDM, Fig. 5.7b), and of about 8.7% for $Z_T = 0.63$ (test 11MDM, Fig. 5.8b).

5.2.1 *Comparison between experimental and CFD data*

The experimental results presented above were used to perform the first ever assessment of a CFD software for Non-Ideal Compressible-Fluid Dynamics flows of interest for ORC applications (Gori et al., 2017). Simulations of the most non-ideal (04MDMa, 10MDMa, 13MDMa and 11MDMa) and of the most ideal (04MDMe, 10MDMh, 13MDMe and 11MDMh) nozzle flows have been carried out. The CFD code used here is the SU2 suite (Vitale et al., 2015) coupled with thermodynamic and transport models implemented in RefProp (Thol et al., 2017).
The computational domain considered is $2D$ and limited to the converging and the diverging sections of the nozzle. The conditions of the fluid at the inlet boundary reproduce the total condition measured experimentally within the settling chamber. No boundary

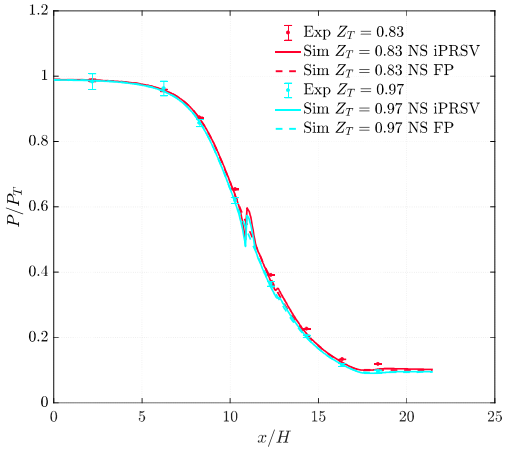

(a) *Pressure profiles of 04MDMa (red symbols) and of 04MDMe (light blue symbols). Measured data (symbols) are plotted together simulated ones (solid lines and dashed lines).*

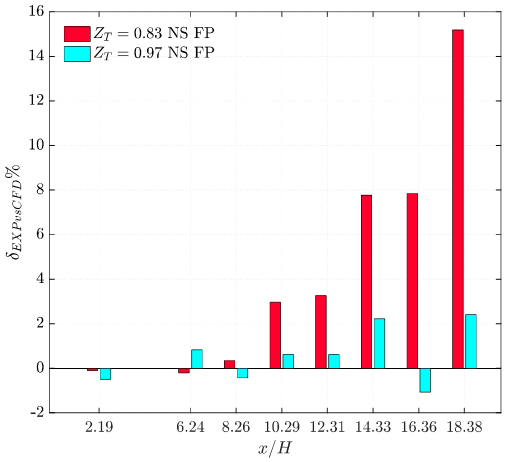

(b) *Percentage discrepancies between measured and simulated pressure ratios (Eq. (92)) for the most non-ideal (red bar) and the most ideal (light blue bar) conditions of test 04MDM.*

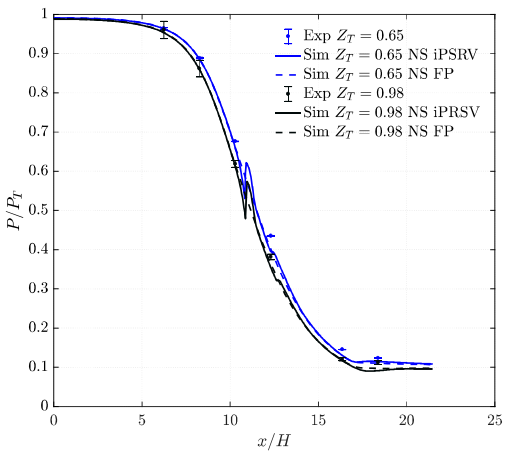

(c) *Pressure profiles from 10MDM4a (blue symbols) and 10MDMh (black symbols). Measured data (symbols) are plotted together simulated ones (solid lines and dashed lines).*

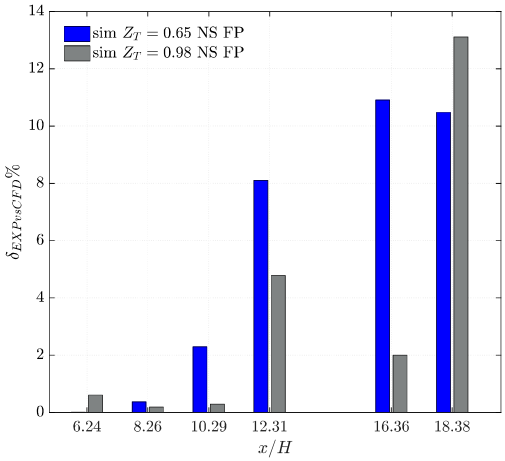

(d) *Percentage discrepancies between measured and simulated pressure ratios (Eq. (92)) for the most non-ideal (blue bar) and the most ideal (black bar) conditions of test 10MDM*

Figure 5.9: Nozzle *M2*: Comparison between CFD simulated and measured data.

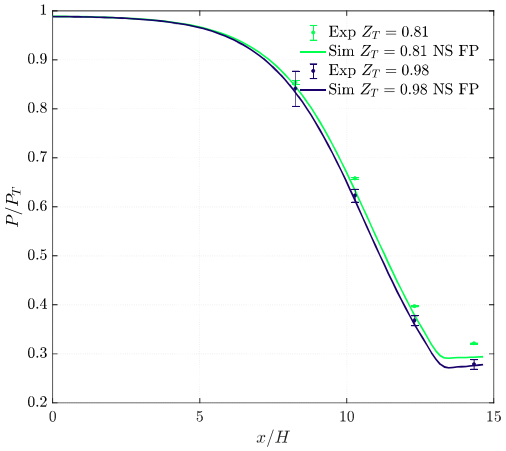

(a) *Pressure profiles of 13MDM4a (green symbols) and of 13MDMe (deep purple symbols). Measured data (symbols) are plotted together simulated ones (solid lines and dashed lines).*

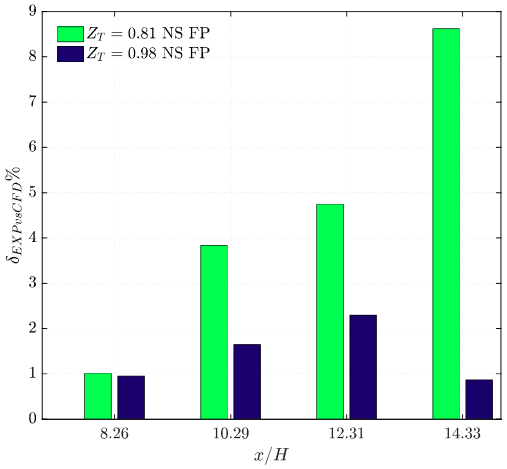

(b) *Percentage discrepancies between measured and simulated pressure ratios (Eq. (92)) for the most non-ideal (green bar) and the most ideal (deep purple bar) conditions of test 13MDM*

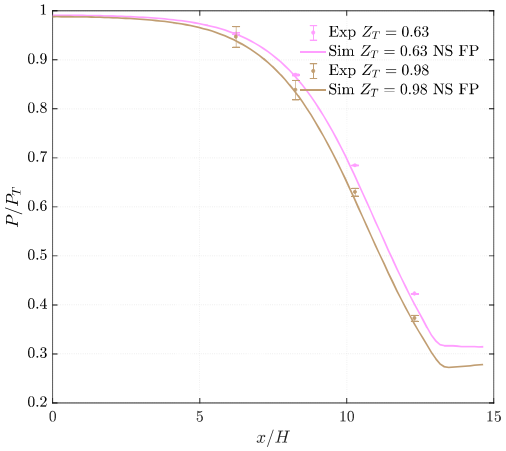

(c) *Pressure profiles from 11MDM4a (pink symbols) and 11MDMh (brown symbols). Measured data (symbols) are plotted together simulated ones (solid lines and dashed lines).*

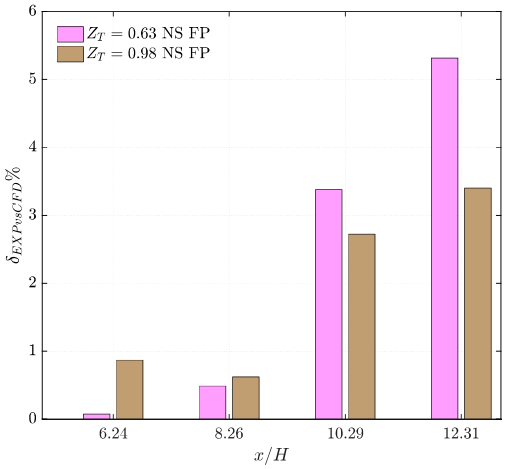

(d) *Percentage discrepancies between measured and simulated pressure ratios (Eq. (92)) for the most non-ideal (pink bar) and the most ideal (brown bar) conditions of test 11MDM*

Figure 5.10: Nozzle *M15*: Comparison between CFD simulated and measured data.

condition is required at the exit section due to the supersonic character of the flow. Numerical simulations were first carried out using different levels of grid resolution to evaluate the dependency of the solution on the spatial discretization. The turbulence model adopted was the $k-\omega$ SST.

Figures 5.9 and 5.10 report a comparison between the measured and the computed pressure ratios along the two nozzle axis. The figures 5.9a and 5.9c referring to nozzle *M2* report two different CFD simulation results for both conditions Z_{Tmin} and Z_{Tmax}. Indeed, two simulations were carried out: one considering the presence of the step at the throat (solid lines) and the other considering a clean nozzle geometry (dashed lines). The presence of the step produce the complex flow structures already explained in sections 4.2.1 and previously in section 2.4.1.3. In order reproduce these structures with a CFD calculation, it is necessary to have finer meshes and to perform a local grid refinement using a grid adaptation method. This slows down the calculation and it was thus decided not to couple it with the Span-Wagner model of (Thol et al., 2017) but with the simpler and hard coded iPRSV thermodynamic model instead. This consistently speeds up the computation without affecting significantly the results obtained. A thorough comparison between CFD calculation made adopting different equation of states is carried out in (Zocca, 2018) and it confirms the suitability of iPRSV model in this contest.

Figures 5.9a and 5.9c show clearly that the bigger differences between the simulations with and without the step are concentrated in the close proximity of the throat ($x/H = 10.29$) where a visible bump in the pressure ratio profile is located. The pressure ratio first decreases because of the presence of an expansion fan at the edge of the step and then suddenly increases through the shock wave that is formed at the reattachment point. Another expansion fan brings the pressure ratio profile to superimpose again to the one that would have been obtained without the presence of the step. Another bump is located downstream at around $x/H = 12.7$ where the first reflection of the shock crosses the nozzle axis.

It can be noticed that the dashed profiles and the solid ones in figures 5.9a and 5.9c depart from each other only locally in correspondence of the two bumps. Indeed, it was proved by (Zocca et al., 2018) that the shock waves originated are so weak that the flow can be still considered isentropic. The CFD simulation obtained neglecting the presence of the step is equivalent to the one considering it in all the axial coordinate where static pressures are measured. For this reason all further considerations are made using the data obtained from simulations not considering the step in the nozzle geometry.

Figures 5.9b, 5.9d, 5.10b and 5.10d report the percentage discrepancy existing between the simulated and the measured data (Eq.(92)).

$$\delta_{CFDvsExp}\% = \left[\frac{\left(\frac{P}{P_T}\right)_{exp} - \left(\frac{P}{P_T}\right)_{CFD}}{\left(\frac{P}{P_T}\right)_{exp}} \right] \cdot 100 \tag{92}$$

The accordance between the two set of data is almost perfect for all the axial coordinate placed before the throat. At the geometrical throat x/H = 10.29 the percentage deviation increases even though it is always below 5%; it can also be noticed that, for the most non-ideal conditions simulated, the increasing trend of the percentage deviation continue up to the last axial coordinate analyzed. Moreover, the discrepancy, between the simulated and the measured data, is bigger for the most non-ideal conditions considered with the only exception of the axial coordinate x/H = 18.38 in nozzle *M2* at condition 10MDMh (Fig. 5.9d).
Therefore, it can be concluded that, when almost ideal conditions are considered (Z_T = 0.97 ÷ 0.98), the accordance between the simulations and the experiments is perfect given that the discrepancies are almost always below 5%. Nevertheless, the same is not true when the most non-ideal conditions are considered (Z_T = 0.63 ÷ 0.81). Deviations are not negligible, especially in proximity of nozzle exit where they can be as high as 10% (Fig.s 5.9b, 5.9d). These are the location where the boundary layer plays the major role since it is increasing going towards the nozzle exit. The turbulence model used is not specifically calibrated for non-ideal compressible flows so it can underestimate the boundary layer thickness when non-ideal effects come to play a preponderant role. Moreover, the thermodynamic model itself ((Thol et al., 2017)) is more accurate in dilute conditions and this can contribute to increase the discrepancies between simulated and measured results going from more ideal towards more non-ideal flow conditions.
It can be concluded that still some work has to be done in order to achieve a better agreement between simulations and experiments in non-ideal compressible flows. In particular new measurements leading towards more accurate thermodynamic models are needed, especially in the region close to the critical point, (Merle and Cinnella, 2015). Moreover, many authors are focusing on obtaining better calibrated turbulence models suitable for simulating such flows (Giauque et al., 2017; Sciacovelli et al., 2018; Sciacovelli et al., 2017b; Sciacovelli et al., 2017a; Nemati et al., 2015).

5.3 SCHLIEREN IMAGES AND MACH NUMBER MEASUREMENTS

Schlieren images of all the nozzle flows listed in Table 5.2 were extracted; they are reported in figures 5.11, 5.12 and 5.13. The images taken from test 04MDM result brighter than the others. This test was one of the first ever performed with an organic fluid. The back plate was still perfectly mirror polished and no sign of oxidation was present. As the experimental campaign proceeded the mirror on the back plate became more opaque and the resulting images were less bright.
The throat region is in general brighter going from the upper to the lower reported images. This is due to the fact that the upper images are characterized by higher total pressure and higher non-ideal effects and, thus, by more severe measuring range issues (see Sec. 2.4.1.3). In particular, conditions 10MDMa Fig. 5.12a, 10MDMb Fig. 5.12c, 10MDMc Fig. 5.12e, 11MDMa Fig. 5.12b, 11MDMb Fig. 5.12d and 11MDMc Fig. 5.12f present a throat

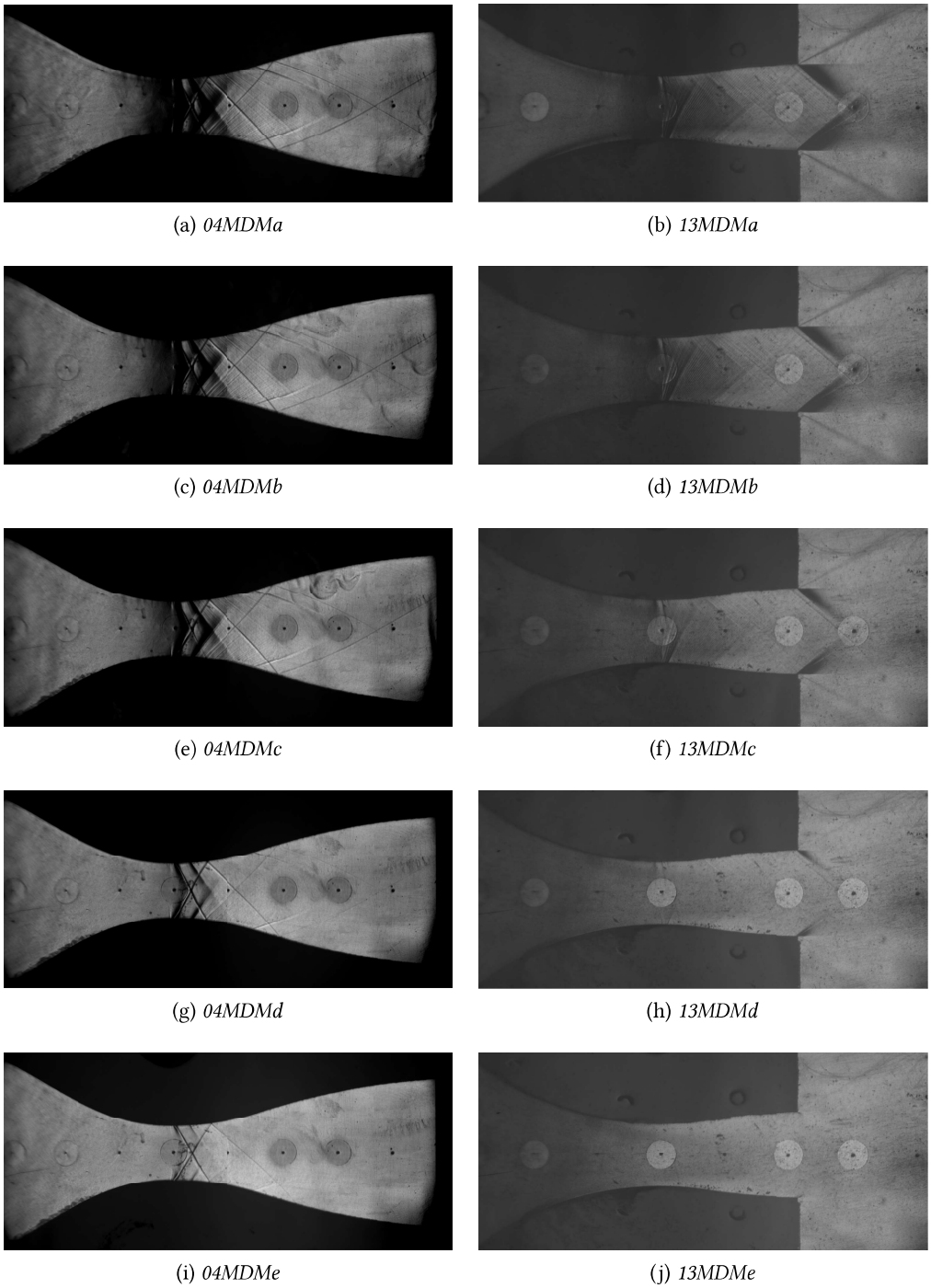

(a) *04MDMa* (b) *13MDMa*

(c) *04MDMb* (d) *13MDMb*

(e) *04MDMc* (f) *13MDMc*

(g) *04MDMd* (h) *13MDMd*

(i) *04MDMe* (j) *13MDMe*

Figure 5.11: Schlieren images extracted from tests 04MDM and 13MDM. Conditions *a* to *e* listed in Tab. 5.2

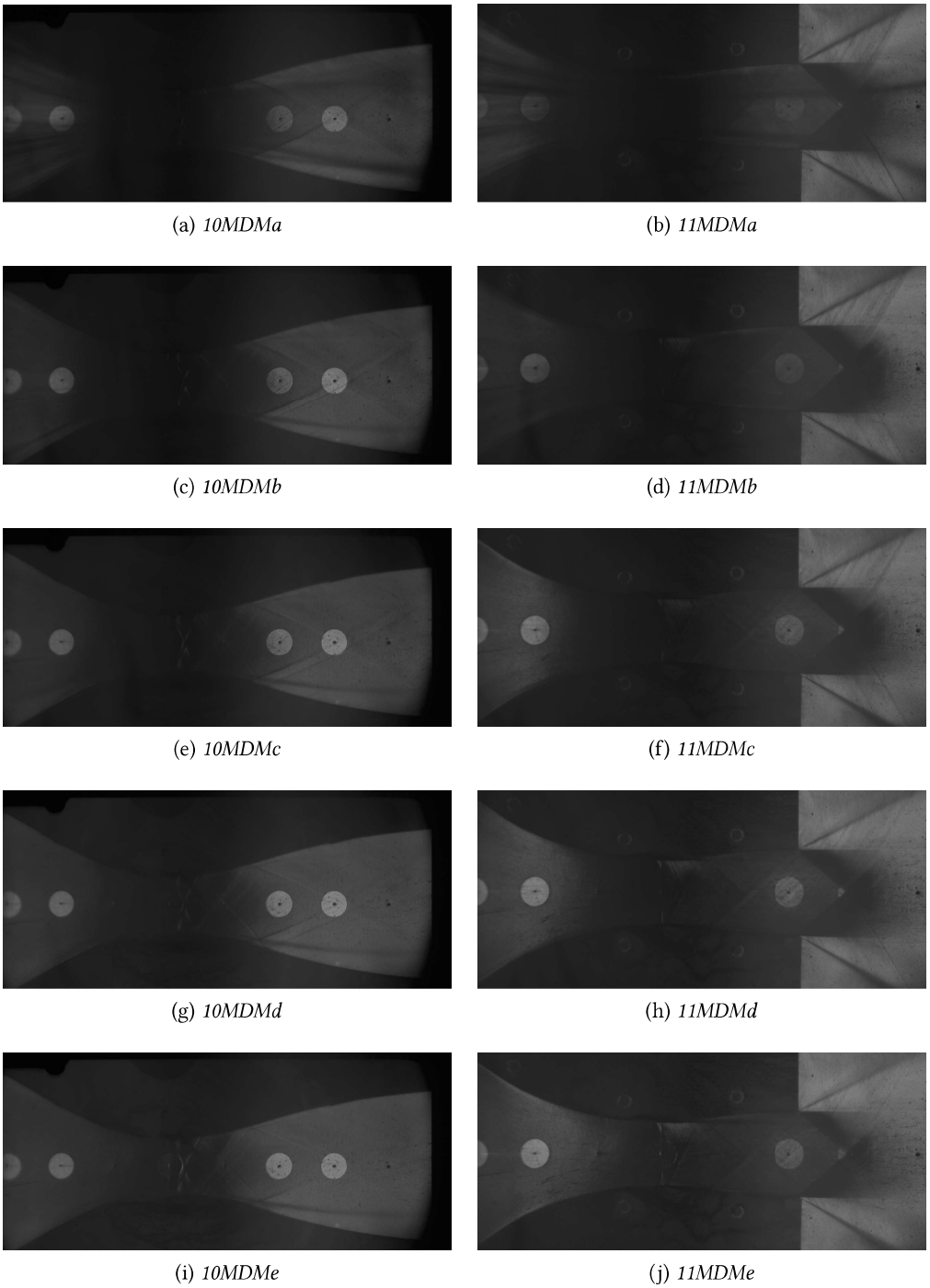

(a) *10MDMa* (b) *11MDMa*

(c) *10MDMb* (d) *11MDMb*

(e) *10MDMc* (f) *11MDMc*

(g) *10MDMd* (h) *11MDMd*

(i) *10MDMe* (j) *11MDMe*

Figure 5.12: Schlieren images extracted from tests 10MDM and 11MDM. Conditions *a* to *e* listed in Tab. 5.2

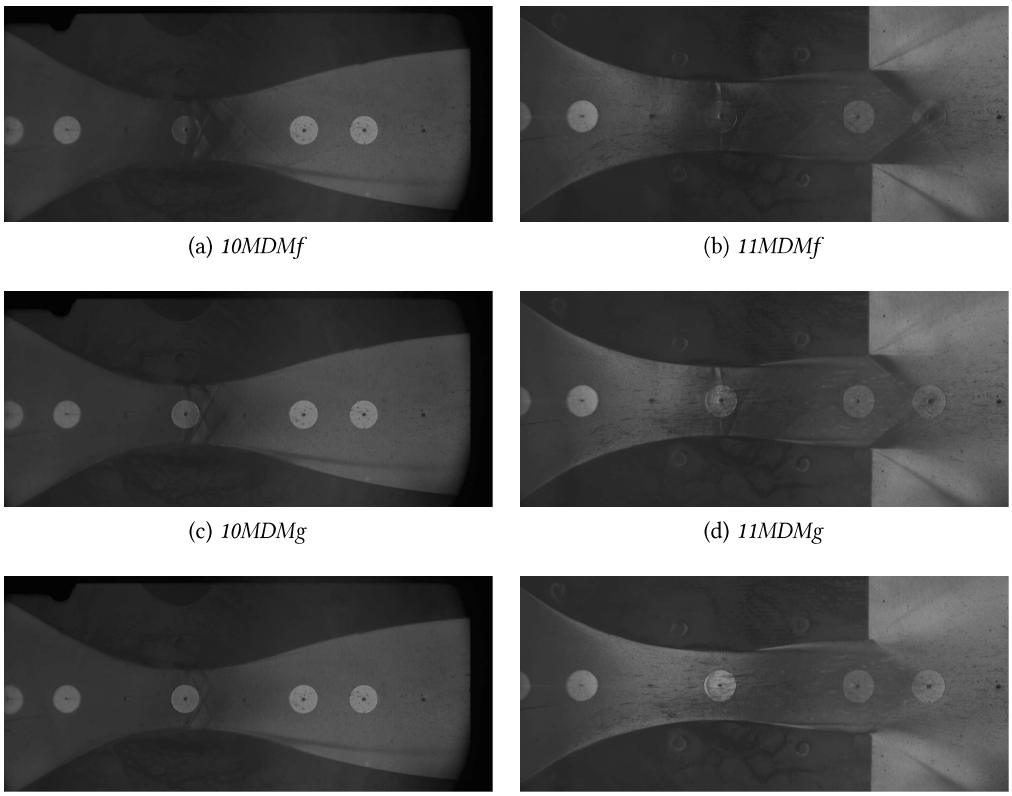

(a) *10MDMf* (b) *11MDMf*

(c) *10MDMg* (d) *11MDMg*

(e) *10MDMh* (f) *11MDMh*

Figure 5.13: Schlieren images extracted from tests 10MDM and 11MDM. Conditions f to h listed in Tab. 5.2

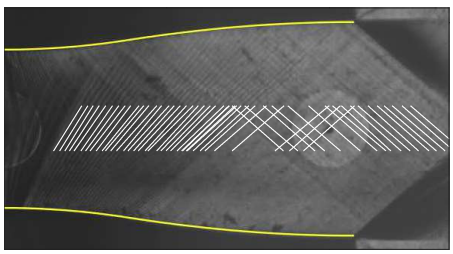

(a) *13MDMa*

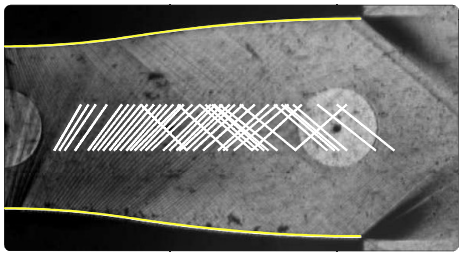

(b) *13MDMc*

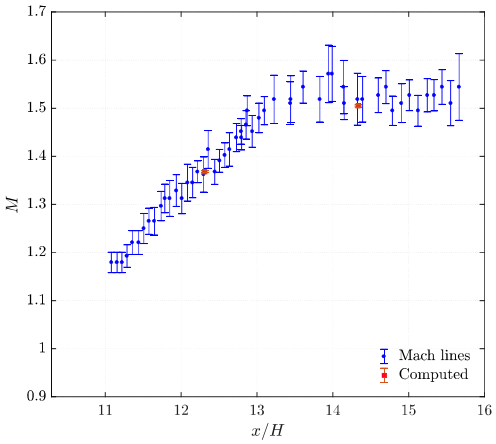

(c) *13MDMa*

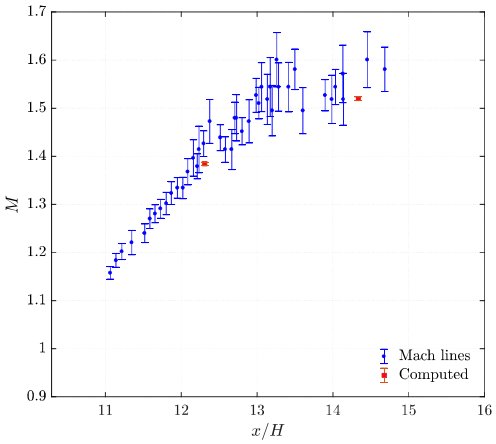

(d) *13MDMc*

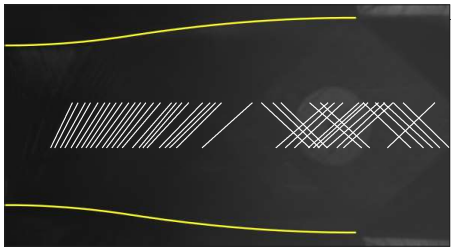

(e) *11MDMb*

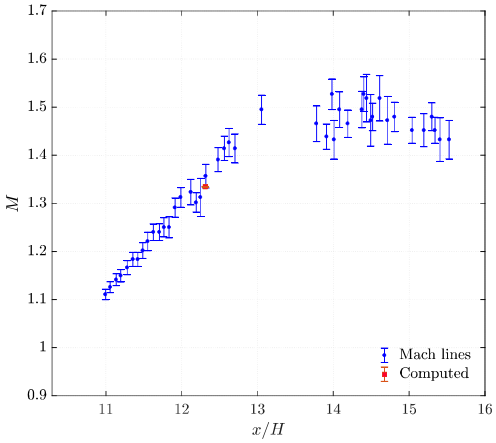

(f) *11MDMb*

Figure 5.14: Schlieren images (*a*), (*b*), (*e*) with extracted Mach lines and Mach number distribution along the nozzle axis (*c*), (*d*) and (*f*). Mach numbers measured through the slope of Mach waves (blue dots) are plotted together with the one computed from the static pressures measured and total conditions (red square).

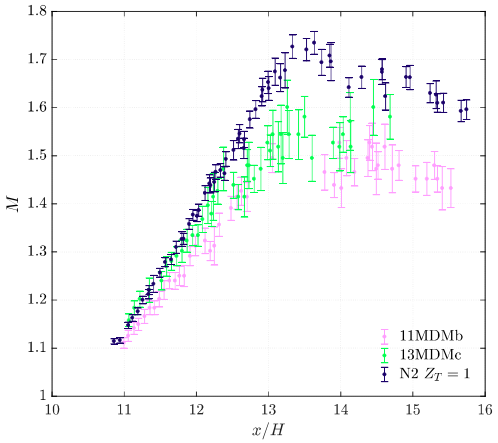

Figure 5.15: Comparison between measured Mach number distributions for test 11MDMb at $Z_T = 0.65$ (pink dots), test 13MDMc at $Z_T = 0.9$ (green dots) and test 14N2 with nitrogen ($Z_T = 1$) (deep purple dots).

region that is almost completely dark. Indeed, they belong to the highly non ideal test runs.

The complex flow structures developed at the throat are visible in all the schlieren images obtained with nozzle *M2* (left side of figures 5.11, 5.12 and 5.13). However, both shock and expansion fans appear dark in most of the images because of the measuring range issues. The fans become brighter in the most dilute condition analyzed: 04MDMd Fig. 5.11g, 04MDMe Fig. 5.11i, 10MDMg Fig. 5.13c and 10MDMh Fig. 5.13e.

The detection of Mach waves in nozzle *M2* is prevented by the presence of the shock and of its reflections and by the low roughness at the walls. Mach waves are instead well visible in some of the images obtained for nozzle *M15*, in particular in images 5.11b, 5.11d, 5.11f, 5.12d, 5.12f, 5.12h, 5.12j, and 5.13b. Unfortunately, images 5.11h, 5.11j, 5.13d and 5.13f are characterized by too dilute conditions and their low total pressure makes the refractive index gradient related to the Mach waves too low to be detectable by the optical apparatus used. On the other side, Figure 5.12b is affected too much by the measuring range issues related to the high total pressure characterizing 11MDMa nozzle flow.

Therefore the algorithm presented in section 2.4.2 was applied to figures 5.11b, 5.11f and 5.12d corresponding to conditions 13MDMa $Z_T = 0.81$, 13MDMc $Z_T = 0.9$ and 11MDMb $Z_T = 0.65$. The algorithm was applied to a rectangle cut around the nozzle axis and going from the geometrical throat to the end of the nozzle. By virtue of symmetry, the flow velocity at the centerline is parallel to the axis, and the angle between the Mach wave and the velocity is simply the wave slope with respect to the axis (see Eq. (49)). This makes the detection of Mach lines from schlieren image a powerful method to obtain a direct measurement of the local Mach number.

Figures 5.14c, 5.14d and 5.14f report the measured Mach number trend together with the corresponding uncertainty bars. As clearly pointed out in section 2.4.2.5, the uncertainty

U_M of Mach measurement increases with Mach number, given the angular uncertainty U_α , which is related to the sub-image dimension and to the camera resolution. Indeed, the uncertainty propagated to Mach number reads as follows:

$$U_M = M\sqrt{M^2 - 1}U_\alpha \tag{93}$$

where the term $M\sqrt{M^2 - 1}$ increases almost quadratically with Mach number above $M \approx 1.2$. Therefore, the increased uncertainty is due to the dependence of the Mach number on the Mach line slope α , through the inverse sine function ($M = 1/sin(\alpha)$). At small supersonic Mach numbers α is close to 90° and the function sin^{-1} is almost insensitive to angular variation related to uncertainty; conversely, its sensitivity to angular changes increases with Mach number especially at high M where the trend is strongly non-linear. This entails an increasing uncertainty, in particular above $M = 1.5$.
In figures 5.14c, 5.14d and 5.14f a comparison is also given between the measured Mach number and those calculated using pressure and temperature measurements $M = M(P, s(P_T, T_T))$, through the RefProp model. Results are in good accordance thus confirming the accuracy of the thermodynamic model employed.
Figure 5.15 contains a comparison between the local Mach number measured at the nozzle axis for 11MDMb $Z_T = 0.65$ and for 13MDMc $Z_T = 0.90$. These values were chosen as the minimum and the maximum total compressibility factors at which schlieren images quality is good enough to allow the detection of Mach lines. The comparison shows that as the non-ideal effects increase, the Mach value decreases. Although, a partial overlap of uncertainty bars is present, especially at the expansion end the trend is clearly visible, in particular, within the region of higher gradients, up to $M \approx 1.55$. This represents a further proof of the dependence of the nozzle flow field on the stagnation conditions, for a given geometry and working fluid.
Figure 5.15 contains also the Mach profile measured using nitrogen as working fluid in the same nozzle *M15* (see Sec. 4.3.2). Since nitrogen can be considered as a PIG, the profile of Mach on the nozzle axis is not influenced by the total conditions. Thus, the data reported are representative of any nitrogen nozzle flow for this given geometry. As expected, because of the different molecular complexity of the two fluids, the profile obtained with nitrogen is higher than any profile obtained with MDM. The discrepancy grows going towards the nozzle exit; this is due by the fact that at the throat $M \longrightarrow 1$ regardless of the operating fluid. However, this discrepancy affects significantly the exit Mach number, thus, to design a nozzle to reach a specific Mach at the exit the operating fluid should be taken into account as reported in (Spinelli et al., 2011).

5.4 SPEED OF SOUND

The speed of sound along the nozzle axis can be calculated from the measured total conditions and static pressure by following the isentropic hypothesis as explained in section 4.3. This calculation requires to use a thermodynamic model, which, here, was

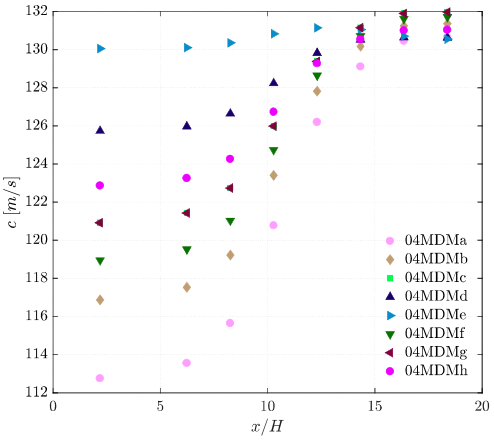

(a) *Nozzle M2, test 04MDM: profiles of speed of sound.*

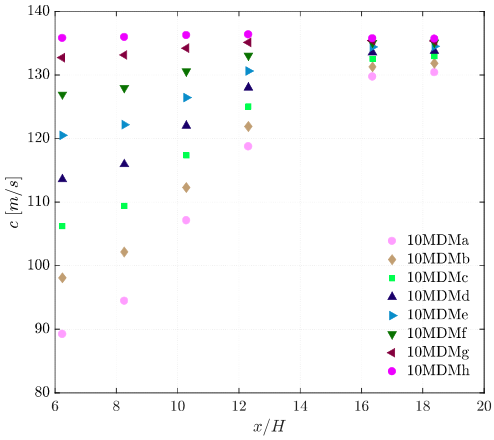

(b) *Nozzle M15, test 10MDM: profiles of speed of sound.*

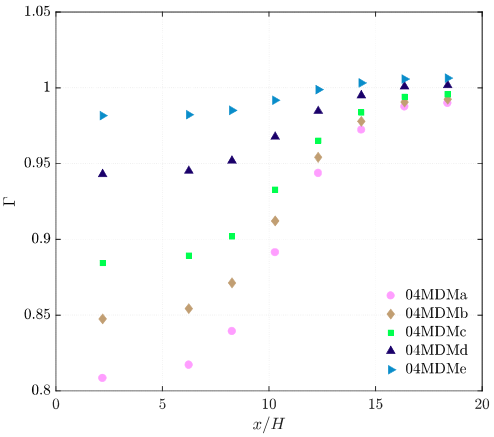

(c) *Nozzle M2, test 04MDM: profiles of fundamental derivative of gas-dynamic.*

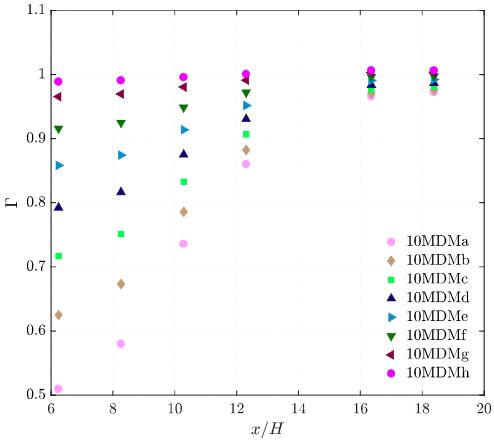

(d) *Nozzle M2, test 10MDM: profiles of fundamental derivative of gas-dynamic.*

Figure 5.16: Nozzle *M2*. Speed of sound and Γ distributions along the nozzle axis for the flows analyzed in the previous sections.

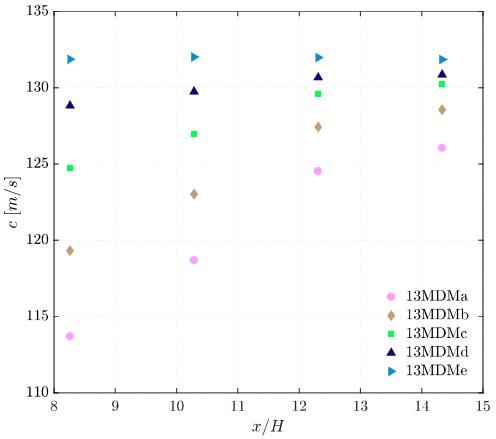

(a) *Nozzle M15, test 13MDM: profiles of speed of sound.*

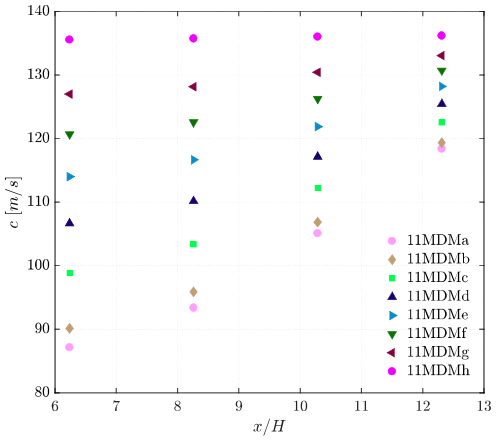

(b) *Nozzle M15, test 11MDM: profiles of speed of sound.*

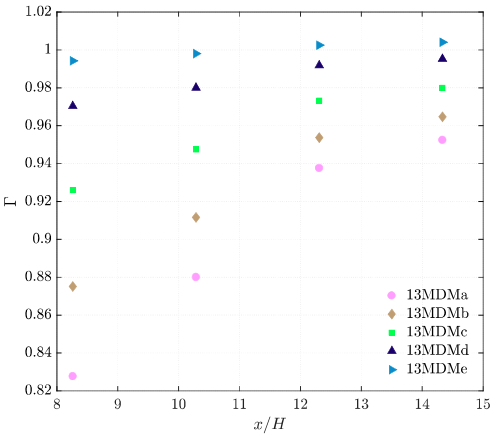

(c) *Nozzle M15, test 13MDM: profiles of fundamental derivative of gas-dynamic.*

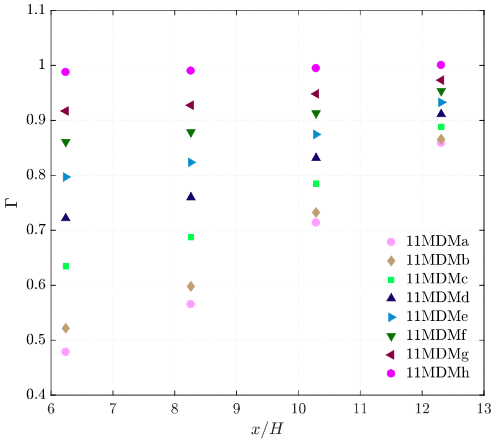

(d) *Nozzle M15, test 11MDM: profiles of fundamental derivative of gas-dynamic.*

Figure 5.17: Nozzle *M15*. Speed of sound and Γ distributions along the nozzle axis for the flows analyzed in the previous sections.

the one presented by (Thol et al., 2017) and coded in RefProp.
The calculated profiles of speed of sound are plotted in figures 5.16a, 5.16b, 5.17a and 5.17b for tests 04MDM, 10MDM, 13MDM and 11MDM respectively. It can be noticed that, all the nozzle flows analyzed present an increasing speed of sound along the axis up to $x/H = 13$. The growth is stronger in the flows characterized by the most non ideal total conditions, thus the one marked with the first letters of the alphabet; from *a* to *c* for the moderately non-ideal tests 04MDM and 13MDM, from *a* to *f* for the highly non-ideal tests 10MDM and 11MDM.
The increasing of *c* along an isentropic expansion is one of the peculiar non-ideal effects predicted by the *quasi-one-dimensional* nozzle theory explained in section 3.2.1. It occurs only if the fundamental derivative of gas-dynamic Γ is lower than one and this is confirmed by figures 5.16c, 5.16d, 5.17c and 5.17d that show the evolution of Γ along the nozzle axis. Γ increases going towards the nozzle exit as pressure and temperature decrease and the conditions become more dilute. Moreover the highly-non ideal tests (10MDM Fig. 5.16d, 11MDM Fig. 5.17d) present flows characterized by lower values of Γ that are as low as $\Gamma = 0.5$. The last conditions extracted from each test show $\Gamma \approx 1$ and its value go beyond one in the last axial locations $x/H > 13$.
To conclude, the calculated speed of sound show an increasing trend along the isentropic expansion for most of the condition analyzed. This trend is supported by a calculated $\Gamma < 1$ and it proves that the nozzle flows analyzed are non-ideal.

6 MM VAPOR EXPANSION CAMPAIGN

This chapter presents the experimental campaign conducted with siloxane fluid MM. Nozzles *M15* and *M16* were tested in a wide range of inlet conditions in order to explore systematically the thermodynamic region included between the vapor saturation curve and the critical temperature. Conditions ranged from highly non-ideal to almost ideal gas conditions, with a compressibility factor evaluated at total conditions (*total compressibility factor*, Z_T) ranging between 0.57 and 0.98.
Results from the present experimental campaign allowed to verify that nozzle expansion is influenced by total inlet conditions because of the non-ideal nature of the flow (section 6.2). Moreover, sections 6.3.1 and 6.3.2 respectively discuss if either the total compressibility factor alone or the total fundamental derivative of gas-dynamic alone are sufficient to assess the level of non-ideality of a nozzle flow and thus, to characterize the expansion flow and predict pressure ratio profiles. The effect of total temperature was isolated and analyzed in depth in section 6.3.3. Finally, the results obtained with nozzle *M15* were compared with those obtained with siloxane fluid MDM in section 6.4. It was thus possible to carry out a comparison between two different organic vapors flowing in the same nozzle and sharing the same total reduced conditions.

6.1 CONSISTENCY AND REPETABILITY ASSESSMENT

Test ID	Nozzle	Most non-ideal condition $P_T\ [bar]\ ;\ T_T\ [^\circ C]$	Least non-ideal condition $P_T\ [bar]\ ;\ T_T\ [^\circ C]$
14MM	*M15*	$P_T = 12.19 \pm 0.01$ $T_T = 223.3 \pm 0.8$ $Z_T = 0.64$	$P_T = 2.31 \pm 0.01$ $T_T = 221.7 \pm 0.8$ $Z_T = 0.95$
15MM	*M15*	$P_T = 10.70 \pm 0.01$ $T_T = 218.0 \pm 0.8$ $Z_T = 0.69$	$P_T = 2.11 \pm 0.01$ $T_T = 215.5 \pm 0.8$ $Z_T = 0.95$
16MM	*M15*	$P_T = 11.86 \pm 0.01$ $T_T = 223.4 \pm 0.8$	$P_T = 2.11 \pm 0.01$ $T_T = 222.6 \pm 0.8$

Continued from previous page

Test ID	Nozzle	Most non-ideal condition $P_T\ [bar]\ ;\ T_T\ [^\circ C]$	Least non-ideal condition $P_T\ [bar]\ ;\ T_T\ [^\circ C]$
		$Z_T = 0.66$	$Z_T = 0.95$
17MM	*M15*	$P_T = 10.50 \pm 0.01$ $T_T = 217.2 \pm 0.8$ $Z_T = 0.69$	$P_T = 1.70 \pm 0.01$ $T_T = 210.9 \pm 0.8$ $Z_T = 0.96$
18MM	*M15*	$P_T = 10.91 \pm 0.01$ $T_T = 228.1 \pm 0.8$ $Z_T = 0.72$	$P_T = 1.73 \pm 0.01$ $T_T = 223.9 \pm 0.8$ $Z_T = 0.96$
19MM	*M15*	$P_T = 7.39 \pm 0.01$ $T_T = 193.8 \pm 0.8$ $Z_T = 0.76$	$P_T = 1.43 \pm 0.01$ $T_T = 195.9 \pm 0.8$ $Z_T = 0.96$
20MM	*M15*	$P_T = 11.74 \pm 0.01$ $T_T = 227.7 \pm 0.8$ $Z_T = 0.68$	$P_T = 2.09 \pm 0.01$ $T_T = 220.8 \pm 0.8$ $Z_T = 0.95$
26MM	*M15*	$P_T = 8.13 \pm 0.01$ $T_T = 213.3 \pm 0.8$ $Z_T = 0.77$	$P_T = 0.73 \pm 0.01$ $T_T = 207.3 \pm 0.8$ $Z_T = 0.98$
38MM	*M15*	$P_T = 7.35 \pm 0.01$ $T_T = 204.3 \pm 0.8$ $Z_T = 0.78$	$P_T = 0.73 \pm 0.01$ $T_T = 201.6 \pm 0.8$ $Z_T = 0.98$

Table 6.1: List of the test runs belonging to the *MM vapor expansion campaign* concerning nozzle *M15*. Each test run is composed by several different steady states characterized by different total conditions going from the initial to the final one that are here reported.

Test ID	Nozzle	Most non-ideal condition $P_T\ [bar]\ ;\ T_T\ [^\circ C]$	Least non-ideal condition $P_T\ [bar]\ ;\ T_T\ [^\circ C]$
21MM	*M16*	$P_T = 10.58 \pm 0.02$ $T_T = 222.1 pm 1.5$ $Z_T = 0.71$	$P_T = 0.84 \pm 0.02$ $T_T = 215.5 \pm 1.5$ $Z_T = 0.98$
26MM	*M16*	$P_T = 10.61 \pm 0.02$ $T_T = 226.1 \pm 0.8$ $Z_T = 0.72$	$P_T = 0.83 \pm 0.02$ $T_T = 217.9 \pm 0.8$ $Z_T = 0.98$
27MM	*M16*	$P_T = 8.10 \pm 0.02$ $T_T = 198.5 \pm 0.8$ $Z_T = 0.74$	$P_T = 0.67 \pm 0.02$ $T_T = 203.6 \pm 0.8$ $Z_T = 0.98$
28MM	*M16*	$P_T = 8.37 \pm 0.02$ $T_T = 200.8 \pm 0.8$ $Z_T = 0.73$	$P_T = 0.73 pm 0.02$ $T_T = 204.4 \pm 0.8$ $Z_T = 0.98$
29MM	*M16*	$P_T = 6.127 \pm 0.03$ $T_T = 183.6 \pm 0.8$ $Z_T = 0.786$	$P_T = 0.865 \pm 0.03$ $T_T = 194.1 \pm 0.8$ $Z_T = 0.977$
30MM	*M16*	$P_T = 7.80 \pm 0.02$ $T_T = 206.8 \pm 0.8$ $Z_T = 0.77$	$P_T = 0.57 \pm 0.02$ $T_T = 202.9 \pm 0.8$ $Z_T = 0.99$
31MM	*M16*	$P_T = 6.27 \pm 0.02$ $T_T = 185.3 \pm 0.8$ $Z_T = 0.78$	$P_T = 0.65 \pm 0.02$ $T_T = 193.49 \pm 0.8$ $Z_T = 0.98$
32MM	*M16*	$P_T = 11.21 \pm 0.02$ $T_T = 232.1 \pm 0.8$ $Z_T = 0.72$	$P_T = 0.84 \pm 0.02$ $T_T = 220.8 \pm 0.8$ $Z_T = 0.98$
33MM	*M16*	$P_T = 12.29 \pm 0.04$ $T_T = 234.5 \pm 0.8$ $Z_T = 0.69$	$P_T = 1.61 \pm 0.04$ $T_T = 221.7 \pm 0.8$ $Z_T = 0.96$

Continued from previous page

Test ID	Nozzle	Beginning total condition $P_T\ [bar]\ ;\ T_T\ [^\circ C]$	End total condition $P_T\ [bar]\ ;\ T_T\ [^\circ C]$
34MM	*M16*	$P_T = 18.94 \pm 0.02$ $T_T = 255.4 \pm 0.8$ $Z_T = 0.54$	$P_T = 2.14 \pm 0.02$ $T_T = 233.4 \pm 0.8$ $Z_T = 0.96$
39MM	*M16*	$P_T = 18.80 \pm 0.02$ $T_T = 256.6 \pm 0.8$ $Z_T = 0.56$	$P_T = 2.46 \pm 0.02$ $T_T = 234.0 \pm 0.8$ $Z_T = 0.95$
40MM	*M16*	$P_T = 18.97 \pm 0.02$ $T_T = 259.4 \pm 0.8$ $Z_T = 0.57$	$P_T = 2.63 \pm 0.02$ $T_T = 234.5 \pm 0.8$ $Z_T = 0.95$

Table 6.2: List of the test runs belonging to the *MM vapor expansion campaign* concerning nozzle *M16*. Each test run is composed by several different steady states characterized by different total conditions going from the initial to the final one that are here reported.

Tables 6.1 and 6.2 report all the test runs performed that have been selected to study the expansion of MM vapor inside the two nozzles *M15* and *M16*. Each test run represents a sequence of steady state expansions ranging between the most non ideal and the most ideal one, which are those listed in tables 6.1 and 6.2. The evolution of the total conditions measured during each of the selected test runs is reported in a $P - T$ diagram in figures 6.1a and 6.2a for nozzles *M15* and *M16* respectively. As already pointed out in the previous chapter 5 about the *MDM vapor expansion campaign*, consistency and repeatability of the *MM vapor expansion campaign* data set can be assessed only by comparing static pressures measured in different test but sharing the same total condition in terms of temperature and pressure. Indeed, most of the expansions studied take place in the non-ideal compressible regime and are expected to be dependent on the corresponding total conditions.

Concerning the test runs carried out with nozzle *M15*, it can be seen in Figure 6.1a that several tests share the same total conditions. Four sets of corresponding tests, (*05MM*, *06MM*), (*12MM*, *19MM*), (*13MM*, *17MM*) and (*14MM*, *16MM*, *18MM*, *20MM*), can be used for the comparison. It was decided here to report only the analysis of tests (*14MM*, *16MM*, *18MM*, *20MM*) since they belong to the larger available set.

Figure 6.1b reports the static pressures measured during the chosen tests while figures 6.1 *c-f* presents a detail for each of the axial coordinate at which static pressures were

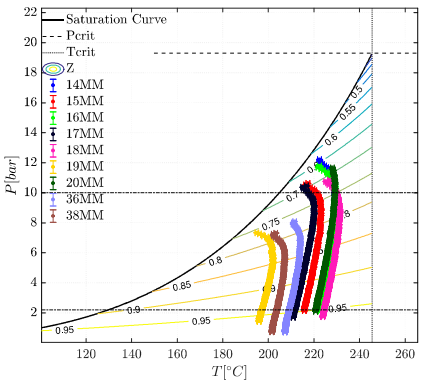

(a) *$P-T$ diagram with the total conditions reached during test runs conducted with nozzle M15. The solid black line is the saturation curve, the dashed black line is the MDM critical pressure and the dotted black line is the MDM critical temperature. The two dashed-dotted horizontal black lines mark the range in which tests 14MM, 16MM, 18MM, and 20MM share the same total conditions.*

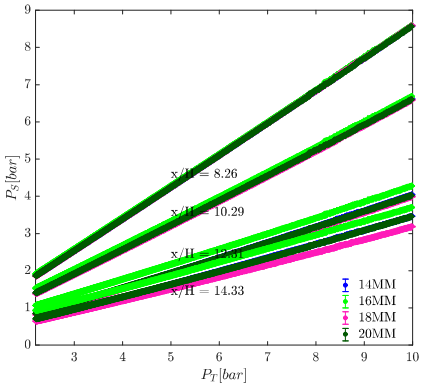

(b) *Static pressure P_s measured at different axial locations in tests 14MM, 16MM, 18MM, and 20MM plotted against the corresponding measured total pressure in the range $P_T = [2.2 \div 10]$ bar where the total temperature for the four tests are matching. Curves are parametrized by the non-dimensional axial coordinate x/H. It is indicated in the labels and it specifies the pressure measurements location. For each coordinate an enlargement is plotted below for a clearer comparison of results.*

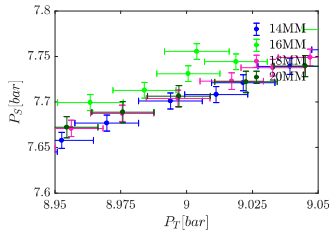

(c) x/H = 8.26

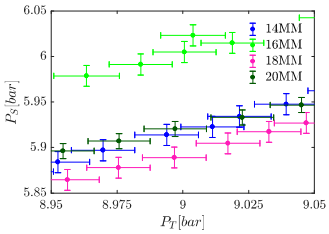

(d) x/H = 10.29

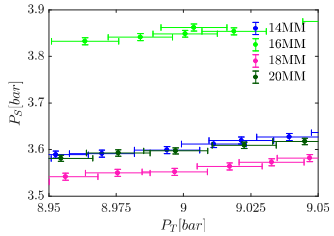

(e) x/H = 12.31

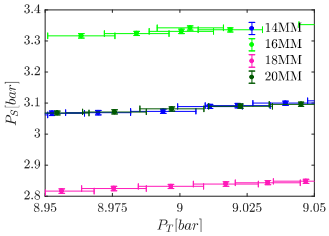

(f) x/H = 14.33

Figure 6.1: Nozzle *M15* operated with MM, consistency and repeatability analysis.

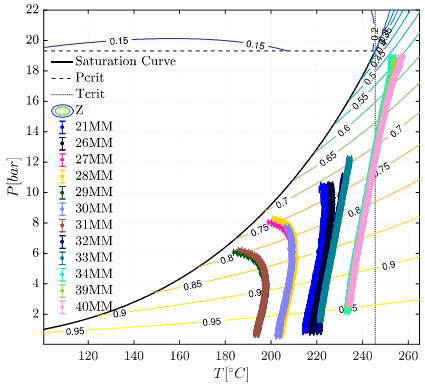

(a) *P – T diagram with the total conditions reached during test runs conducted with nozzle M16. The solid black line is the saturation curve, the dashed black line is the MDM critical pressure and the dotted black line is the MDM critical temperature.*

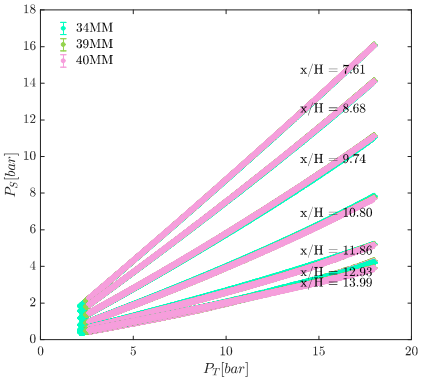

(b) *Static pressure P_s measured at different axial locations in tests 34MM, 39MM and 40MM plotted against the corresponding measured total pressure bar. Curves are parametrized by the non-dimensional axial coordinate x/H. It is indicated in the labels and it specifies the pressure measurements location. For each coordinate an enlargement is plotted below for a clearer comparison of results.*

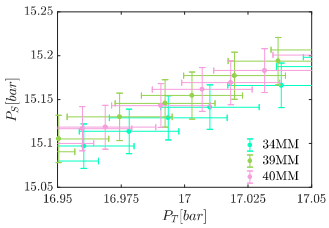

(c) x/H = 7.61

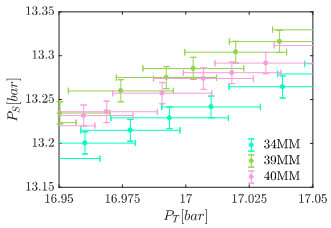

(d) x/H = 8.68

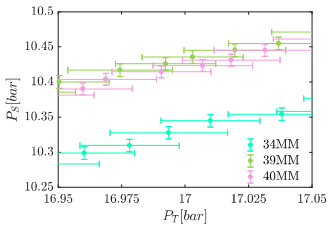

(e) x/H = 9.74

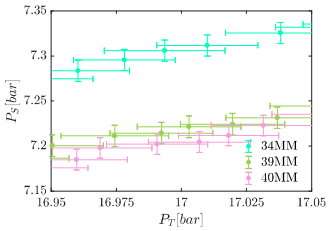

(f) x/H = 10.8

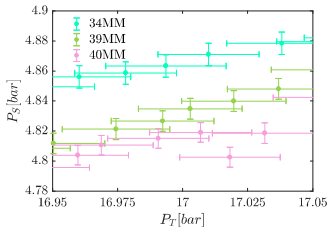

(g) x/H = 11.86

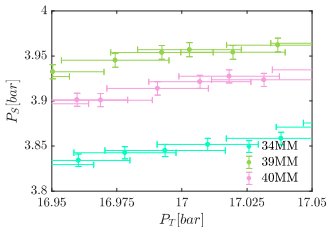

(h) x/H = 12.93

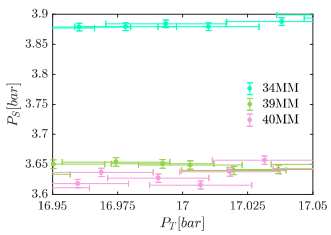

(i) x/H = 13.99

Figure 6.2: Nozzle *M16* operated with MM, operated with MM, consistency and repeatability analysis.

Test ID	Nozzle	P_T $[bar]$	T_T $[^\circ C]$	Z_T	Γ_T
40MMa	*M16*	18.87	256.8	0.55	0.60
40MMb	*M16*	16.99	252.8	0.60	0.60
40MMc	*M16*	15.08	249.5	0.65	0.64
40MMd	*M16*	13.16	246.7	0.70	0.70
40MMe	*M16*	11.21	244.3	0.75	0.75
40MMf	*M16*	9.14	241.7	0.80	0.81
40MMg	*M16*	6.96	239.0	0.85	0.96
40MMh	*M16*	4.72	236.2	0.90	0.92

Table 6.3: Total conditions of expansions extracted from test *40MM*.

measured. It can be noticed that at coordinates $x/H = 8.26$ and $x/H = 10.29$ three out of four tests are consistent with each others, the only exception is test *16MM*. The data coming from test *18MM* are off at coordinates $x/H = 12.31$ and $x/H = 14.33$, for this reason this test together with test *16MM* were discarded and not taken in to consideration for further analysis. Given the agreement shown by tests *14MM* and *20MM* the experimental data concerning nozzle *M15* prove their consistency and repeatability.
For what concerns nozzle *M16* the set of test runs composed by tests *34MM*, *39MM* and *40MM* was chosen for the assessment since it encompass the tests reaching the most non-ideal conditions. By looking at the enlargements in Figure 6.2 it is clear that, while tests *39MM* and *40MM* match quite well, test *34MM* is off in most of the coordinates measured. Test *34MM* was indeed discarded while tests *39MM* and *40MM* were used for further analysis since they proved their consistency and repeatability.
It is worth mentioning that all of the tests used in the following sections showed results confirmed by at least one other corresponding test; thus, all further conclusion are based on repeated measurements.

6.2 EXPERIMENTAL EVIDENCE OF NON-IDEAL COMPRESSIBLE FLUID EFFECTS

Test 40MM was the one achieving the most non-ideal total conditions of the whole experimental campaign. It was possible to extract from this test, nozzle expansions characterized by total compressibility factors ranging from $Z_T^{min} = 0.57$ to $Z_T^{max} = 0.95$. Figure 6.3a reports the total conditions that are listed in Table 6.3 plotted on a $P - T$ diagram with a Z contour. Figure 6.3b shows the corresponding isentropic expansions on a $T - s$ diagram also reporting a Z contour.
The pressure ratio distribution measured along the nozzle axis in all the considered

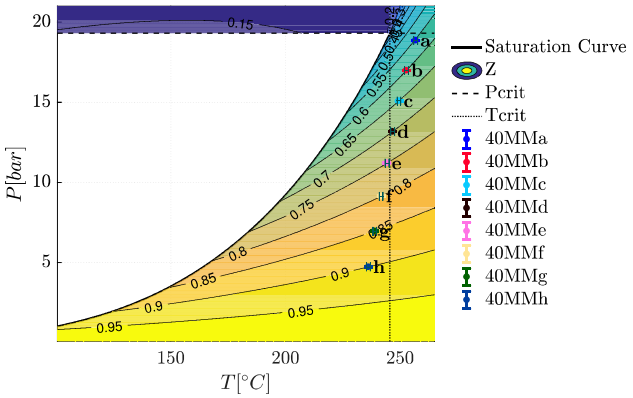

(a) *Total conditions plotted on a $P - T$ diagram together with a Z contour, the saturation curve (black line), critical pressure (dashed black line) and critical temperature (dotted black line).*

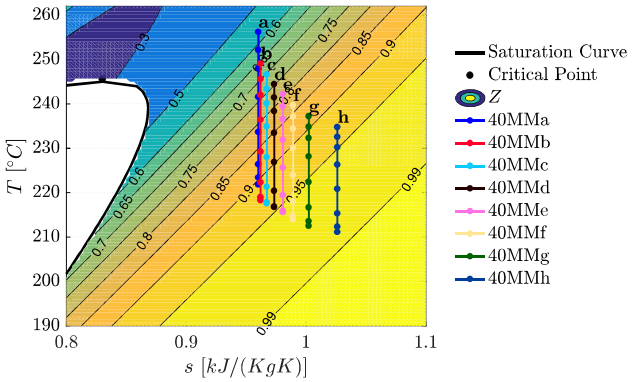

(b) *Isentropic nozzle expansions plotted on a $T - s$ diagram together with the saturation curve (black line) . the coloured dots correspond to the static temperatures computed from the static pressures measured along the nozzle axis.*

Figure 6.3: Expansions extracted from test *40MM*.

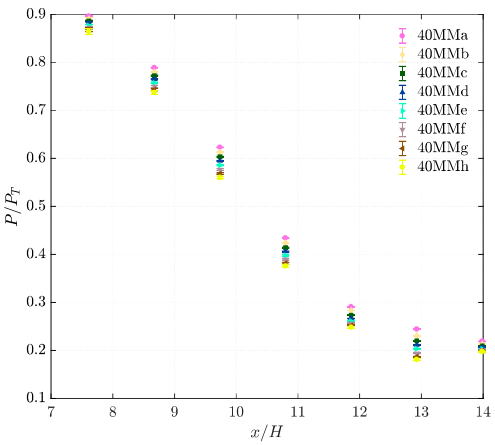

(a) *P/P_T trends along the nozzle axis extracted from test 40MDM.*

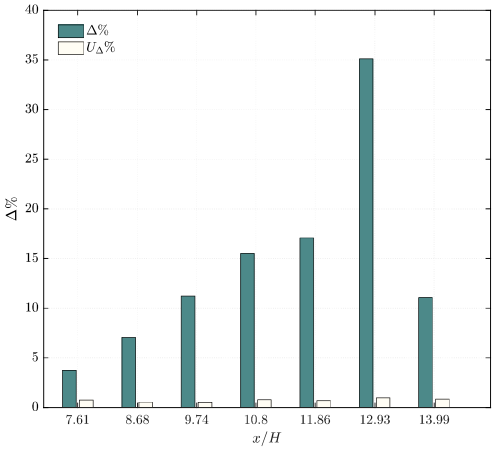

(b) *Bar plot reporting $\Delta\%$ Eq. (94) and $U_{\Delta\%}$ Eq. (97).*

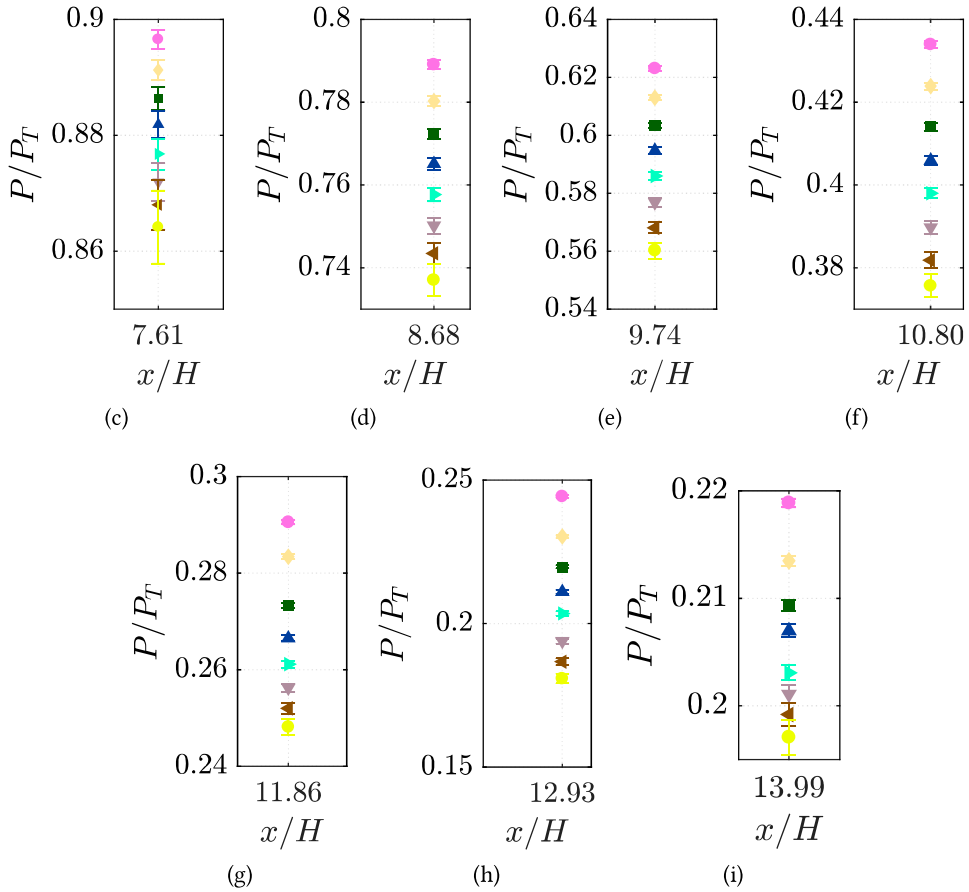

Figure 6.4: Pressure ratios measured in nozzle *M16* during test *40MM* characterized by different total conditions.

expansions can be used to prove the influence of non-ideal fluid effects similarly to the analysis carried out for the *MDM vapor expansion campaign* (see Sec.5.2). Figure 6.4 shows the pressure ratio profiles measured for nozzle flows from *40MMa* to *40MMh*. It can be noticed that pressure ratios decrease going from the most non-ideal condition *40MMa* characterized by $Z_T^{min} = 0.57$ to the most ideal one *40MMh* having a $Z_T^{max} = 0.95$. The details reported in Figure 6.4 form *(c)* to *(i)* make clear that the uncertainty bars do not overlap proving that the trend is undoubtedly ascribed to non-ideal effects. The same trend was found also in chapter 5 where different MDM expansions were analyzed (see Sec.5.2).

Moreover, Figure 6.4b shows a bar plot comparing the percentage difference $\Delta\%$, (Eq.(95)) calculated between the pressure ratio Π measured in correspondence of the minimum and the maximum Z_T, with its uncertainty $U_\Delta\%$ obtained propagating the uncertainties U_P and U_{P_T} related respectively to the static and the total pressure measurements.

$$\Delta = \left(\frac{P}{P_T}\right)_{Z_T=Z_T^{min}} - \left(\frac{P}{P_T}\right)_{Z_T=Z_T^{max}} = \Pi(Z_T^{max}) - \Pi(Z_T^{min}) \tag{94}$$

$$\Delta\% = \frac{\Delta}{\Pi(Z_T^{min})} \cdot 100 \tag{95}$$

$$U_\Pi = \left(\frac{P}{P_T}\right)\sqrt{\frac{U_P^2}{P^2} + \frac{U_{P_T}^2}{P_T^2}} \tag{96}$$

$$U_\Delta = \sqrt{U_{\Pi(Z_T^{max})}^2 + U_{\Pi(Z_T^{min})}^2} \tag{97}$$

$$U_\Delta\% = \frac{100}{\Pi(Z_T^{min})} \cdot \sqrt{U_{\Pi(Z_T^{max})}^2 + \left(\frac{\Pi(Z_T^{max}}{\Pi(Z_T^{min}}\right)^2 \cdot U_{\Pi(Z_T^{min})}^2} \tag{98}$$

$$\tag{99}$$

The bar plot shows that the decreasing trend is confirmed at each axial location and that, in percentage terms, the difference grows up to the axial location $x/H = 12.93$ where the pressure ratio at Z_T^{min} is 1.35 times the one at Z_T^{max}. As expected $\Delta\%$ is lower at the first axial location $x/H = 7.61$ where the error bars of the pressure ratio measured are overlapping for some of the conditions analyzed (see Fig. 6.4c). Indeed, at this location the expansion process is at its initial stage, thus the pressure ratio is close to one independently on the total condition considered.

In the last portion of the nozzle core ($x/H \geq 12.93$) the expansion is concluded, since it ends some millimeters before the nozzle outlet section. Indeed, the nozzle is designed to achieve uniform outlet conditions. Thus, in the last part, the expansion on the axis is concluded but the walls rotate the outer flow in order to achieve a uniform axial velocity at the outlet. However, the nozzle is designed for specific total conditions which are close to the conditions reached at the beginning of test *40MM*. Indeed, conditions from *a* to *d* show static pressure diminishing up to the last tap in $x/H = 13.99$. Conditions from *e* to *h* exhibit, instead, pressure ratio growing from $x/H = 12.93$ to $x/H = 13.99$ (see Fig.s

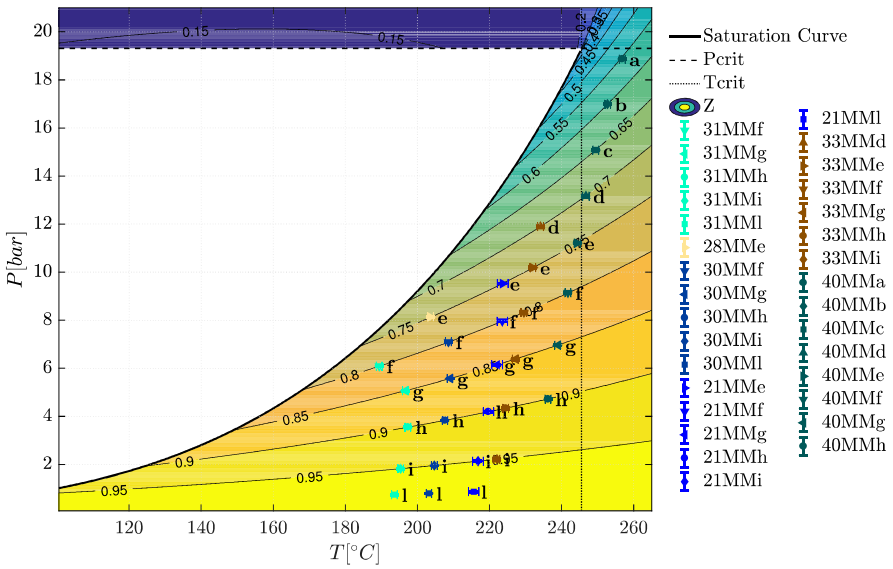

Figure 6.5: $P - T$ diagram with Z contour reporting the total conditions characterizing all the expansions analyzed to assess the influence of Z_T total compressibility factor on the pressure ratio profiles.

6.4g, 6.4h). This can be explained by the fact that, going towards far off design conditions, the shape of the last part of the nozzle walls is no more adequate to turn properly the flow. The effect on the axis is a mild re-compression going from the second last to the last pressure tap. The value of $\Delta\%$ diminishes too from $x/H = 12.93$ to $x/H = 13.99$.

6.3 ANALYSIS OF THE NOZZLE FLOW EXPANSION

6.3.1 *Influence of total compressibility*

The results presented within section 6.2 prove the dependence of pressure ratio profiles on the total conditions at which the nozzle is operated. Total pressure P_T and total temperature T_T are the two quantities univocally characterizing the operating condition of a nozzle flow. However, if coupled with a suitable thermodynamic model (here the one presented in (Thol et al., 2017) has been used), they can be used to compute the total compressibility factor $Z_T = P_T/(T_T R_{MM} \rho(T_T, P_T))$.
The total compressibility factor characterizes the volumetric behavior of a non-ideal gas in a specific thermodynamic point. Several tests were made in order to acquire experimental data of expansions having different total conditions in term of P_T and T_T but sharing the same total compressibility factor Z_T, in order to investigate whether parameter Z_T alone is sufficient to assess the level of non-ideality of a nozzle flow and thus, to characterize the expansion and predict pressure ratios.

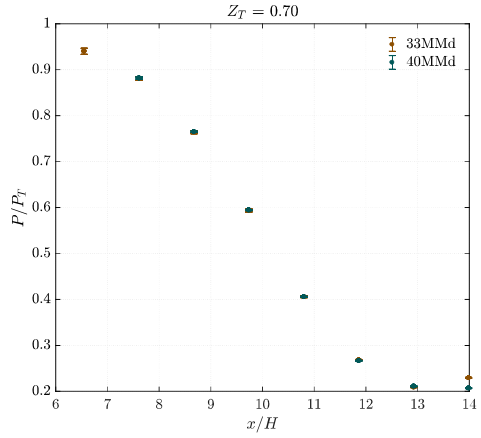

(a) *Pressure ratio profiles along the nozzle axis for all different total conditions sharing* $Z_T = 0.70$.

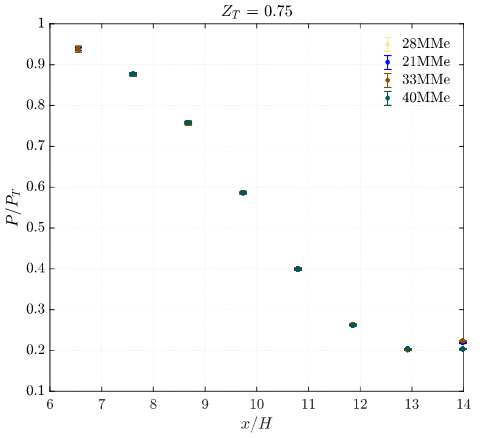

(b) *Pressure ratio profiles along the nozzle axis for all different total conditions sharing* $Z_T = 0.75$.

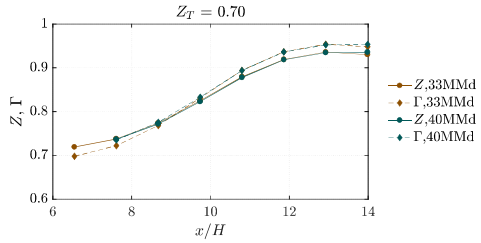

(c) Z *and* Γ *profiles on the nozzle axis of different expansions sharing the same* $Z_T = 0.70$*, computed from the static pressure measurements as* $Z(P, s)$ *and* $\Gamma(P, s)$.

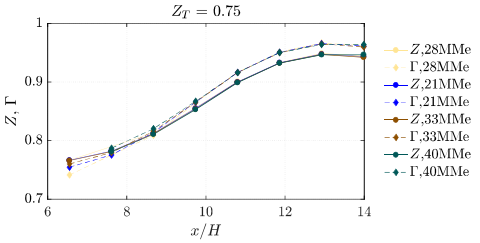

(d) Z *and* Γ *profiles on the nozzle axis of different expansions sharing the same* $Z_T = 0.75$*, computed from the static pressure measurements as* $Z(P, s)$ *and* $\Gamma(P, s)$.

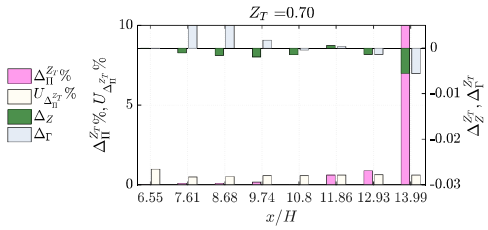

(e) $\overline{Z_T} = 0.70$*: The left axis reports in pink bars the percentage difference* $\Delta_\Pi^{\overline{Z_T}}$% *(Eq.* (100)*) between pressure ratio and in white bars their uncertainty* $U_{\Delta_\Pi^{\overline{Z_T}}}$% *(Eq.* (101)*). The right axis reports in green bars the differences between compressibility factors* $\Delta_Z^{\overline{Z_T}}$ *(Eq.* (102)*) and in gray bars the differences between the fundamental derivative of gas-dynamic* $\Delta_\Gamma^{\overline{Z_T}}$ *(Eq.* (103)*).*

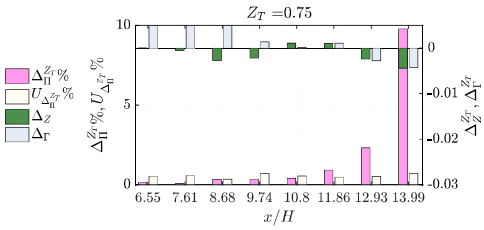

(f) $\overline{Z_T} = 0.75$*: The left axis reports in pink bars the percentage difference* $\Delta_\Pi^{\overline{Z_T}}$% *(Eq.* (100)*) between pressure ratio and in white bars their uncertainty* $U_{\Delta_\Pi^{\overline{Z_T}}}$% *(Eq.* (101)*). The right axis reports in green bars the differences between compressibility factors* $\Delta_Z^{\overline{Z_T}}$ *(Eq.* (102)*) and in gray bars the differences between the fundamental derivative of gas-dynamic* $\Delta_\Gamma^{\overline{Z_T}}$ *(Eq.* (103)*).*

Figure 6.6: MM flow of nozzle *M16* operated at different operating conditions sharing the same $Z_T = 0.70$ (left charts) and $Z_T = 0.75$ (right charts).

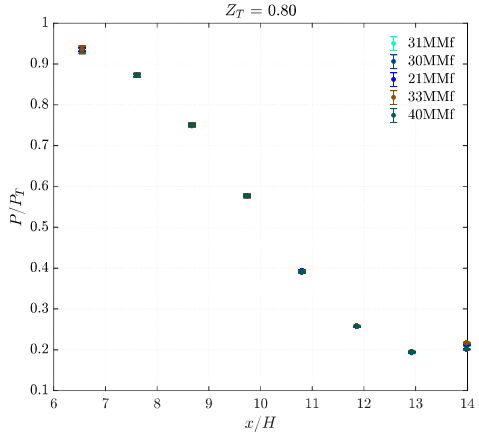

(a) *Pressure ratio profiles along the nozzle axis for all different total conditions sharing* $Z_T = 0.80$.

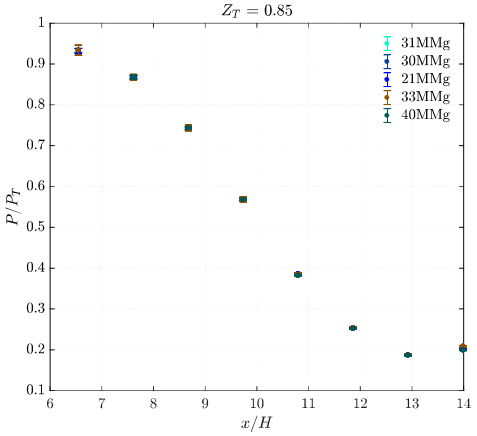

(b) *Pressure ratio profiles along the nozzle axis for all different total conditions sharing* $Z_T = 0.85$.

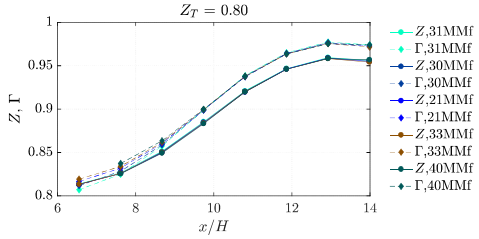

(c) Z *and* Γ *profiles on the nozzle axis of different expansions sharing the same* $Z_T = 0.80$*, computed from the static pressure measurements as* $Z(P, s)$ *and* $\Gamma(P, s)$.

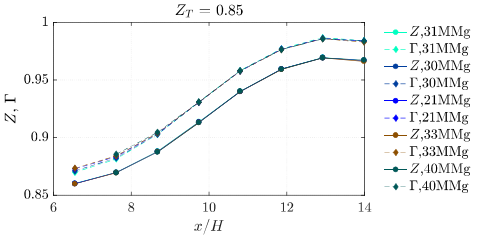

(d) Z *and* Γ *profiles on the nozzle axis of different expansions sharing the same* $Z_T = 0.85$*, computed from the static pressure measurements as* $Z(P, s)$ *and* $\Gamma(P, s)$.

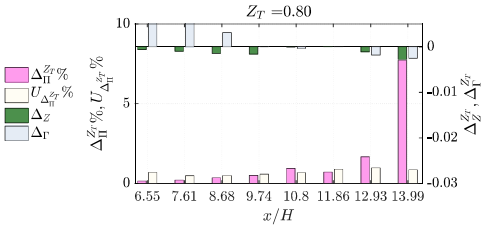

(e) $\overline{Z_T} = 0.80$*: The left axis reports in pink bars the percentage difference* $\Delta_\Pi^{\overline{Z_T}}\%$ *(Eq.* (100)*) between pressure ratio and in white bars their uncertainty* $U_{\Delta_\Pi^{\overline{Z_T}}}\%$ *(Eq.* (101)*). The right axis reports in green bars the differences between compressibility factors* $\Delta_Z^{\overline{Z_T}}$ *(Eq.* (102)*) and in gray bars the differences between the fundamental derivative of gas-dynamic* $\Delta_\Gamma^{\overline{Z_T}}$ *(Eq.* (103)*).*

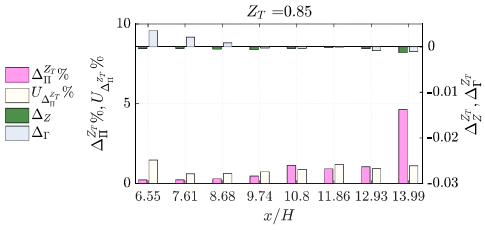

(f) $\overline{Z_T} = 0.85$*: The left axis shows in pink bars the percentage difference* $\Delta_\Pi^{\overline{Z_T}}\%$ *(Eq.* (100)*) between pressure ratio and in white bars their uncertainty* $U_{\Delta_\Pi^{\overline{Z_T}}}\%$ *(Eq.* (101)*). The right axis reports in green bars the differences between compressibility factors* $\Delta_Z^{\overline{Z_T}}$ *(Eq.* (102)*) and in gray bars the differences between the fundamental derivative of gas-dynamic* $\Delta_\Gamma^{\overline{Z_T}}$ *(Eq.* (103)*).*

Figure 6.7: MM flow of nozzle *M16* operated at different operating conditions sharing the same $Z_T = 0.80$ (left charts) and $Z_T = 0.85$ (right charts).

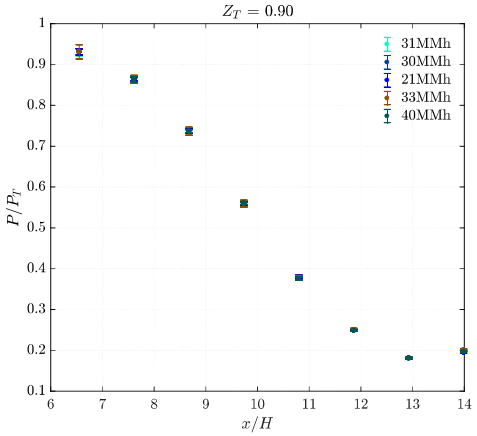

(a) *Pressure ratio profiles along the nozzle axis for all different total conditions sharing* $Z_T = 0.90$.

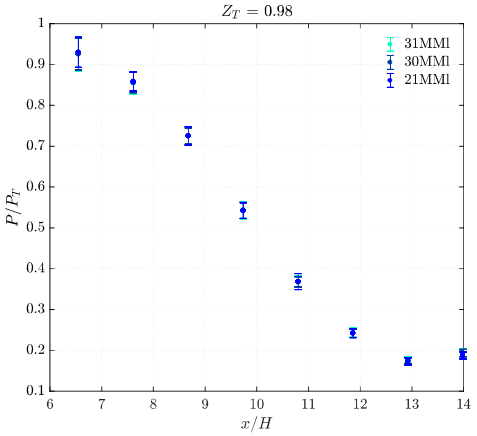

(b) *Pressure ratio profiles along the nozzle axis for all different total conditions sharing* $Z_T = 0.98$.

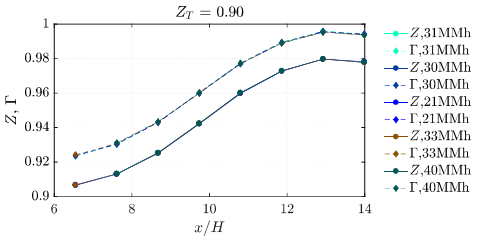

(c) Z *and* Γ *profiles on the nozzle axis of different expansions sharing the same* $Z_T = 0.90$*, computed from the static pressure measurements as* $Z(P, s)$ *and* $\Gamma(P, s)$.

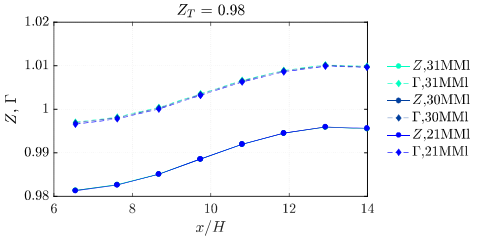

(d) Z *and* Γ *profiles on the nozzle axis of different expansions sharing the same* $Z_T = 0.98$*, computed from the static pressure measurements as* $Z(P, s)$ *and* $\Gamma(P, s)$.

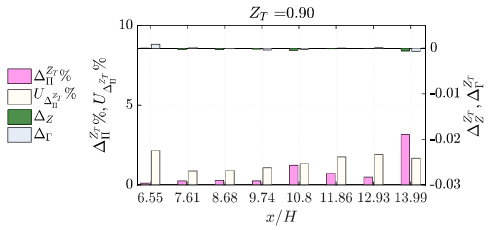

(e) $\overline{Z_T} = 0.90$*: The left axis shows in pink bars the percentage difference* $\Delta_\Pi^{\overline{Z_T}}\%$ *(Eq. (100)) between pressure ratio and in white bars their uncertainty* $U_{\Delta_\Pi^{\overline{Z_T}}}\%$ *(Eq. (101)). The right axis reports in green bars the differences between compressibility factors* $\Delta_Z^{\overline{Z_T}}$ *(Eq. (102)) and in gray bars the differences between the fundamantal derivative of gas-dynamic* $\Delta_\Gamma^{\overline{Z_T}}$ *(Eq. (103)).*

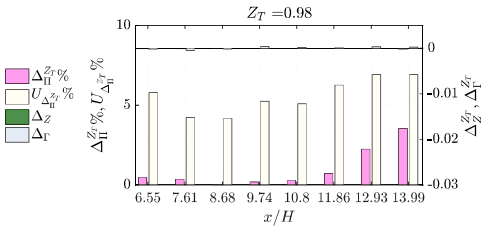

(f) $\overline{Z_T} = 0.98$*: The left axis reports in pink bars the percentage difference* $\Delta_\Pi^{\overline{Z_T}}\%$ *(Eq. (100)) between pressure ratio and in white bars their uncertainty* $U_{\Delta_\Pi^{\overline{Z_T}}}\%$ *(Eq. (101)). The right axis reports in green bars the differences between compressibility factors* $\Delta_Z^{\overline{Z_T}}$ *(Eq. (102)) and in gray bars the differences between the fundamantal derivative of gas-dynamic* $\Delta_\Gamma^{\overline{Z_T}}$ *(Eq. (103)).*

Figure 6.8: MM flow of nozzle *M16* operated at different operating conditions sharing the same $Z_T = 0.90$ (left charts) and $Z_T = 0.98$ (right charts).

Figure 6.5 reports the total conditions of the nozzle flows selected for the assessment. The comparisons between pressure ratio profiles of different tests at different total conditions and same Z_T are reported in Figures 6.6a, 6.6b, 6.7a, 6.7b, 6.8a and 6.8b for Z_T ranging from 0.70 to 0.98.

The number of measured pressure profiles to be compared are fewer for $Z_T = 0.70$ than for higher Z_T, since lower values of Z_T can be found only in a small thermodynamic region close to the critical point (see Fig. 6.5). It can be noticed that pressure ratio profiles are almost superimposed except from the last available axial position at $x/H = 13.99$. Figures 6.6c, 6.6d, 6.7c, 6.7d, 6.8c and 6.8d report the profile of the compressibility factor Z computed using the static pressures measured along the nozzle axis. Starting from the same value of Z_T does not necessarily result in obtaining the same Z profiles. However, for the conditions analyzed the Z profile found are superimposed except in the last axial location $x/H = 13.99$ where there is a small discrepancy for the lower analyzed Z_T (See Fig.s 6.6c, 6.6d, 6.7c and 6.7d). This is coherent with the fact that the maximum pressure profile deviations are registered at that location.

The profile of Γ_T is also shown together with the Z_T one. Expansions characterized by the same Z_T are not characterized by the same Γ_T. Indeed, the profiles of Γ are not superimposed in the first axial locations measured while they collapse to one another as the expansion proceeds. They start to separate themselves again in $x/H = 13.99$ where also the profiles of Z are not superimposed as they instead were in the other axial locations. This is true for the comparisons carried out at smaller Z_T. As Z_T increases the profiles of Γ tend to collapse to one another.

The relative distance between pressure ratio profiles was quantified by calculating $\Delta_{\Pi}^{\overline{Z_T}}\%$ Eq. (100) and $U_{\Delta_{\Pi}^{\overline{Z_T}}}\%$ Eq. (101), while the deviation of compressibility factor Z and of fundamental derivative of gas-dynamics Γ along the nozzle is provided by $\Delta_{Z}^{\overline{Z_T}}$ Eq. (102) and by $\Delta_{\Gamma}^{\overline{Z_T}}$ Eq. (103).

$$\Delta_{\Pi}^{\overline{Z_T}}\% = \frac{max\left[\Pi(\overline{Z_T})\right] - min\left[\Pi(\overline{Z_T})\right]}{min\left[\Pi(\overline{Z_T})\right]} \cdot 100 \tag{100}$$

$$U_{\Delta_{\Pi}^{\overline{Z_T}}}\% = \frac{100}{min\left[\Pi(\overline{Z_T})\right]} \cdot \sqrt{U^2_{max\left[\Pi(\overline{Z_T})\right]} + U^2_{min\left[\Pi(\overline{Z_T})\right]} \cdot \left(\frac{max\left[\Pi(\overline{Z_T})\right]}{min\left[\Pi(\overline{Z_T})\right]}\right)^2} \tag{101}$$

$$\Delta_{Z}^{\overline{Z_T}} = Z_{max\left[\Pi(\overline{Z_T})\right]} - Z_{min\left[\Pi(\overline{Z_T})\right]} \tag{102}$$

$$\Delta_{\Gamma}^{\overline{Z_T}} = \Gamma_{max\left[\Pi(\overline{Z_T})\right]} - \Gamma_{min\left[\Pi(\overline{Z_T})\right]} \tag{103}$$

where $max\left[\Pi(\overline{Z_T})\right]$ and $min\left[\Pi(\overline{Z_T})\right]$ refer to the maximum and the minimum value of pressure ratio registered in a specific axial location among all the expansions sharing the same $\overline{Z_T}$. The two quantities $\Delta_{\Pi}^{\overline{Z_T}}\%$ and $U_{\Delta_{\Pi}^{\overline{Z_T}}}\%$ are reported in the bar plots of figures 6.6e, 6.6f, 6.7e, 6.7f, 6.8e and 6.8f where it can be noticed that $\Delta_{\Pi}^{\overline{Z_T}}\%$ is markedly greater than $U_{\Delta_{\Pi}^{\overline{Z_T}}}\%$ only at $x/H = 13.99$. $\Delta_{Z}^{\overline{Z_T}}$ and $\Delta_{\Gamma}^{Z_T}$ are also reported and, at all axial locations where

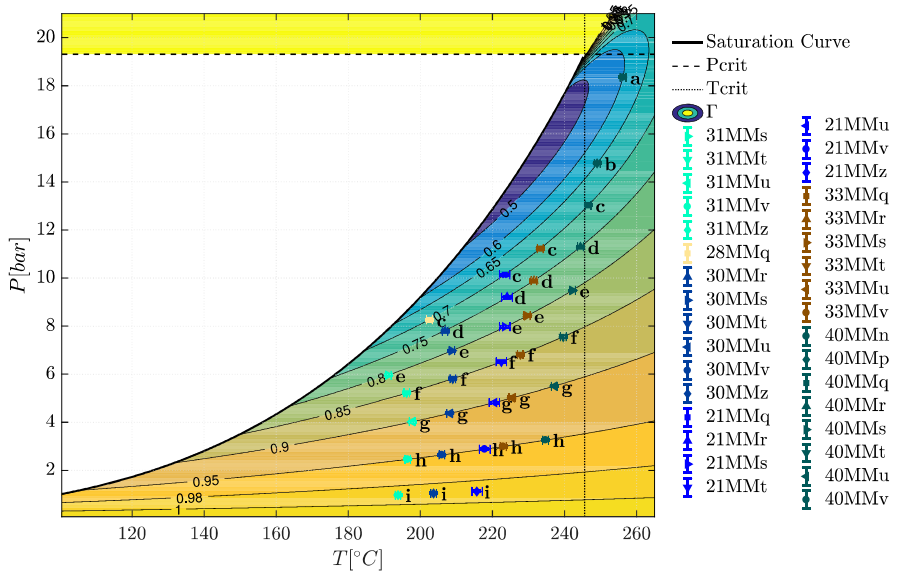

Figure 6.9: $P - T$ diagram with Γ contour reporting the total conditions characterizing the expansions analyzed to assess the influence of the total fundamental derivative of gas-dynamic Γ_T on pressure ratio profiles.

$\Delta_{\Pi}^{Z_T}\%$ is greater than $U_{\Delta_{\Pi}^{\overline{Z_T}}}\%$, they have always a sign opposite to $\Delta_{\Pi}^{Z_T}\%$. This is consistent with the fact that pressure ratios measured in thermodynamic conditions where non-ideal compressible effects are stronger are expected to be higher than pressure ratios measured where Z is closer to one and Γ is higher. It can be noticed that, for increasing $\overline{Z_T}$, the value of $\Delta_{\Pi}^{\overline{Z_T}}\%$ generally decrease and at $\overline{Z_T} = 0.98$ the difference between the pressure profiles never overcomes the measurement uncertainty.
Analyzing the whole data set spacing from $\overline{Z_T} = 0.7$ to $\overline{Z_T} = 0.98$ it can be concluded that, within the thermodynamic region explored, pressure ratio profiles of nozzle flows characterized by same $\overline{Z_T}$ and different total conditions are superimposed with the only exception of the last axial coordinate analyzed. In this region pressure ratio can no more be considered dependent only on $\overline{Z_T}$ but also the values of T_T or P_T play a role, thus indicating a higher sensitivity of the nozzle outlet section to the operating conditions, as already pointed out by the analysis of non-ideal effects carried out in section 6.2. However the influence of operating conditions diminishes going towards expansions characterized by higher $\overline{Z_T}$ and vanishes at $\overline{Z_T} = 0.98$.

6.3.2 *Influence of fundamental derivative of gas-dynamic*

An analysis similar to the one presented in the previous section was carried out to assess the influence of Γ_T on the nozzle flow expansion. Several expansions sharing the same Γ_T but having different total conditions (P_T, T_T) were compared; their total

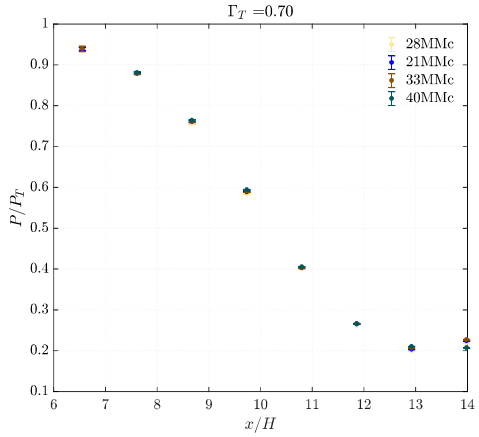

(a) *Pressure ratio profiles along the nozzle axis for all different total conditions sharing* $\Gamma_T = 0.70$.

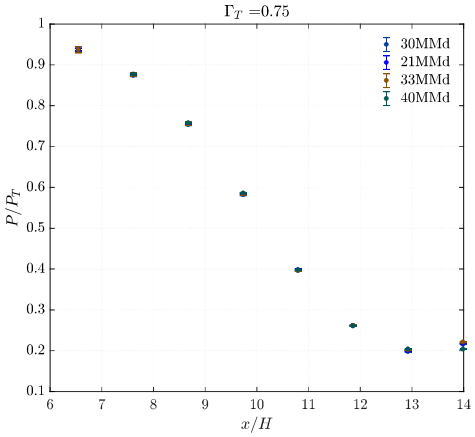

(b) *Pressure ratio profiles along the nozzle axis for all different total conditions sharing* $\Gamma_T = 0.75$.

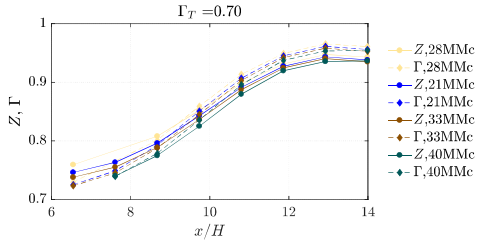

(c) Z *and* Γ *profiles on the nozzle axis of different expansions sharing the same* $\Gamma_T = 0.70$*, computed from the static pressure measurements as* $Z(P, s)$ *and* $\Gamma(P, s)$.

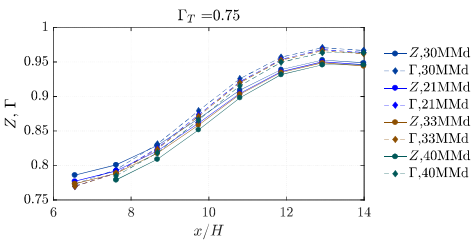

(d) Z *and* Γ *profiles on the nozzle axis of different expansions sharing the same* $\Gamma_T = 0.75$*, computed from the static pressure measurements as* $Z(P, s)$ *and* $\Gamma(P, s)$.

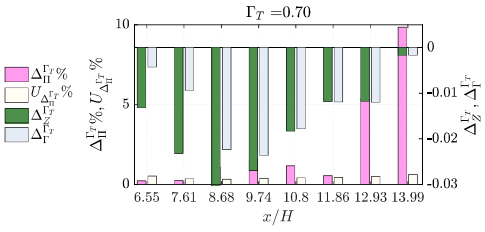

(e) $\overline{\Gamma_T} = 0.70$*: The left axis shows in pink bars the percentage difference* $\Delta_{\Pi}^{\overline{\Gamma_T}}\%$ *(Eq.* (104)*) between pressure ratio and in white bars their uncertainty* $U_{\Delta_{\Pi}^{\overline{\Gamma_T}}}\%$ *(Eq.* (105)*). The right axis reports in green bars the differences between compressibility factors* $\Delta_Z^{\overline{\Gamma_T}}$ *(Eq.* (106)*) and in gray bars the differences between the fundamantal derivative of gas-dynamic* $\Delta_{\Gamma}^{\overline{\Gamma_T}}$ *(Eq.* (107)*).*

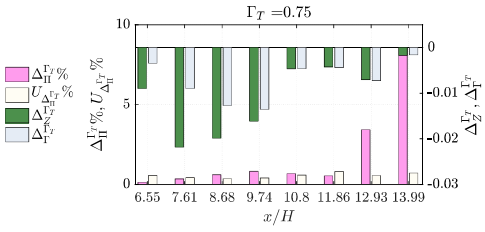

(f) $\overline{\Gamma_T} = 0.75$*: The left axis shows in pink bars the percentage difference* $\Delta_{\Pi}^{\overline{\Gamma_T}}\%$ *(Eq.* (104)*) between pressure ratio and in white bars their uncertainty* $U_{\Delta_{\Pi}^{\overline{\Gamma_T}}}\%$ *(Eq.* (105)*). The right axis reports in green bars the differences between compressibility factors* $\Delta_Z^{\overline{\Gamma_T}}$ *(Eq.* (106)*) and in gray bars the differences between the fundamental derivative of gas-dynamic* $\Delta_{\Gamma}^{\overline{\Gamma_T}}$ *(Eq.* (107)*).*

Figure 6.10: MM flow of nozzle *M16* operated at different operating conditions sharing the same $\Gamma_T = 0.70$ (left charts) and $\Gamma_T = 0.75$ (right charts).

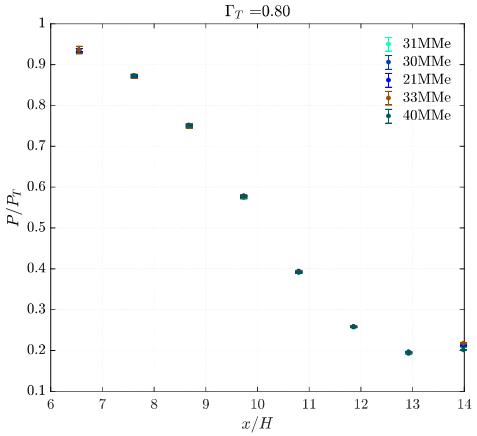

(a) *Pressure ratio profiles along the nozzle axis for all different total conditions sharing* $\Gamma_T = 0.80$.

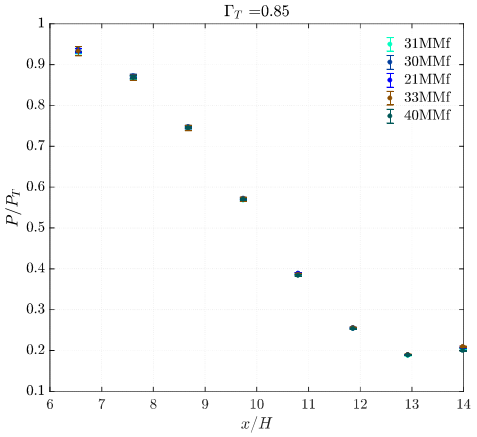

(b) *Pressure ratio profiles along the nozzle axis for all different total conditions sharing* $\Gamma_T = 0.85$.

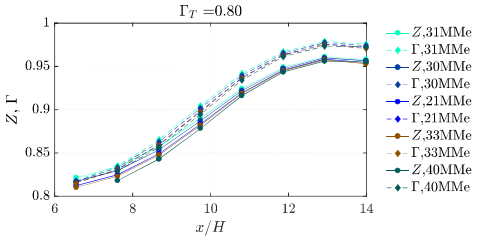

(c) Z *and* Γ *profiles on the nozzle axis of different expansions sharing the same* $\Gamma_T = 0.80$*, computed from the static pressure measurements as* $Z(P, s)$ *and* $\Gamma(P, s)$.

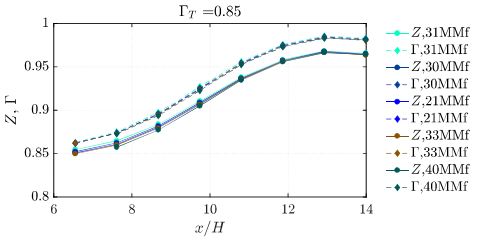

(d) Z *and* Γ *profiles on the nozzle axis of different expansions sharing the same* $\Gamma_T = 0.85$*, computed from the static pressure measurements as* $Z(P, s)$ *and* $\Gamma(P, s)$.

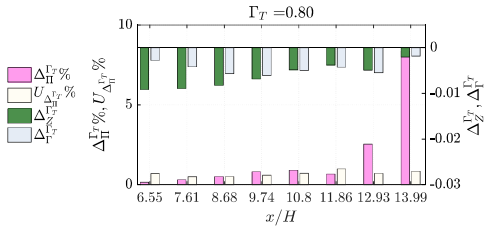

(e) $\overline{\Gamma_T} = 0.80$*: The left axis shows in pink bars the percentage difference* $\Delta_\Pi^{\overline{\Gamma_T}}\%$ *(Eq.* (104)*) between pressure ratio and in white bars their uncertainty* $U_{\Delta_\Pi^{\overline{\Gamma_T}}}\%$ *(Eq.* (105)*). The right axis reports in green bars the differences between compressibility factors* $\Delta_Z^{\overline{\Gamma_T}}$ *(Eq.* (106)*) and in gray bars the differences between the fundamantal derivative of gas-dynamic* $\Delta_\Gamma^{\overline{\Gamma_T}}$ *(Eq.* (107)*).*

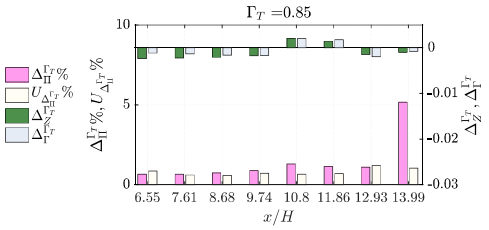

(f) $\overline{\Gamma_T} = 0.85$*: The left axis shows in pink bars the percentage difference* $\Delta_\Pi^{\overline{\Gamma_T}}\%$ *(Eq.* (104)*) between pressure ratio and in white bars their uncertainty* $U_{\Delta_\Pi^{\overline{\Gamma_T}}}\%$ *(Eq.* (105)*). The right axis reports in green bars the differences between compressibility factors* $\Delta_Z^{\overline{\Gamma_T}}$ *(Eq.* (106)*) and in gray bars the differences between the fundamantal derivative of gas-dynamic* $\Delta_\Gamma^{\overline{\Gamma_T}}$ *(Eq.* (107)*).*

Figure 6.11: MM flow of nozzle *M16* operated at different operating conditions sharing the same $\Gamma_T = 0.80$ (left charts) and $\Gamma_T = 0.85$ (right charts).

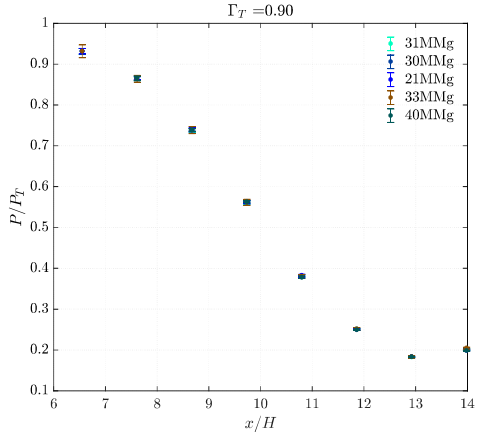

(a) *Pressure ratio profiles along the nozzle axis for all different total conditions sharing* $\Gamma_T = 0.90$.

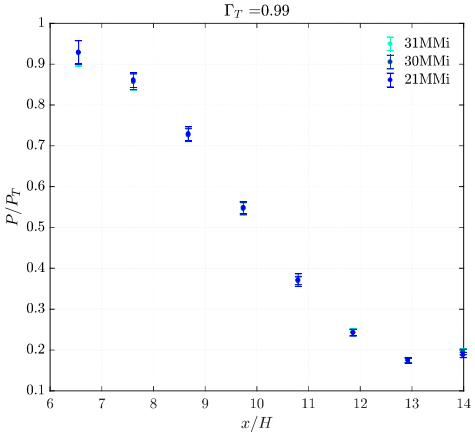

(b) *Pressure ratio profiles along the nozzle axis for all different total conditions sharing* $\Gamma_T = 0.98$.

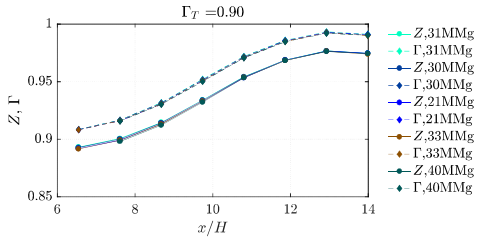

(c) *Z and* Γ *profiles on the nozzle axis of different expansions sharing the same* $\Gamma_T = 0.90$*, computed from the static pressure measurements as* $Z(P, s)$ *and* $\Gamma(P, s)$.

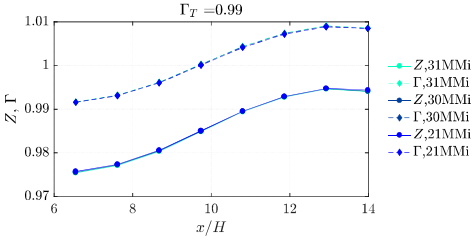

(d) *Z and* Γ *profiles on the nozzle axis of different expansions sharing the same* $\Gamma_T = 0.98$*, computed from the static pressure measurements as* $Z(P, s)$ *and* $\Gamma(P, s)$.

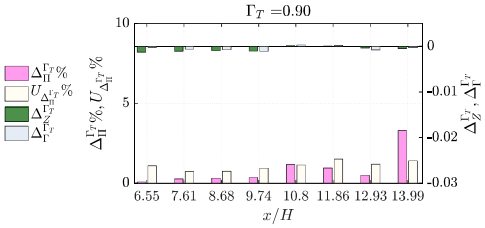

(e) $\overline{\Gamma_T} = 0.90$*: The left axis shows in pink bars the percentage difference* $\Delta_\Pi^{\overline{\Gamma_T}}$% *(Eq.* (104)*) between pressure ratio and in white bars their uncertainty* $U_{\Delta_\Pi^{\overline{\Gamma_T}}}$% *(Eq.* (105)*). The right axis reports in green bars the differences between compressibility factors* $\Delta_Z^{\overline{\Gamma_T}}$ *(Eq.* (106)*) and in gray bars the differences between the fundamantal derivative of gas-dynamic* $\Delta_\Gamma^{\overline{\Gamma_T}}$ *(Eq.* (107)*).*

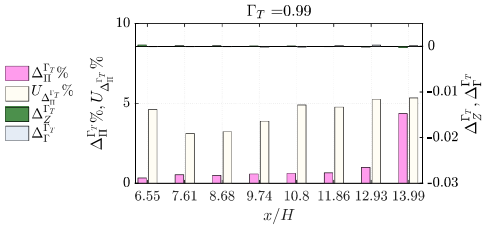

(f) $\overline{\Gamma_T} = 0.98$*: The left axis shows in pink bars the percentage difference* $\Delta_\Pi^{\overline{\Gamma_T}}$% *(Eq.* (104)*) between pressure ratio and in white bars their uncertainty* $U_{\Delta_\Pi^{\overline{\Gamma_T}}}$% *(Eq.* (105)*). The right axis reports in green bars the differences between compressibility factors* $\Delta_Z^{\overline{\Gamma_T}}$ *(Eq.* (106)*) and in gray bars the differences between the fundamantal derivative of gas-dynamic* $\Delta_\Gamma^{\overline{\Gamma_T}}$ *(Eq.* (107)*).*

Figure 6.12: MM flow of nozzle *M16* operated at different operating conditions sharing the same $\Gamma_T = 0.90$ (left charts) and $\Gamma_T = 0.98$ (right charts).

conditions are all plotted in Figure 6.9 on a $P - T$ diagram reporting also a contour of Γ. The pressure profiles are compared in figures 6.10a, 6.10b, 6.11a, 6.11b, 6.12a and 6.12b and they refer to values of Γ_T ranging from 0.70 to 0.99. It can be noticed that even though the profiles are close to one another, they exhibit higher deviation than what was observed comparing profiles sharing the same Z_T (see Sec. 6.3.1). Indeed, figures 6.10e, 6.10f, 6.11e, 6.11f, 6.12e and 6.12f report the values of $\Delta_{\Pi}^{\overline{\Gamma_T}}\%$ and $U_{\Delta_{\Pi}^{\overline{\Gamma_T}}}\%$ calculated as:

$$\Delta_{\Pi}^{\overline{\Gamma_T}}\% = \frac{max\left[\Pi(\overline{\Gamma_T})\right] - min\left[\Pi(\overline{\Gamma_T})\right]}{min\left[\Pi(\overline{\Gamma_T})\right]} \cdot 100 \tag{104}$$

$$U_{\Delta_{\Pi}^{\overline{\Gamma_T}}}\% = \frac{100}{min\left[\Pi(\overline{\Gamma_T})\right]} \cdot \sqrt{U^2_{max\left[\Pi(\overline{\Gamma_T})\right]} + U^2_{min\left[\Pi(\overline{\Gamma_T})\right]} \cdot \left(\frac{max\left[\Pi(\overline{\Gamma_T})\right]}{min\left[\Pi(\overline{\Gamma_T})\right]}\right)^2} \tag{105}$$

$$\Delta_{Z}^{\overline{\Gamma_T}} = Z_{max\left[\Pi(\overline{\Gamma_T})\right]} - Z_{min\left[\Pi(\overline{\Gamma_T})\right]} \tag{106}$$

$$\Delta_{\Gamma}^{\overline{\Gamma_T}} = \Gamma_{max\left[\Pi(\overline{\Gamma_T})\right]} - \Gamma_{min\left[\Pi(\overline{\Gamma_T})\right]} \tag{107}$$

where $max\left[\Pi(\overline{\Gamma_T})\right]$ and $min\left[\Pi(\overline{\Gamma_T})\right]$ refers to the maximum and the minimum value of pressure ratio registered in a specific axial location among all the expansions sharing the same $\overline{\Gamma_T}$.

As already seen in the previous analysis (Sec. 6.3.1) the highest values of $\Delta_{\Pi}^{\overline{\Gamma_T}}\%$ are at location $x/H = 13.99$. Going from $\overline{\Gamma_T} = 0.70$ to $\overline{\Gamma_T} = 0.90$ they stay markedly grater that the values of their uncertainties $U_{\Delta_{\Pi}^{\overline{\Gamma_T}}}\%$ up to $\overline{\Gamma_T} = 0.90$. The discrepancies detected between the highest and the lowest pressure profiles are significant also at $x/H = 12.93$ and they exceed than their uncertainties up to $\Gamma = 0.80$. The values of $\Delta_{\Pi}^{\overline{\Gamma_T}}\%$ registered there are greater than those of $\Delta_{\Pi}^{\overline{Z_T}}\%$ discussed in the previous analysis.

The profiles of Γ and of Z calculated from the static pressure measured along the nozzle axis are reported in figures 6.10c, 6.10d, 6.11c, 6.11d, 6.12c and 6.12d. As already discussed speaking about Z in the previous analysis, also concerning Γ starting from the same value of $\overline{\Gamma_T}$ does not guarantee the same Γ profiles along the nozzle axis. Indeed, differently from what found in section 6.3.1 analyzing the Z profile of expansions having the same Z_T, here there is a noticeable discrepancy between the Γ profiles of expansions sharing the same $\overline{\Gamma_T}$ when $\overline{\Gamma_T}$ is lower than 0.85. Figures 6.10e, 6.10f and 6.11e report the difference $\Delta_{\Gamma}^{\overline{\Gamma_T}}$ (Eq. (107)) which increases along the axis up to the first pressure tap located after the geometrical throat $(x/H)_{th} = 9.256$. On the other hand, the discrepancies in the Z profiles are larger since profiles sharing the same Γ_T do not necessarily share the same Z_T. However they are high for expansions sharing small values of $\overline{\Gamma_T}$ while they tend to collapse to one another as $\overline{\Gamma_T}$ increases.

In conclusion, in the thermodynamic region here explored, the pressure ratio profiles of nozzle expansions sharing the same $\overline{\Gamma_T}$ can be considered as superimposed up to $x/H = 12.93$ if $\overline{\Gamma_T}$ is greater than 0.85. If $\overline{\Gamma_T}$ is included between 0.70 and 0.85 the dependency of

Test ID	Nozzle	$P_T\ [bar]$	$T_T\ [^\circ C]$	Z_T	Γ_T
33MMx	*M16*	12.28	234.3	0.687	0.654
40MMy	*M16*	13.68	247.5	0.687	0.681
40MMz	*M16*	14.58	248.6	0.663	0.654

Table 6.4: Total conditions characterizing the expansion analyzed to assess comparatively the influence of Z_T and of Γ_T on pressure ratio profiles.

pressure ratio on the specific total condition (P_T, T_T) has been observed also in x/H = 12.93.

6.3.2.1 *Comparative analysis on the influence of Z_T and Γ_T*

The previous sections 6.3.1 and 6.3.2 showed that the parameter Z_T is better suited, to identify a nozzle flow expansion in terms of pressure ratio profiles, than parameter Γ_T, since the values of $\Delta_{\Pi}^{\overline{\Gamma_T}}\%$ found are larger that the values of $\Delta_{\Pi}^{\overline{Z_T}}\%$. In order to analyze better this finding a comparison is presented in this section. Three different expansions are analyzed, the first one identified as *33MMx* is characterized by Z_T = 0.687 and Γ_T = 0.654. Other two expansion processes were chosen in order to be placed respectively on the iso-line of Z_T = 0.687 (*40MMy*) and of Γ_T = 0.654 (*40MMz*) but closer to the critical point with respect to the first chosen expansion *33MMx*. The total conditions characterizing these three expansions are plotted in Figure 6.13a and listed in Table 6.4, while the three expansions are plotted on a $T - s$ diagram in Figure 6.13b.
The two figures 6.13a and 6.13b show a coloured contour of Z superimposed to the iso-lines of Γ. The first thing to notice is that the iso-lines of Γ are non-monotonic near to the critical point while the iso-lines of Z do not show the same behavior. As a consequence the Γ iso-lines are approximatively parallel to the Z iso-lines in the thermodynamic region located at low pressures (bottom of P_T diagram Fig. 6.13a and bottom-right of $T - s$ diagram Fig.6.13b). Contrarily, Γ and Z iso-lines diverge in thermodynamic region closer to the critical point; where the Γ iso-lines tend to be steeper than the Z iso-lines. The three expansions analyzed here are chosen on purpose the closer to the critical point as they could be given the available measurements data. Therefore, since T_T of expansions *40MMy* and *40MMz* are very similar, the expansions *33MMx* and *40MMy* sharing the same Z_T are characterized by total pressure that are closer to each other with respect to the total pressures of expansions *33MMx* and *40MMz* sharing the same Γ_T (see Table 6.4). This is consistent with the fact that the pressure ratio profile of expansion *40MMy* are closer to those of expansion *33MMx*, than that of *40MMz*. Figure 6.14a report the pressure ratio profiles of *33MMx* and *40MMy* while Figure 6.14b report the ones of *33MMx* and *40MMz*. Both set of profiles are well overlapped to each other up to x/H = 11.86; profiles

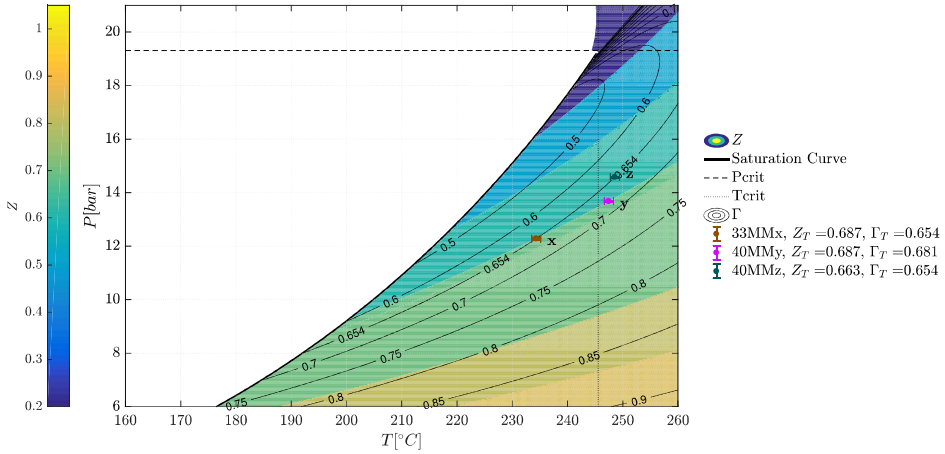

(a) *P – T diagram with Z contour and superimposed Γ iso-lines reporting the total conditions of the three expansions 33MMx, 40MMy and 40MMz.*

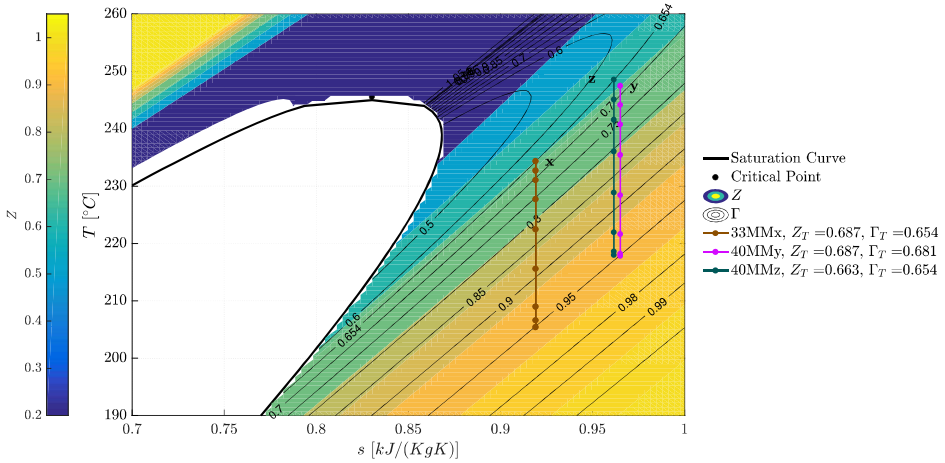

(b) *T – s diagram with Z contour and superimposed Γ iso-lines reporting the three expansions 33MMx, 40MMy and 40MMz.The dots correspond to the static temperatures computed from the static pressures measured.*

Figure 6.13

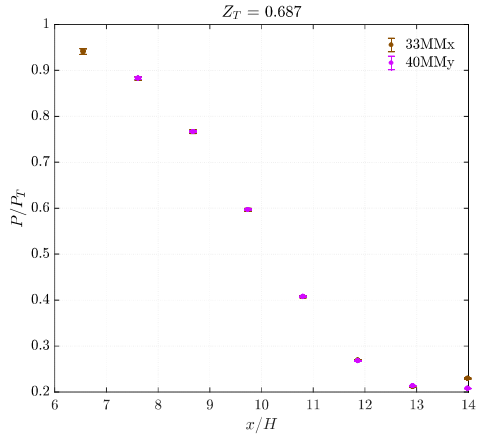

(a) *Pressure ratio profiles along the nozzle axis for the two expansions sharing* $Z_T = 0.687$ *(see Tab. 6.4).*

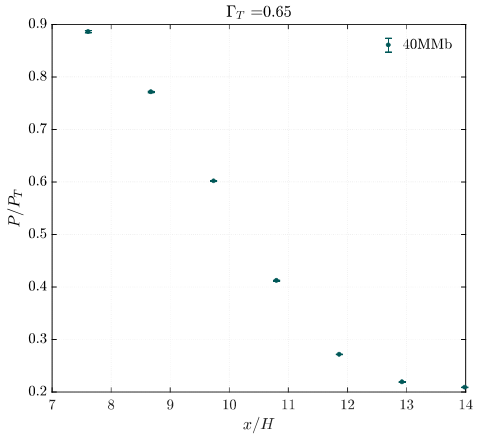

(b) *Pressure ratio profiles along the nozzle axis for the two expansions sharing* $\Gamma_T = 0.654$ *(see Tab. 6.4).*

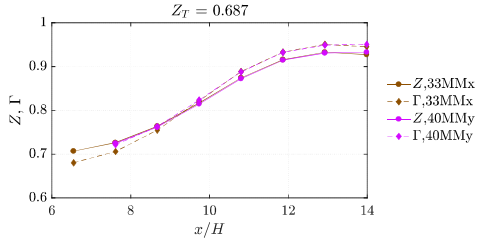

(c) *Z and* Γ *profiles on the nozzle axis for the two expansions sharing the same* $Z_T = 0.687$*, computed from the static pressure measurements as* $Z(P, s)$ *and* $\Gamma(P, s)$*.*

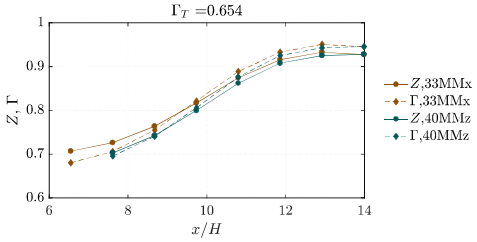

(d) *Z and* Γ *profiles on the nozzle axis for the two expansions sharing the same* $\Gamma_T = 0.654$*, computed from the static pressure measurements as* $Z(P, s)$ *and* $\Gamma(P, s)$*.*

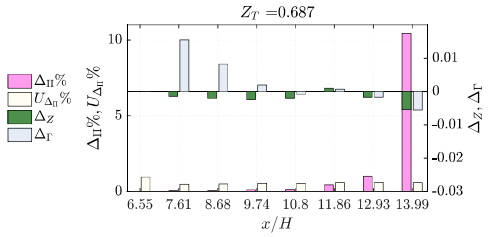

(e) $\overline{Z_T} = 0.687$*: The left axis shows in pink bars the percentage difference* $\Delta_\Pi^{\overline{Z_T}}$% *between pressure ratio and in white bars their uncertainty* $U_{\Delta_\Pi^{\overline{Z_T}}}$%*. The right axis reports in green bars the differences between compressibility factors* $\Delta_Z^{\overline{Z_T}}$ *and in gray bars the differences between the fundamantal derivative of gas-dynamic* $\Delta_\Gamma^{\overline{Z_T}}$*.*

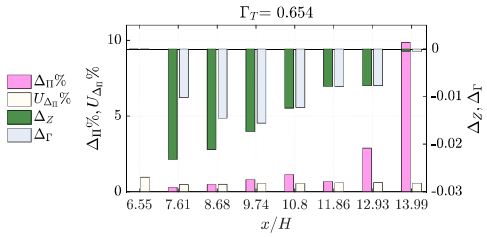

(f) $\overline{\Gamma_T} = 0.654$*: The left axis shows in pink bars the percentage difference* $\Delta_\Pi^{\overline{\Gamma_T}}$% *between pressure ratio and in white bars their uncertainty* $U_{\Delta_\Pi^{\overline{\Gamma_T}}}$%*. The right axis reports in green bars the differences between compressibility factors* $\Delta_Z^{\overline{\Gamma_T}}$ *and in gray bars the differences between the fundamantal derivative of gas-dynamic* $\Delta_\Gamma^{\overline{\Gamma_T}}$*.*

Figure 6.14

33MMx and *40MMy* diverge only in the last axial location x/H = 13.99 while profiles *33MMx* and *40MMz* show an appreciable discrepancy also in x/H = 12.93. This qualitative findings are confirmed by the values of Δ_Π% and of its uncertainty U_{Δ_Π}% shown in figures 6.14e and 6.14f. Here Δ_Π% is computed as the percentage difference between each of the two pressure ratios of tests *40MMy* and *40MMz* with respect to the pressure ratio measured in *33MMx*.

Figures 6.14c and 6.14d report the profiles of Z and Γ computed from the static pressured measured along the nozzle axis. It can be noticed that the Z profiles of expansions *33MMx* and *40MMy* are almost superimposed except in the last axial location x/H = 13.99 and their profile of Γ are also superimposed in the central part of the nozzle while they differ in the initial part where it was expected since the two expansions do not share the same initial Γ_T. On the other hand, both Z and Γ profiles of expansions *33MMx* and *40MMz* differ clearly except in the last axial location x/H = 13.99. This can be explained by the fact that the beginning of expansion *40MMz* is located in a region where the Γ iso-line in the $T - s$ diagram (Fig. 6.13b) start to diverge consistently while expansions *33MMx* and *40MMy* start in regions where they are almost parallel. This is a consequence of the fact that the Γ iso-lines are, steeper than the Z iso-lines close to the critical point. The fact that the total temperatures T_T^{40MMy} and T_T^{40MMz} are close led to the fact that, keeping the same Γ_T^{33MMx}, expansion *40MMz* start closer to the critical point than expansion *40MMy*, which instead keep the same Z_T^{33MMx}.

It can be concluded that in the thermodynamic region explored parameter Z_T performs better as univocal identifier of nozzle expansion flow behavior. Even though the dependence of pressure profiles on the total condition (P_T, T_T) has been proven, the value of Z_T alone can still be used to predict a nozzle flow with a good approximation. Parameter Γ_T instead performs worse and this can be related to the shape of Γ iso-lines in the thermodynamic region of interest.

6.3.3 *Influence of total temperature*

In ORC turbines, the total inlet temperature can vary by effect of different level of super-heating. For this reason, it is of interest for turbine operation to estimate how such variation affects the flow expansion. The influence of total temperature can be isolated by comparing pressure ratios of tests in conditions having same total pressure, but different T_T. Figure 6.15a reports all total conditions of nozzle expansions analyzed to assess the influence of T_T.

In Figures 6.15b, 6.15c, 6.15d, 6.15e, 6.15f, 6.15g, 6.15h and 6.15i pressure ratios measured at different total temperatures but same total pressure are shown at all available measured positions along the nozzle axis. Excluding the first two axial location where the pressure ratio are still close to one and the last axial location where the pressure gradient is near to zero, a clear trend can be noticed: the pressure ratio increases as the total temperature decreases. This is consistent with the fact that lower T_T at constant P_T leads to lower

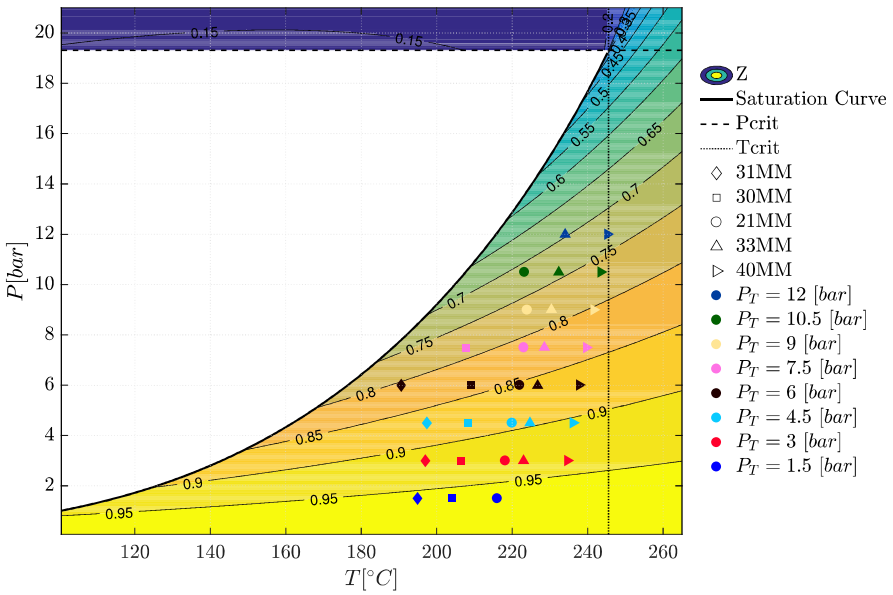

(a) *P – T diagram with Z contour reporting the total conditions of the expansions analyzed to assess the influence of the total temperature T_T on pressure ratio profiles.*

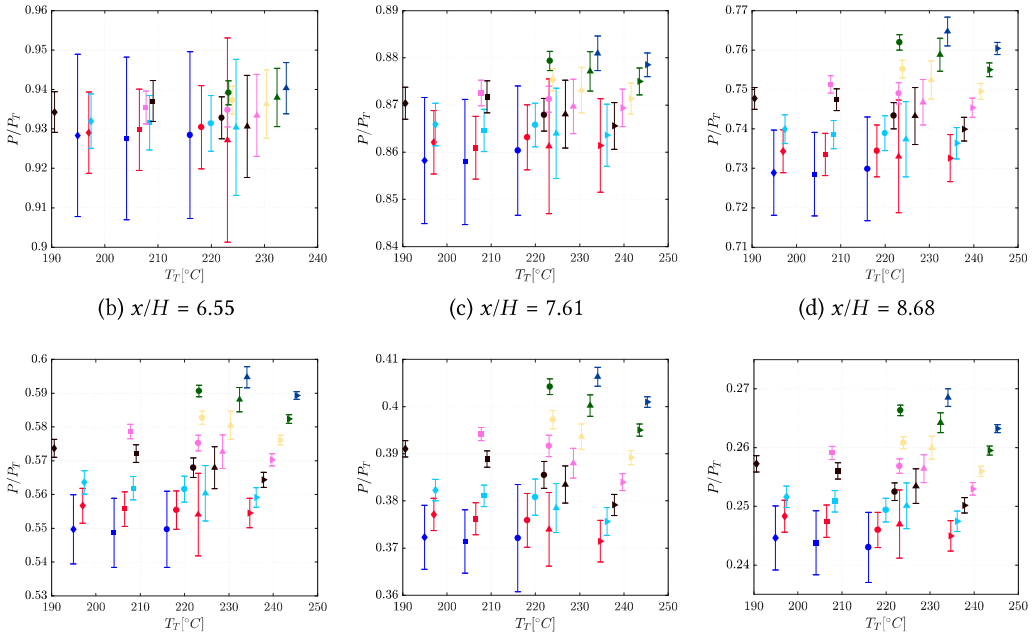

(b) x/H = 6.55 (c) x/H = 7.61 (d) x/H = 8.68

(e) x/H = 9.74 (f) x/H = 10.80 (g) x/H = 11.86

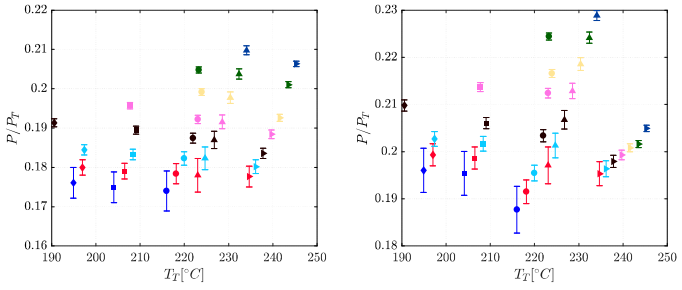

(h) x/H = 12.93 (i) x/H = 13.99

Figure 6.15

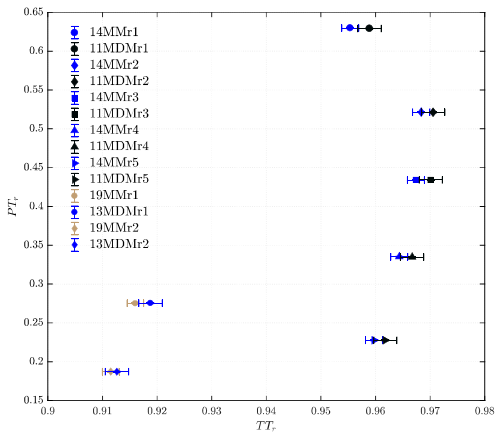

Figure 6.16: $P_r - T_r$ diagram reporting the total reduced conditions (listed in Tabel 6.5)of the expansions analyzed to carry out the comparison between MM and MDM nozzle flows.

total compressibility factors Z_T, thus higher non-ideal effects. Moreover the influence of a change in the total temperature is stronger in thermodynamic regions closer to the critical point due to higher Z variation for the same change in temperature. Indeed, as the total pressure decreases, pressure ratio trends with total temperature flatten and tend to remain constant (blue and red dots in Figures 6.15e, 6.15e), consistently with the approaching of ideal conditions.

6.4 COMPARISON BETWEEN MDM AND MM NOZZLE FLOWS EXPANSIONS

Nozzle *M15* was used in the *MDM vapor expansion* experimental campaign presented in chapter 5. Here a comparison between the MDM and MM nozzle flows is carried out. Test conditions with fluid MM were chosen in order to have the same total reduced conditions ($T_{Tr} = T_T/T_{critical}, P_{Tr} = P_T/P_{critical}$) as the one of fluid MDM. All total conditions considered for the comparison are listed in Table 6.5.
The Van der Waals equation of state is the simplest one capable of modelling non-ideal compressible effects. Its simplicity makes it a powerful tool for making qualitative considerations even though its quantitative accuracy is lower than other more complex equation of states. Following the Van der Waals model, two different fluids characterized by the same reduced conditions also share the same compressibility factor. Meaning that the Van der Waals model implies that the volumetric behavior of two fluid will be the same at if compared at constant reduced conditions. Table 6.5 reports the value of Z_T computed with a more accurate, state-of-the-art equation of state (Thol et al., 2017), for conditions sharing the same values of total reduced pressure PT_r and total reduced temperature TT_r. It can be seen that the values of Z_T differ by less than 1.5% between MM and MDM. This is an indication that the two fluids show a very similar volumetric behaviour if compared

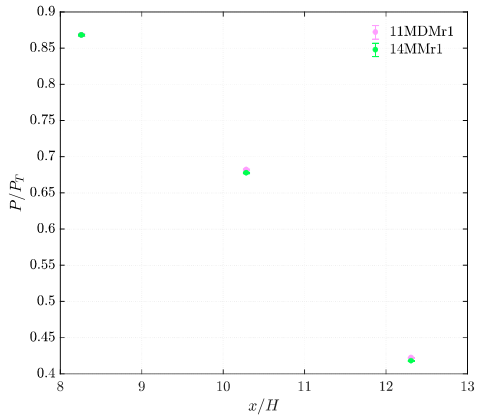

(a) *Pressure ratio profiles of expansions 11MDMr1 and 14MMr1.*

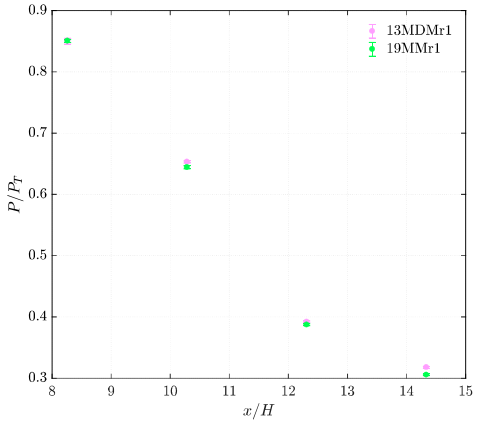

(b) *Pressure ratio profiles of expansions 13MDMr1 and 19MMr1.*

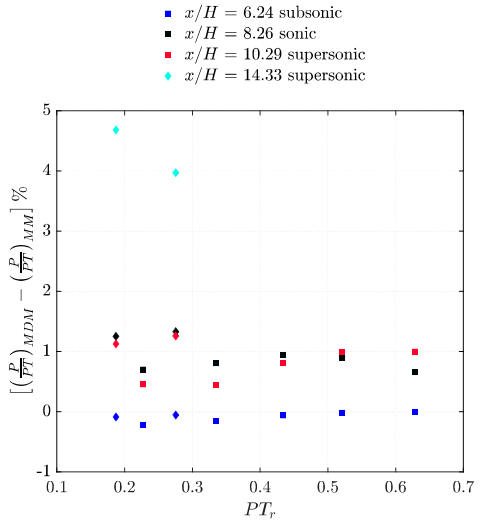

(c) *Percentage difference between MDM and MM pressure ratios. Each data set refer to a different axial location.*

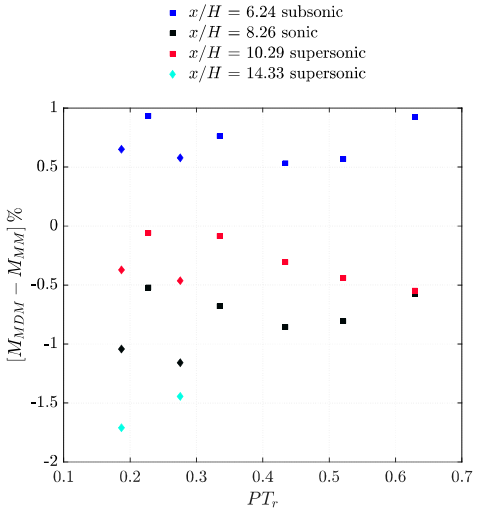

(d) *Percentage difference between MDM and MM Mach numbers. Each data set refer to a different axial location.*

Figure 6.17

		MM			MDM		
TT_r	PT_r	T_T [°C]	P_T [bar]	Z_T	T_T [°C]	P_T [bar]	Z_T
0.96	0.63	222.4	12.162	0.656	268.97	9.044	0.652
0.97	0.522	229.1	10.071	0.746	275.57	7.494	0.756
0.97	0.434	228.6	8.380	0.797	275.31	6.240	0.806
0.967	0.335	227.1	6.475	0.848	273.39	4.814	0.855
0.96	0.228	224.7	4.397	0.899	270.61	3.272	0.904
0.92	0.275	202.0	5.314	0.849	246.3	3.960	0.854
0.91	0.187	199.7	3.618	0.900	242.8	2.691	0.892

Table 6.5: Analysed conditions for comparison purposes between MM and MDM expansions.

at same reduced total conditions, as predicted following the Van der Waals model.
Indeed, pressure ratio profiles along the nozzle axis obtained for the analysed reduced conditions are almost superimposed, as shown in Figures 6.17a and 6.17b for two different total reduced condition. The maximum difference is located in the last pressure tap $x/H = 14.33$, whose measurements are available only in Figure 6.17b. Moreover the lower value of P/P_T is always achieved with fluid MM, as expected since it is less complex than fluid MDM.
Indeed, following the simplified approach if a *quasi-1D* flow coupled with the politropic Van der Waals equations of state one can find that the pressure ratio at any position of the nozzle axis is a function of the total reduced condition and of the complexity of the fluid. In order to find the pressure ratio in any axial location of a nozzle one must first solve the system of equation reported in (108), which holds for an isentropic nozzle flow where the total enthalpy h_T is conserved. Equations (108) permit to find the condition at the throat, here identified by the subscript t.

$$\begin{cases} h_T(T_T, v_T) = h(T_t, v_t) + \frac{1}{2}c^2(T_t, v_t) \\ s(T_T, v_T) = s(T_t, v_t) \end{cases} \tag{108}$$

The thermodynamic properties enthalpy h (Eq. (112)), entropy s (Eq. (113)) and sound velocity c (Eq. (114)) are computed from the Van der Waals volumetric equation of state (Eq. (109)) coupled with an expression for the isochoric specific heat capacity C_v computed

as the sum of an ideal-gas contribution $C_{vi} = (RN)/(2Mm)$ and a real-gas residual that is only dependent on the pressure (Eq. (111)).

$$P(T, v) = \frac{1}{Mm}\frac{RT}{v-b} - \frac{a}{v^2} \tag{109}$$

$$\tilde{P}(\tilde{T}, \tilde{v}) = \frac{8\tilde{T}}{3\tilde{v}-1} - \frac{3}{\tilde{v}^2} \tag{110}$$

$$C_v(T, v) = \frac{R}{2}\frac{N}{Mm} + T\int_{\infty}^{v}\left(\frac{\partial^2 P}{\partial T^2}\right)_v dv \tag{111}$$

$$h(T, v) = \frac{RT}{Mm} * \left[\frac{N}{2} + \frac{v}{v-b}\right] - \frac{2a}{v} + e_0 = \frac{RT_c\tilde{T}}{Mm}\left[\frac{N}{2} + \frac{\tilde{v}}{\tilde{v}-1/3}\right] - \frac{9RT_c}{4\tilde{v}Mm} + e_0 \tag{112}$$

$$s(T, v) = s_0 + \frac{NR}{Mm2}\ln\left(\frac{T}{T_0}\right) + \frac{R}{Mm}\ln\left(\frac{v-b}{v_0-b}\right) = s_0 + \frac{NR}{2Mm}\ln\left(\frac{\tilde{T}}{\tilde{T}_0}\right) + \frac{R}{Mm}\ln\left(\frac{\tilde{v}-1/3}{\tilde{v}_0-1/3}\right) \tag{113}$$

$$c^2(T, v) = v^2\left[\frac{RT(N+2)}{NMm(v-b)^2} - \frac{2a}{v^3}\right] = \frac{RT_c}{Mm}\left[\frac{N+2}{N}\cdot\frac{\tilde{v}^2}{(\tilde{v}-1/3)^2}\cdot\tilde{T} - \frac{9}{4\tilde{v}}\right] \tag{114}$$

Here the superscript $\tilde{}$ identifies the reduced conditions, the subscript c identifies the critical conditions, the subscript 0 identifies the standard conditions, R is the universal gas constant equal to $R = 8.314\, Jmol^{-1}K^{-1}$, Mm is the molecular mass, and N is the number of active degrees of freedom or energy modes, translational, rotational, and vibrational, of the fluid evaluated at its critical temperature. Both the translational and the rotational modes are assumed to be fully excited, whereas the activation of the vibrational ones occurs only at temperatures higher than the vibrational temperature associated with each mode.

Substituting equations (112), (114) and (113) in system (108) one can find that the conditions at the throat (T_t, v_t) are a function of the reduced total condition and N.

$$(T_t, v_t) = f(\tilde{T}_T, \tilde{v}_T, N) \tag{115}$$

Another system of equation (Eq. (116)) is solved to compute the conditions in term of temperature and specific volume (T, v) at any axial position; system (116) expressing the mass flow and entropy conservation.

$$\begin{cases} A\dfrac{1}{v}\sqrt{2[h_T - h(v, T)]} = A_t c_t \dfrac{1}{v_t} \\ s(T_T, v_T) = s(T, v) \end{cases} \tag{116}$$

Here A is the passage area at the axial coordinate where the conditions are to be found and A_t is the throat area. Again, substituting equations (112), (113) and (114) one can find

that the reduced condition at any axial location $(\tilde{T}, \tilde{v})$ are a function only of the total reduced conditions and of the number of active degrees of freedom.

$$(\tilde{T}, \tilde{v}) = f(\tilde{T}_T, \tilde{v}_T, N) \tag{117}$$

This implies that also the pressure ratio would be a function of the same quantities since it can be computed as $(\tilde{P}(\tilde{T}, \tilde{v})/\tilde{P}_T)$.
The two fluids MM and MDM show comparable complexities even though $N_{MDM} = 115$ is higher than $N_{MM} = 77.4$, this is consistent with the fact that the pressure ratios are quite close and the MM one are slightly lower.
Figures 6.17c and 6.17d report the percentage difference, calculated with respect of the MM data, of the pressure ratio and the Mach numbers of the two fluids at different axial positions. It can be concluded both in term of pressure ratios and of Mach number on the axis, that, in the thermodynamic region covered, the pressure ratio differences are lower than 5% for the axial coordinate $x/H = 14.33$ and lower than 1.5% for all others. Discrepancies in the Mach number are lower than 2% everywhere. Considering errors lower that 5% adequate to make a first approximation, non-dimensional nozzle flows on the axis for the two fluid MM and MDM can be approximated one with the other if the same total reduced conditions are maintained.

7

CONCLUSIONS

Results of three experimental campaigns carried out to study non-ideal compressible flows of high molecular complexity vapors in supersonic nozzles were presented. Nozzle expansion processes were selected as the most significant ones, for both fundamental research in non-ideal compressible fluid dynamics and industrial applications, especially for ORC power systems. A correct modeling of such unconventional fluid flows, by either theoretical or computational tools, demands detailed and reliable experimental data, which were still not available in the open literature, also due to difficulties of performing accurate measurements in high temperature and potentially condensing vapor flows. The reported measurements represent the first results obtained, aiming at overcoming the lack of experimental data and providing a reference dataset.

Several tests were performed on the nozzle test section of the TROVA, at the CREA of Politecnico di Milano, Italy. The thesis presents detailed insights into the operations of a wind tunnel for organic vapors (Sec. 1.4). The fluids investigated were siloxane MDM, and siloxane MM which are particularly suited for the proposed study, due to both their high molecular complexity and their wide application on ORC power systems. The thesis provides an extensive assessment of the measurement techniques suitable to perform experiments in non-ideal compressible fluid flows (Chap. 2). An ad-hoc calibration technique for piezo-resistive pressure transducer is presented (Sec. 2.2.1) together with technical details regarding pressure tap and test section design (Sec. 2.2). A novel technique capable of automatically detecting in schlieren images flow structures locally approximable with straight lines was presented in section 2.4. The method permits to obtain local Mach number measurements on the axis of the supersonic region of nozzle flows.

Three different experimental campaigns were carried out employing four different nozzles (Chap.s 4, 5 and 6). The flow field was investigated in terms of pressure distribution at the axis, of inlet total temperature and pressure and of schlieren visualization, which provided a direct measurement of the Mach number at the centerline of the nozzle diverging portion. Both MDM and MM nozzle flows proven to be non-ideal, since the inlet thermodynamic conditions significantly affect both the pressure ratio and the Mach number distribution along the nozzle axis (Sec.s 5.2, 6.2), contrarily to the well know behavior of perfect gases. Indeed, the very same nozzles operated with nitrogen showed no such dependence on total conditions (Sec. 4.2).

Within the *MM vapor expansion campaign* several tests were made with the aim of systematically exploring the thermodynamic region included between the vapor saturation curve and the critical temperature, which is the region where ORC turbines operate. The measurements obtained were used to assess if either the total compressibility factor

alone or the total fundamental derivative of gas-dynamic alone are sufficient to assess the level of non-ideality of a nozzle flow and thus, to characterize the expansion flow and predict pressure ratio profiles (Sec.s 6.3.1, 6.3.2, 6.3.2.1). It was concluded that, in the thermodynamic region explored, parameter Z_T performs better as univocal identifier of a nozzle expansion. Indeed, pressure ratio can be considered as a function only of Z_T with an error lower than 5%. Parameter Γ_T, instead, performs worse and this can be related to the shape of Γ iso-lines in the thermodynamic region of interest.
The influence of total temperature on the flow field was also analyzed by comparing pressure ratios distribution of tests in conditions exhibiting same total pressure, but different T_T (Sec. 6.3.3). A clear trend was found: the pressure ratio increases as the total temperature decreases, consistently with consequent change in Z_T.
A comparison between MM and MDM nozzle flows at the same total reduced conditions was performed (Sec. 6.4). It was concluded that, in the thermodynamic region explored pressure ratio profile of MM and MDM flows differ less than 1.5% for all axial coordinate up to x/H = 12.3 and less than 5% in x/H = 14.33.
The present thesis provides significant validation data for the improvement of state-of-the-art thermodynamic models and of design tools for siloxane fluids. The comparisons between CFD simulated and measurements data presented in sections 5.2.1 confirmed that still some work is required in order to achieve a better agreement between simulations and experiments in non-ideal compressible flows. In particular more accurate thermodynamic models are needed together with turbulence models better calibrated for non-ideal compressible flows.
Hence, the present study confirms the need of accounting for non ideal effects in the design and analysis of component operating in the non-ideal compressible regime of molecularly complex vapor. Also, the measurement techniques selected proven their suitability in detecting non-ideal behaviors in compressible flows. A reliable methodology is therefore reported, which is applicable to perform experiments on high temperature and potentially condensing vapor flows in highly non-ideal thermodynamic conditions. This allows to provide the demanded experimental data and to establish reference test cases for non-ideal compressible flows.
Future works will focus on broaden the measurement techniques applicable to non-ideal compressible flows. In particular on-going studies on the insemination process of organic vapors will probably lead to the possibility of performing LDV measurements, which would permit the direct acquisition of local velocity data. Moreover, the TROVA facility is being used to study non-ideal compressible flows around diamond-shaped airfoils, this will lead to a better understanding of the losses introduced by shock waves. Finally, the opportunity of using the TROVA as a wind tunnel for calibrating directional pressure probes for organic fluids is being analyzed. This would lead to the possibility of performing detailed measurements in actual turbines. These huge experimental efforts run in parallel with the creation of improved numerical tools, better tuned with the peculiar features of non-ideal compressible flows.

LIST OF FIGURES

LIST OF TABLES

8

ACRONYMS

ORC Organic Rankine Cycle

NICFD Non Ideal Compressible Fluid Dynamics
is a branch of fluid mechanics studying the actual characteristics of dense vapors, supercritical flows and compressible two-phase flows, namely whereby the thermodynamic behavior of the fluid differs considerably from that of an ideal gas.

CFD Computational Fluid Dynamics

LDV Laser Doppler Velocimetry
technique of using the Doppler shift in a laser beam to measure the velocity in transparent or semi-transparent fluid flows.

PIV Particle Image Velocimetry
optical method to obtain velocity vector fields in fluid flows seeded with tracer particles.

TROVA Test Rig for Organic VApors
Facility dedicated to the study of compressible fluid flows of organic fluids situated at Politecnico di Milano.

CREA Compressible fluid dynamic for Renewable Energy Applications laboratory
Inter-departmental laboratory operating in the field of non-ideal compressible fluid dynamics, with a special focus on applications for renewable energy systems.

MDM octamethyltrisiloxane $C_8H_{24}O_2Si_3$

MM hexamethyldisiloxane $C_6H_{18}O_3Si_3$

HFS Hydrofluorocarbons
are refrigerants containing Hydrogen, Fluorine, and Carbon.

R245fa Pentafluoropropane $C_3H_3F_5$

SU2 SU2
is an open-source collection of software tools written in C++ and Python for the analysis of partial differential equations (PDEs) and PDE-constrained optimization problems on unstructured meshes with state-of-the-art numerical methods.

CSP Concentrating Solar Power

CHP Combined Heat and Power

CCHP Combined Cooling, Heat and Power

ORCHID Organic Rankine Cycle Hybrid Integrated Device

LPV Low Pressure Vessel

HPV High Pressure Vessel

PID Proportional–Integral–Derivative
is a control loop feedback mechanism.

MCV Main Control Valve

BPCV By-Pass Control Valve

SSE Sum of Squared Errors
is a measure of the discrepancy between the data and an estimation model.

RMSE Root Mean Square Error
is a frequently used measure of the differences between values predicted by a model or an estimator and the values observed.

ZOH Zero Order Hold
is a mathematical model of the practical signal reconstruction done by a conventional digital-to-analog converter (DAC). That is, it describes the effect of converting a discrete-time signal to a continuous-time signal by holding each sample value for one sample interval.

TLS Total Least Square

PIG Polytropic Ideal Gas

iPRSV improved Peng Robinson Stryjek–Vera
thermodynamic model suiable for organic fluids presented in Stelt et al., 2012

BIBLIOGRAPHY

Alan, L., J. Kastengren, J.C. Dutton, and G.S. Elliot (2005). "A method for measuring recompression shock unsteadiness applied to two supersonic wakes." In: *Experiments in Fluids* 39, pp. 140–151 (cit. on p. 39).

Bahamonde, Sebastian, Matteo Pini, Carlo De Servi, Antonio Rubino, and Piero Colonna (2017). "Method for the Preliminary Fluid Dynamic Design of High-Temperature Mini-Organic Rankine Cycle Turbines." In: *Journal of Engineering for Gas Turbines and Power* 139.8. DOI: doi:10.1115/1.4035841 (cit. on pp. 4, 5).

Bradley, D. and G. Roth (2007). "Adapting thresholding using the integral image." In: *Journal of Graphics* 12, pp. 13–21 (cit. on p. 58).

Bufi, E. A. and P. Cinnella (2018). "Preliminary design method for dense-gas supersonic axial turbine stages." In: *Journal of Engineering for Gas Turbines and Power* 140, 112605–1:11 (cit. on p. 5).

Casati, Emiliano, Salvatore Vitale, Matteo Pini, Giacomo Persico, and Piero Colonna. "Centrifugal Turbines for Mini-Organic Rankine Cycle Power Systems." In: *Journal of Engineering for Gas Turbines and Power* 136 (12). DOI: doi:10.1115/1.4027904 (cit. on p. 4).

Cho, S.., Y. Jung, and C. Cho (2018). "Experimental study on the organic rankine cycle for recovering waste thermal energy." In: *International Journal of Renewable Energy Research* 8.1, pp. 120–128 (cit. on p. 10).

Cho, Soo-Yong, Chong-Hyun Cho, and Sang-Kyu Choi (2015). "Experiment and cycle analysis on a partially admitted axial-type turbine used in the organic Rankine cycle." In: *Energy* 90, pp. 643 –651. ISSN: 0360-5442. DOI: https://doi.org/10.1016/j.energy.2015.07.092. URL: http://www.sciencedirect.com/science/article/pii/S0360544215009871 (cit. on pp. 6–8, 10).

Colonna P. and, Guardone A., N.R. Nannan, and C. Zamfirescu (2008a). "Design of the Dense Gas Flexible Asymmetric Shock Tube." In: *Journal of Fluids Engineering* 130.3. ISSN: doi:10.1115/1.2844585 (cit. on pp. 7, 11).

Colonna, P., J. Harinck, S. Rebay, and A. Guardone (2008b). "Real-Gas Effects in Organic Rankine Cycle Turbine Nozzles." In: *Journal of Propulsion and Power* 24, pp. 282–294 (cit. on pp. 3, 114).

Colonna, P., E. Casati, C. Trapp, T. Mathijssen, J. Larjola, T. Turunen-Saaresti, and A. Uusitalo (2015a). "Organic Rankine Cycle Power Systems: From the Concept to Current Technology, Application, and an Outlook to the Future." In: *Journal of Engineering for Gas Turbine and Power* 137, pp. 100801–100801–19 (cit. on p. 4).

Colonna, P., A. Guardone, N. R. Nannan, and C. Zamfirescu (2015b). "The flexible asymmetric shock tube (FAST): a Ludwieg tube facility for wave propagation measurement

in high-temperature vapours of organic fluids." In: *Experiments in Fluids* 56 (cit. on pp. 7, 11).

Conti, C.C., A. Spinelli, A. Guardone, F. Cozzi, G. Cammi, and M. Zocca (2017). "Schlieren visualization of non-ideal compressible fluid flows." In: *12th International Conference on Heat Transfer, Fluid Mechanics and Thermodynamics, HEFAT2017* (cit. on p. 42).

Cozzi, F., A. Spinelli, M. Carmine, R. Cheli, M. Zocca, and A. Guardone (2015). "Evidence of complex flow structures in a converging-diverging nozzle caused by a recessed step at the nozzle throat." In: *45th AIAA Fluid Dynamics Conference, Dallas, TX, USA, 22-26 June* (cit. on p. 43).

Cozzi, F., E. Gottlich, L. Angelucci, V. Dossena, and A. Guardone (2017). "Development of a background-oriented schlieren technique with telecentric lenses for supersonic flow." In: *Journal of Physics: Conference Series*. Vol. 778. Chap. 1 (cit. on p. 38).

Duda, Richard O. and Peter E. Hart (1972). "Use of the hough trasformation to detect lines and curves in pictures." In: *Graphics and Image Processing* (cit. on p. 60).

Dùra Galiana, F. J., A. P. S. Wheeler, and J. Ong (2016). "A Study of Trailing-Edge Losses in Organic Rankine Cycle Turbines." In: *Journal of Turbomachinery* 138 (cit. on pp. 3, 7, 11).

D'Angelo, S., D. Vimercati, and A. Guardone (2018). "A unified description of oblique waves in ideal and non-ideal steady supersonic flows around compressive and rarefactive corners." In: *Acta Mech* 229, p. 2585. DOI: https://doi.org/10.1007/s00707-018-2130-6 (cit. on p. 2).

Estruch, D., N.J. Lawson, G. MacManus, K.P. Garry, and L. Stollery (2008). "Measurement of shock wave unsteadiness using a high-speed schlieren system and digital image processing." In: *Review of Scientific Instruments* 79 (cit. on p. 39).

Evaluation of measurement data, Supplement 2 to the 'Guide to the expression of uncertainty in measurement' , Extension to any number of output quantities (2008). Joint Committee for Guides in Metrology (cit. on p. 27).

Fergason, Stephen, Brian Argrow, and Alberto Guardone (2003). "Construction and Validation of a Dense Gas Shock Tube." In: *Journal of Thermophysics and Heat Transfer - J THERMOPHYS HEAT TRANSFER* 17, pp. 326–333. DOI: 10.2514/2.6789 (cit. on pp. 7, 11).

Fu, Ben-Ran, Yuh-Ren Lee, and Jui-Ching Hsieh (2015). "Design, construction, and preliminary results of a 250-kW organic Rankine cycle system." In: *Applied Thermal Engineering* 80, pp. 339 –346. ISSN: 1359-4311. DOI: https://doi.org/10.1016/j.applthermaleng.2015.01.077. URL: http://www.sciencedirect.com/science/article/pii/S1359431115001064 (cit. on pp. 6, 10).

– (2016). "Experimental investigation of a 250-kW turbine organic Rankine cycle system for low-grade waste heat recovery." In: *International Journal of Green Energy* 13.14, pp. 1442–1450. DOI: 10.1080/15435075.2016.1212353. eprint: https://doi.org/10.1080/15435075.2016.1212353. URL: https://doi.org/10.1080/15435075.2016.1212353 (cit. on p. 10).

Gallarini, S, A. Spinelli, F. Cozzi, and A. Guardone (2016). "Design and Commissioning of a Laser Doppler Velocimetry seeding system for non-ideal fluid flows." In: *12th International Conference on Heat Transfer, Fluid Mechanics and Thermodynamics* (cit. on p. 19).

Ghio, R., C. Raffaeli, A. Sabattini, V. Dossena, A. Fusetti, A. Spinelli, C. Osnaghi, and F. Cozzi (2017). "Experimental and numerical analysis of supersonic blade profiles developed for highly loaded impulse type steam turbine stages." In: *12th European Conference on Turbomachinery Fluid Dynamics and Thermodynamics, ETC 2017* (cit. on p. 38).

Giauque, Alexis, Christophe Corre, and Matteo Menghetti (2017). "Direct numerical simulations of homogeneous isotropic turbulence in a dense gas." In: *Journal of Physics: Conference Series* 821, p. 012017. DOI: 10.1088/1742-6596/821/1/012017 (cit. on p. 118).

Gladstone, J. H. and T. P. Dale (1864). *Researches on the refraction, dispersion and sensitiveness of liquids*. Phil. Trans. Royal Soc. London (cit. on p. 40).

Golub, G. H. and C. F. Van Loan (1980). "An analysis of the total least squares problem." In: *SIAM Journal on Numerical Analysis* 17, 883– 893 (cit. on p. 35).

Gori, G., M. Zocca, G. Cammi, A. Spinelli, and A. Guardone (2017). "Experimental assessment of the open-source SU2 CFD suite for ORC applications." In: *Energy Procedia* 129. 4th International Seminar on ORC Power SystemsSeptember 13-15th 2017POLITECNICO DI MILANOBOVISA CAMPUSMILANO, ITALY, pp. 256 –263. ISSN: 1876-6102. DOI: https://doi.org/10.1016/j.egypro.2017.09.151. URL: http://www.sciencedirect.com/science/article/pii/S1876610217340171 (cit. on pp. 3, 114).

Guardone, A., A. Spinelli, and V. Dossena (2013). "Influence of Molecular Complexity on Nozzle Design for an Organic Vapor Wind Tunnel." In: *Journal of Engineering for Gas Turbines and Power* 135 (cit. on p. 71).

Han, Sangjo, JongBeom Seo, and Bum-Seog Choi (2014). "Development of a 200 kW ORC radial turbine for waste heat recovery." In: *Journal of Mechanical Science and Technology* 28.12, pp. 5231–5241. ISSN: 1976-3824. DOI: 10.1007/s12206-014-1147-6. URL: https://doi.org/10.1007/s12206-014-1147-6 (cit. on pp. 5, 6, 8, 9).

Harinck, J., A. Guardone, and P. Colonna (2009). "The influence of molecular complexity on expanding flows of ideal and dense gases." In: *Physics of Fluids (1994-present)* 21.8 (cit. on pp. 2, 3).

Head, A. J., C. De Servi, E. Casati, M. Pini, and P. Colonna (2016). "Preliminary design of the ORCHID: A facility for studying non-ideal compressible fluid dynamics and testing ORC expanders." In: *Proceedings of ASME Turbo Expo* (cit. on pp. 8, 11).

Hung, P. C., G. Irwin, R. Kee, and S. McLoone (2005). "Difference equation approach to two-thermocouple sensor characterization in constant velocity flow environments."

English. In: *Review of Scientific Instruments* 76.2. Cited By :27, pp. 024902–1–024902–10. URL: www.scopus.com (cit. on pp. 32, 34).

Kaczmarczyk, Tomasz, Grzegorz Zywica, and Eugeniusz Inhatowicz (2018). "Experimental research on the domestic ORC micro power plant with a commercial biomass boiler." In: *E3S Web Conf.* 46, p. 00021. DOI: 10.1051/e3sconf/20184600021. URL: https://doi.org/10.1051/e3sconf/20184600021 (cit. on p. 9).

Kaczmarczyk, Tomasz Z., Grzegorz Żywica, and Eugeniusz Ihnatowicz (2017). "The impact of changes in the geometry of a radial microturbine stage on the efficiency of the micro CHP plant based on ORC." In: *Energy* 137, pp. 530 –543. ISSN: 0360-5442. DOI: https://doi.org/10.1016/j.energy.2017.05.166. URL: http://www.sciencedirect.com/science/article/pii/S0360544217309556 (cit. on pp. 6, 9).

Kang, Seok Hun (2012). "Design and experimental study of ORC (organic Rankine cycle) and radial turbine using R245fa working fluid." In: *Energy* 41.1. 23rd International Conference on Efficiency, Cost, Optimization, Simulation and Environmental Impact of Energy Systems, ECOS 2010, pp. 514 –524. ISSN: 0360-5442. DOI: https://doi.org/10.1016/j.energy.2012.02.035. URL: http://www.sciencedirect.com/science/article/pii/S0360544212001302 (cit. on pp. 6, 9).

– (2016). "Design and preliminary tests of ORC (organic Rankine cycle) with two-stage radial turbine." In: *Energy* 96, pp. 142 –154. ISSN: 0360-5442. DOI: https://doi.org/10.1016/j.energy.2015.09.040. URL: http://www.sciencedirect.com/science/article/pii/S0360544215012505 (cit. on pp. 5, 6, 9).

Keulen, L., S. Gallarini, C. Landolina, A. Spinelli, P. Iora, C. Invernizzi, L. Lietti, and A. Guardone (2018). "Thermal stability of hexamethyldisiloxane and octamethyltrisiloxane." In: *Energy* 165, pp. 868–876 (cit. on p. 16).

Klonowicz, Piotr, Aleksandra Borsukiewicz-Gozdur, Paweł Hanausek, Władysław Kryłłowicz, and Dieter Brüggemann (2014). "Design and performance measurements of an organic vapour turbine." In: *Applied Thermal Engineering* 63.1, pp. 297 –303. ISSN: 1359-4311. DOI: https://doi.org/10.1016/j.applthermaleng.2013.11.018. URL: http://www.sciencedirect.com/science/article/pii/S1359431113008065 (cit. on pp. 5–7, 10).

Lemmon, E. W., M. L. Huber, and M. O. McLinden (2013a). "NIST reference database 23: reference fluid thermodynamic and transport properties– REFPROP, version 9.1." In: *Standard Reference Data Program* (cit. on p. 5).

– (2013b). *NIST Standard Reference Database 23: Reference Fluid Thermodynamic and Transport Properties-REFPROP, Version 9.1, National Institute of Standards and Technology.* URL: https://www.nist.gov/srd/refprop (cit. on p. 17).

Li, Maoqing, Jiangfeng Wang, Lin Gao, and Yiping Dai (2012). "Performance Evaluation of a Turbine Used in a Regenerative Organic Rankine Cycle." In: *Proceedings of ASME*

Turbo Expo, Copenhagen, Denmark 6. DOI: doi:10.1115/GT2012-68441 (cit. on p. 10).

Lo, Rong-Chin and Wen-Hsiang Tsai (1995). "Gray-scale Hough trasform for thick line detection in grey-scale images." In: *Pattern Recognition* 28, pp. 647–661 (cit. on pp. 55, 62).

Luxa, Martin, Jaromír Příhoda, David Šimurda, Petr Straka, and Jaroslav Synáč (2016). "Investigation of the compressible flow through the tip-section turbine blade cascade with supersonic inlet." In: *Journal of Thermal Science* 25.2, pp. 138–144. ISSN: 1993-033X. DOI: 10.1007/s11630-016-0844-0. URL: https://doi.org/10.1007/s11630-016-0844-0 (cit. on p. 38).

Menter, Florian R. (1994). "Two-equation eddy-viscosity turbulence models for engineering applications." In: *AIAA*, pp. 1598–1605 (cit. on p. 75).

Merle, X. and P. Cinnella (2015). "Bayesian quantification of thermodynamic uncertainties in dense gas flows." In: *Reliability Engineering and System Safety* 134, pp. 305 –323 (cit. on p. 118).

Metrology, Joint Committee for Guides in (2008). *Evaluation of measurement data, Supplement 1 to the 'Guide to the expression of uncertainty in measurement', Propagation of distributions using a Monte Carlo method*. Bureau International des Pois et Mesures (cit. on p. 27).

Moffat, R.J. (1988). "Describing the Uncertainties in Experimental Results." In: *Journal of Fluids Engineering* 1:3-17 (cit. on p. 26).

Nemati, Hassan, Ashish Patel, Bendiks Jan Boersma, and Rene Pecnik (2015). "Mean statistics of a heated turbulent pipe flow at supercritical pressure." In: *International Journal of Heat and Mass Transfer* 83, pp. 741 –752. ISSN: 0017-9310. DOI: https://doi.org/10.1016/j.ijheatmasstransfer.2014.12.039. URL: http://www.sciencedirect.com/science/article/pii/S0017931014011478 (cit. on p. 118).

Ozawa, H. and S. J. Laurence (2018). "Experimental investigation of the shock-induced flow over a wall-mounted cylinder." In: *Journal of Fluid Mechanics* 849, 1009–1042. DOI: 10.1017/jfm.2018.433 (cit. on p. 38).

Passmann, Maximilian, Felix Reinker, Karsten Hasselmann, Stefan aus der Wiesche, and Franz Joos (2016). "Development and Design of a Two-Stage Contraction Zone and Test Section of an Organic Rankine Cycle Wind Tunnel." In: *Procceding of ASME Turbo Expo 2016, Seoul, South Korea* 3. ISSN: doi:10.1115/GT2016-56580 (cit. on pp. 7, 11).

Pei, Gang, Jing Li, Yunzhu Li, Dongyue Wang, and Jie Ji (2011a). "Construction and dynamic test of a small-scale organic rankine cycle." In: *Energy* 36.5, pp. 3215 –3223. ISSN: 0360-5442. DOI: https://doi.org/10.1016/j.energy.2011.03.010. URL: http://www.sciencedirect.com/science/article/pii/S0360544211001666 (cit. on pp. 6, 9).

Pei, Gang, Yun-zhu Li, Jing Li, and Jie Ji (2011b). "Performance evaluation of a micro turbo-expander for application in low-temperature solar electricity generation." In: *Journal*

of Zhejiang University-SCIENCE A 12.3, pp. 207–213. ISSN: 1862-1775. DOI: 10.1631/jzus.A1000105. URL: https://doi.org/10.1631/jzus.A1000105 (cit. on p. 9).

Persico, G., P. Gaetani, and A. Guardone (2005). "Dynamic calibration of fast-response probes in low-pressure shock tubes." In: *Meas. Sci. Technol.* 16, pp. 1751–1759 (cit. on p. 19).

Persico, Giacomo, Alessandro Romei, Vincenzo Dossena, and Paolo Gaetani (2018). "Impact of shape-optimization on the unsteady aerodynamics and performance of a centrifugal turbine for ORC applications." In: *Energy* 165, pp. 2 –11. ISSN: 0360-5442. DOI: https://doi.org/10.1016/j.energy.2018.09.044. URL: http://www.sciencedirect.com/science/article/pii/S0360544218318048 (cit. on p. 5).

Pini, M., C. De Servi, M. Burigana, S. Bahamonde, A. Rubino, S. Vitale, and P. Colonna (2017). "Fluid-dynamic design and characterization of a mini-ORC turbine for laboratory experiments." In: *Energy Procedia* 129. 4th International Seminar on ORC Power SystemsSeptember 13-15th 2017POLITECNICO DI MILANOBOVISA CAMPUSMILANO, ITALY, pp. 1141 –1148. ISSN: 1876-6102. DOI: https://doi.org/10.1016/j.egypro.2017.09.186. URL: http://www.sciencedirect.com/science/article/pii/S1876610217341000 (cit. on p. 11).

Quoilin, Sylvain, Martijn Van Den Broek, Sébastien Declaye, Pierre Dewallef, and Vincent Lemort (2013). "Techno-economic survey of Organic Rankine Cycle (ORC) systems." In: *Renewable and Sustainable Energy Reviews* 22, pp. 168 –186. ISSN: 1364-0321. DOI: https://doi.org/10.1016/j.rser.2013.01.028. URL: http://www.sciencedirect.com/science/article/pii/S1364032113000592 (cit. on p. 4).

Raffel, Markus (2015). "Background-oriented schlieren (BOS) techniques." In: *Experiments in Fluids* 56.3. Published online: 06. March 2015, Online ISSN 1432-1114, Nr. 56:6, pp. 1–17. URL: http://elib.dlr.de/95959/ (cit. on p. 38).

Reinker, Felix, Eugeny Y. Kenig, Max Passmann, and Stefan aus der Wiesche (2017). "Closed Loop Organic Wind Tunnel (CLOWT): Design, Components and Control System." In: *Energy Procedia* 129. 4th International Seminar on ORC Power Systems, pp. 200 –207. ISSN: 1876-6102. DOI: https://doi.org/10.1016/j.egypro.2017.09.158 (cit. on p. 11).

Rinaldi, E., R. Pecnik, and P. Colonna (2016). "Unsteady Operation of a Highly Supersonic Organic Rankine Cycle Turbine." In: *Journal of Turbomachinery* 138 (cit. on p. 3).

Sauer, R. (1947). *General characteristics of the flow through nozzles at near critical speeds.* TM 1147. NACA (cit. on p. 71).

Sauret, E. and G. Yuantong (2014). "Three-dimensional off-design numerical analysis of an organic Rankine cycle radial-inflow turbine." In: *Applied Energy* 135 (cit. on p. 3).

Schuster, A., S. Karellas, and R. Aumann (2010). "Efficiency optimization potential in supercritical Organic Rankine Cycles." In: *Energy* 35.2. ECOS 2008 21st International

Conference, on Efficiency, Cost, Optimization, Simulation and Environmental Impact of Energy Systems, pp. 1033 –1039. ISSN: 0360-5442. DOI: http://dx.doi.org/10.1016/j.energy.2009.06.019. URL: http://www.sciencedirect.com/science/article/pii/S0360544209002382 (cit. on p. 3).

Sciacovelli, L. and P. Cinnella (2014). "Numerical Study of Multistage Transcritical Organic Rankine Cycle Axial Turbines." In: *Journal of Engineering for Gas Turbines and Power* 136 (cit. on p. 3).

Sciacovelli, Luca, Paola Cinnella, and Xavier Gloerfelt (2017a). "DNS of supersonic turbulent channel flows of dense gases." In: *Journal of Fluid Mechanics* 821, pp. 153–199. DOI: 10.1017/jfm.2017.237 (cit. on p. 118).

Sciacovelli, Luca, Paola Cinnella, and Francesco Grasso (2017b). "Small-scale dynamics of dense gas compressible homogeneous isotropic turbulence." In: *Journal of Fluid Mechanics* 825, pp. 515–54. DOI: 10.1017/jfm.2017.415 (cit. on p. 118).

Sciacovelli, Luca, Paola Cinnella, and Xavier Gloerfelt (2018). "A Priori Tests of RANS Models for Turbulent Channel Flows of a Dense Gas." In: *Flow Turbulence and Combustion* 101, 295–315. DOI: 10.1007/s10494-018-9938-y (cit. on p. 118).

Settles, G. S. (2001). *Schlieren and Shadowgraph techniques. Visualizing Phenomena in Transparent Media.* Springer-Verlag Berlin Heidelberg (cit. on p. 40).

Seume, J R, M Peters, and H Kunte (2017). "Design and test of a 10kW ORC supersonic turbine generator." In: *Journal of Physics: Conference Series* 821.1, p. 012023. URL: http://stacks.iop.org/1742-6596/821/i=1/a=012023 (cit. on pp. 6, 8, 10).

Shao, Long, Xinling Ma, Xinli Wei, Zhonglan Hou, and Xiangrui Meng (2017a). "Design and experimental study of a small-sized organic Rankine cycle system under various cooling conditions." In: *Energy* 130, pp. 236 –245. ISSN: 0360-5442. DOI: https://doi.org/10.1016/j.energy.2017.04.092. URL: http://www.sciencedirect.com/science/article/pii/S0360544217306588 (cit. on p. 9).

Shao, Long, Jie Zhu, Xiangrui Meng, Xinli Wei, and Xinling Ma (2017b). "Experimental study of an organic Rankine cycle system with radial inflow turbine and R123." In: *Applied Thermal Engineering* 124, pp. 940 –947. ISSN: 1359-4311. DOI: https://doi.org/10.1016/j.applthermaleng.2017.06.042. URL: http://www.sciencedirect.com/science/article/pii/S1359431117339200 (cit. on pp. 6, 9).

Smith, N. T., M. J. Lewis, and R. Chellappa (2014). "Detection, localization and tracking of shock contour salient points in schlieren sequences." In: *AIAA Journal* 52.6, pp. 1249–1264. DOI: 10.2514/1.J052367 (cit. on p. 39).

Span, S. and W. Wagner (2003a). "Equations of State for Technical Applications I. Results for Nonpolar Fluids." In: *International Journal of Thermophysics* 24, pp. 41–109 (cit. on p. 5).

Span, S. and W. Wagner (2003b). "Equations of State for Technical Applications I. Simultaneously Optimized Functional Forms for Nonpolar and Polar Fluids." In: *International Journal of Thermophysics* 24, pp. 1–39 (cit. on p. 5).

Spinelli, A., V. Vandecauter, A. Guardone, and V. Dossena (2011). "Nozzle design for an organic vapor wind tunnel." In: *9th European Conference on Turbomachinery: Fluid Dynamics and Thermodynamics, ETC 2011 - Conference Proceedings*. Vol. 2, pp. 1161–1170 (cit. on pp. 3, 124).

Spinelli, A., M. Pini, V. Dossena, P. Gaetani, and F. Casella (2015). "Design, Simulation and Construction of a Test Rig for Organic Vapors." In: *Journal of Engineering for Gas Turbine and Power* 135, pp. 042304–042304–10 (cit. on pp. 7, 11, 12, 67, 101).

Spinelli, A., F. Cozzi, G. Cammi, M. Zocca, P. Gaetani, V. Dossena, and A. Guardone (2016). "Preliminary characterization of an expanding flow of siloxane vapor MDM." In: *Journal of Physics: Conference Series* 821.1. DOI: https://doi.org/10.1088/1742-6596/821/1/012022 (cit. on pp. 7, 11).

Spinelli, A., G. Cammi, M. Zocca, S. Gallarini, F. Cozzi, P. Gaetani, V. Dossena, and A. Guardone (2017). "Experimental observation of non-ideal expanding flows of Siloxane MDM vapor for ORC applications." In: *Energy Procedia* 129. 4th International Seminar on ORC Power SystemsSeptember 13-15th 2017POLITECNICO DI MILANOBOVISA CAMPUSMILANO, ITALY, pp. 1125 –1132. ISSN: 1876-6102. DOI: https://doi.org/10.1016/j.egypro.2017.09.237. URL: http://www.sciencedirect.com/science/article/pii/S1876610217341565 (cit. on p. 7).

Spinelli, Andrea, Giorgia Cammi, Simone Gallarini, Marta Zocca, Fabio Cozzi, Paolo Gaetani, Vincenzo Dossena, and Alberto Guardone (2018). "Experimental evidence of non-ideal compressible effects in expanding flow of a high molecular complexity vapor." In: *Experiments in Fluids* 59.8, p. 126. ISSN: 1432-1114. DOI: 10.1007/s00348-018-2578-0. URL: https://doi.org/10.1007/s00348-018-2578-0 (cit. on pp. 3, 7, 11).

Stelt, T.P. van der, N.R. Nannan, and P. Colonna (2012). "The iPRSV equation of state." In: *Fluid Phase Equilibria* 330, pp. 24–35. ISSN: 0378-3812 (cit. on pp. 51, 170).

Stryjek, R. and J. H. Vera (1986). "An Improved Peng-Robinson Equation of State for Pure Compounds and Mixtures." In: *Canadian Journal of Chemical Engineering* 64, pp. 323–333 (cit. on pp. 5, 75).

Tagawa, M. and Y. Ohta (1997). "Two-thermocouple probe for fluctuating temperature measurement in combustion: Rational estimation of mean and fluctuating time constants." In: *Combustion and Flame* 109.4, pp. 549 –560. ISSN: 0010-2180. DOI: https://doi.org/10.1016/S0010-2180(97)00044-8. URL: http://www.sciencedirect.com/science/article/pii/S0010218097000448 (cit. on p. 32).

Tagawa, M., T. Shimoji, and Y. Ohta (0998). "A two-thermocouple probe technique for estimating thermocouple time constants in flows with combustion: in situ parameter

identification of a first-order lag system." In: *Review of Scientific Instruments* 69.9, pp. 3370–3378 (cit. on p. 32).

Tartière, Thomas and Marco Astolfi (2017). "A World Overview of the Organic Rankine Cycle Market." In: *Energy Procedia* 129. 4th International Seminar on ORC Power SystemsSeptember 13-15th 2017POLITECNICO DI MILANOBOVISA CAMPUSMILANO, ITALY, pp. 2 –9. ISSN: 1876-6102. DOI: https://doi.org/10.1016/j.egypro.2017.09.159. URL: http://www.sciencedirect.com/science/article/pii/S1876610217340286 (cit. on p. 4).

Thol, M., F.H. Dubberke, E. Baumhögger, J. Vrabec, and R. Span (2017). "Speed of Sound Measurements and Fundamental Equations of State for Octamethyltrisiloxane and Decamethyltetrasiloxane." In: *Journal of Chemical and Engineering Data* 62.9, pp. 2633–2648. DOI: 10.1021/acs.jced.7b00092 (cit. on pp. 33, 68, 70, 75, 113, 114, 117, 118, 127, 139, 154).

Thompson, Philip A. (1971). "A Fundamental Derivative in Gasdynamics." In: *Physics of Fluids (1958-1988)* 14.9, pp. 1843–1849 (cit. on pp. 2, 113).

Turunen-Saaresti, Teemu, Antti Uusitalo, and Juha Honkatukia (2016). "Design and testing of high temperature micro-ORC test stand using Siloxane as working fluid." In: *Journal of Physics: Conference Series: Proceedings of NICFD 2016* 821.1. URL: http://iopscience.iop.org/article/10.1088/1742-6596/821/1/012024/meta (cit. on pp. 5, 8, 9).

Twomey, Braden, Andras Nagy, Hugh Russell, Andrew Rowlands, Jason Czapla, Rajinesh Singh, Carlos A de M Ventura, and Ingo Jahn (2016). "The University of Queensland Refrigerant and Supercritical CO2 Test Loop." In: *Proceedings of ASME Turbo Expo*. DOI: doi:10.1115/GT2016-58110 (cit. on pp. 6, 9).

Uusitalo, Antti, Juha Honkatukia, and Teemu Turunen-Saaresti (2017). "Evaluation of a small-scale waste heat recovery organic Rankine cycle." In: *Applied Energy* 192, pp. 146–158. ISSN: 0306-2619. DOI: https://doi.org/10.1016/j.apenergy.2017.01.088. URL: http://www.sciencedirect.com/science/article/pii/S0306261917300995 (cit. on p. 9).

Vimercati, D., G. Gori, A. Spinelli, and A. Guardone (2017). "Non-ideal effects on the typical trailing edge shock pattern of ORC turbine blades." In: *Energy Procedia* 129. 4th International Seminar on ORC Power SystemsSeptember 13-15th 2017POLITECNICO DI MILANOBOVISA CAMPUSMILANO, ITALY, pp. 1109 –1116. ISSN: 1876-6102. DOI: https://doi.org/10.1016/j.egypro.2017.09.231. URL: http://www.sciencedirect.com/science/article/pii/S1876610217341498 (cit. on p. 3).

Vimercati, Davide, Giulio Gori, and Alberto Guardone (2018). "Non-ideal oblique shock waves." In: *Journal of Fluid Mechanics* 847, 266–285. DOI: 10.1017/jfm.2018.328 (cit. on p. 2).

Vitale, S., G. Gori, M. Pini, A. Guardone, T. D. Economon, F. Palacios, J. J. Alonso, and P. Colonna (2015). "Extension of the SU2 Open Source CFD code to the simulation of

turbulent flows of fluids modelled with complex thermophysical laws." In: *22nd AIAA Computational Fluid Dynamics Conference* (cit. on pp. 3, 75, 106, 114).

Vitale, Salvatore, Tim A. Albring, Matteo Pini, Nicolas R. Gauger, and Piero Colonna. "Fully turbulent discrete adjoint solver for non-ideal compressible flow applications." In: *Journal of the Global Power and Propulsion Society* 1, pp. 252 –270. ISSN: 2515-3080. DOI: 10.22261/JGPPS.Z1FVOI. URL: https://journal.gpps.global/a/Z1FVOI/ (cit. on p. 5).

White, Martin T. and Abdulnaser I. Sayma (2018). "Design of a Closed-Loop Optical-Access Supersonic Test Facility for Organic Vapours." In: *Proceedings of ASME Turbo Expo, Oslo, Norway* 3, V003T28A002. DOI: doi:10.1115/GT2018-75301 (cit. on pp. 8, 11).

Yang, Yi, Yaowu Huo, Wenkai Xia, Xurong Wang, Pan Zhao, and Yiping Dai (2017). "Construction and preliminary test of a geothermal ORC system using geothermal resource from abandoned oil wells in the Huabei oilfield of China." In: *Energy* 140, pp. 633 –645. ISSN: 0360-5442. DOI: https://doi.org/10.1016/j.energy.2017.09.013. URL: http://www.sciencedirect.com/science/article/pii/S0360544217315190 (cit. on pp. 7, 8, 10).

Zimmerschied, Ralf and Rolf Isermann (2010). "Nonlinear time constant estimation and dynamic compensation of temperature sensors." In: *Control Engineering Practice* 18.3, pp. 300 –310. ISSN: 0967-0661. DOI: https://doi.org/10.1016/j.conengprac.2009.11.008. URL: http://www.sciencedirect.com/science/article/pii/S096706610900224X (cit. on p. 35).

Zocca, M., A. Spinelli, F. Cozzi, and A. Guardone (2018). "Influence of a recessed step at the throat section of a supersonic nozzle." In: *The Aeronautical Journal* 122.1251, 715–732. DOI: 10.1017/aer.2018.5 (cit. on pp. 71, 93, 117).

Zocca, Marta, Alberto Guardone, Giorgia Cammi, Fabio Cozzi, and Andrea Spinelli (2019). "Experimental observation of oblique shock waves in steady non-ideal flows." In: *Experiments in Fluids* 60.6, p. 101. ISSN: 1432-1114. DOI: 10.1007/s00348-019-2746-x. URL: https://doi.org/10.1007/s00348-019-2746-x (cit. on p. 56).

Zocca, Marta Maria (2018). "Experimental observation of supersonic non-ideal compressible-fluid flows." PhD thesis. Politecnico di Milano. URL: http://hdl.handle.net/10589/137310 (cit. on p. 117).

Zucrow, M. H. and J. D. Hoffman (1977). *Gas dynamics: multidimensional flow*. Vol. 2. Wiley, John & Son (cit. on p. 71).